Politecnico di Bari

Department of Electrical and Information Engineering
ELECTRICAL AND INFORMATION ENGINEERING
Ph.D. Program
SSD: ING-IND/33– ELECTRICAL POWER SYSTEMS

Final Dissertation

Methodologies and experiences for design, planning and operation in Microgrid framework

---

by
Benedetto Aluisio

Referees:

Prof. Stefano Massucco
(University of Genoa)

Prof. Selvarasan Iniyan
(Anna University, Chennai, India)

Supervisors:

Prof. Michele Antonio Trovato

_____

Eng. Chiara Vergine (Terna S.p.A.)

_____

Coordinator of Ph.D Program:
Prof. Vittorio Passaro.

_____

Course n°30, 01/11/2014-31/10/2017

Index

Summary

The thesis aims to inspect various aspects concerning the Microgrid (MG), as a way to integrate distributed electricity generation technologies, storage and loads. In this framework, the energy management represents a remarkable issue both in grid connected and islanded mode. This action is typically performed in the MG in two stages: a day-ahead planning, called to determine generation profiles of controllable sources according to forecasts, and real time dispatching, in order to smooth out load variation and renewable power fluctuations. In a centralized control scheme, the SCADA system is in charge of this function.

One of the main topics of this work is to draw up methodologies for day-ahead planning and operation of the Experimental MG realized at premises of the Power System Laboratory at Politecnico di Bari, including fuel-based and renewable production facilities, energy storage and loads. To this purpose, different procedures for day-ahead scheduling are proposed in Chapter 1, based on suitable models and according to specific operation strategies. The results of this step are validated by means of static and dynamic assessment. Moreover, experimental test of actual system operation according to planned power levels is provided.

A further characteristic of a MG is the contemporary coverage of thermal and electric demand. In this multi-energy system, the flexibility and economic operation is provided through CHPs facility and energy storage systems. In Chapter 2, planning procedures involving models for integrated water-based thermal supply infrastructure and dealing with occupant thermal comfort are proposed. In particular, the influence of thermal and electric energy storage is investigated in day-ahead operation planning, and the behaviour of different heating sources and thermal storage is assessed through a detailed engineering model. The procedures are applied to a configuration of Experimental Microgrid with empowered thermal section.

In Chapter 3, methodologies to deal with the diffusion of the Electric Vehicles (EV) are investigated. In particular, the integration of EV parking lot in MG as well as new concept of Electric vehicle supply infrastructure (EVSI) are evaluated. In the first case, the day-ahead planning of MG with a fleet of EV is investigated, focusing on interactions between EV aggregator and MG operator. In the latter, structures for AC and DC EVSI are presented, that include energy storage system, PV plant, charging points, also in V2G configuration and a common bus. In particular, the optimal design of an AC and DC EVSI is proposed, aiming at defining the size and technology of devices. The DC solution is designed on different configurations in order to realize a demonstrator in the Bari port area, in the framework of the CONNECT project, financed in the H2020 call ECSEL 2016.

Publications related to Ph.D. activity

{1} B. Aluisio, A. Cagnano, E. De Tuglie, M. Dicorato, G. Forte, M. Trovato, "An architecture for the monitoring of microgrid operation", Proc. of 2016 IEEE Workshop on Environmental, Energy, and Structural Monitoring Systems - Bari, Italy, 13-14 June 2016, pp. 1-6, ISBN: 978-1-5090-2370-7.

{2} B. Aluisio, M. Dicorato, G. Forte, M. Trovato, "Hybrid Energy Storage System Optimization for Improving Wind Power Integration", Proc. of PSCC 2016 – 19th Power Systems Computation Conference, June 20-24 2016, Genoa, Italy, pp. 1-6, ISBN: 978-88-941051-2-4.

{3} B. Aluisio, A. Cagnano, E. De Tuglie, M. Dicorato, G. Forte, M. Trovato, "Procedures for day-ahead operation planning of heat and power supplying Smart Grid", Proc. of 2016 UPEC Universities' Power Engineering Conference 2016 – Coimbra, Portugal, 6-9 Sept. 2016, pp. 1-6, ISBN: 978-1-5090-4650-8.

{4} B. Aluisio, A. Cagnano, E. De Tuglie, M. Dicorato, G. Forte, M. Trovato, "PrInCE lab microgrid: Early experimental results", Proc. of 2016 AEIT International Annual Conference 2016 - Capri, Italy, 5-7 Oct. 2016, pp. 1-6, ISBN: 978-8-8872-3730-6.

{5} B. Aluisio, M. Dicorato, G. Forte, M. Trovato, A. Sallati, C. Gadaleta, C. Vergine, F. Ciasca, "The application of a flow-based methodology for yearly network analysis according to market data", Proc. of EEM2017 – 14th International Conference on the European Energy Market, Dresden (Germany), 6-9 June 2017, pp. 1-6, ISBN: 978-1-5090-5499-2.

{6} B. Aluisio, M. Dicorato, G. Forte, M. Trovato, "An optimization procedure for Microgrid day-ahead operation in the presence of CHP facilities", Sustainable Energy, Grids and Networks, Volume 11, September 2017, Pages 34-45, Elsevier Science, ISSN: 2352-4677

{7} B. Aluisio, M. Bronzini, M. Dellapigna, M. Dicorato, G. Forte, M. Trovato, "Network Assessment in Static and Dynamic Conditions of Microgrid Optimal Operation Plan", Proc. of 2017 AEIT International Annual Conference – 20-22 Sept. 2017, Cagliari, Italy.

{8} B. Aluisio, M. Dicorato, G. Forte, R. Sbrizzai, M. Trovato, M. Mega "Energy Efficiency Improvements in Port Areas: towards an Integrated Energy Management", Proc. of 2017 AEIT International Annual Conference – 20-22 Sept. 2017, Cagliari, Italy.

{9} B. Aluisio, M. Dicorato, G. Forte, M. Trovato, "A Monte-Carlo Based Procedure for Optimal Sizing of Integrated Electric Vehicle Supply Infrastructure", Proc. of IEEE PES Innovative Smart Grid Technology Europe (ISGT Europe 2017) – 27-29 Sept. 2017, Turin, Italy.

{10} B. Aluisio, M. Dicorato, G. Forte, M. Trovato, "Embedding Energy Storage for Multi-Energy Microgrid Optimal Operation", Proc. of IEEE PES Innovative Smart Grid Technology Europe (ISGT Europe 2017) – 27-29 Sept. 2017, Turin, Italy.

{11} B. Aluisio, A. Conserva, M. Dicorato, G. Forte, M. Trovato, "Optimal operation planning of V2G-equipped Microgrid in the presence of EV aggregator", Electric Power Systems Research, Volume 152, November 2017, Pages 295–305, Elsevier Science, ISSN 0378-7796.

{12} B. Aluisio, M. Dicorato, G. Forte, G. Litrico, M. Trovato, "Integration of heat production and thermal comfort models in microgrid operation planning", under revision at Applied Energy, Elsevier Science.

1. Procedure for Microgrid management and test in experimental facility

Microgrids are more and more called to satisfy, through the management of distributed generation sources and the electricity network, the demand for energy by local users. In particular, the operation of different energy sources has to be monitored and controlled by means of the Energy Management Systems (EMS) both in the grid-connected and islanded modes. In the first case, the MG can be seen as a single controllable unit by the grid operator whereas in the islanded mode the successful balance between internal load and planned generation is also required. However, the simultaneous production of electrical and thermal energy by means of Combined Heat and Power (CHP) systems represents one of the features of a Microgrid and can contribute to improve system reliability, efficiency and economic performance. To this purpose, in this section procedures for day-ahead scheduling of a CHP-based Microgrid is developed, aiming to minimize operation and emission costs of Microgrid components in the presence of electric and thermal loads and renewable forecasts. This procedures are modelling in linear and non linear mathematical formulation, in order to appreciate the behaviour of main MG devices. Since, the real-time operation microgrid control strategies yielded by optimal daily plan trough a procedure for minute-by-minute program definition is proposed. In this way, the network assessment with a detailed static and dynamic models of system is performed. Finally, to reproduce the verified optimal plan is tested in the actual microgrid operation, with a view to highlight peculiarities of the devices to be included in the procedure and to improve the fitness to actual operation of the devices. The described methodologies are evaluated and tested on the experimental facility realized in the Electric Power System laboratory of Politecnico di Bari. In the following sub-section, key details of the PrInCE experimental microgrid are illusted

1.1 Experimental facility

In the PrInCE experimental microgrid developed at Power and Energy System Laboratory (PEnSy-Lab) of the Politecnico di Bari. The system involves different commercial generators, usually aimed to operate as a single power source for a load with grid support. Moreover, the presence of cogeneration systems and the possibility to include thermal demand can open the field to several field tests. The general outline of PrInCE microgrid is illustrated in Fig. 1.1. It is a low-voltage network including several devices for energy production, storage and demand. In particular, generation facilities involve:

- a gas-fueled CHP system, equipped with two variable-speed engines with total 105 kW rated electric power, controlled by means of inverters, with an embedded 10 kW lead-acid energy storage on the DC-link;
- a gas microturbine with 30 kW nominal power, able to perform cogeneration tasks in electric-following or thermal-following modalities;
- a photovoltaic field composed of five 10-kW sub-arrays, each with a separate inverter and a different panel technology (triple-junction a-Si; Mono-Si; Poly-Si; CIS; Mono N-Type).

Energy storage systems are represented by:

- an high-temperature battery, based on sodium-nickel cells working at roughly 260 °C, with nominal power of 60 kW and a discharge duration of 3 hours, equipped with state-of-charge (SOC) monitoring;

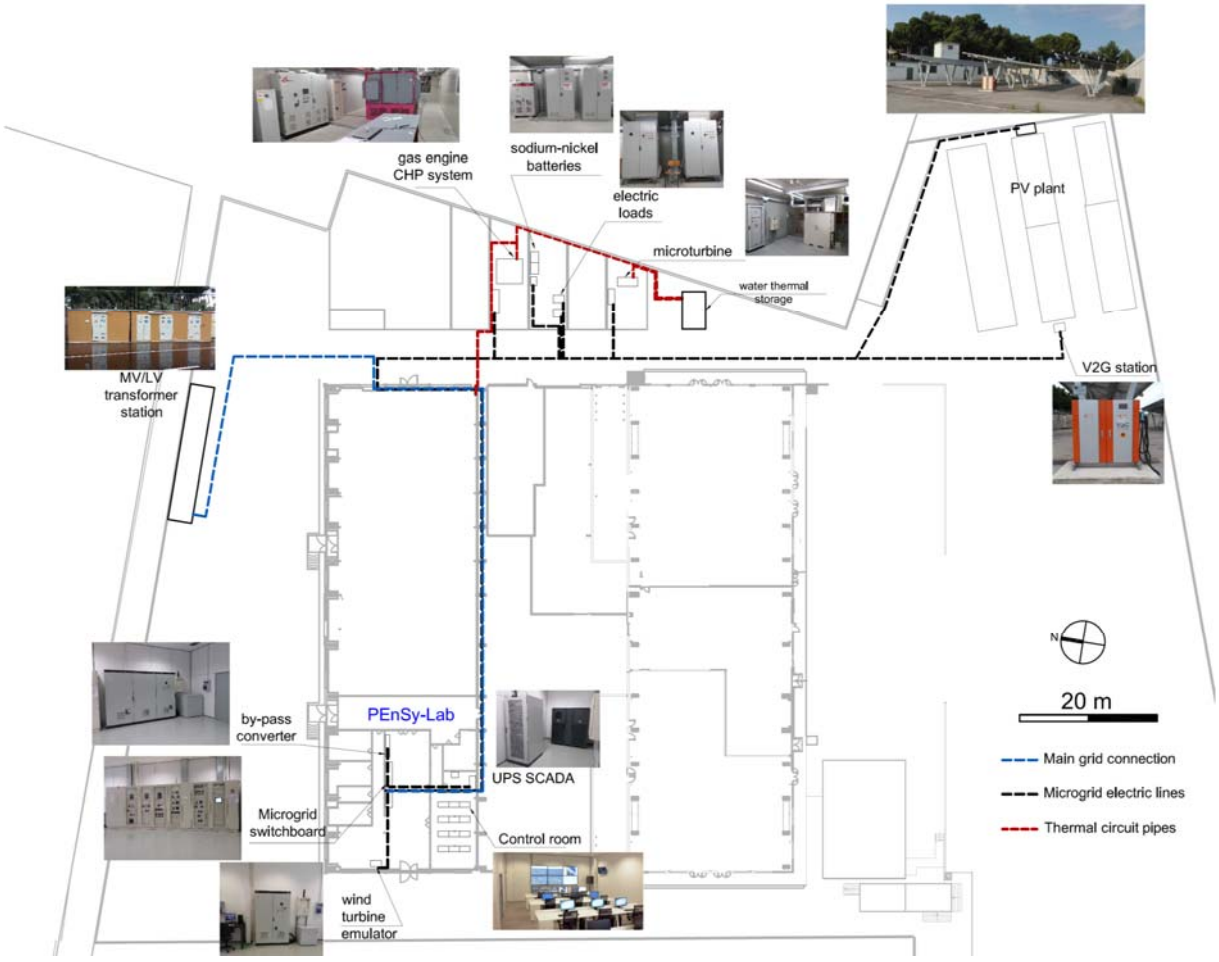

Fig. 1.1. Layout of components of PrInCE microgrid

- a DC station for Plug-in Electric Vehicles able to perform controlled charge as well as vehicle-to-grid skills up to 10 kW.

Inverter-based devices are provided as well:

- a wind turbine emulator, with 60 kVA rated power, based on a back-to-back converter withdrawing energy from the main network and injecting it in the microgrid according to proper static and dynamic models of different mini-wind generators and to measurement coming from an anemometer;
- two programmable loads, with 150 kVA rated power each, able to replicate active and reactive power needs of different kinds of load as well as voltage dependence of power demand through typical polynomial functions;
- a by-pass converter, with 200 kVA rated power, which allows the power exchange with the main network to be fixed at a specified value.

The facility can host other plug-in load/generation devices, up to a residual capacity of 100 kW. The auxiliary services needed to run and control all the components are fed by means of a dedicated line of the microgrid switchboard, equipped with a 30-kW UPS device.

The possibility to feed a part of actual electric loads of the warehouse hosting the PEnSy-Lab and other test facilities of Politecnico di Bari has been provided, by means of suitable integration devices. The same process can be implemented for thermal demand, by means of proper heat exchangers linked up to microgrid CHP devices and water tanks for thermal storage.

The microgrid is normally operated in grid-connected mode, by closing the interfacing switch as represented in the one-line diagram reported in Fig. 1.2, where the line lengths are reported as well. In grid-connected condition, the power generation levels of microgrid components are usually determined in advance according to a cost minimization function [1][2], and a further control is performed in order to cope with variations of renewable sources and load.

Islanded operation mode is provided as well, in order to prove both the ability of the system to deal with mode transition and the adequacy of internal sources to comply with balancing and regulation issues [3][4][5]. Moreover, on isochronous frequency control is adopted, since one of the devices is called to operate as voltage forming [6][7]. This task can be executed by the gas-based CHP system, by the microturbine or by the sodium-nickel battery. The first is able to manage dynamically the transitions thanks to the internal storage, whereas the microturbine needs to start over the system from blackout and the battery can be limited by its SOC.

Each of these three devices is commercialized as a back-up supply and is equipped with a separate circuit for preferential loads. The activation of this circuit, i.e. the microgrid stand-alone operation, is actuated by opening the corresponding line disconnector located in an ad hoc local switchboard illustrated in Fig. 1.2. Proper interlocks between those disconnectors and main line switches avoid either the presence of two independent voltage forming sources on the islanded microgrid or the operation in grid-connected mode with an internal voltage source.

The reconnection to the main network is operated by synchronizing the internal voltage source with the external reference voltage (Vref in Fig. 1.2), by activating a separate disconnector. The voltage synchronization in amplitude and phase, within a narrow threshold, is verified by a synchrocheck device on the interfacing switch.

The presence of the by-pass converter allows to realize programmed transitions from grid-connected to islanded mode, by reducing the power flow on the switch and controlling the power exchange through the converter.

As can be seen in Fig. 1.2, all the devices connected to the MG are equipped with inverters. This allows to put inforce distributed control and regulation tasks, even on reactive power, whereas the disadvantage is the absence of rotating devices directly connected to the system, suffering from the lack of inertia [8][9]. This may cause faster and larger frequency deviations after an event (e.g. islanding). Hence, proper setting of local controller needs to be investigated.

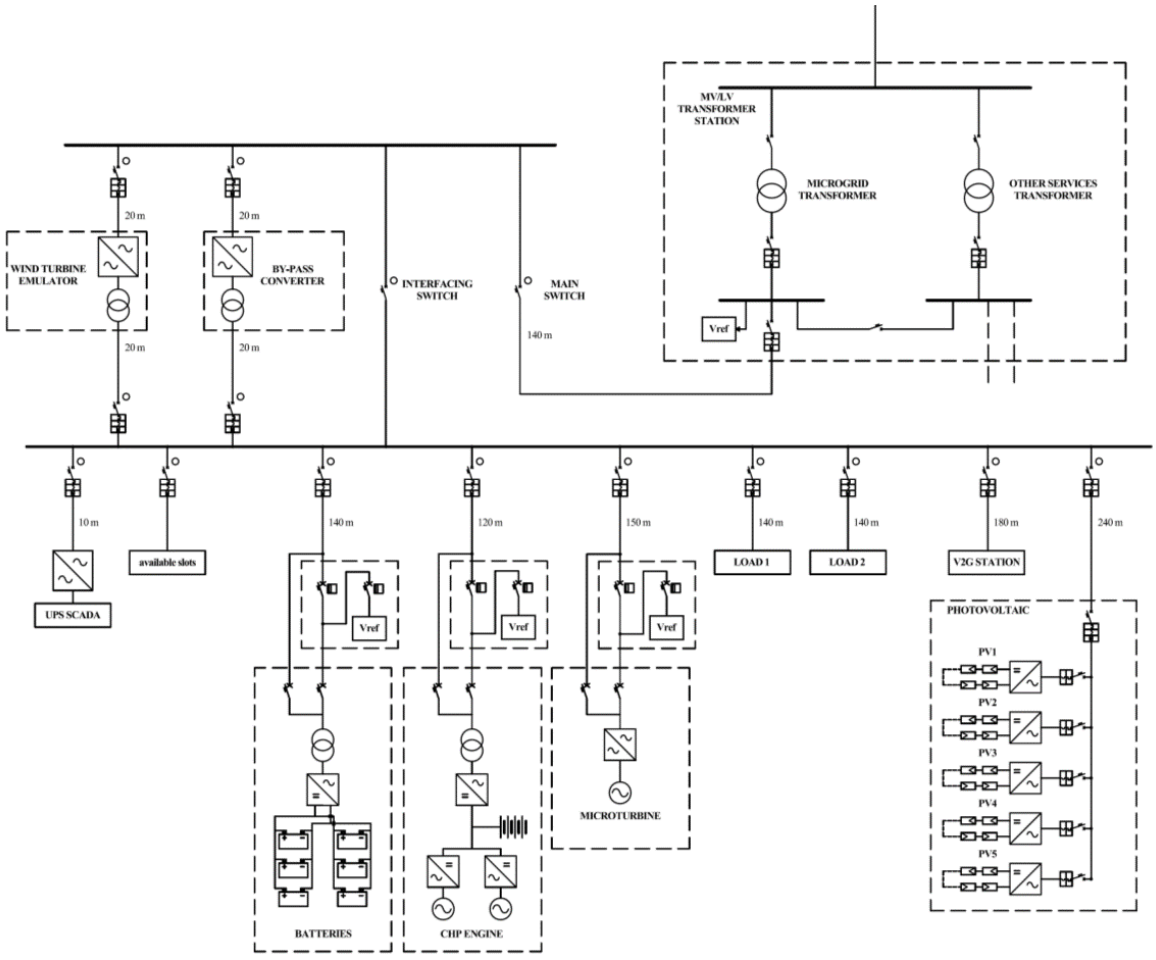

Figure 1.2. One-line diagram of the PrInCE microgrid

The MG is supervised and controlled by a SCADA system exploiting an Ethernet network communication adopting fully redundant connections in optical fiber among nodes. The

network is based on Modbus TCP/IP communication protocol, and the SCADA platform is fully programmable according to the requirements of the research group, that can implement proper functions. In Fig. 1.3 the control architecture of the SCADA system integrated into the MG is shown.

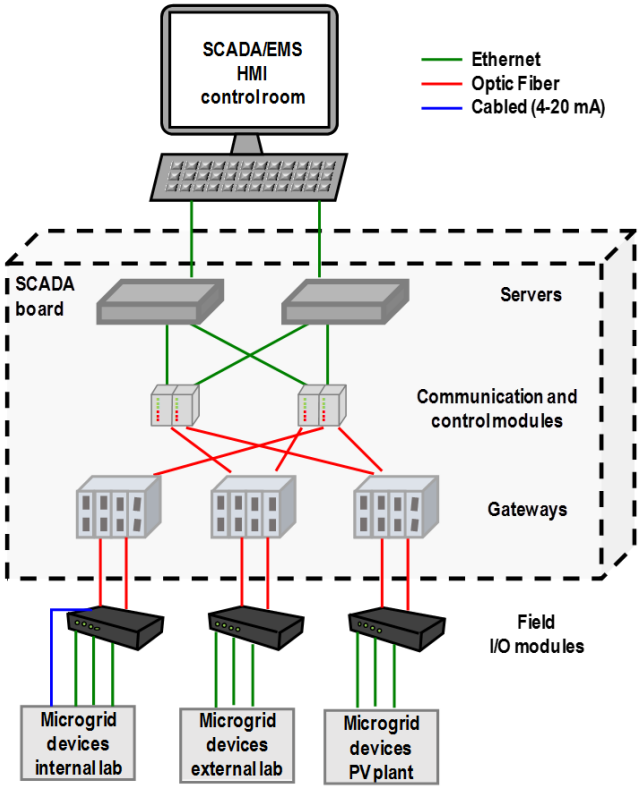

Figure 1.3. SCADA architecture of the experimental MG.

The field communication includes gateways connected to distribuited controllers (Programmable Logic Controllers – PLCs) by fiber optic, conveying monitoring and control signals from/to MG field devices, via Ethernet cables. Unit-level controllers are in charge of local monitoring and data exchange. Since each component of the MG is equipped with its own communication platform. In this way, suitable protocol converters and gateways are installed at device premises. Moreover, fast control actions, for instance to ensure secure operation and to verify actual implementation of control signals, are based on a cabled logic on a 4-20 mA measurement system in the general electric panel, close to the SCADA system servers.

The SCADA architecture is based on two control levels. The upper control level implements the Energy Management functions to control and coordinate actions of all the devices to ensure the optimal operation, from an economical point of view, of the MG. Local controllers or actuators accomplish the lower control level. Centralized control actions are evaluated by the

EMS through appropriate control strategies aimed at optimizing the MG with respect to economic objectives and operational security issues.

The main EMS functions are the following:

- mode transition between grid-connected and stand-alone and vice versa, involving proper sub-functions for power flow shifting, load shedding and generation shedding;
- operation programming through a day-ahead planning, including renewable generation forecast, load forecast and techno-economic data collection;
- online operation, consisting in regulation sharing in the case of sudden variations in voltage and power regulation, in security checks for operation of switches and disconnectors.

1.2 Procedures for day-ahead operation planning

In this sub-section, different formulations of a day-ahead operation planning are proposed, characterized by linear or non-linear objective function and constraints, to be implemented in a general EMS for the MG management. A particular focus is devoted to coordinate the production of electric power through dispatchable generators and storage devices to satisfy the internal energy demand. Furthermore, thermal energy model is provided, coupled to the electricity production through combined heat and power systems. The developed strategies are characterized by the minimization of operation and equivalent emission cost, subject to dynamic constraints related to energy balances and technical limits of the considered devices. The implementation of the approaches, on the aforementioned test bed system, permit to compare relevant results and define the best feet solution, in different operating conditions and connection schemes.

1.2.1 Problem formulations

The general formulation of a day-ahead operation planning in a MG framework is linked to an optimization problem, where the function $f(\mathbf{x})$ is minimized subject to equality and inequality constraints, named $g(\mathbf{x})$ and $h(\mathbf{x})$ respectively. Hence, the proposed approach involves the minimization of daily operation cost of the MG, in the face of a forecasted generation from non-dispatchable sources (e.g. wind and photovoltaic systems) and the load demand (in terms of electric and thermal energy).

$$\begin{aligned} &\min f(\mathbf{x}) \\ &s.t. \begin{cases} g(\mathbf{x}) = 0 \\ h(\mathbf{x}) \leq 0 \end{cases} \end{aligned} \tag{1.1}$$

The objective function $f(\mathbf{x})$ represents the operation cost in the considered time horizon, divided into N_t time steps with Δt duration, determined as follows:

$$f(\mathbf{x}) = \sum_{t=1}^{N_t} \left[\sum_{k=1}^{N_k} \left(OC(k,t) + EC(k,t) \right) + \sum_{s=1}^{N_s} OS(s,t) + C_g(t) \right] \tag{1.2}$$

In particular, the components of the objective function can be expressed as:

- operation cost related to the operation of k-th fuel-based generation unit at time t $OC(k,t)$;
- emission cost related to the operation of k-th fuel-based generation unit at time t $EC(k,t)$;
- operation cost related to the of s-th energy storage unit at time t $OS(s,t)$;
- cost for energy withdrawal from the distribution network $C_g(t)$.

Moreover, the cost components related to electric power production devices depend on power production level $P(k,t)$ as follows:

$$OC(k,t) = \frac{uc(k) \cdot \Delta t \cdot P(k,t)}{H(k) \cdot \eta_E(k)} \tag{1.3.a}$$

$$EC(k,t) = ue \cdot \varepsilon_E(k) \cdot \Delta t \cdot P(k,t) \tag{1.3.b}$$

where $uc(k)$, $H(k)$ and $\eta_E(k)$ stand for unitary fuel cost, fuel heating value and electric efficiency, respectively; whereas ue and $\varepsilon_E(k)$ represent unitary emission cost and electric emission factor. For cogeneration systems, the thermal power $Q(k,t)$ is connected to electric power by the ratio of the efficiencies, as follows:

$$Q(k,t) = \frac{\eta_t(k)}{\eta_E(k)} \cdot P(k,t) \tag{1.3.c}$$

where $\eta_t(k)$ stand for thermal efficiency.

For thermal generation units, costs are related to thermal power production level $Q(k,t)$ as follows:

$$OC(k,t) = \frac{uc(k) \cdot \Delta t \cdot Q(k,t)}{H(k) \cdot \eta_t(k)} \tag{1.4.a}$$

$$EC(k,t) = ue \cdot \varepsilon_t(k) \cdot \Delta t \cdot Q(k,t) \tag{1.4.b}$$

where $\varepsilon_t(k)$ represent thermal emission factor.

Operation cost of the s-th energy storage device can be expressed as:

$$OS(s,t) = ec(s) \cdot soc(s,t) + pc(s) \cdot \left[P_d(s,t) + P_c(s,t) \right] \tag{1.5}$$

where $soc(s,t)$ represents the state of charge of the ESS, related to energy exploitation cost $ec(s,t)$, $P_d(s,t)$ and $P_c(s,t)$ represent discharge and charge power of the ESS, and $pc(s,t)$ stand for power exploitation cost.

Grid connection costs are based on the grid energy exchange:

$$C_g(t) = gc(t) \cdot P_w(t) \cdot \Delta t - gr(t) \cdot P_j(t) \cdot \Delta t \tag{1.6}$$

where $P_w(t)$ and $P_j(t)$ represent purchased power from the grid and sold power to the distribution network, respectively, whereas $gc(t)$ and $gr(t)$ stand for unitary cost of grid energy withdrawal and unitary revenue for injected energy, respectively.

The coverage of internal energy demand of the MG at each time interval *t* is expressed by means of the following expressions:

$$\sum_{k=1}^{N_k} P(k,t) + \sum_{s=1}^{N_s} \left[P_d(s,t) - P_c(s,t) \right] + \tilde{P}_R(t) + \left[P_w(t) - P_j(t) \right] = \tilde{P}_L(t) \tag{1.7.a}$$

$$\sum_{k=1}^{N_k} Q(k,t) \geq \tilde{Q}_L(t) \tag{1.7.b}$$

where $\tilde{P}_R(t)$, $\tilde{P}_L(t)$ and $\tilde{Q}_L(t)$ correspond to forecasted values of power generation from non-programmable renewable sources, electric power demand and thermal power demand, respectively.

Electric storage devices are characterized for each time step *t* by the update of $soc(s,t)$, as follows:

$$E(s,t) = E(s,t-1) + \eta_c(s) \cdot \Delta t \cdot P_c(s,t) - \frac{\Delta t \cdot P_d(s,t)}{\eta_d(s)} \tag{1.8}$$

where $\eta_c(s)$ and $\eta_d(s)$ stand for charge and discharge efficiency, respectively.

In order to avoid contemporaneous charge and discharge of storage devices, as well as power withdrawal and injection at the Point of Common Coupling (PCC), the following conditions are imposed:

$$P_c(s,t) \cdot P_d(s,t) = 0 \tag{1.9.a}$$

$$P_w(t) \cdot P_j(t) = 0 \tag{1.9.b}$$

Therefore, state variables include:

- electric and thermal power generation from fuel-based units, $P(k,t)$ and $Q(k,t)$;
- power withdrawn and injected at grid connection point, $P_w(t)$ and $P_j(t)$;

- discharge and charge power and state of charge of storage devices, $P_d(s,t)$, $P_c(s,t)$ and $soc(s,t)$.

Each of these variables is non-negative and suitably bounded due to installed size limits.

The day-ahead programming of MG operation, exploiting the previous relations could be expressed in a linear formulation considering all efficiencies and factors as constants. In the linear formulation, the objective function is given by the sum of (1.3.a), (1.3.b), (1.4.a), (1.4.b) and (1.5). Whereas equality constraints are given by (1.3.c), where applicable, as well as (1.7.a) and (1.8). Finally, inequality constraints are reported by (1.7.b) and bounds on state variables.

However, electric and thermal efficiencies of fuel-based electricity generation devices, like reciprocating internal combustion engines or micro-turbine systems, are more specifically represented by piecewise linear or polynomial functions of the power production level. Therefore, the objective function and the constraints become non-linear. As well as the presence of constraints (1.9.a) and (1.9.b) involves further non-linearity.

In the explained relations the islanded operation mode shall remain valid, by discarding all contributions introduced by $P_w(t)$ and $P_j(t)$. Moreover, in this condition, the environmental impact could be further limited by capping the contribution of fuel-based generation devices to load coverage in the presence of low renewable production, by means of the following relation:

$$\sum_{k=1}^{N_k} P(k,t) \le \alpha \cdot \tilde{P}_L(t) \quad \forall t \ni ' \frac{\tilde{P}_R(t)}{\tilde{P}_L(t)} \le \delta_R \tag{1.10}$$

1.2.2 Test system

The optimization of day-ahead operation plan is performed for a test MG shown in Fig. 1.4, where the electric part of the system is represented in black and the thermal part in red. This system represents a configuration of the testbed MG described in sub-section 1.1, where thermal sector is empowered and the influence of electric vehicles is neglected. Therefore, the test system includes:

- a gas-fueled internal combustion engine (ICE) in cogeneration layout, with installed electric power 105 kW, nominal thermal power 180 kW, rated electric efficiency 31.5%, thermal efficiency 56%;
- a gas microturbine (μTG) in cogeneration layout, with installed electric power 28 kW, nominal thermal power 57 kW; rated electric efficiency 24.8%, thermal efficiency 50%;
- a photovoltaic field (PV) composed of five sections with 10 kW peak power each;

- a mini-wind system (WT), based on two 12-kW horizontal axis wind turbines and four 10-kW vertical axis wind turbines, respectively;
- two energy storage facilities, based on a 25 kWh / 8 kW lead-acid battery system (ESS1) with 75% charge/discharge efficiency and a 180 kWh / 45 kW sodium-nickel battery system (ESS2) with 85% charge/discharge efficiency;
- a 75-kW wood-fueled boiler (Boiler1) with 82.5% rated efficiency and a 20-kW pellet-fueled boiler (Boiler2) with 88% rated efficiency;
- an industrial load with maximum electric and thermal demand equal to 200 kW and 300 kW, respectively;
- grid connection with 200 kW maximum exchange.

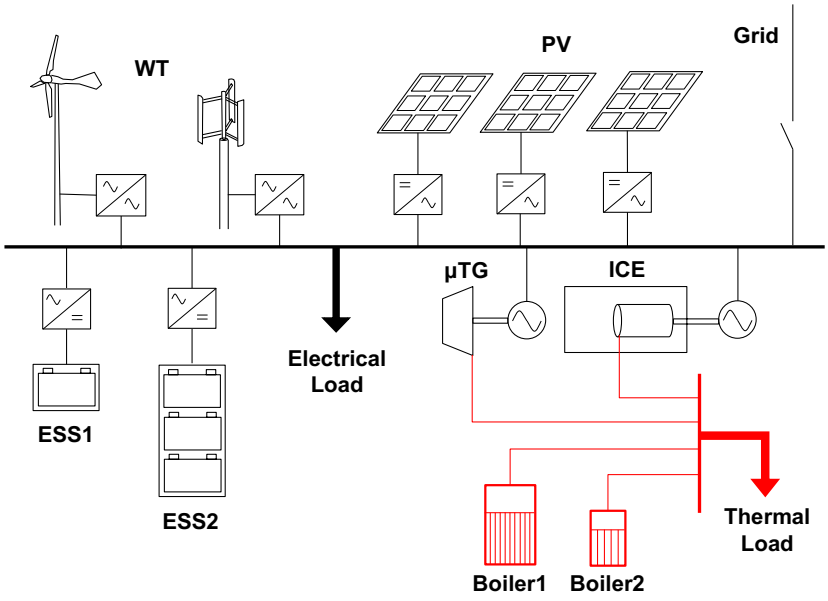

Figure 1.4. Test MG layout

1.2.3 Test cases and results

The analysis is organized applying to the described system, in grid-connected (Case G) and in islanded (Case I) condition, the linear (Case L) and non-linear (Case N) formulations of the day-ahead operation planning problem. Typical winter day and summer day are accounted, with meteorological conditions of Bari, Italy: relevant load and renewable generation curves are reported in Fig. 1.5. It is assumed that the cogeneration units are operating in electric-driven mode, and the boilers are considered thermal energy generators.

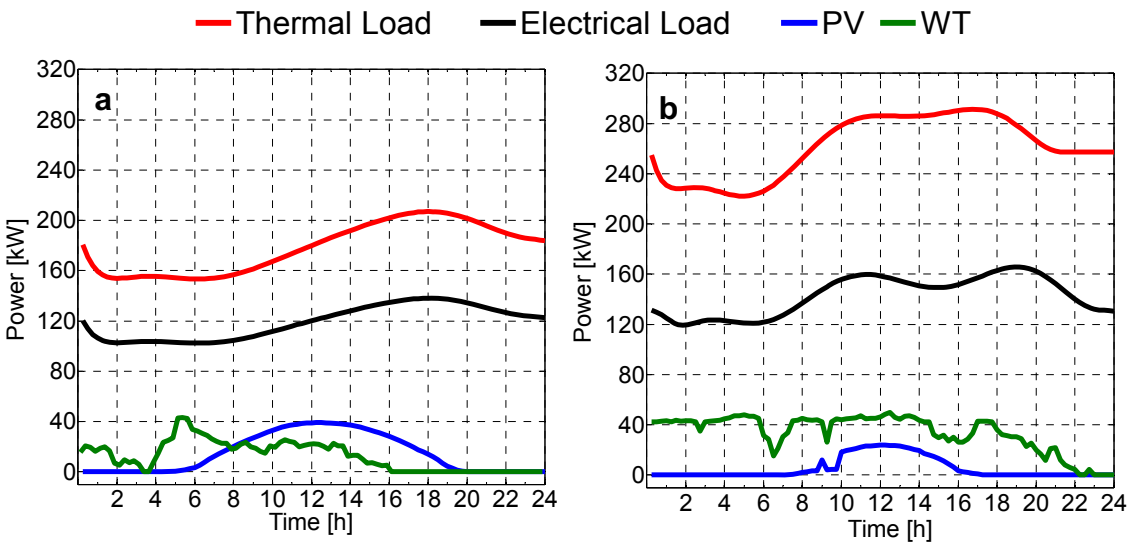

Figure 1.5. Load and renewable production in summer (a) and winter day (b)

The day-ahead operation planning is evaluated on N_t = 96 time steps with a duration of 15 minutes, in accordance with input data. As regards to constraint (1.10) in islanded conditions, $\alpha = 0.9$ and $\delta_R = 0.1$ are assumed. Italian tariffs for electricity and gas are accounted and storage operation costs are neglected.

The procedures in the several cases are simulated by exploiting MATLAB® optimization tools *linprog* and *fmincon*, and parallel calculus is adopted to deal with non-linear problems. The procedure is run on an Intel ® Xeon ® E5-1620 3.50 GHz with 16 GB RAM, operating system Windows 7 (64 bit) and MATLAB® 2012b.

In the following, simulation results are shown. In particular, in Fig. 1.6, the electric power production in the winter day is reported in the grid-connected mode and stand-alone mode, in the linear and nonlinear formulations. Analogously, in Fig. 1.7 the thermal power production in the winter day is illustrated. Furthermore, electric and thermal generation for the summer day are shown in Fig. 1.8 and Fig. 1.9, respectively. In Figg 1.6 and 1.8, negative values represent charge power of ESSs or power delivery to the grid.

It can be observed that the ICE provides a larger contribute to satisfy electrical and thermal load. Whereas, the μTG shows higher production in the evening to balance the lack of renewable energy. In the linear formulation, efficiencies of ICE and μTG are constant, therefore ICE is cheaper and it is exploited often close to the nominal value. When electric power demand is higher, the μTG gives contribution. On the other hand, in non-linear formulation, the advantage in the use of one of the two cogeneration devices depends on the operating point, yielding a deeper exploitation of the μTG in the evening.

Moreover, it can be noted that in the grid connected mode, the MG withdraws power from the distribution grid in the evening, when renewable sources are lacking and the electricity cost is smaller. In any case, no power delivery from the MG to the distribution grid is observed due to the low sold price. In the islanded mode, the contribution of ESS2 is remarkable, since it charges (negative values) in the central hours of the day with large renewable contribution and it is discharged in the remaining periods, as shown in Fig. 1.7.

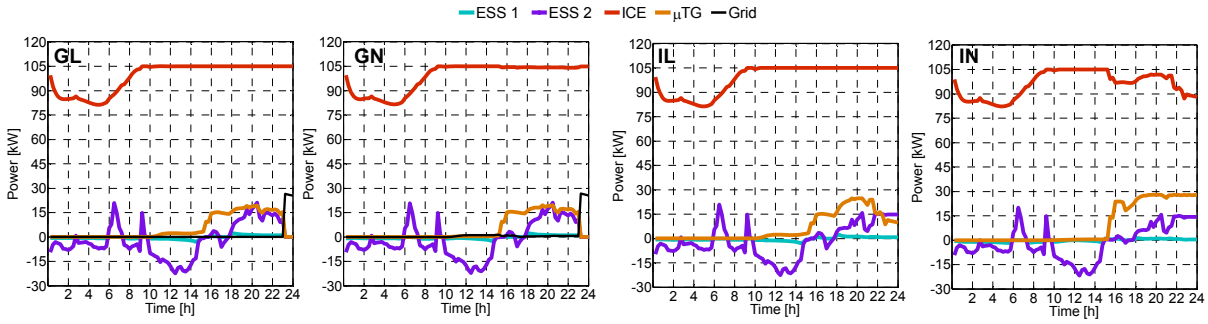

Figure 1.6. Electric power production in winter day in the four cases.

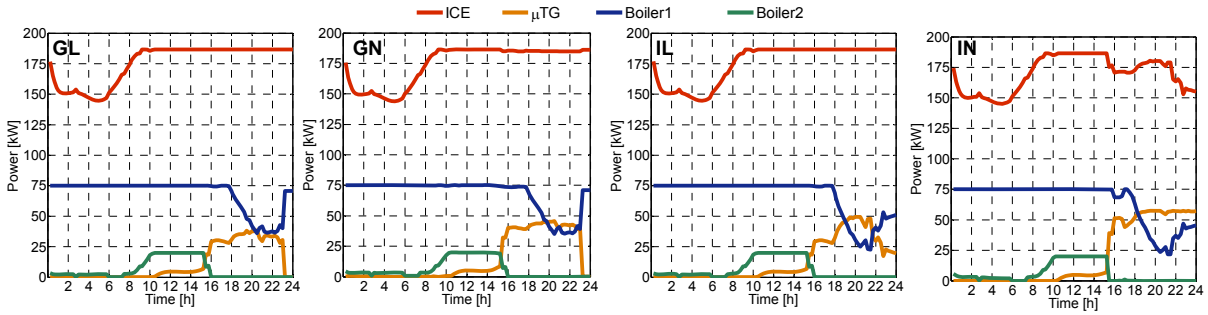

Figure 1.7. Thermal power production in winter day in the four cases.

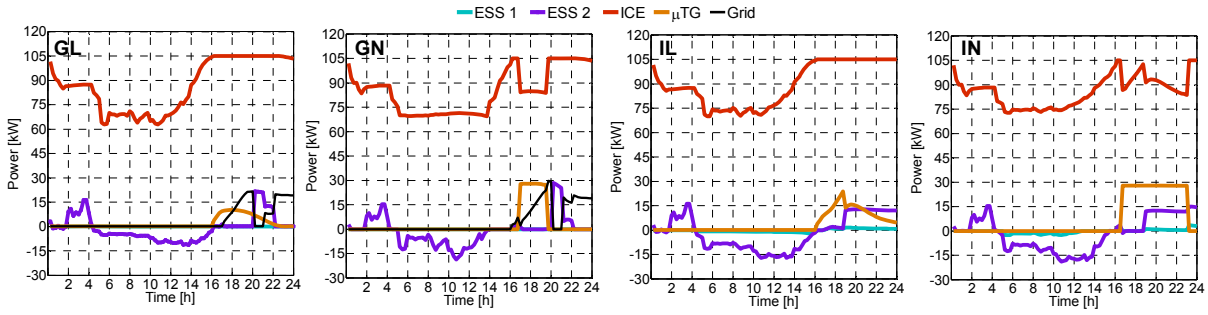

Figure 1.8. Electric power production in summer day in the four cases.

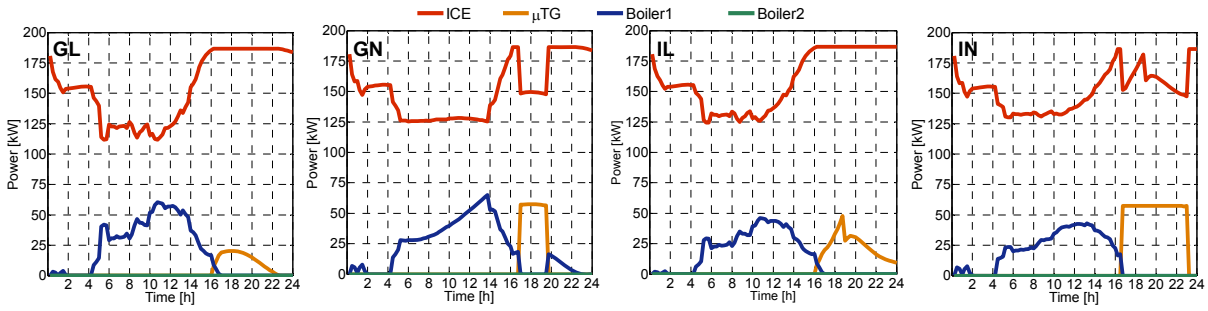

Figure 1.9. Thermal power production in summer day in the four cases.

The trends of the state-of-charge for the two ESSs are reported in Figure 1.10 and Figure 1.11 for winter and summer days, respectively, in the four considered cases. It can be seen that, during winter day, the behavior of ESS2 is almost similar in all cases, whereas by considering IN case the ESS1 shows a lower exploitation. In summer day, grid-connected condition involves only ESS2 activation, whereas ESS1 keeps in idle state. In islanded mode, as stated previously, the exploitation is deeper, and a preventive discharge is observed for ESS2 in early morning making it available to store renewable-based energy in central hours of the day.

In each case study, thermal power balance is satisfied, notwithstanding this in islanded mode a higher part of thermal energy is released to the atmosphere, allowing the electrical load tracking by cogeneration systems. In the winter day, the Boiler 1 runs close to its rated power in the first hours of the day, and in the central hours the Boiler 2 is employed at maximum capacity to cover peak load. Boiler contribution is lower in the evening due to the μTG intervention. Since thermal load is lower in the summer day, Boiler 2 gives negligible contribution, whereas Boiler 1 covers the load when it is not affordable to produce by μTG.

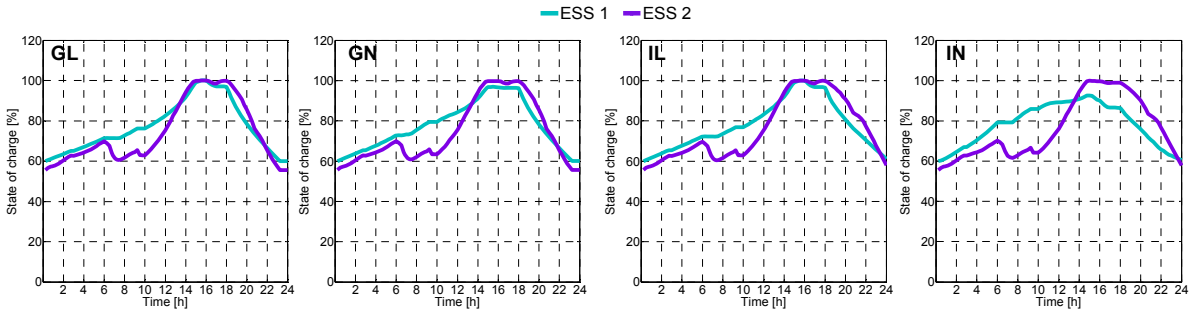

Figure 1.10. Storage state-of-charge in winter day in the four cases.

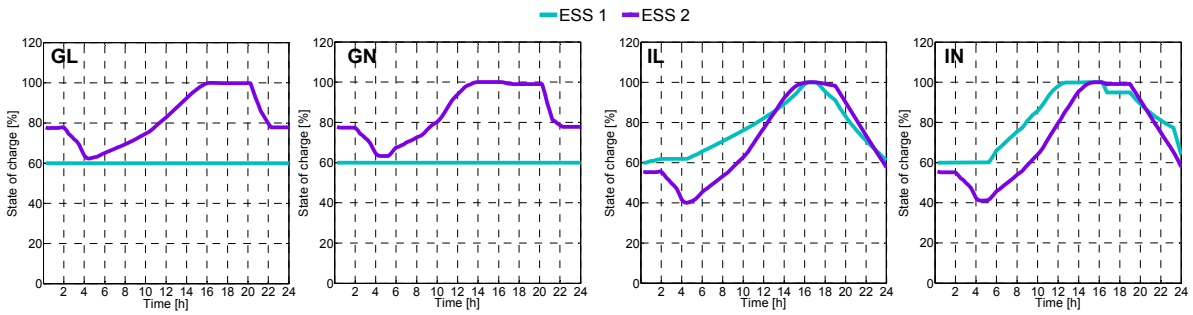

Figure 1.11. Storage state-of-charge in summer day in the four cases.

The economic performances of the different cases are reported in Table 1.1, in particular the obtained values are referred to the objective function yields of the optimization. It could be

noted that the non-linear formulation is cheaper in each case, due to more refined efficiency functions of ICE and μTG, with savings ranging between 1% and 2.5%.

Whereas, the islanded case is more expensive than grid-connected by 4-5%. The main cost contribution to daily cost comes by gas purchase, from 81% in winter grid-connected cases to 94% in summer islanded cases. Emission daily cost ranges from 3.89 € in summer GN case to 6.90 € in winter IL case.

Table. 1.1. Total Daily Cost [€]

Case	Winter	Summer
GL	578.49	413.24
GN	573.37	402.95
IL	596.01	427.42
IN	586.44	422.00

Computation efforts are compared in Table 1.2. It can be observed that iteration number and computation time are higher in non-linear formulation, albeit compatible with day-ahead procedures. Moreover, the islanded condition requires higher efforts.

Table. 1.2. Computation Efforts Comparison

Case	Iteration number		Computation time [s]	
	Winter	Summer	Winter	Summer
GL	12	14	0.129	0.133
GN	71	40	112.59	286.65
IL	13	13	0.129	0.130
IN	113	250	108.77	274.78

It should be noted that the solution in islanded operation mode is obtained with a higher iteration number, due to the necessity of evaluating with deeper detail the ESS performance to compensate the lack of energy exchange with the distribution network and to suitably exploit of the renewable generation.

1.2.4 Conclusions

In this subsection, the day-ahead operation planning of a MG has been formulated, in order to cover electricity and thermal demand, and solved through linear and non-linear approaches. The proposed methodology has been proved on a configuration of Prince experimental MG in grid-connected and islanded operation conditions. The analysis of simulation results has put in evidence that non-linear formulation, involving a more refined device model, has yielded less expensive solutions, with a better performance of the system with respect to linear formulation both in grid connected and islanded mode. The observed computational effort is still compatible with SCADA/EMS function timing for the investigated case. Whereas, the linear formulation has required shorter solution time, turning out to be suitable in a multi-MG framework, with more complex systems and mutual interaction

1.3 An optimization procedure for Microgrid day-ahead operation in the presence of CHP facilities

The aim of this sub-section is to propose a procedure for optimal day-ahead operation scheduling of a MG, which is one of the tasks performed by MG Central Controller. A particular focus is devoted to proper modelling of CHP operation suitable for microgrid size and their integration with back-up boilers, in order to cover electric and thermal demand. A detailed characterization of MG components and electric/thermal load is provided, along with relevant suitable constraints, and differentiated costs for power exchange from/to the distribution network at PCC are considered. The presence of several loads in the same MG with independent thermal demand and connected to common network is considered as well. In addition, different operation strategies for CHP-based generators are embedded in the procedure, to the purpose of verify the effectiveness of electric and thermal demand coverage assumptions. A non-linear formulation of day-ahead scheduling problem is provided and the procedure is carried out in MatLab by means of the SQP solver. The proposed methodology is tailored to be implemented in a SCADA/EMS system of the experimental MG described in sub-section 1.1. In particular, the results of program development, hereinafter, are presented and the implementation in the MG facility is shown in the following sub-sections.

1.3.1 Literature Review

The energy management in the MG is typically performed in two stage, in particular day-ahead planning is called to determine generation profiles of controllable sources according to forecast demand, whereas real time dispatching involves adjustments in order to smooth out load variation and renewable power fluctuations [10][11].

The optimal scheduling of MG components is an attractive issue in the system operation. Indeed, it is remarkable both for the goal to be pursued (minimum-cost, maximum-profit and/or reliable operation) and the MG configuration (grid-connected or islanded).

Different solutions have been addressed to the MG energy management problem. A thorough review of relevant methodologies, classified according to objective functions, optimization techniques, solution approaches and exploited software tools is reported in [12].

In [13], a focus on the operation procedure is proposed, with the purpose of minimizing operation cost through the coordination between DG sources and batteries. In [14], two strategies for the optimal management of ESS in a MG are proposed. An economic benefit maximization problem is considered in [15], where minimum on-off time constraints and ramping constraints are taken into account. In [2], user costs for Load Shedding are considered

using PowerWorld Simulator®. A strategy for managing a MG containing PVs and hybrid ESSs is proposed in [16]. Whereas, an operation planning of MG based on time-of-use pricing is developed in [4], with the goal to determine a scheduling of MG components that depends on electricity price trend. Moreover, multi-objective optimization problems are evaluated to MG operation planning. In particular the environmental and economic optimization problem is considered in [17], in which pollutant emissions are taken into account through an equivalent cost. In [18], the objective function integrates both the cost and network reconfiguration problem. In [19], both day-ahead operational scheduling and unit commitment problems are considered in the presence of controllable loads. In [20], several objectives are weighed in a single function in order to prove the effectiveness of weighing coefficients.

The forecast of generated power from renewable sources represent a remarkable aspect in MG operation programming. To this purpose, several methods are performed based on Neural Networks, stochastic approach and robust optimization. In [21] Neural Networks with different approaches are proposed. A Stochastic approach is used in [22], to take into account prediction uncertainty in MG operation programming. Robust optimization is accounted in [23] to account for reserve needs to deal with possible deviations of wind generation from forecast levels, whereas load uncertainty and reliability costs are added in [24].

In the last year, the optimization of MG operation is focused to ensure the satisfaction of electric and thermal demands. In particular, the use of Combined Heat and Power (CHP) systems enforces the interactions among different energy forms and improve the efficiency of energy supply in a MG [25]. In [26] CHP modelling is accounted along with an operating strategy of thermal storage in order to determine hourly MG plan. An advanced model of CHP, including cooling demand and involving ambient influence, is developed in [11]. The influence of heat pumps in the satisfaction of electric and thermal demand of a domestic MG is tackled in [27]. The optimal dispatch of microgrid with CHP based on probabilistic algorithm accounting for load and renewable probability distribution function and with linear CHP costs is presented in [28], whereas in [29] the daily scheduling of CHP-based MG is based on a stochastic model involving CHP cost as quadratic function of electric and heat power production and considering feasible operating region linking electric and heat output typical of combined-cycle plants. Moreover, in [30] economic emission load dispatch scheduling in a MG with CHPs is based on quadratic cost function and the determination of emission merit order according to Differential Evolution Technique. In [31] linear formulation of the production cost function is provided in combination with the coordination cost to cover both heat and power demands. A linear problem of optimal scheduling of a CHP system in thermal following mode with energy storage

is described in [32]. The influence of different price on operation planning of energy smart homes including CHP is depicted in [33].

The novel contributions proposed in this sub-section are reported in the following, compared to the approaches in literature dealing with the operation planning of CHP-based MG:

- The characterization of typical operating modalities of CHP systems, as described in [34] and [35] for autonomous systems, in MG operation planning framework. These strategies are usually neglected in other formulations or only one of them is assumed [32][36].
- The adoption of realistic nonlinear efficiency functions for CHPs, instead of constant values as in [25][33][37][38].
- The integration in a single MG, sharing all electric production facilities, of several sources for the coverage of distinct thermal loads instead of considering a single aggregate thermal demand. Moreover, the presence of excess heat ensures higher flexibility [30][39].
- The analysis on day-ahead horizon with 15-min programming time step, more and more necessary to capture variations of renewable production [40], assuming a further control stage, closer to real time operation, to cover the deviations from forecast values [41].
- The exploitation of Sequential Quadratic Programming (SQP) method for the solution of the complete nonlinear optimization problem instead of mixed-integer linear programming that can lose information [42] or mixed-integer nonlinear programming that could not reach feasible point [43].
- The simulation results are tested on real CHP system operation integrated in an experimental MG.

1.3.2 Nomenclature

Indices:

i Micro-Turbine in cogeneration layout (MT)

k Reciprocating-Engine in cogeneration layout (RE)

j Boiler

s Energy Storage System (ESS)

z Electrical Load

h Thermal Load

g Photovoltaic system (PV)

r Wind Turbine (WT)

t Time step

Parameters:

n_M Total number of MTs

n_R Total number of REs

n_B Total number of boilers

n_S Total number of ESSs

n_L Total number of electrical loads

n_H Total number of thermal loads

n_{PV} Total number of PVs

n_{WT} Total number of WTs

N Total number of time steps $(t = 1,2,...,N)$

Input Variables:

P_{zt}^{L} Electric power consumption by z-th load in the t-th time step

P_{gt}^{V} Electric power generated by g-th PV in the t-th time step

P_{rt}^{W} Electric power generated by r-th WT in the t-th time step

Q_{ht} Thermal power demand of h-th load in the t-th time step

State Variables:

P_{it}^{M} Electric power generated by i-th MT in the t-th time step

P_{kt}^{R} Electric power generated by k-th RE in the t-th time step

P_{st}^{C} Charging power of s-th ESS in the t-th time step

P_{st}^{D} Discharging power of s-th ESS in the t-th time step

E_{st} State Of Charge (SOC) of s-th ESS in the t-th time step

P_{Pt} Electric power withdrawn from distribution network at Point of Common Coupling (PCC)

in the *t*-th time step

P_{Dt} Electric power delivered to distribution network at PCC in the *t*-th time step

Q_{jt}^{B} Thermal power generated by the *j*-th boiler in the *t*-th time step

Cost items:

$C(P_{it}^{M})$ operation cost of *i*-th MT in the *t*-th time step

$S(P_{it}^{M})$ emission cost of *i*-th MT in the *t*-th time step

$C(P_{kt}^{R})$ operation cost of *k*-th RE in the *t*-th time step

$S(P_{kt}^{R})$ operation cost of *k*-th RE in the *t*-th time step

$C(Q_{jt}^{B})$ operation cost of *j*-th boiler in the *t*-th time step

$S(Q_{jt}^{B})$ emission cost of *j*-th boiler in the *t*-th time step

$C(P_{Pt})$ cost for electricity purchase at PCC

$R(P_{Dt})$ revenue for electricity delivery at PCC

Constants:

$\overline{P}_{i}^{M}, \underline{P}_{i}^{M}$ Upper and lower limits of P_{it}^{M}

$\overline{P}_{k}^{R}, \underline{P}_{k}^{R}$ Upper and lower limits of P_{kt}^{R}

$\overline{Q}_{j}^{B}, \underline{Q}_{j}^{B}$ Upper and lower limits of Q_{jt}^{B}

$\overline{P}_{Pt}, \overline{P}_{Dt}$ Upper limits of P_{Pt} and P_{Dt} at time *t*

$\overline{P}_{s}^{C}, \overline{P}_{s}^{D}$ Upper limits of P_{st}^{C} and P_{st}^{D}

$\overline{E}_{s}, \underline{E}_{s}$ Upper and lower limits of E_{st}

Δt Amplitude of the *t*-th time step

1.3.3 Modeling of Microgrid components

The different technologies suitable in a MG context can be divided in groups. Technologies based on non-programmable renewable energy sources (RES), such as wind speed, solar radiation and water flow, yield electric power with a lower possibility of control and dispatch, therefore their contribution should be predicted with a good accuracy to avoid remarkable variations in real time operation. An ESS can influence the operation of the MG by performing several tasks, such as improve the reliability and mitigate the uncertainty of electricity production by RESs. Whereas, MTs and REs generate electrical power and useable exhaust heat which can provide hot water or process heat, and can operate with different fuels, allowing flexibility in the case of fuel unavailability and volatile fuel prices. Moreover, boilers usually compensate the action of CHP systems to cover thermal demand variations.

In this sub-section, the MG components are modelled in the economic and operation perspective in a day-ahead time interval are described. To this purpose, energy production facilities based on non-programmable renewable energy sources have generally negligible operation costs, since no buying cost is associated to the source, whereas their production level in each interval of the day-ahead horizon is linked to expected value of the forecast of source availability. Moreover, since they take part to the MG that is a single entity interfacing the distribution network and eventually the market, nor economic penalizations are ascribable to forecast errors neither specific incentive schemes are accounted. On the other hand, programmable energy production devices (e.g. fuel-based generation devices, as well as external grid) can be fully controlled but incur in remarkable short-term operation costs. Energy storage devices present generally no variable cost, but are subject to internal state variation and conversion losses.

The proposed distinction is reflected in the following formulation of device models for day-ahead operation planning. In fact, WT and PV power production is linked to local weather condition forecasts and no variable cost is accounted, whereas variable costs are considered for MT, RE, boilers and grid connection. Storage devices involve loss terms with no variable cost.

1.3.3.1 Wind turbine

The power generated by the *r*-th WT in the *t*-th time step, according to a forecasted value of wind speed v_{rt}, depending on ground clearance and roughness, is evaluated as follows:

$$P_{rt}^{W} = \begin{cases} f(v_{rt}) & \underline{v}_r \le v_{rt} \le \tilde{v}_r \\ \tilde{P}_r^{W} & \tilde{v}_r \le v_{rt} \le \overline{v}_r \\ 0 & else \end{cases} \tag{1.11}$$

where $\tilde{P}_r^W$ is the rated power of the WT, $\underline{v}_r, \tilde{v}_r, \overline{v}_r$ represent the cut-in, rated and cut-off wind speed, respectively, and $f(v_{rt})$ is a polynomial function determined by the specific power-speed curve of the WT. Suitable forecasting procedure or historical data can be adopted to obtain v_{rt} over a time step [44].

1.3.3.2 Photovoltaic plant

The electric power generated of the *g*-th PV plant at the *t*-th time interval is expressed as follows:

$$P_{gt}^V = \gamma_g \cdot n_g^V \cdot \zeta_g^V(\theta_{gt}) \cdot A_g \cdot I_{gt} \tag{1.12}$$

where I_{gt} [kW/m^2] is the incident irradiance on panel surface, taking into account direct, diffuse and reflected components [45], A_g [m^2] is the panel area, n_g^V is the number of panels in the PV system, $\zeta_g^V(\theta_{gt})$ is panel efficiency depending on its temperature θ_{gt} [46], γ_g is a degradation coefficient that includes panel shading, inverter and asymmetries losses. Solar irradiance can be estimated according to forecast procedures or historical data [47].

1.3.3.3 Energy storage system

The ESS is characterized by its charge and discharge rate and mainly energy content, or State Of Charge (SOC) in day ahead operation. The SOC of the *s*-th ESS in *t*-th time stage is linked to the value at previous stage $t\_$, as follows:

$$E_{st} = (1 - q_s^D) \cdot E_{st\_} + \left(P_{st}^C \cdot \Delta t \cdot \psi_s^C \left(P_{st}^C \right) \right) - \left(\frac{P_{st}^D \cdot \Delta t}{\psi_s^D \left(P_{st}^D \right)} \right) \tag{1.13.a}$$

where $\psi_s^C \left(P_{st}^C \right)$ and $\psi_s^D \left(P_{st}^D \right)$ are the charging and the discharging efficiency of the *s*-th ESS, respectively, depending on charge and discharge power level, and the self-discharging effect q_s^D is determined with respect to the level of available capacity at previous stage [48][49]. At the first time step, $t = 1$, it is assumed that $t\_ = N$ so that the same state is present at the extremes of each day. Moreover, the following relation holds, in order to fix the SOC at the beginning of programming horizon to a value $E_s^{'}$ able to guarantee an efficient daily operation in any condition.

$$E_{sN} = E_s^{'} \tag{1.13.b}$$

The values of SOC and charge/discharge power are limited by specific characteristics of the ESS based on nameplate data provided by manufacturer, as follows:

$$\underline{E}_s \le E_{st} \le \bar{E}_s \tag{1.14.a}$$

$$0 \le P_{st}^C \le \bar{P}_s^C \tag{1.14.b}$$

$$0 \le P_{st}^D \le \bar{P}_s^D \tag{1.14.c}$$

In particular, maximum SOC value in equation (1.14.a) is determined as $\bar{E}_s = \mu_s \cdot E_s^{nom}$ where E_s^{nom} is the nominal energy capacity of the ESS and μ_s represents the capacity reduction factor. This factor depends on the utilization history of the ESS, i.e. equivalent cycles at the defined depth of discharge [50][51][52], from the beginning of exploitation, and it is updated for the analysis of different days.

Moreover, the ESS is connected to MG by a single point, therefore it can be only charged or discharged in each time step. Therefore, the following condition holds:

$$P_{st}^C \cdot P_{st}^D = 0 \tag{1.14.d}$$

1.3.3.4 MicroTurbine in Cogeneration Layout

The operation cost of *i*-th MT can be expressed as follows [53], in each time step:

$$C(P_{it}^M) = \varphi_i^M \cdot \frac{\Delta t \cdot P_{it}^M}{H_i^M \cdot \eta_i(P_{it}^M)} \tag{1.15}$$

where φ_i^M [€ per fuel unit] is the cost of fuel (generally natural gas), H_i^M [kWh per fuel unit] is the lower heating value of fuel and $\eta_i(P_{it}^M)$ is the electrical efficiency at specific level of power production P_{it}^M. The latter has to be within technical limits of the MT:

$$\underline{P}_i^M \le P_{it}^M \le \bar{P}_i^M \tag{1.16}$$

Whenever the *i*-th MT operates in CHP mode, the thermal energy provided in the *t*-th time stage Q_{it}^M can be obtained by the following expression [54]

$$Q_{it}^M = P_{it}^M \cdot \frac{\xi_i^M}{\eta_i(P_{it}^M)} \tag{1.17}$$

where ξ_i^M represents the thermal efficiency.

The impact of pollutant emissions based on the power production, the equivalent cost of CO_2 emissions is employed, by means of a unit penalty cost σ_E [€/kg]. This item of cost associated to the *i*-th MT can be expressed as follows:

$$S(P_{it}^M) = \sigma_E \cdot \varepsilon_i(P_{it}^M) \cdot \Delta t \cdot P_{it}^M \tag{1.18}$$

where $\varepsilon_i(P_{it}^M)$ [kg/kWh] is the emission factor of the i-th MT, determined as $\varepsilon_i(P_{it}^M) = \bar{\varepsilon}_i^M / \eta_i(P_{it}^M)$, being $\bar{\varepsilon}_i^M$ a constant emission factor depending on the consumption of the fuel in the i-th MT.

Moreover, ramping limits can be neglected in the day-ahead horizon with reasonably wide time interval [11].

1.3.3.5 Reciprocating-Engine in Cogeneration Layout

The operation cost of *k*-th RE system in the *t*-th time stage can be expressed as the following expression [55]:

$$C(P_{kt}^R) = \varphi_k^R \cdot \frac{\Delta t \cdot P_{kt}^R}{H_k^R \cdot \eta_k(P_{kt}^R)} \tag{1.19}$$

where φ_k^R [€ per fuel unit] is the fuel cost, H_k^R [kWh per fuel unit] is the lower heating value of fuel, $\eta_k(P_{kt}^R)$ is the electrical efficiency. Power production of the RE P_{kt}^R is bounded by technical features:

$$\underline{P}_k^R \le P_{kt}^R \le \bar{P}_k^R \tag{1.20}$$

Moreover, in CHP mode, the thermal power output from *k*-th RE system at the *t*-th time step Q_{kt}^R can be evaluated as follows [54]:

$$Q_{kt}^R = P_{kt}^R \cdot \frac{\xi_k^R}{\eta_k(P_{kt}^R)} \tag{1.21}$$

where ξ_k^R is the thermal efficiency.

The equivalent cost of CO_2 emissions can be determined as:

$$S(P_{kt}^R) = \sigma_E \cdot \varepsilon_k(P_{kt}^R) \cdot \Delta t \cdot P_{kt}^R \tag{1.22}$$

where $\varepsilon_k(P_{kt}^R)$ [kg/kWh] is the emission factor of the k-th RE, derived by the expression $\varepsilon_k(P_{kt}^R) = \bar{\varepsilon}_k^R / \eta_k(P_{kt}^R)$, being $\bar{\varepsilon}_k^R$ a constant emission factor depending on the burnt fuel in the *k*-th RE.

1.3.3.6 Boiler

The operation cost of the *j*-th boiler in the *t*-th time stage can be expressed as [56]:

$$C(Q_{jt}^B) = \varphi_j^B \cdot \frac{\Delta t \cdot Q_{jt}^B}{H_j^B \cdot \xi_j^B} \tag{1.23}$$

where φ_j^B is the fuel cost [€ per fuel unit], H_j^B [kWh per fuel unit] is the lower heating value, ξ_j^B is the thermal efficiency. The useable thermal power by the *j*-th boiler Q_{jt}^B is limited in the range:

$$\underline{Q}_j^B \le Q_{jt}^B \le \bar{Q}_j^B \tag{1.24}$$

The equivalent cost of CO_2 emissions from the *j*-th boiler can be evaluated by the expression:

$$S(Q_{jt}^B) = \sigma_E \cdot \varepsilon_j(Q_{jt}^B) \cdot \Delta t \cdot Q_{jt}^B \tag{1.25}$$

where $\varepsilon_j(Q_{jt}^B)$ [kg/kWh] is the emission factor of the *j*-th boiler depending on thermal power production.

1.3.3.7 Power exchange at PCC

In the grid-connected mode, the cost of electric energy withdrawal from the distribution network in the *t*-th time step is given by the expression:

$$C(P_{Pt}) = \pi_{Pt} \cdot \Delta t \cdot P_{Pt} \tag{1.26}$$

where π_{Pt} [€/kWh] is the unitary electricity purchase price, and P_{Pt} is limited by contractual conditions with the distribution system operator and the size of connection equipment:

$$0 \ge P_{Pt} \ge \bar{P}_{Pt} \tag{1.27}$$

Whereas, the revenue from the energy injected to the distribution network can be expressed as:

$$R(P_{Dt}) = k_D \cdot \pi_{Dt} \cdot \Delta t \cdot P_{Dt} \tag{1.28}$$

where π_{Dt} is the electricity selling price, $k_D < 1$ is a factor that takes into account the administrative of connection service [57]. Analogously to power purchase, the delivered amount P_{Dt} has to respect a maximum value:

$$0 \geq P_{Dt} \geq \overline{P}_{Dt} \tag{1.29}$$

In order to avoid bidirectional power exchange at PCC in a single *t*-th time step, the following condition holds:

$$P_{Pt} \cdot P_{Dt} = 0 \tag{1.30}$$

1.3.4 Day-ahead energy management problem

In this sub-section, a nonlinear optimization procedure is proposed for the day-ahead scheduling of the MG sources in order to cover the internal electric and thermal load profile by minimizing operation costs and environmental impacts.

1.3.4.1 Problem formulation

The MG energy management function is performed through the solution of a non-linear optimization problem, aiming to find a minimum value of an objective function subject to equality and inequality constraints, that can be formulated in the following canonical form:

$$\begin{aligned} &\min_{\boldsymbol{x}} J(\boldsymbol{x}) \\ &\text{subject to } \begin{cases} \boldsymbol{g}(\boldsymbol{x}) = \boldsymbol{0} \\ \boldsymbol{h}(\boldsymbol{x}) \leq \boldsymbol{0} \end{cases} \end{aligned} \tag{1.31}$$

where $\boldsymbol{x}$ is a $(n_M + n_R + n_B + 3 \cdot n_S + 2) \cdot N$ dimensional vector including the subsets of variables $\{P_{it}^M\}, \{P_{kt}^R\}, \{Q_{jt}^B\}, \{P_{st}^C\}, \{P_{st}^D\}, \{E_{st}\}, \{P_{Pt}\}, \{P_{Dt}\}$ and $J(\boldsymbol{x})$ includes the MG operation and emission costs over the total time interval $N \cdot \Delta t$, expressed as follows:

$$\begin{aligned} J(\boldsymbol{x}) = \sum_{t=1}^{N} \Bigg\{ & C(P_{Pt}) - R(P_{Dt}) + \sum_{i=1}^{n_M} \Big[C(P_{it}^M) + S(P_{it}^M) \Big] + \\ & + \sum_{k=1}^{n_R} \Big[C(P_{kt}^R) + S(P_{kt}^R) \Big] + \sum_{j=1}^{n_B} \Big[C(Q_{jt}^B) + S(Q_{jt}^B) \Big] \Bigg\} \end{aligned} \tag{1.32}$$

Equality constraints in (1.31) include the subsets: (1.13.a), involving $n_S \cdot N$ linear relations for all storage devices in the whole time horizon; (1.13.b), with n_S linear equations; (1.14.d), constituting $n_S \cdot N$ non-linear conditions; (1.30), corresponding to N non-linear constraints. Moreover, the electrical power balance of the MG in the *t*-th time step should be imposed, so

that the sum of consumption profile of electricity MG users and net power interchange with the distribution network is equals to the production of internal energy sources, neglecting MG losses in the day-ahead programming stage, as follows:

$$\sum_{z=1}^{n_L} P_{zt}^{L} + (P_{Dt} - P_{Pt}) = \sum_{i=1}^{n_M} P_{it}^{M} + \sum_{k=1}^{n_R} P_{kt}^{R} + \sum_{s=1}^{n_S} (P_{st}^{D} - P_{st}^{C}) + \sum_{g=1}^{n_{PV}} P_{gt}^{V} + \sum_{r=1}^{n_{WT}} P_{rt}^{W} \tag{1.33}$$

By considering that the electricity balance over all the planning horizon involves N linear constraints, the set of equality constraints $\boldsymbol{g}(\boldsymbol{x}) = \boldsymbol{0}$ includes $(2 \cdot n_S + 2) \cdot N + n_S$ relations.

Furthermore, inequality constraints in (1.31) are represented by the subsets: (1.14.a)-(1.14.c), constituting $6 \cdot n_S \cdot N$ linear conditions; (1.16), involving $2 \cdot n_M \cdot N$ linear relations; (1.20), yielding $2 \cdot n_R \cdot N$ linear constraints; (1.24), constituting $2 \cdot n_B \cdot N$ linear inequalities; (1.27) and (1.29), giving rise to $2 \cdot N$ linear relations each. Moreover, thermal power balance is guaranteed, based on technologies involved in thermal energy production, i.e. CHP units and Boilers. In accordance with the operation criteria of the MG, the possibility that a part of thermal energy can be released to the atmosphere at a given time period is considered. In particular, it is supposed that a part of the exhaust air after combustion, controlled by means of valves, passes through the exchangers to give useful heat, and a ventilation system, whose electric demand can be considered negligible, lets exhausts leave the thermal supply. In addition, the presence of different thermal loads, i.e. groups of users served by a determined subset of thermal power sources in the MG framework, is accounted. The link between the *h*-th thermal load and the thermal power sources of MG at the *t*-th time period can be expressed by the following inequality:

$$Q_{ht} \le \sum_{i=1}^{n_M} a_{hi}^{M} \cdot Q_{it}^{M} + \sum_{k=1}^{n_R} a_{hk}^{R} \cdot Q_{kt}^{R} + \sum_{j=1}^{n_B} a_{hj}^{B} \cdot Q_{jt}^{B} \tag{1.34}$$

where Q_{it}^{M} and Q_{kt}^{R} are evaluated by the non-linear expressions (1.17) and (1.21), respectively. Moreover, the coefficients a_{hi}^{M}, a_{hk}^{R} and a_{hj}^{B} are equal to 1 if the correspondent *i*-th MT, *k*-th RE or *j*-th boiler, respectively, is connected to the *h*-th thermal load, otherwise they are equal to zero.

Since the thermal power balance for all thermal users over the planning horizon involves $n_H \cdot N$ non-linear relations, the size of inequality constraint set $\boldsymbol{h}(\boldsymbol{x}) \le \boldsymbol{0}$ is $(2 \cdot n_M + 2 \cdot n_R + 2 \cdot n_B + 6 \cdot n_S + n_H + 4) \cdot N$.

The described methodology has the advantage to include further thermal technologies in MG planning through the specific model of devices. The adopted models allow to catch the behaviour of MG-sized devices in the day-ahead horizon, where the ramping limits can be neglected and steady-state conditions can be considered valid for each time step. Moreover, it is worth to remark that the procedure is able to perform the islanded mode condition of MG operation in defined time steps, by assuming $\overline{P}_{Pt} = 0$ and $\overline{P}_{Dt} = 0$. In this way, the objective function is not affect by the grid costs in a specific time stage, however the electricity balance cannot rely on flexibility ensured by distribution network exchange. Hence, the optimal day-ahead operation plan is provided, considering the sole MG internal sources.

1.3.4.2 CHP Operation Strategies

The solution of problem (1.31) yields the optimal values of the outputs of CHP devices, boilers and ESS, based on expected contributions by PV and WT systems, to cover the load demand. However, ad hoc strategies for managing CHP units can be required to improve long-term technology performance and to deal with specific needs [35]:

C1. *electrical load tracking*: selected CHP units are managed with the aim of following the evolution of electricity load;

C2. *thermal load tracking*: specified CHP units are operated with the objective of following the behavior of defined heating loads;

C3. *on-off operation:* the CHP units are operated at the rated power over defined time periods.

The C1 strategy can be easily handled, by adding to the problem (1.31), for each time stage, the following equality constraint:

$$\alpha_t \cdot \sum_{z=1}^{n_L} P_{zt}^L = \left[\sum_{i=1}^{n_M} b_{it}^M \cdot P_{it}^M + \sum_{k=1}^{n_R} b_{kt}^R \cdot P_{kt}^R \right] \cdot \beta_t \tag{1.35}$$

where the coefficient α_t $(0 \le \alpha_t \le 1)$ represents the portion of electrical load that is covered at the *t*-th step by the *i*-th MT or the *k*-th RE, operating in according with the value of binary factors b_{it}^M and b_{kt}^R, respectively, equal to 1. At the *t*-th time step, the C1 strategy is activated by $\beta_t = 1$ and $\alpha_t \neq 0$, whereas, if C1 strategy cannot be applied $\beta_t = 0$, ($\alpha_t = 0$). Therefore, the activation of C1 strategy yields the increase of equality constraints to a total of $(2 \cdot n_S + 3) \cdot N + n_S$ relations.

The C2 strategy is imposed, for the *h*-th thermal load and for the *t*-th time step, the following equality condition:

$$\alpha_{ht} \cdot Q_{ht} = \left[\sum_{i=1}^{n_M} u_{it}^M \cdot a_{hi}^M \cdot Q_{it}^M + \sum_{k=1}^{n_R} u_{kt}^R \cdot a_{hk}^R \cdot Q_{kt}^R \right] \cdot \beta_{ht} \tag{1.36}$$

where the coefficient α_{ht} $(0 \le \alpha_{ht} \le 1)$ represents the portion of *h*-th thermal load that is fed at the *t*-th step by the *i*-th MT or the *k*-th RE. These latter are selected by the imposed value of binary factors u_{it}^M and u_{kt}^R, respectively, equal to 1. At the *t*-th time step and for the *h*-th thermal load, the C2 strategy is in force if $\beta_{ht} = 1$ and $\alpha_{ht} \neq 0$, whereas, as long as $\beta_{ht} = 0$, C2 strategy is not applied ($\alpha_{ht} = 0$). Therefore, the presence of C2 strategy involves a total of $(2 \cdot n_S + 2 + n_H) \cdot N + n_S$ equality constraints.

Finally, the C3 strategy can be implemented by introducing, for the *i*-th MT and/or the *k*-th RE, the following relations:

$$\beta_{it}^M \cdot P_{it}^M = \beta_{it}^M \cdot \bar{P}_{it}^M \tag{1.37.a}$$

$$\beta_{kt}^R \cdot P_{kt}^R = \beta_{kt}^R \cdot \bar{P}_{kt}^R \tag{1.37.b}$$

The strategy is activated, for the *i*-th MT or the *k*-th RE, in the *t*-th time step when the binary factors β_{it}^M or β_{kt}^R assume a value equal to 1, respectively. Whereas, as long as $\beta_{it}^M = 0$ or $\beta_{kt}^R = 0$, the C3 strategy is not applied. Therefore, the presence of C3 strategy involves a total of $(2 \cdot n_S + 2 + n_M + n_R) \cdot N + n_S$ equality constraints.

1.3.5 Test system

The proposed optimization procedure and CHP strategies are applied to the test MG shown in Fig. 1.12, where the representation of each device embeds the relevant power conversion stage.

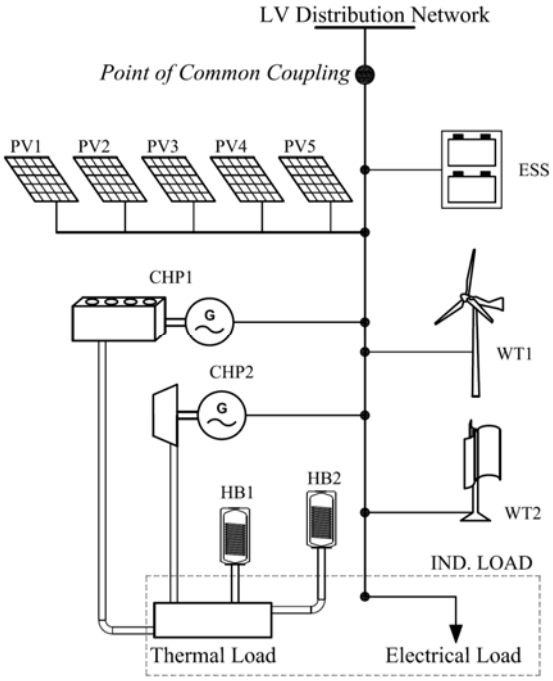

Figure. 1.12. The test MG.

The test MG represents a selected configuration of experimental facility realized at premises of the Power and Energy System laboratory of Politecnico di Bari, with improved thermal section, currently under integration. The aforementioned experimental facility includes the following devices:

- a gas-fueled CHP system, equipped with two variable-speed REs with total 105 kW rated electric power;
- a gas MT with 30 kW nominal power;
- a 50-kW photovoltaic plant composed of five sub-arrays with different panel technologies;
- a sodium-nickel battery working at roughly 260 °C, with a discharge duration of 3 hours;
- a 60-kVA wind turbine emulator, based on a back-to-back converter controlled according to models of different mini-wind generators and to measurement of an anemometer;
- two programmable loads, with 150 kVA rated power each, able to replicate active and reactive power needs of different kinds of load;
- a by-pass converter, with 200 kVA rated power, which allows the power exchange with the distribution network at PCC limited to a specified value.

The proposed day-ahead operation planning function is aimed to be implemented in the SCADA system by means of software integration ensured by Open Platform Communication (OPC) environment. Therefore, the proposed procedure is currently object of real-world implementation.

The main features of test MG components, according to the relations reported in section 1.3.3, are described in Table 1.3 for renewable-based components and in Table 1.4 for other devices. For the employed ESS, available depth of discharge is 80%, self-discharging effect is assumed negligible in the daily time horizon, charge and discharge efficiencies are observed to be quite independent on power levels, and no previous exploitation is assumed, therefore ESS maximum SOC is equal to rated capacity. The amount of power exchange at PCC is capped at 200 kW on both withdrawal and delivery.

Table 1.3. Characteristics of renewable devices in the Test MG

Device Name	Description	Rated electric power [kW]	Cut-in / Nominal / Cut-off wind speed [m/s]	PV panel power [W] / module number / nominal efficiency [%]
WT1	33-kW horizontal axis wind turbine	33	3.5 / 11 / 20	
WT2	two 6-kW vertical axis wind turbines	12	5 / 14 / 25	
PV1	photovoltaic triple junction a-Si modules	9.216		144 / 64 / 7.7
PV2	photovoltaic mono-crystalline Si modules	10.53		270 / 39 / 16.6
PV3	photovoltaic poly-crystalline Si modules	10.5		250 / 42 / 15.4
PV3	photovoltaic CIS technology	9.6		150 / 64 / 12.2
PV3	photovoltaic mono N-type modules	9.9		300 / 33 / 18.3

Table 1.4. Characteristics of non-renewable devices in the Test MG

Device Name	Description	Rated electric (charge/discharge) power [kW]	Rated thermal power [kW]	Rated capacity [kWh]	Rated electric (charge/discharge) efficiency	Rated thermal efficiency
ESS	sodium-nickel chloride battery system	44 / 48	---	141	85% / 85%	---
CHP1	gas-fuelled RE in cogeneration mode	105	180	---	31.5% (Fig. 1.13)	50%
CHP2	gas MT in cogeneration mode	28	57	---	24.8% (Fig. 1.13)	50%
B1	wood-fuelled boiler		20			82.5%
B2	pellet-fuelled boiler		75			88.2%

The electric efficiency trends of CHP systems according to power production level are expressed by means of the following third-order polynomial equations and their trends are depicted in Fig. 1.13 according to power output in p.u. of nominal power:

$$CHP1:\ \eta_k(P_{kt}^R) = 2.21e-7\cdot(P_{kt}^R)^3 - 7.47e-5\cdot(P_{kt}^R)^2 + 8.06e-3\cdot(P_{kt}^R) + 3.707e-2 \quad (1.38.a)$$

$$CHP2:\ \eta_i(P_{it}^M) = 2.22e-6\cdot(P_{it}^M)^3 - 3e-4\cdot(P_{it}^M)^2 + 1.397e-2\cdot(P_{it}^M) + 3.905e-2 \quad (1.38.b)$$

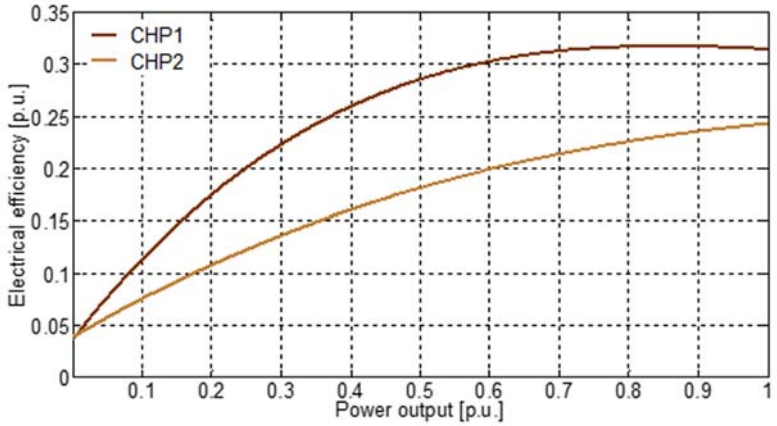

Fig. 1.13. Electric efficiency trends of CHP systems in the test MG.

Thermal efficiency has been considered constant to the rated values reported in Table 1.4 both for CHP and boilers, since no remarkable variations are observed during operation.

Emission factor for gas burning in CHP1 and CHP2 involves $\bar{\varepsilon}_k^R = \bar{\varepsilon}_i^M = 0.1404\,\text{kg/kWh}_{\text{pr}}$ obtaining, at nominal power, 0.453 kg/kWh for CHP1 and 0.560 kg/kWh for CHP2, according to the nameplate data. Whereas, emission factor for boilers is constant, though suitably low (0.002 kg/kWh) due to the exploitation of renewable fuels, whose burning is not related to proper emissions.

Moreover, for each CHP, the minimum production level is set to zero, compatibly to the observed low minimum stable production (roughly 1 kW). Daily curves of electrical and thermal load demand are taken from data of industrial users by an Italian distribution company. Weather data for the forecast of renewable sources production are taken from meteorological stations placed in the considered location [59]. Electric energy purchasing price is determined as the sum of market prices and service costs according to Italian rules, whereas electric energy selling price is defined by the Italian energy authority [57]. Finally, fuel costs are constant in each time step, according to data by a fuel distribution company [60] and are equal to 0.51 €/m^3 for gas, 0.17 €/kg for wood, 0.32 €/kg for pellet, and emission cost is equal to 5.7 €/t [61].

The proposed non-linear optimization methodology is implemented, dividing the day into N = 96 time steps of 15 minutes each, in MatLab® environment and solved through *fmincon* function in Optimization Toolbox exploiting SQP method [62], that has been proved robust for the solution of nonlinear optimization problems, even in non-convex formulations, and it is characterized by superlinear convergence [63][64]. The SQP method is based on the formulation, for each major iteration, of a Quadratic Programming subproblem based on a quadratic approximation of the Lagrangian function with positive semidefinite Hessian matrix and linearized constraints, whose solution is used to find a possible direction for a line search procedure with step length according to a merit function [65][66]. The SQP efficiently looks

for a local solution, and the solution search is improved starting from a feasible initial point [66] as a typical nonlinear programming method. In the proposed procedure the initial point is obtained by solving a linearized version of the problem, as suggested in [67]. The linearized problem is built by assuming efficiencies at rated levels, irrespective of power amount, in (1.13.a), (1.15), (1.17), (1.18), (1.19), (1.21), (1.22), and neglecting nonlinear constraints (1.14.d) and (1.30) on bidirectional power flow.

1.3.6 Test cases and results

Simulations are carried out according to data of a typical summer working day, where forecast electricity load amounts to 3,422 kWh in the whole day with a power peak of 165 kW at hour 18. Daily load is covered for the 14.4% by forecast RES production, with a peak of 60 kW at hour 12. Moreover, a single thermal load is considered, analogously to the situation of the experimental facility. It amounts to 4,329 kWh with a maximum of 215 kW at hour 18. The initial SOC of ESS is set to 0.80 p.u. of rated capacity. Trends of electricity price for the day under investigation are shown in Fig. 1.14. It is worth to remark that purchasing price varies on hourly basis according to market influence, whereas selling price assumes only 3 different values in the day.

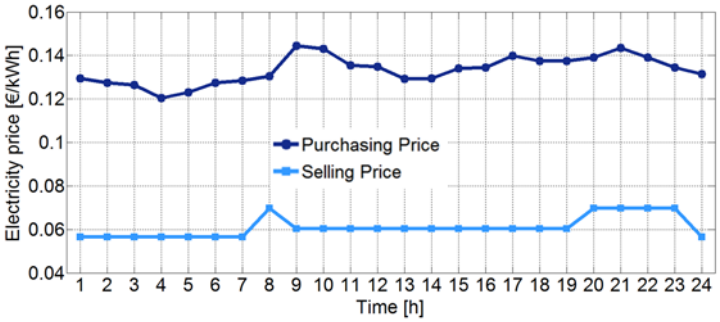

Fig. 1.14. Electricity price.

Simulations are carried out by applying each CHP strategy described in paragraph 1.3.4.2, and relevant results are compared to the reference solution of the problem reported in paragraph 1.3.4.1 (Base Case).

The diagrams of electric power balance and thermal power balance for the Base Case are shown in Figs. 1.15 and 1.16, respectively. It can be pointed out that, for the considered day, 75.0% of the daily electric load is satisfied by CHP systems, 8.0% by electricity exchange at PCC, and the share of ESS is 2.8% , concentrated in early morning and in peak price period in the evening. The sum of these contributions and RES-based production (14.4%, as previously stated) exceeds the total daily load, since the supplemental share (3.8%) relates to the charging of the ESS in central hours of the day, and this is ascribable to the compliance with the constraint

(3.b). This yields an increase of total MG electricity demand (sum of electric load and ESS charge power), shown in red dashed line in Fig. 1.15.

The coverage of thermal load is mainly performed by CHPs, with 83.6% contribution of RE (CHP1) and 12.9% by MT (CHP2). These systems work in a different manner, since CHP1 behaves according to load variations, whereas CHP2 is off in early morning and evening, and in central hours of the day it runs at maximum power output. Moreover, B1 helps covering morning peak, contributing by 3.2% to cover thermal load demand, whereas 0.3% of load is covered by B2 in central hours of the day, before CHP2 is on.

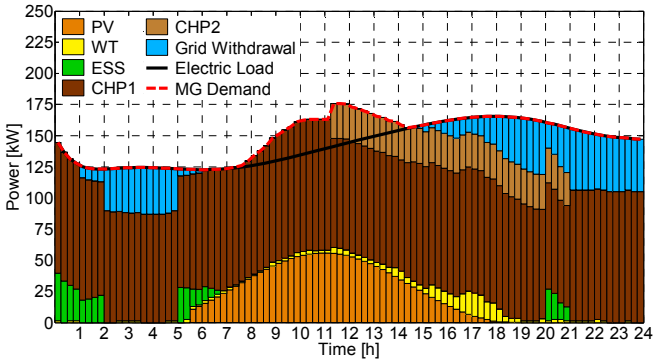

Fig. 1.15. Base Case Strategy: electrical power balance.

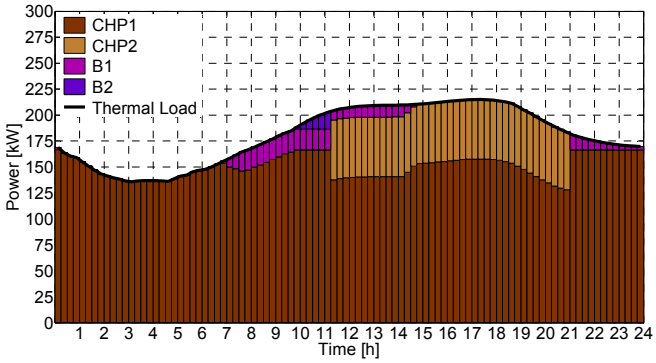

Fig. 1.16. Base Case Strategy: thermal power balance.

In order to verify the feasibility of C1 strategy, in the problem formulation the eq. (1.35) is considered as equality constraints, assuming $\alpha_t = 0.8$ and involving both CHP systems over the whole day ($b_{it}^M = 1$ and $b_{kt}^R = 1 \ \forall t$). Complying with this requirement, the sum of CHP should contribute to cover the 80% of electric load profile for each time step of the considered day, as can be seen in Fig. 1.17. The CHP systems contribute to cover load profile with a share of 69% and 11% for CHP1 and CHP2, respectively. Since the modulation is mainly performed by CHP1 during off-peak load, whereas CHP2 is run almost close to nominal value in the second half of the day. Whereas 2.8% of daily electric load is satisfied by ESS and 7.4% by electricity exchange at PCC. The total MG demand is 3.8% higher than load, due to ESS charging.

Moreover, 0.8% of internal production is sold to the grid in central hours of the day (i.e. when renewables exceed the remaining 20% of load), as reported in Fig. 1.17 through the difference between the envelope of bars and the dashed red curve.

Thermal power balance is illustrated in Fig. 1.18. In this case, thermal load is mainly satisfied by CHP systems, and an excess thermal power is registered (roughly 5.9% of the total daily amount), especially in the morning and in the presence of peak electric load, as a by-product of electric load tracking. B2 is off over the whole day and B1 contributes only by 1.4% to load coverage in peak intervals, when the contemporaneous extra-production by RES does not allow CHPs to produce more thermal power.

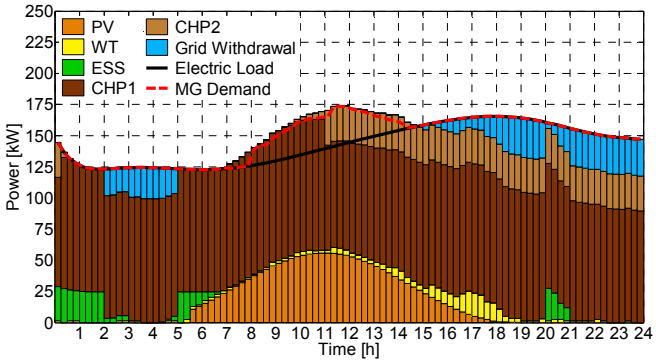

Fig. 1.17. C1 Strategy: electrical power balance.

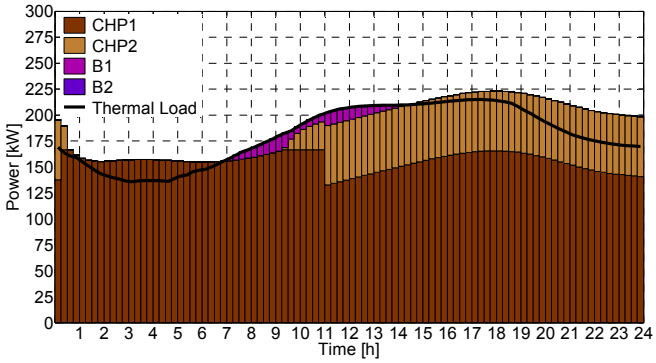

Fig. 1.18. C1 Strategy: thermal power balance.

The C2 strategy described in sub-section 1.3.4.2 is implemented by adding eq. (1.36) to the set of equality constraints and setting the coefficient $\alpha_{ht} = 0.8$ for the whole day. Both CHP systems are involved in the strategy, i.e. $u_{it}^{M} = 1$ and $u_{kt}^{R} = 1 \ \forall t$.

The relevant electric power sharing is illustrated in Fig. 1.19. It can be noted that 61.6% of electric load is matched by CHP systems, 25.0% by electricity exchange at PCC and the contribution of ESS is less intense, at 2.7%. The total MG demand is 3.7% higher than load profile, corresponding to ESS charge, and no grid injection is observed.

Thermal power balance is reported in Fig. 1.20. It can be observed that CHP units cover the prescribed amount of thermal load according to economic merit. Indeed, CHP1 is working

throughout the day and covers 70.3% of thermal demand, and CHP2 is exploited only in periods with higher demand, satisfying 9.7%. Furthermore, B1 runs close to its rated power covering 10.5% of thermal demand, whereas more expensive B2 has a daily demand share of 11.0%, most concentrated in peak demand hours.

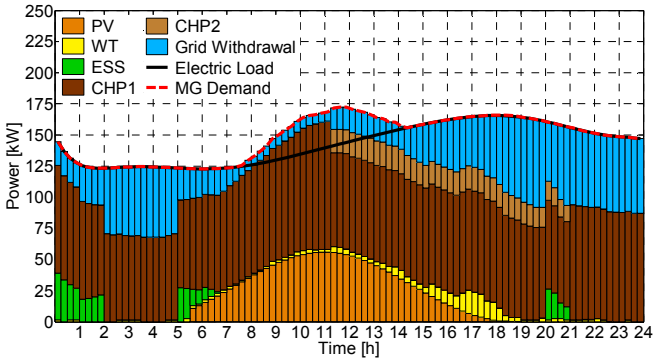

Fig. 1.19. C2 Strategy: electrical power balance.

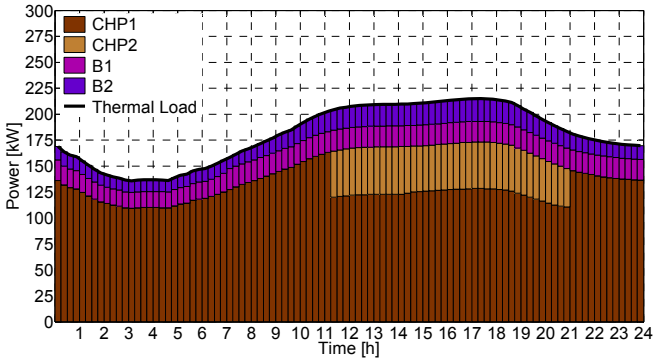

Fig. 1.20. C2 Strategy: thermal power balance.

The C3 strategy is considered by including eq. (1.37.a)-(1.37.b) in problem formulation. In particular, it is investigated the number of time step when the strategy yields the most efficient MG operating condition. This preliminary analysis yielded the activation of C3 strategy in the period from hour 11 to hour 19 for CHP1 ($\beta_{kt}^{R} = 1 \ \forall t \in [45,76]$), whereas for CHP2 it is not considered.

The electric power balance is reported in Fig. 1.21. The strategy implementation leads to CHP systems cover 76.0% of load. The exchange power at PCC reach an omount to 11.2% of load is observed and ESS contribute to 2.8%. Total MG generation exceeds the imposed load by 4.4%. The production surplus at strategy activation yields an excess production amounting to 0.6% of the load, that is sold to the distribution network, whereas the remaining 3.8% is dedicated to ESS charge.

Thermal power balance in Fig. 1.22 shows that CHP systems are entrusted to cover 98.1% of thermal demand (CHP1 covers 86.7% and CHP2 11.4%), whereas boilers are called to satisfy

the residual demand until hour 11, and in the peak hours they are unexploited. A slight excess of thermal power production is observed in the period of strategy activation.

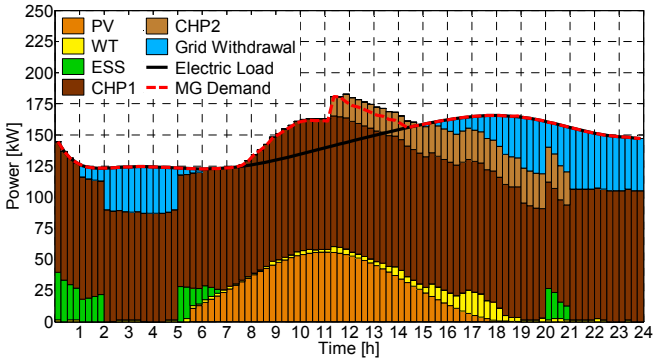

Fig. 1.21. C3 Strategy: electrical power balance.

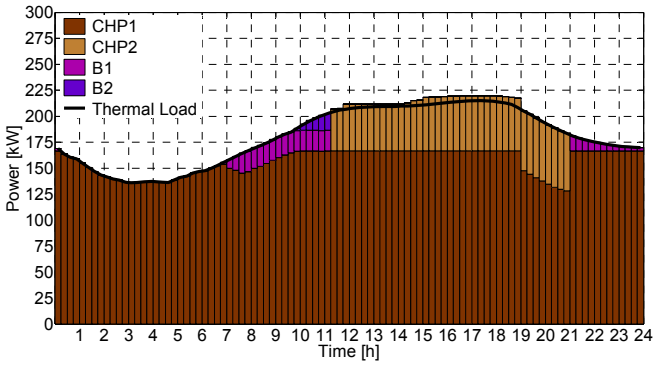

Fig. 1.22. C3 Strategy: thermal power balance.

Technical and economic issues of the implemented strategies in the day-ahead operation planning of the MG can be compared. In particular, in Table 1.5 the total daily cost of each strategy is reported, and the contribution of main cost items is detailed.

Table 1.5. Daily cost and contributions

Strategies / Costs	Base Case	C1	C2	C3
Electricity purchase	€ 52.87	€ 33.66	€ 114.16	€ 51.20
CHP fuel cost	€ 440.87	€ 477.17	€ 367.77	€ 448.22
Boiler fuel cost	€ 8.19	€ 3.25	€ 51.96	€ 6.53
Energy selling revenue	€ 0.00	– € 1.61	€ 0.00	– € 1.28
Emission cost	€ 4.69	€ 4.99	€ 3.90	€ 4.74
TOTAL COST	**€ 506.62**	**€ 517.46**	**€ 537.79**	**€ 509.41**

It can be observed C2 strategy reveals the most expensive, with a maximum difference of 6% with respect to the Base Case.

One of the main factors yielding differences in daily cost is the amount of electricity exchange at PCC with the distribution network, whose trends, determined as $P_{Pt} - P_{Dt}$, are shown in Fig.

1.23. In fact, the highest positive values, i.e. power withdrawal P_{Pt}, are reached in C2 strategy and the lowest values are observed in C1 strategy. It can be pointed out that, in all cases, the electricity withdrawal is reduced when electricity cost is higher (hours 20-21). Power delivery P_{Dt} is observed in cases C1 and C3 in central hours of the day, when the excess comes for free from renewables due to the application of specific strategy. Whereas, fuel cost is higher in Case C1 due to the more intense exploitation of the CHP systems.

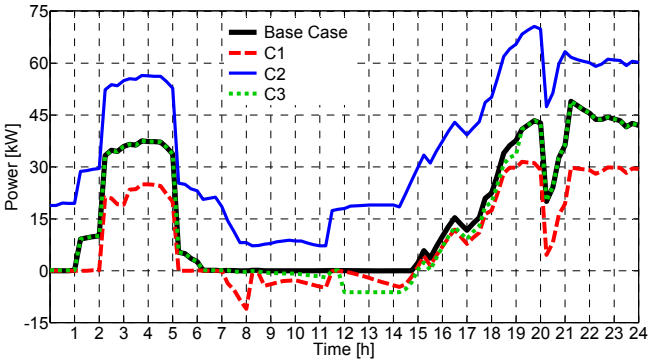

Fig. 1.23. Electricity exchange at PCC with the distribution network in the strategies.

SOC trends for ESS, in p.u. of total capacity, are illustrated in Fig. 1.24. It can be noted that SOC at the end of the day to initial value is reported, according to the constraint (1.13.b). This behavior contributes to extend ESS life as well, since it depends on the number of charge/discharge cycles [32].

Moreover, ESS store excess energy especially in hours 9-13 when RES production is high and the electricity price is generally low. This yields an increase of total MG demand, and limits power injection into the network. In fact, storing energy in excess production periods and using it, to cover the demand in peak price periods (hours 20-21), reveals in general more convenient than selling excess production and buying energy in peak price hours. Moreover, the ESS is discharged until hour 6, covering part of the load demand and avoiding network withdrawal, in order to be ready to charge in the presence of excess power. Correspondently, minimum SOC of 30 kWh (0.21 p.u.) is observed in C3, along with maximum daily energy of 94.4 kWh. Slight differences are observed with respect to Base Case in C1, with deeper discharge in hour 3. Minimum exploitation of ESS is observed in C2 with daily energy supply of 91.5 kWh, and those differences are highlighted in the details at bottom of Fig. 1.24.

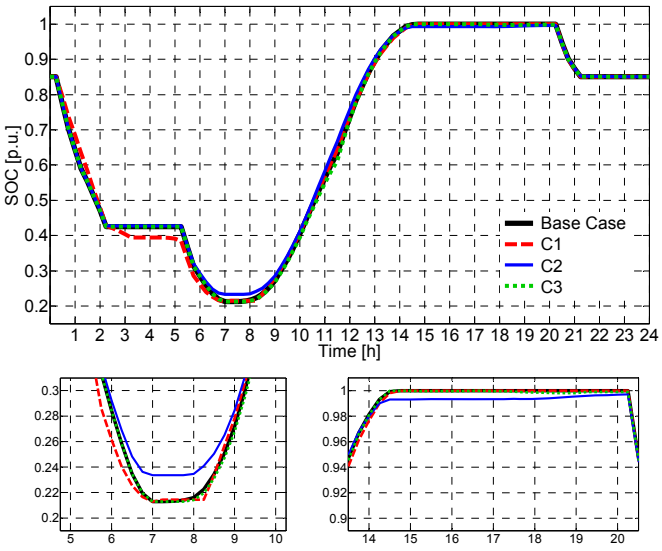

Fig. 1.24. SOC of ESS in the strategies.

It can be observed that in Base Case and C2 the thermal demand is strictly satisfied during the day, i.e. constraint (1.34) reduces to an equality, whereas the excess thermal power is due only to CHP strategies. Boilers are usually called to compensate for peak load due to less efficiency, and B2 reveals the second choice. In addition, in C1 and C3 Strategies the CHP systems reach a global average efficiency, given by the sum of electrical and thermal efficiencies, higher than 75%. This threshold often characterizes cogeneration devices with high-efficiency systems.

As regards the emission impact, the contribution in terms of cost is between 0.75% to 1.0% of total daily cost. In particular, C1 strategy shows higher emissions (1,241 kg of CO_2 in a day), whereas C2 reveals the less pollutant one (971 kg of CO_2 in a day). However, it can be seen that higher emissions are not related to higher total cost.

In CHP operation programs resulting from the procedure, it is observed that production level does not fall below experimental minimum amount (1 kW), since the corresponding low efficiency, and consequent high cost, makes it inconvenient to use CHP below 1 kW with respect to other sources. This allows to achieve analogous results with respect to other approaches introducing integer decision variables [29][68].

In order to validate the optimality of the achieved solution, obtained by the NLP formulation solved through SQP starting from the solution of the linearized problem, a set of further 100 starting points satisfying the constraints of the linearized problem is exploited [69]. These initial values are generated by stochastic variations of the linearized problem solution, according to normal distributions with zero mean and 20% as confidence interval for each state variable. The problem is therefore solved through SQP by using each of these starting points, and the obtained

results for the Base Case are reported in Fig. 1.25, where their cumulative distribution is compared with the solution of the proposed method.

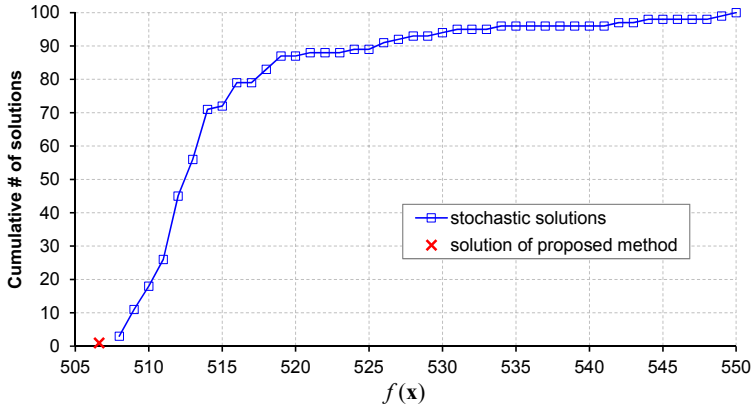

Fig. 1.25. Comparison of solutions with different starting points in the Base Case.

It can be seen that the solution obtained by means of the proposed case base method is the lowest, and most of solutions with stochastic starting points are close, but not better. Analogous results are obtained for the other three cases. Therefore, these results confirm that the overall proposed procedure for NLP problem solution, where the starting point is the solution of the linearized problem, reasonably guarantees the achievement of the optimal solution.

1.3.7 Conclusions

In this section, an optimization procedure for the day-ahead operational scheduling of a MG has been proposed. A non-linear programming problem is formulated, accounting for actual features of DG technologies and for different energy pricing schemes. Moreover, with respect to previous section, different strategies have been exploited according to operating modes of CHP systems. These strategies have been tested by implementing case studies on an experimental MG and comparing technical and economic outcomes. Simulation results have proved that the different strategies remarkably affect operation costs, reaching significant reduction of primary energy consumption and pollutant emissions. Strategy effectiveness depends on MG structure and particular condition of the considered day. The proposed approach is flexible enough to incorporate other types of DG units.

1.4 Static and Dynamic assessment of Microgrid Optimal Operation Plan

In order to achieve a deeper integration of MG in the distribution network and to enhance its performances, a proper control system has to be embedded. This system is called to perform various actions, such as minimize total cost for energy supply, increase of service availability for customers, reduce environmental impact. This is realized by means of a SCADA architecture, dealing with centralized and/or decentralized control schemes [70].

One of the main functions to be dealt with by the SCADA system is the Energy Management, linked to the optimal operation of internal sources with the objectives of improving economic and technical performances. This is in general realized in two steps [11][41]. First, a day-ahead operation planning problem is performed, by means of proper equivalent representation of MG components and accounting for suitable intervals, generally ranging between 15 minutes and 1 hour. These intervals are related to the granularity of adequate day-ahead forecasts of renewable source availability and of load, as well as to price schemes in force (i.e. flat, multi-level or time-of-use) [47]. In a second stage, the control system is called to manage MG real time operation, in response to expected or unpredicted variations affecting the devices. This function is intended to check for violations of node voltage and branch ratings, and to assess dynamic responses even in islanding conditions.

However, in order to translate the day-ahead operation plan into feasible working conditions, some procedures should be accounted. In particular, taking the cue from bulk power system management, the transition between two production setpoints should be properly programmed [71] in order to account for further functional behavior features and to ensure plan compliance. Moreover, preventive dynamic security assessment can point out critical operating conditions from the point of view of security, thus allowing the implementation of corrective control actions [72].

The aim of this section is to investigate several aspects of MG management between these two stages, where a set of further actions are required to the MG SCADA system. In particular, the elaboration to obtain a feasible minute-by-minute plan starting from hourly or 15-min references yielded by day-ahead optimal programming is performed. This plan is therefore applied to MG network model, first in static conditions by means of AC load flow analysis [73]-[76], and further in dynamic conditions by setting specific control models of devices [77]-[79]. Tests are carried out on specific configurations of the experimental microgrid testbed realized in the Electric Power System laboratory of Politecnico di Bari.

1.4.1 Methods and tools

The day-ahead operational plan provides as a result a sequence of active power setpoints for each MG device. These values are collected in a vector $\mathbf{P_j}$ for each device *j*:

$$\mathbf{P_j} = \left[P_{j,1}, P_{j,2}, \dots, P_{j,t}, \dots, P_{j,N_t} \right] \tag{1.39}$$

where *t* represents the generic time step $t = 1,\dots,N_t$.

In order to smooth out the sudden variations that can occur at the transition between two intervals, the 15-min setpoints are translated in a minute-by-minute plan, as depicted in Fig. 1.26. This action is performed keeping the total energy of the device, by transferring some amount of energy between a defined number of minutes.

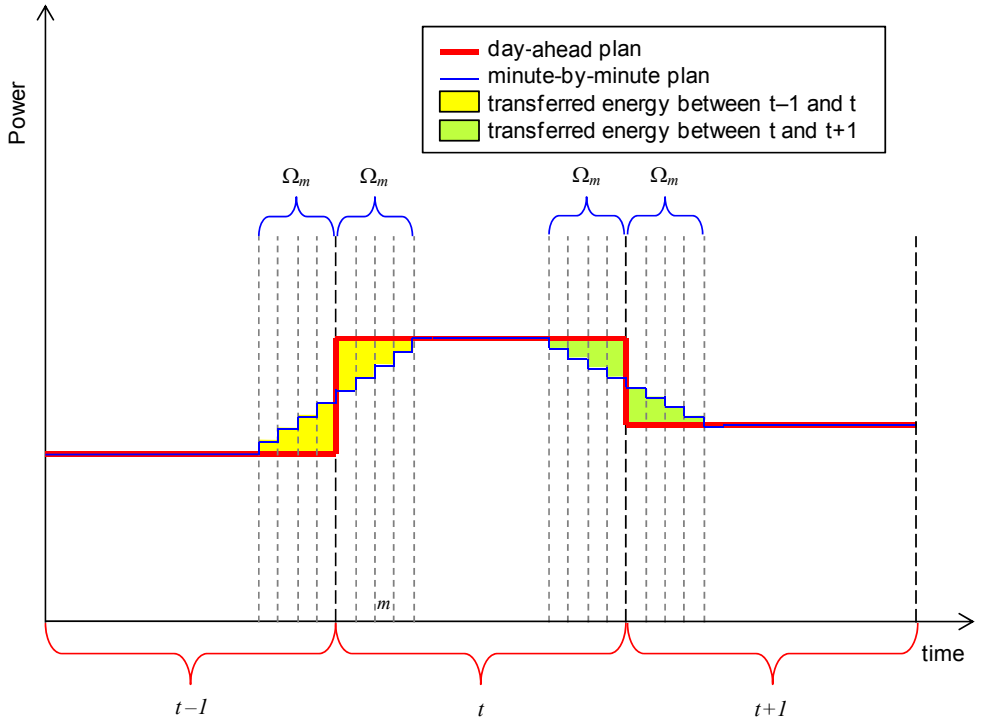

Fig. 1.26. From day-ahead plan to minute-by-minute plan.

By indicating with *m* the generic minute of the day, $m = 1,\dots,N_m$, and with M_t the number of minutes in a single interval *t*, the smoothing action is performed for $2 \cdot \Omega_m$ minutes over two contiguous intervals as follows:

$$P_{j,m} = P_{j,t} + \left(t \cdot M_t - m + 1\right) \cdot \left(\frac{P_{j,t+1} - P_{j,t}}{2 \cdot \Omega_m} \right) \tag{1.40.a}$$
$$\forall m \ni' \; t \cdot M_t - \Omega_m + 1 \le m \le t \cdot M_t$$

$$P_{j,m} = P_{j,t} + \left(\left(t-1\right) \cdot M_t - \Omega_m - m + 1\right) \cdot \left(\frac{P_{j,t} - P_{j,t-1}}{2 \cdot \Omega_m} \right) \tag{1.40.b}$$
$$\forall \; m \ni' \; \left(t-1\right) \cdot M_t + 1 \le m \le \left(t-1\right) \cdot M_t + \Omega_m$$

$$P_{j,m} = P_{j,t} \quad \text{otherwise} \tag{1.40.c}$$

This process allows a suitable operational margins to each device and to preserve energy balance, preventing losses of revenue and reducing stresses induced by sudden variations. This is particularly true for CHP operation, since any variation of electric power can infer a variation in thermal output.

The MG static model is based on power flow method, determining a snapshot of network behaviour in each operating condition. In this model, generators, storage devices and loads are represented as controlled power sources/sinks, where active power derives from the minute-by-minute plan. The task of voltage regulation is entrusted to grid connection, or to a suitable internal source in intervals where islanding operation is provided. The determination of power flows in the MG is therefore carried out independently for each minute, obtaining a daily profile for voltage and current throughout the MG network:

$$\begin{aligned} &\tilde{P}_{i,m} - P_{i,m}\left(\vartheta, V\right) = 0 \quad \forall i,m \\ &\tilde{Q}_{i,m} - Q_{i,m}\left(\vartheta, V\right) = 0 \quad \forall i,m \end{aligned} \tag{1.41.a}$$

where i indicates the generic network node, and the net power injection at m-th minute in the i-th node is:

$$\tilde{P}_{i,m} = \sum_{j \in i} P_{j,m} \tag{1.41.b}$$

indicating with $j \in i$ the set of devices connected to node i, and assuming power generation positive and power withdrawal negative. It is worth to remark that classical methodologies for load flow simplification are not applicable to LV network (e.g. fast decoupled load flow, DC load flow), therefore full AC load flow resolution techniques are considered. Unbalanced load flow solutions should be adopted if power distribution among phases is not symmetrical [80].

MG dynamic model includes the representation of the main variables involved in electromechanical transient analysis of power production and delivery. This is realized neglecting faster dynamics related to electric transients, considering algebraic network equations and including device response or control functions in the range from tens of milliseconds to some seconds [81]. Under these assumption, trends for instantaneous effective values of each variable are derived through the following formulation:

$$\begin{cases} \dot{\mathbf{x}} = \mathbf{f}\left(\mathbf{x}, \mathbf{v}, \mathbf{r}\right) \\ \mathbf{I}\left(\mathbf{x}, \mathbf{v}\right) - \mathbf{Y} \cdot \mathbf{v} = \mathbf{0} \end{cases} \tag{1.42}$$

where $\mathbf{x}$ is the set of state variables of all devices, $\mathbf{v}$ is the vector of voltage levels at all network nodes, includes the relation between net current injection, state and voltage for all devices, $\mathbf{Y}$

is the nodal admittance matrix and **r** is the vector of inputs, including the planned power level of devices and variations of uncontrollable sources.

This formulation is particularly challenging in MG where lots of power electronic interfaces are present, and proper models should be adopted in order not to lose information about the behaviour of both primary energy source and network connection [82][83]. In this work, literature-based models including basic features of experimental devices are exploited. For instance, in Fig. 1.27 the adopted dynamic model of the storage system is reported. In particular, it involves power and voltage measurements along with the reference signal coming from day-ahead planning. It includes a model of DC side and battery depending on State of Charge (SOC), detailed in Fig. 1.28, a PQ control aimed at defining reference current on a d-q frame (see Fig. 1.29), and a charge controller for proper limitations and feedbacks, in order to drive the inverter for the interface with the MG network.

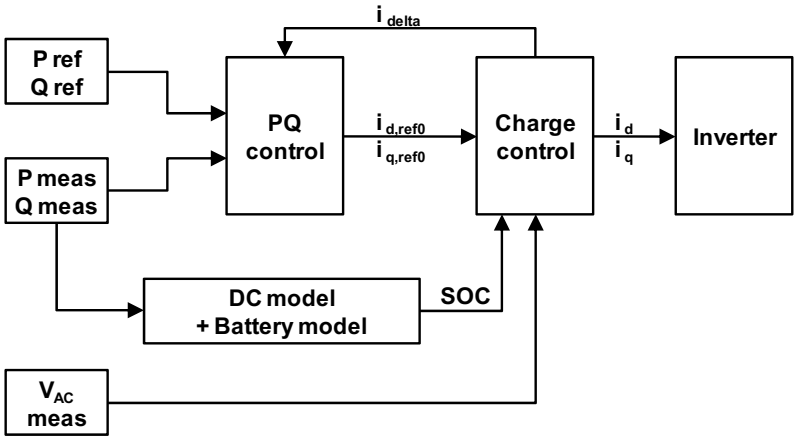

Fig. 1.27. Dynamic control scheme of energy storage device.

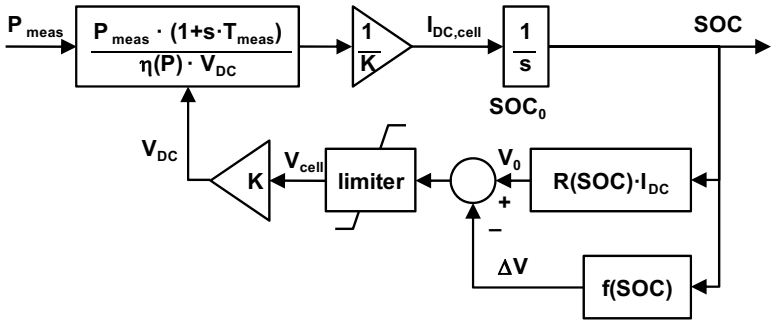

Fig. 1.28. Battery and DC-side model of the energy storage device.

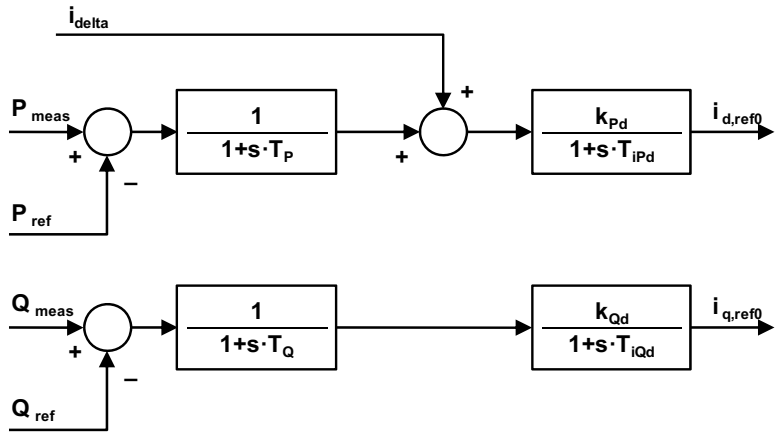

Fig. 1.29. PQ control of the energy storage device.

Moreover, in Fig. 1.30, the dynamic model of wind turbine is reported. It includes an aerodynamic model for power conversion and active control, according to the specific turbine regulation strategy and dynamic response, the model of generator dynamics (in this case, a PMSG) with relevant control, and PQ control of full scale converter.

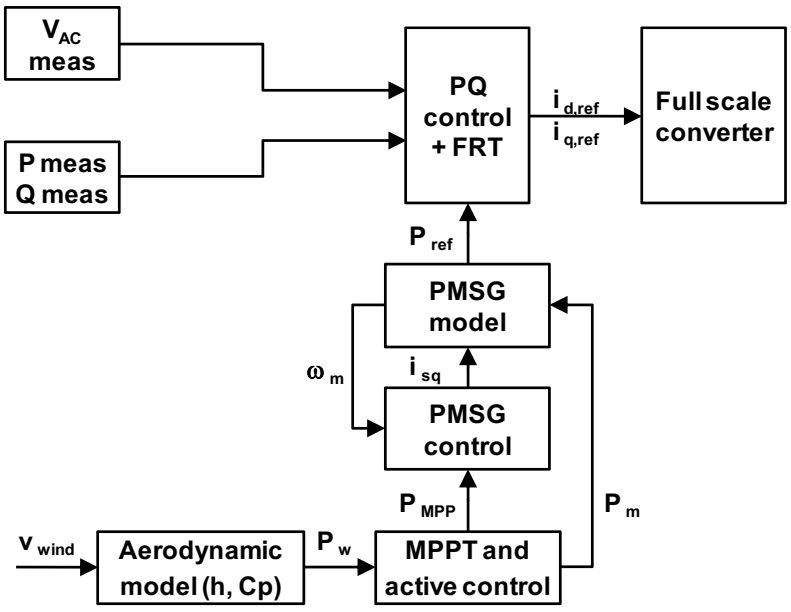

Fig. 1.30. Dynamic model of a PMSG-based wind turbine.

The day-ahead operation plan is elaborated through the solution of a non-linear programming problem implemented in Matlab® environment. From this starting point, the determination of the minute-by-minute program is performed in Matlab as well. Finally, the plan is automatically imported in DigSilent PowerFactory®, where network assessment, both static and dynamic, is carried out. In particular, the execution of multiple load flow analysis and of transient stability

analysis with variable inputs are managed by means of a specific procedure in DigSilent Programming Language (DPL).

1.4.2 Test and Results

The proposed approach is applied to a suitable configuration of the experimental MG built at premises of Electric Power System laboratory of Politecnico di Bari. The components of test MG have been described in section 1.3,whereas the network model is depicted in Fig. 1.31.

All these components, actually realized and installed in the framework of the experimental MG testbed, are interfaced to the AC internal network by means of power converters, in order to enhance their performances. This in turn implies the need of proper dynamic models for distributed generation and storage devices, in order to reproduce the behaviour of actual systems and the control strategies implemented in the converters.

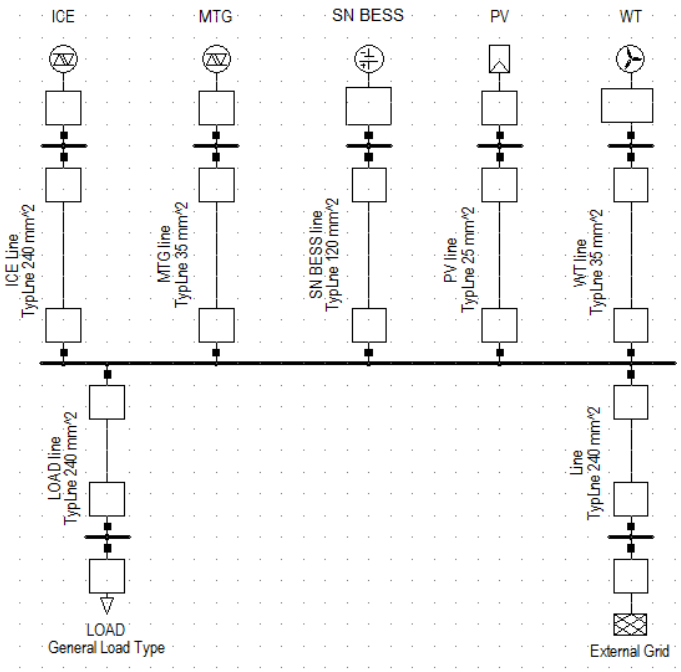

Figure 1.31. Test MG network model.

1.4.2.1 Static network validation

The results of the day-ahead programming procedure of the MG, applied to a typical summer day, are reported in Fig. 1.32. It can be seen that the day-ahead plan is obtained with 15-min interval, according to suitable forecasts of wind and solar availability taken by a local weather station [59].

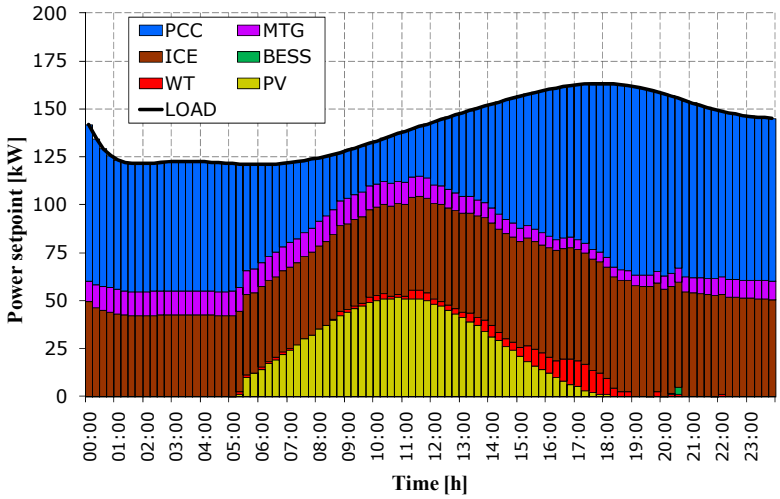

Figure 1.32. Day-ahead operational plan.

The determination of the minute-by-minute plan in the proposed test is performed for $2 \cdot \Omega_m$ = 14 minutes over two contiguous intervals, therefore the set-point changes slightly every minute. Whereas, for devices based on non-dispatchable renewable sources (PV, WT), the network analysis involves the same forecast values of the day-ahead plan. Sensitivity analysis according to uncertainty levels or updated forecast in a shorter time frame could be accounted as well.

After this process, the static assessment of MG network behaviour is performed by N_m = 1440 successive power flow analyses. According to the implemented control strategy in the experimental testbed, in grid-connected mode all the internal devices are represented by PQ buses, whereas the external grid node, or PCC, is accounted as the reference bus (i.e. at nominal voltage with null phase), slacking network losses. Moreover, due to the limited extension of the network, reactive power production is set to zero for all devices (the reactive charging of lines comes from the external network). Relevant results are reported in Fig. 1.33 , where a screenshot of network at a defined time instant is reported.

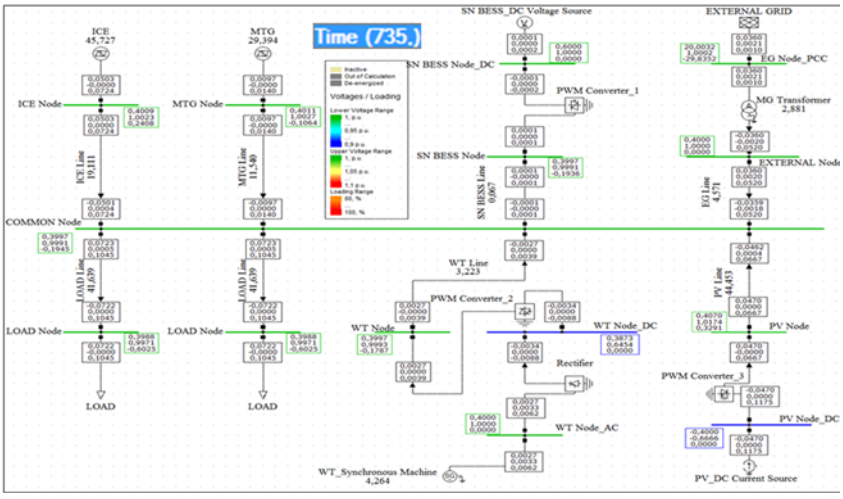

Figure 1.33. An example of static network assessment through DigSilent.

Moreover, in Fig. 1.34 and 1.35 daily voltage magnitudes at each node of the MG and daily loading rates for each line, respectively, are reported over the whole day. It can be seen that, thanks to the radial structure of the MG, typical of low-voltage networks, voltage values are always included in an acceptable range, between 0.98 and 1.02 p.u., and line loading is well below the maximum available flow, therefore no remarkable operation problems can be addressed in static network assessment. It can be noted that line loading does not assume remarkable values since the connections are mostly designed to limit voltage drop, exploiting larger cable sections. Therefore, the analysis has bought out that the static grid model could be included in planning stage, though slight influence is expectable with the adopted radial network architecture.

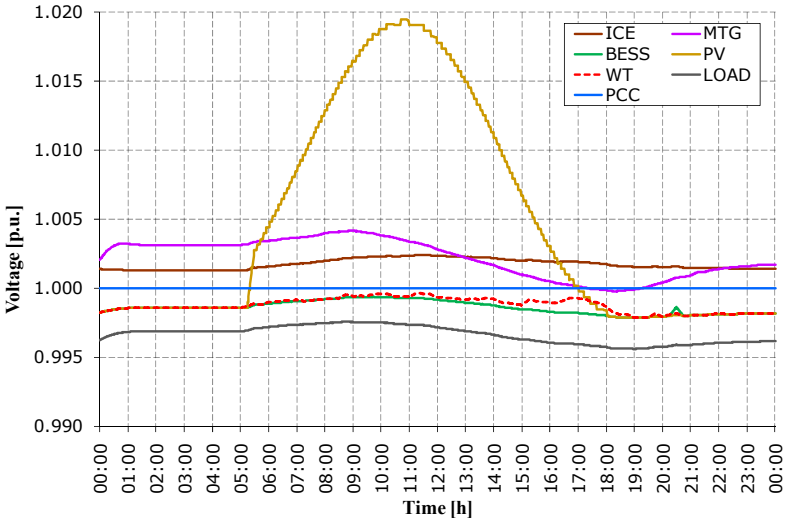

Figure 1.34. Daily overview of minute-by-minute node voltage.

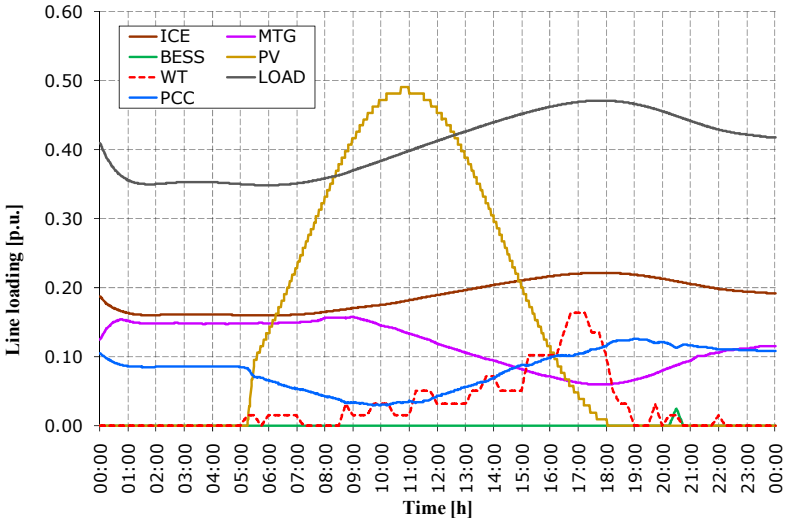

Figure 1.35. Daily overview of minute-by-minute line loading.

1.4.2.2 Dynamic network validation

The dynamic analysis is carried out for an entire day, in which gas-based systems are lacking. The MG generation is supported by PV, WT, BESS and grid connection at PCC. These sources are not able to satisfy the full load demand, therefore load curtailment is preventively evaluated. In Fig. 1.36, the dynamic behaviour of the BESS under minute-by-minute setpoint decrease over a 5-min interval is reported. It can be seen that the response is prompt, reaching the setpoint in less than 1 s with negligible damping, due to the absence of rotating parts and the fast time constants of the control scheme. Analogous behaviour is observed in the presence of setpoint increase and with negative power level (corresponding to charge). A comparison of planned SOC behaviour and the dynamic assessment trend over the whole day is reported in Fig. 1.37.

Figure 1.36. Dynamic behaviour of BESS in a 5-min time window.

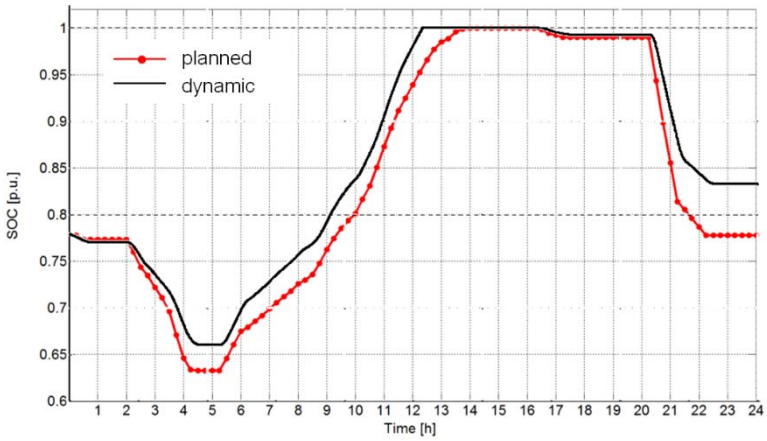

Figure 1.37. SOC of BESS in day-ahead plan and in dynamic assessment.

It can be seen that the dynamic assessment leads to analogous SOC trend though with slower discharge and faster charge, due to the dynamic battery model, involving the definition of

voltage and current according to SOC. The effect of charge controller is pointed out when SOC reaches the upper limit of 1 p.u., when the charge process is arrested at roughly 12:15, notwithstanding relevant setpoints are present until 14:00.

The influence of dynamic models is further illustrated in Fig. 1.38, reporting in the upper part the planned trend of active power of the involved devices, and in the lower section the trends obtained by daily dynamic analysis with minute-by-minute setpoints. It can be seen that PV shows limited deviations, whereas WT is slightly delayed due to the time constants related to aerodynamic and machine model, and BESS is limited in charge between hour 12 and 14, as expected from the analysis of Fig. 1.37. Finally, the power exchange at PCC is in charge to cover those variations, in order to ensure the power demand and balance network losses, summing up to roughly 4 kW (as per comparison of the trends in the last hours of the day).

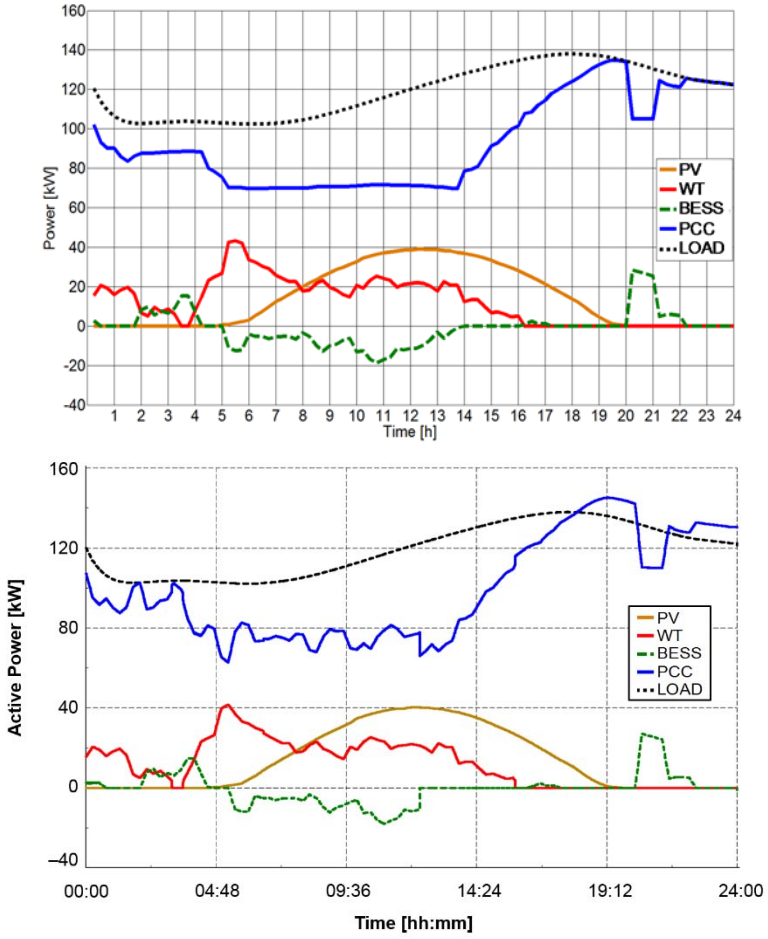

Figure 1.38. Power levels of MG devices in day-ahead plan (upper) and in dynamic assessment (lower).

1.4.3 Conclusions

The methodologies and tools useful for the assessment of MG behaviour between the elaboration of day-ahead plan and real-time operation have been analyzed. In particular, a procedure to obtain a feasible minute-by-minute plan starting from hourly or 15-min references yielded by day-ahead optimal programming has been formalized. Therefore, the application of minute-by-minute plan to static network model by means of full AC load flow analysis has been proposed. Possible violations of feasible range of node voltage and line loading are checked through this method. Moreover, proper dynamic assessment has been analyzed, highlighting the importance of exploiting suitable models of MG devices for electromechanic stability analysis. The proposed methods have been applied to selected configurations and operating conditions of the experimental MG testbed of Politecnico di Bari, constituted by a radial symmetric three-phase AC LV network. Results have shown the potential usefulness of these analyses, pointing out the need of refined models, even coming from field experience, to account for several aspects of device behaviour that could be shadowed by simple models in day-ahead programming stage.

1.5 PrInCE lab microgrid: early experimental results

As stated in the previous section, the operation of the experimental facility is managed by the definition of an operation program, defined the day before the actual implementation. Since the facility includes programmable loads, these are supposed to be known in advance. Whereas, adequate forecasts are evaluated for wind speed and for solar radiation, according to locally available meteorological data history. Moreover, the planning procedure accounts for costs of electric energy, involving day-ahead electricity market yields, as well as fuel costs, and the coverage of fictitious thermal demand. The procedure for obtaining the operation plan has been thoroughly described in the paragraph 1.3. In Fig. 1.39, a 3-h time period of the electric power operation plan obtained for a sunny working day of July is illustrated, by exploiting the characteristic wind speed-power of a 50-kW horizontal axis wind generator.

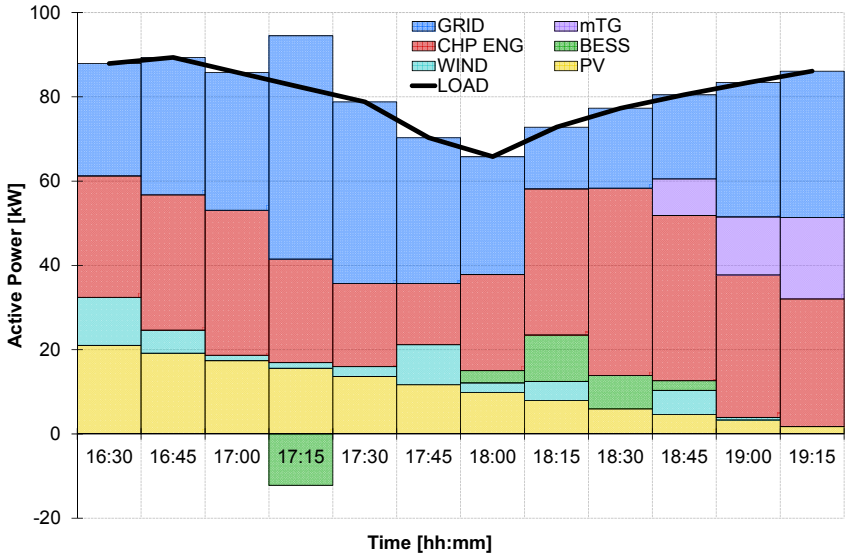

Figure 1.39. Day-ahead operation plan of the considered time horizon.

The aim of the test is to reproduce the presented plan in the actual microgrid operation, and to highlight peculiarities of the devices to be included in the procedure in order to improve the fitness to actual operation of the devices. Therefore, the experimental microgrid is operated for the described 3-h time horizon, by sending the active power set-points to CHP engine (CHP ENG), microturbine (MTG), battery (BESS) and both programmable loads (LOAD), and considering the actual power production from photovoltaic system (PV) and wind emulator (WIND). Test results are reported in Fig. 1.40 for renewable-based devices, in Fig. 1.41 for fuel-based devices, in Fig. 1.42 for BESS (including the trends for SOC) and in Fig. 1.43 for loads and grid exchange (GRID).

For renewable sources, see Fig. 1.40, the difference between 15-min day-ahead forecast (forec) and actual trends is almost negligible for PV, except the temperature effect, whereas it reveals more remarkable for wind, where the production is low but with fast variations and some time shifting effects are observed. Moreover, it is worth to remark that, when the wind speed is lower than cut-in speed of the chosen turbine, some losses are observed, from 0.3 to 0.6 kW.

Both fuel-based technologies, CHP ENG and MTG, show a mismatch between the setpoint (s.p.) and actual value measured at microgrid common bus, as can be seen in Fig. 1.41, due to the presence of internal losses and services and marginally to connection losses. It can be remarked that CHP ENG shows more remarkable transient effects, with deeper spikes, at 17:45 when one of the two motors is shut down, and at 18:15 when it is turned on again, due to internal sharing logics of the machine. Whereas, at 18:45, the microturbine is started, since it cannot be kept in idle state, and during the acceleration stage it absorbs some power. The check performed on this process has caused a delay in sending the setpoint to CHP ENG. However, MTG response to setpoint is quite faster than CHP one.

The response of BESS to active power setpoint (positive for discharge, negative for charge) is quite fast, see Fig. 1.42, though showing some differences between positive variations, where a smooth response is observed, and negative ones, where an initial spike is noted. A different behaviour can be observed at the beginning and at the end of the time window, where 0 kW are required from the BESS. In particular, at first the BESS is ready to accept the setpoint, therefore it effectively does not exchange power with the microgrid, although the SOC shows an unpredicted reduction with respect to the planned value due to self-discharge effect. This latter is hindered in the last two intervals, where the SOC is kept constant by setting the idle operating condition, that requires roughly 2.2 kW of power drawn.

The response of programmable loads is quite fast and affordable, as shown in Fig. 1.43. However, in order to keep the system working correctly, the need of roughly 9.9 kW for auxiliary services (AUX in Fig. 1.43) arises during operation, notwithstanding this is not considered in day-ahead plan. All the described variations, involving dynamic behaviour and lower power yields with respect to the plan, affect the power exchange level, called to balance the system in grid-connected mode. The effect of measurements discretization can be highlighted on grid exchange, where only deep variations are catched.

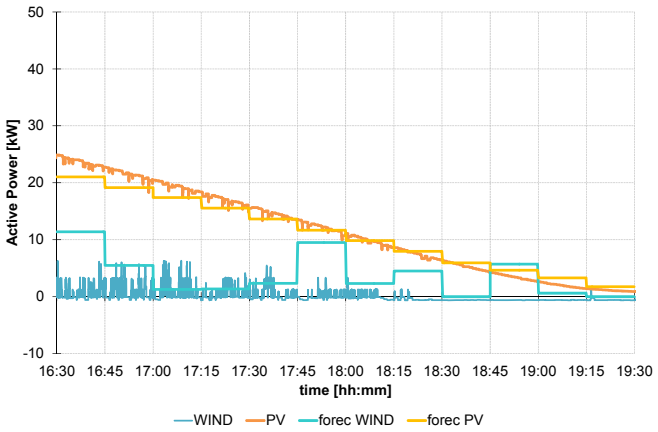

Figure 1.40. Forecast and actual operation of renewable-based devices.

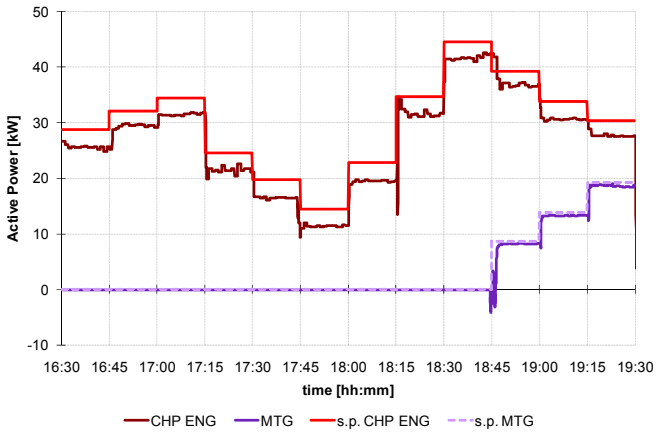

Figure 1.41. Planned and actual operation of fuel-based devices.

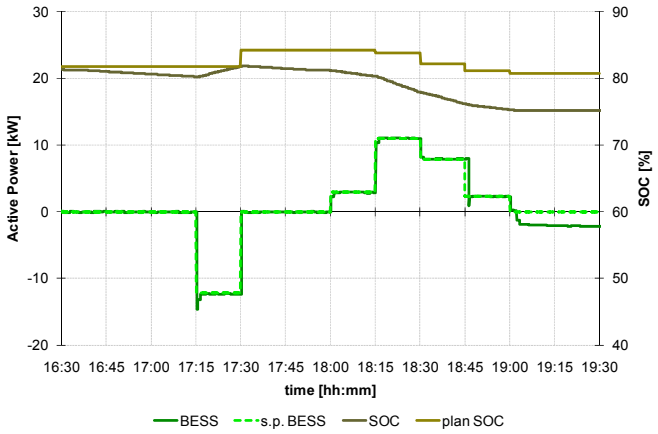

Figure 1.42. Planned and actual operation of BESS.

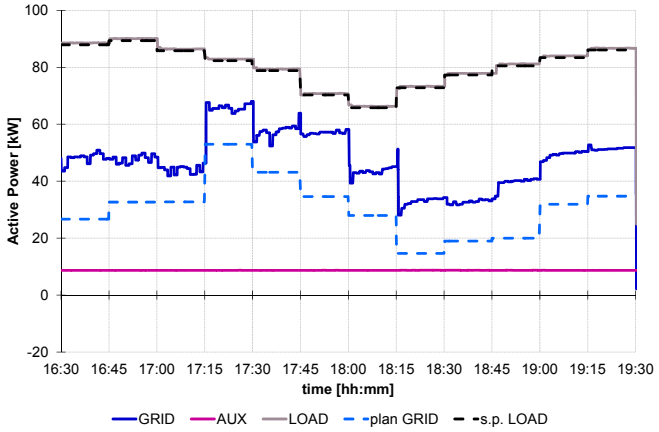

Figure 1.43. Planned and actual operation of load and grid exchange.

In Table 1.6, the actual operation yields on 15-min average are synthetically compared to the operation plan. It can be observed that BESS and LOAD are able to realize the specified setpoints with minimum deviations. Whereas MTG and CHP ENG, when on, show an average reduction of 1 kW and of 3 kW respectively in comparison to setpoint, slightly dependent on the imposed value. The deviation of PV from the ranges between 3 kW in excess and 2 kW lacking, showing a satisfactory compliance. Whereas, the error on wind power is more evident, especially in some intervals, and average forecast of energy yield reveals too high as well.

The total effect of these deviations reflects on the grid power exchange, including 9.9 kW of auxiliary services, ranges between 12 kW and 22 kW of deviation from the plan. In any case, the total power balance of the microgrid is obtained satisfactorily on the 15-min average, showing only up to 1 kW mismatch due to the mentioned measurement issues.

Table 1.6. planned and average actual power in each interval [kW]

Device	BESS		CHP ENG		mTG		LOAD		PV		WIND		GRID		Balance	
Interval	Plan	Avg	Plan	Avg	Plan	Avg	Plan	Avg	Plan	Avg	Plan	Avg	Plan	Avg	Plan	Avg
16:30	0	-0.02	28.8	25.64	0	-0.14	87.9	88.55	21.02	23.72	11.4	0.64	26.68	48.05	0	-0.56
16:45	0	-0.03	32.1	29.15	0	-0.14	89.36	90.04	19.15	21.54	5.48	0.86	32.63	47.79	0	-0.76
17:00	0	-0.04	34.4	31.44	0	-0.14	85.8	86.45	17.41	19.31	1.27	1.00	32.72	44.18	0	-0.61
17:15	-12.2	-12.08	24.6	21.69	0	-0.14	82.3	82.91	15.56	16.99	1.36	0.56	52.98	65.36	0	-0.43
17:30	0	-0.25	19.7	16.31	0	-0.14	78.8	79.35	13.65	14.62	2.34	0.53	43.11	57.70	0	-0.48
17:45	0	-0.05	14.5	11.39	0	-0.14	70.3	70.72	11.68	12.21	9.51	0.03	34.61	57.02	0	-0.15
18:00	2.9	2.81	22.8	19.37	0	-0.14	65.8	66.32	9.83	9.80	2.31	0.05	27.96	43.61	0	-0.70
18:15	11	10.85	34.7	31.18	0	-0.14	72.8	73.19	7.96	7.44	4.51	-0.45	14.63	33.33	0	-0.88
18:30	7.9	7.97	44.5	41.63	0	-0.20	77.3	77.76	5.94	5.33	0	-0.60	18.96	32.77	0	-0.74
18:45	2.3	2.78	39.2	37.36	8.7	7.34	80.5	80.85	4.63	3.45	5.71	-0.61	19.96	39.42	0	-1.00
19:00	0	-1.56	33.8	30.71	13.8	13.12	83.4	83.95	3.31	1.97	0.61	-0.59	31.88	49.32	0	-0.88
19:15	0	-2.15	30.31	27.75	19.3	18.45	86.1	86.66	1.75	1.12	0	-0.57	34.74	51.46	0	-0.49

The comparison of simulation results and field tests yield the refinements to the planning procedure with respect the inclusion of power needs for auxiliary service, the improvement of the model of CHP ENG and MTG to account for the observed deviations and more accuracy methods for renewable source forecast.

The main features of PrInCE lab experimental microgrid have been exposed in this work, that can yield to consider it as a powerful testbench for carrying out several kind of proves on commercial components taking part of an integrated microgrid and verifications on relevant management strategies. The illustrated results of the application of operation programming and control procedures to the experimental facility have shown satisfactory behaviour in sending-receiving setpoints.

2. Thermal demand estimation in Multi-energy Microgrid in the presence of electrical and thermal energy storage

The MG is typically characterized by the integration of electric and thermal vectors mainly to service users that are considered by building, tertiary sector and industrial. However, the presence of different sources and demands gives rise to the necessity of carefully modeling energy needs. In this context, energy storage devices can represent a crucial element in operation decision making. An advanced model for operation planning of a multi-energy microgrid is proposed in this section, with a particular care on integrated water-based thermal supply infrastructure and on occupant thermal comfort. In the first sub-section the influence of thermal and electric energy storage is investigated in day-ahead operation planning. Whereas, in the second sub-section a bottom-up engineering viewpoint is evaluated, involving energy flows interesting user buildings and mass flow rates and temperatures of the thermal production sources. In particular, a temperature-based model of integrated heat supply devices, considering water mass flow rates as well, is accounted. The behaviour of different heating sources and thermal storage is evaluated by means of a detailed model. The presented procedure are applied to a configuration of Experimental Microgrid realized in Electric Power Systems laboratory at Politecnico di Bari with empowered thermal section.

2.1 Influence of energy storage in Multi-energy Microgrid operation

Models for electric and thermal energy storage are included, in order to test the technical and economic effectiveness of their integration. In particular, a model of a multi-energy MG based on physical quantities and on a fully integrated water-based heating system including CHPs and boilers is proposed, in order to investigate the effect of the presence of ESS and TSS on MG operation planning. Moreover, air source HP is considered as a controllable electric load that supplies heat not affecting the modelled water circuit. The adopted approach, based on multi-objective programming aimed at optimizing economic expenses in the presence of thermal comfort constraint, is applied to a configuration layout of the Experimental Microgrid realized in Electric Power Systems laboratory at Politecnico di Bari.

2.1.1 Literature review

The multi-energy system is introduced by [85] including different concepts as energy hub [86], virtual power plant [87] and MG. In this outlook, an essential component is represented by Combined Heat and Power (CHP) systems, that couple electric energy and thermal (heating/cooling) energy supply in MG, that is a crucial aspect to improve their acceptability [88]. An example of sizing methodology for a CHP-based MG is shown in [33]. However, the

main drawback of CHP systems is their strength point itself, since the link between electricity and thermal power involves to choose one as the main product, in electric- or thermal-following strategy, being the other quantity dealt with as a by-product, as shown in the chapter 1. The presence of other flexible components can help optimal CHP use, as well as the response to price dynamics and the increase of robustness against variations of RES availability and energy demand.

In this framework, energy storage devices represent a suitable candidate to uphold multi-energy MGs, allowing for better production and demand matching [90]. Technologies for both electric energy storage system (ESS) and thermal energy storage system (TSS) can reveal useful, though the currently remarkable investment costs may hinder their diffusion. Integrated models of multi-energy systems with CHPs and energy storage devices have been developed in [91], where a CHP integrated with auxiliary boiler and TSS is analyzed with a priority-based methodology to assess the potential of ESS integration. A 24-h scheduling method based on receding horizon for PV-CHP system with TSS is proposed in [92] and the model is based on energy flows. Whereas, an optimal sizing method for residential energy-integrated MG with several production technologies is shown in [93], combined with district heating network.

An important issue in multi-energy systems is thermal comfort of occupants, that can be included in the objective of energy management procedure as in [94], where a detailed building model for determining internal room condition is introduced. In particular, the thermal comfort can be pursued by means of the integration of Heat Pumps (HPs), often associated to ESS and TSS in the MG framework [95][96], and can further represent a part of thermostatically controlled electricity load. For instance, in [97] a Model Predictive Control is carried out for a residential energy system, modelled as an energy hub with storage, in the presence of dynamic model of comfort, as compared to HP-based system. It can be argued that models and methodologies proposed in literature for multi-energy systems are mainly based on superstructure approach [93], accounting for energy flows and neglecting variables describing the behavior of devices (i.e. thermal storage temperature, mass flow rates, …). Moreover, CHP systems are usually dealt with in MG context as single device, possibly integrated by auxiliary boilers.

2.1.2 Multi-energy microgrid operation planning

In order to determine the day-ahead operation programme of a multi-energy microgrid, an optimization problem is carried out, aiming at minimizing an objective function $f(\mathbf{x})$ representing the operation cost in the considered time horizon, divided into N_t time steps with Δt duration, as follows:

$$f(\mathbf{x}) = \sum_{t=1}^{N_t} \left[\sum_{k=1}^{N_k} OC_{k,t} + \sum_{j=1}^{N_j} OC_{j,t} + GC_t \right] \tag{2.1}$$

where $OC_{k,t}$ represents the operation cost of the k-th electric power generation unit at time step t, $OC_{j,t}$ is the operation cost of the j-th thermal power generation unit at time step t, and GC_t stands for the cost for energy withdrawal from the grid connection point at time step t.

Cost items associated to electric power generation units based on power production level $P_{k,t}$ is determined as follows:

$$OC_{k,t} = \frac{cf_k \cdot \Delta t \cdot P_{k,t}}{h_k \cdot \eta_k^E} \tag{2.2}$$

where cf_k, h_k and η_k^E stand for unitary fuel cost, fuel heating value and electric efficiency, respectively. This formulation is appropriate for electric power production units and CHP units. An analogous relation is exploited for the j-th thermal power production unit, where thermal power production level $\dot{Q}_{j,t}$ and thermal efficiency η_j^Q are accounted:

$$OC_{j,t} = \frac{cf_j \cdot \Delta t \cdot \dot{Q}_{j,t}}{h_j \cdot \eta_j^Q} \tag{2.3}$$

Net costs of grid connection are expressed as follows:

$$GC_t = \Delta t \cdot \left(gc_t \cdot P_t^{gw} - gr_t \cdot P_t^{gj} \right) \tag{2.4}$$

where P_t^{gw} represents power purchase from the grid at unitary cost gc_t, whereas and P_t^{gj} is the power sold to the network at unitary price gr_t.

Decision variables include electric power production levels, power-to-heat consumption (by means of HPs), fuel mass flow rates, water flow rates and temperatures, and ambient temperature.

The electric power balance of the MG at each time interval t, neglecting power losses, is expressed as:

$$\sum_{k=1}^{N_k} P_{k,t} + P_t^R + P_t^{gw} = P_t^D + P_t^{gw} + \sum_{h=1}^{N_h} P_{h,t} \tag{2.5}$$

where P_t^R represents forecast power production from RESs, and P_t^D is the predicted electric load demand. Moreover, $P_{h,t}$ is the quota of consumed electric power from the *h*-th heat pump, in order to produce a specified quantity of heat based on the COP, as follows:

$$\dot{Q}_{h,t} = COP_h \cdot P_{h,t} \tag{2.6}$$

As regards thermal demand, it is supposed to be linked to ambient thermal comfort, therefore ensuring suitable temperature levels in user rooms, varying over time:

$$\vartheta_t^{\min} \le \vartheta_t^i \le \vartheta_t^{\max} \tag{2.7}$$

The thermal energy balance is expressed by means of energy flow relation:

$$\dot{Q}_t^Y + \sum_{h=1}^{N_h} \dot{Q}_{h,t} + \dot{Q}_t^S = \dot{Q}_t^D + \dot{Q}_t^W + \dot{Q}_t^V \tag{2.8}$$

The term $\dot{Q}_t^D$ is in charge of accounting for room air temperature deviation ϑ_t^i over time, depending on internal thermal capacity C_a:

$$\dot{Q}_t^D = C_a \cdot \left(\vartheta_t^i - \vartheta_{t-1}^i \right) \tag{2.9}$$

Therefore this quantity is positive (temperature rises) in the case of exceeding heat inlet, given by the yield of water-based heating system $\dot{Q}_t^Y$, heat pumps production $\dot{Q}_{h,t}$ and heating effect of solar irradiance $\dot{Q}_t^S$. Whereas, $\dot{Q}_t^D$ is negative (temperature decreases) in the case of prevalence of heat losses, related to wall conduction $\dot{Q}_t^W$ and air ventilation $\dot{Q}_t^V$, the latters depending on the difference between internal temperature and external temperature ϑ_t^e.

Water-based heating system includes different sources as boilers, and CHPs. For boilers, thermal production level can be connected to fuel mass rate $\dot{m}_{j,t}^f$ and has the effect to heat the water flow $\dot{m}_{j,t}^w$ (with heating value c^w) by a temperature rise $\Delta\vartheta_j^w$:

$$\dot{Q}_{j,t} = \eta_j^Q \cdot \dot{m}_{j,t}^f \cdot h_j = \dot{m}_{j,t}^w \cdot c^w \cdot \Delta\vartheta_j^w \tag{2.10}$$

As regards CHP devices, available thermal power $\dot{Q}_{k,t}^a$ is related to power production, and it can generally be higher than useful effective thermal power $\dot{Q}_{k,t}^u$, accounting for possible wasting

heat to the atmosphere. The term $\dot{Q}^{u}_{k,t}$ depends on the amount of exhausts $\dot{m}^{X}_{k,t}$ flowing in the heat recovery system, with efficiency η^{X}_{k}, inducing a water temperature rise Δt^{w}_{k}:

$$\dot{Q}^{a}_{k,t} = P_{k,t} \cdot \frac{\eta^{Q}_{k}}{\eta^{E}_{k}} = \eta^{Q}_{k} \cdot \dot{m}^{f}_{k,t} \cdot h_{k} \tag{2.11.a}$$

$$\dot{Q}^{a}_{k,t} \geq \dot{Q}^{u}_{k,t} = \eta^{X}_{k} \cdot \dot{m}^{X}_{k,t} \cdot c^{X}_{k} = \dot{m}^{w}_{k,t} \cdot c^{w} \cdot \Delta \vartheta^{w}_{k} \tag{2.11.b}$$

Accounting for the same temperature of cold water, the outlet of boilers and CHPs can be joined giving out the following expressions.

$$\dot{m}^{Y}_{t} = \sum_{k=1}^{N_k} \dot{m}^{w}_{k,t} + \sum_{j=1}^{N_j} \dot{m}^{w}_{j,t} \tag{2.12.a}$$

$$\vartheta^{Y}_{t} = \frac{1}{\dot{m}^{Y}_{t}} \cdot \left(\sum_{k=1}^{N_k} \dot{m}^{w}_{k,t} \cdot \vartheta^{w}_{k,t} + \sum_{j=1}^{N_j} \dot{m}^{w}_{j,t} \cdot \vartheta^{w}_{j,t} \right) \tag{2.12.b}$$

Therefore, heat yield from water-based system to the ambient is determined as follows, where ϑ^{F}_{t} is the known final temperature of water after exchanging heat with the ambient, accounting for relevant heat exchange efficiency η^{Y}:

$$\dot{Q}^{Y}_{t} = \eta^{Y} \cdot \dot{m}^{Y}_{t} \cdot c^{w} \cdot \left(\vartheta^{Y}_{t} - \vartheta^{F}_{t} \right) \tag{2.13}$$

2.1.3 The influence of energy storage systems

In the presence of ESSs, the electric balance (2.5) is modified as follows:

$$\sum_{k=1}^{N_k} P_{k,t} + P^{F}_{t} + P^{gw}_{t} + \sum_{s=1}^{N_s} P^{dc}_{s,t} = P^{D}_{t} + P^{gw}_{t} + \sum_{h=1}^{N_h} P_{h,t} + \sum_{s=1}^{N_s} P^{ch}_{s,t} \tag{2.14}$$

where $P^{dc}_{s,t}$ and $P^{ch}_{s,t}$ represent discharge and charge power for the *s*-th ESS, respectively, limited by nominal rates. Moreover, they determine ESS energy content of the *s*-th ESS $E_{s,t}$ as per the following relation, where η_s is the efficiency and l_s is the loss rate. The energy state is bounded by device ratings as well.

$$E_{s,t} = E_{s,t-1} - l_s + \Delta t \cdot \left(\eta_s \cdot P^{ch}_{s,t} - P^{dc}_{s,t} \big/ \eta_s \right) \tag{2.15}$$

In the presence of TSS, integrated in the water-based heating system, a decoupling between heat production and heat supply is considered. Neglecting water mass losses, the following relation allows to determine variations of TSS temperature ϑ^{T}_{t}, where storage thermal losses

$\dot{Q}_t^{TL}$ are assumed dependent on the difference between storage water temperature and external air temperatures. Therefore, the following relation replaces (2.12.a) and (2.12.b).

$$m_t^T \cdot c^w \cdot \left(\vartheta_t^T - \vartheta_{t-1}^T\right) = \Delta t \cdot \left[\sum_{k=1}^{N_k} \dot{Q}_{k,t}^u + \sum_{j=1}^{N_j} \dot{Q}_{j,t} - \frac{\dot{Q}_t^Y}{\eta^Y} - \dot{Q}_t^{TL}\right] \tag{2.16}$$

Moreover, water mass flow rate in the heat supply plant $\dot{m}_t^Y$ becomes a decision variable, as well as ϑ_t^T, and (2.13) is replaced by the following, with a further term accounting for auxiliary boilers, downline of TSS:

$$\dot{Q}_t^Y = \eta^Y \cdot \dot{m}_t^Y \cdot c^w \cdot \left(\vartheta_t^T - \vartheta_t^F\right) + \sum_{j \notin T} \dot{Q}_{j,t} \tag{2.17}$$

2.1.4 Test cases and Results

The procedure is applied to the test MG shown in Fig. 1, representing a configuration of the experimental MG facility realized in Electric Power System Laboratory at Politecnico di Bari with improved thermal section.

It encompasses two CHP systems, one based on gas combustion engine with 52 kW nominal power (CHP 1) and one based on a 30-kW gas microturbine (CHP 2), two RES-based facilities (a 45-kW photovoltaic plant - PV, and a 50 kW wind turbine system - WT), a 75-kW wood-fueled boiler (Boiler 1), a 20-kW pellet-fueled boiler (Boiler 2), and a 10-kW air-to-water heat pump (HP). Grid power exchange is bounded at 200 kW. The ESS is based on sodium-nickel technology, with 141 kWh capacity, usable energy state range between 0.2 and 1.0 p.u., a maximum charge/discharge power of 48 kW at 0.85 efficiency and negligible internal losses. The TSS is represented by a hot-water storage system made up by three isolated tanks with total capacity of 17 m^3 with nominal temperature of 60°C, maximum range of 55-70°C, and maximum water flow of 1 m^3/h can feed heat supply system.

The energy demand is determined according to the needs of the testbed facility installation area, where a building hosting offices and laboratories is present, with 46200 m^3 volume, occupied from 7 a.m. to 8 p.m., with electric load nominal power of 180 kW. Thermal comfort involves a temperature range of 20÷24°C in working period, 12÷21°C in early morning and 15÷22°C in late evening.

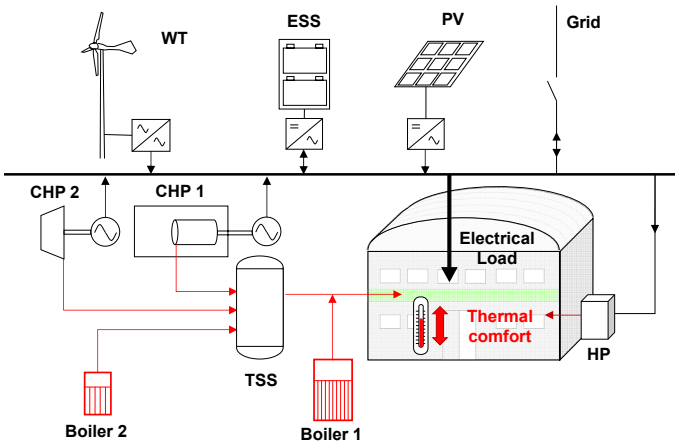

Figure 2.1. Experimental microgrid layout with storage

In order to evaluate the effectiveness of energy storage devices with the proposed approach, four cases are built, named from A to D, by combining the presence of the two storage devices, as synthesized in Table 2.1. Moreover, in order to verify the performances under different bounding conditions, five test days are accounted, characterized by different daily levels of RES-based production, electric demand and external temperature, as reported in Table 2.2. Therefore, 20 procedure runs are carried out.

Table 2.1. Energy Storage Cases

Case Name	A	B	C	D
ESS presence	No	Yes	No	Yes
TSS presence	No	No	Yes	Yes

Table 2.2. Characteristics of Test Days

	Day1	Day2	Day3	Day4	Day5
Forecast PV production [kWh]	85.8	38.1	113.8	68.7	115.3
Forecast WT production [kWh]	903.1	994.8	17.0	425.1	703.5
Average external temperature [°C]	1.32	4.57	10.13	10.3	14.79
Electric load demand [kWh]	1765.8	1712.7	2233.4	2093.9	2233.9

At a first stage, a comparison of operation plan obtained by the solution procedure is performed for Day1 in Cases A and D. In particular, thermal power production, electric power production/consumption and internal temperature trends are illustrated, for Case A and Case D, in Fig. 2.2 and Fig. 2.3, respectively.

As regards thermal power production, it can be seen that the presence of TSS (whose balance is given, in the left part of Fig. 2.3, by the difference of the black trend and the bar envelope) yields generally a smoother production profile, with lower exploitation of CHP 2, with respect to Case A. In Case D, Boiler 1 is auxiliary, therefore it is not connected to TSS.

The electric power balance, reveals that the ESS helps to improve the exploitation of the internal sources, reducing power purchase from the grid and zeroing power injection, due to low unitary revenue. ESS charge is usually observed in intervals with excess RES production with respect to load. Moreover, the presence of TSS helps reducing the recourse to HP for thermal demand coverage, thus the total electricity demand is lower in Case D than in Case A.

Thermal comfort is attained in a more precise way in Case D, where the presence of TSS and the exploitation of Boiler 1, as auxiliary, improve the flexibility of the system. This entails internal temperature trend of close to the minimum limit, not suffering from spikes due to solar irradiance as in Case A.

Behaviours of TSS temperature and ESS energy state (or State-of-charge – SOC) obtained for the Day1 in Case D are reported in Fig. 2.4. It can be seen that both trends are within the specified limits, giving the possibility to exploit storage devices for supplying regulation services in the real time operation, even towards the electric distribution network. Moreover, it can be seen that optimal solution involves the exploitation of storage devices towards minimum available limits at the end of the day.

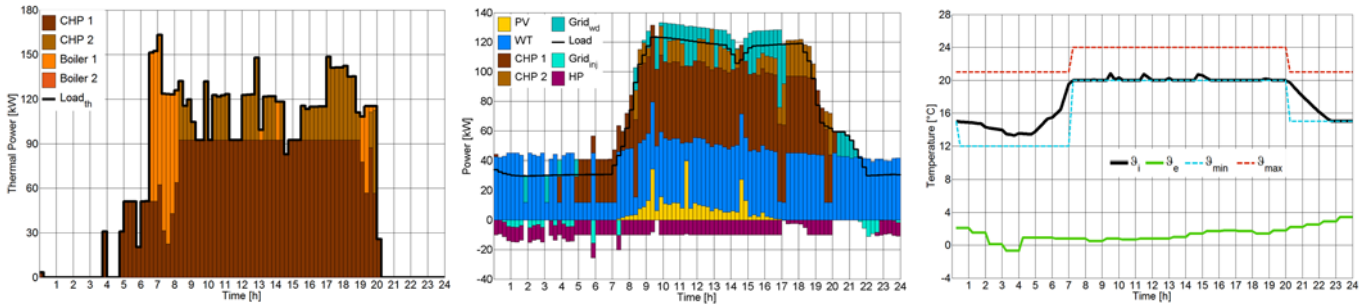

Figure 2.2 Thermal power production (left), electric power production/consumption (middle) and internal/external temperature (right) for Day 1, Case A.

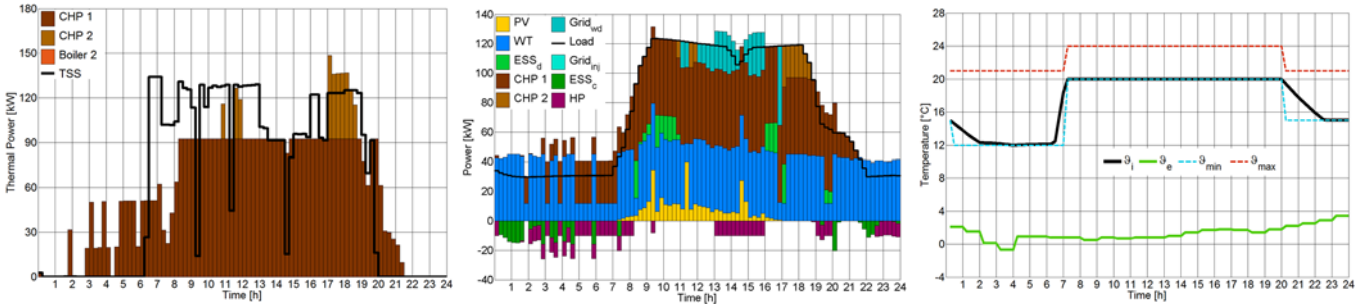

Figure 2.3 Thermal power production (left), electric power production/consumption (middle) and internal/external temperature (right) for Day 1, Case D.

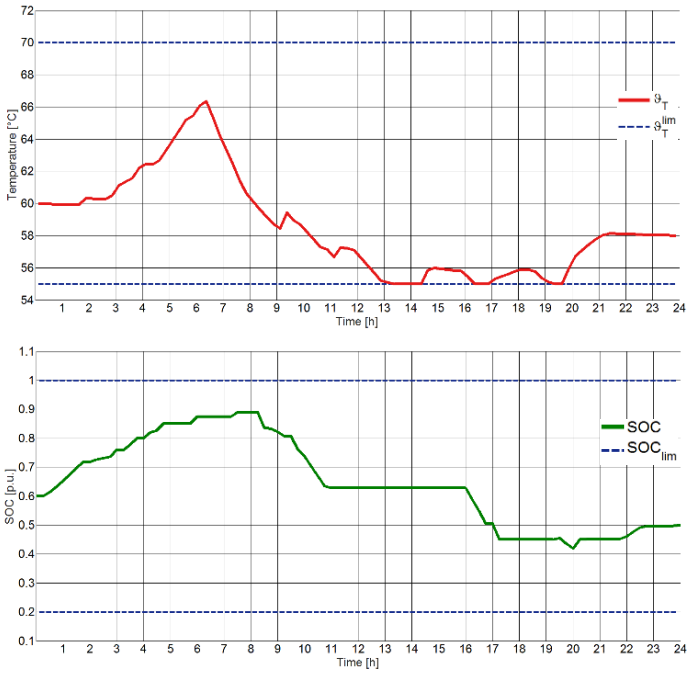

Figure 2.4 TSS temperature (upper) and ESS State Of Charge – SOC (lower) in Day 1 Case D.

The comparison of system optimal performance with varying energy storage configurations and bounding conditions is first executed on total daily cost. In Table 2.3 a synthesis of objective function values is reported for the four cases in the five typical days. It can be seen that the elaboration of optimal operation plan in the presence of storage devices, along with proper electric and thermal models, allows a reduction of total daily cost in a range between 5 € and 22 €, i.e. from 2.5% to 12% of total cost of Case A, according to different daily conditions. In particular, the influence of TSS is more evident in cold days, yielding roughly 9-10% cost reduction in Day1 and Day2 and 1.5-3% in other days. Moreover, in the presence of high RES and CHP production, ESS reveals more effective, indeed a cost reduction contribution ranging between 1% and 3.5%. In fact, in those conditions, thermal power drives the model and CHP electricity production is a by-product, that can be effectively managed by means of ESS. Moreover, it can be observed that Day3 is the most expensive one, due to the reduced renewable contribution.

Table 2.3. Total Daily Cost [€]

Case	Day1	Day2	Day3	Day4	Day5
A	188.93	157.31	310.24	248.19	192.00
B	184.85	151.67	307.58	245.31	190.06
C	170.42	142.21	304.03	241.08	188.99
D	166.96	137.29	301.40	238.18	187.09

Furthermore, comparisons are carried out in Fig. 2.5 and Fig. 2.6, where total cost contributions and electric energy shares are reported according to (2.1) and (2.5)/(2.14), respectively. It can be seen that CHP 2 and Boiler 1 are exploited only in colder conditions, giving a contribution to total cost. Whereas in warmer weather conditions (Day3, Day4 and Day5), HP is exploited only in the absence of TSS (Cases A and B), CHPs give lower contributions due to limited thermal demand and to the respect of balance relation (2.8). Therefore electric demand is covered mainly by grid purchase, that is more convenient than producing electricity by CHP wasting thermal power, in fact in all cases $\dot{Q}^{u}_{k,t} = \dot{Q}^{a}_{k,t}$. Moreover, in these days, when renewable is lacking, no cost-free energy production is available, therefore grid withdrawal is preferred. In all days, when ESS is present, the procedure finds more profitable to charge ESS instead of injecting power to the grid. However, in Day5 ESS is hardly exploited due to lack of excess internal production.

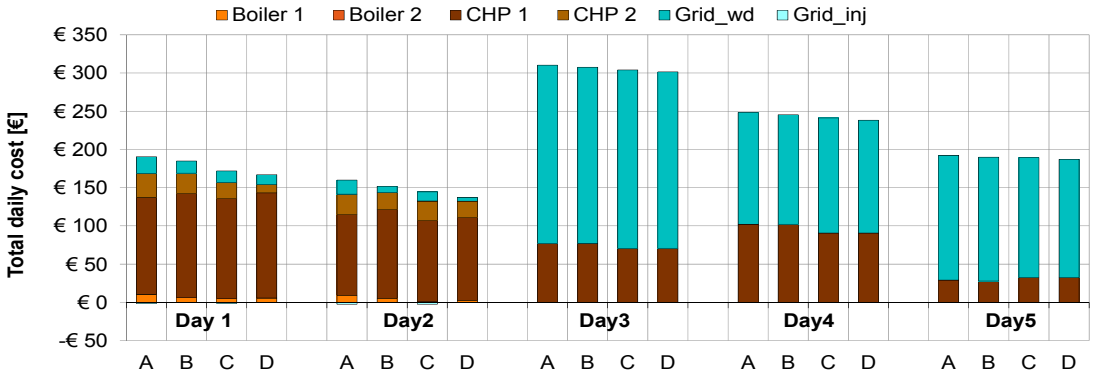

Figure 2.5 Contributions to total daily cost for different Cases and Days.

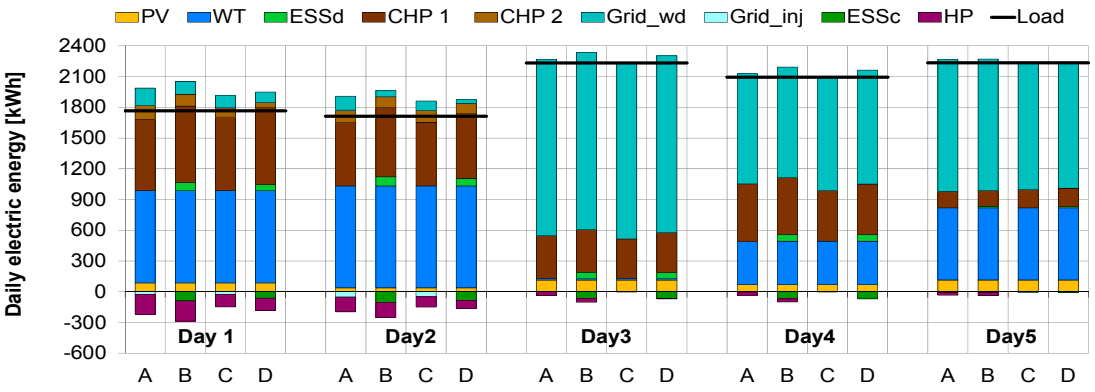

Figure 2.6 Contribution to daily electricity production/consumption for different Cases and Days

The detail of thermal energy shares is illustrated in Table 2.4, according to (2.8) and (2.16). It can be seen that, in warm days, the presence of TSS allows to not exploit the HP and the

auxiliary boiler. Moreover, the efficiency of water-based thermal supply system, given by the ratio of energy yield on energy production, is enhanced by the use of TSS, reaching values between 90% and 95% with respect to 75% in Cases A and B, due to more constant water temperature. The use of detailed building model involves different values of net energy need, given by $\dot{Q}_t^W + \dot{Q}_t^V - \dot{Q}_t^S$, for the four cases of each day. The residual demand assumes positive values in warmer days, meaning that the internal temperature at the end of the day is higher than the starting value, due to lower thermal losses.

Table 2.4. Thermal Energy Contributions [kWh]

Day	Case	Production	Yield	Auxiliary boiler	HP	Net energy need	Residual demand
1	A	1698.8	1260.9		471.1	1732.1	0.0
	B	1669.8	1239.5		479.5	1718.9	0.0
	C	1454.1	1320.0	94.2	295.9	1710.1	0.0
	D	1432.2	1300.1	101.1	296.0	1697.2	0.0
2	A	1513.1	1123.1		379.4	1502.6	0.0
	B	1505.3	1117.3		385.1	1502.4	0.0
	C	1336.9	1214.7	16.5	262.9	1494.1	0.0
	D	1322.8	1202.2	46.7	207.4	1456.3	0.0
3	A	748.1	555.3		103.3	646.1	12.5
	B	743.7	552.0		105.3	644.8	12.5
	C	684.1	653.0	0.0	8.3	622.7	38.7
	D	685.3	654.2	0.0	7.2	622.7	38.7
4	A	991.6	736.0		89.1	817.6	7.5
	B	990.6	735.3		89.1	816.9	7.5
	C	882.0	838.5	0.0	0.0	797.4	41.1
	D	881.9	838.5	0.0	0.0	797.4	41.1
5	A	283.6	210.5		94.0	271.9	32.6
	B	271.2	201.3		102.6	271.4	32.6
	C	315.1	307.0	0.0	0.0	262.2	44.8
	D	315.0	307.0	0.0	0.0	262.2	44.8

2.1.5 Conclusions

The structure of microgrids as multi-energy systems, including CHP devices, represents one of the ways to improve their acceptance and diffusion. The presence of different energy sources and demands requires a particular care on device modeling, accounting for thermal comfort as well. In this framework, the involvement of energy storage devices plays a significant role. In this paragraph, a methodology has been proposed to determine operation planning of a multi-energy microgrid, with improved modeling of CHP-based thermal supply system, in order to cover electric energy needs and ensure thermal comfort of occupants. The approach has been

tested on a configuration of an experimental multi-energy microgrid facility over different load and weather conditions, in order to prove the effect of the adoption of ESS and TSS in the microgrid. Results have revealed the importance of the storage option, implying flexibility improvement of energy management, economic efforts minimization and global microgrid performance enhancement. The presence of ESS has allowed an higher self-sufficiency for electric demand, and the use of TSS has involved a smoother CHP production profile and limited HP exploitation. The proposed approach is flexible enough to envisage its application to different multi-energy microgrids.

2.2 Integration of thermal energy production and thermal comfort models in microgrid operation planning

In this sub-section, a detailed description of multi-source thermal production system in a microgrid framework is aimed to integrate. This formulation involve electric energy production and consumption as well. A bottom-up engineering viewpoint is adopted, engaging energy flows interesting user buildings and mass flow rates and temperatures in the thermal supply facility. In particular, a temperature-based model of integrated heat supply devices, considering water mass flow rates as well, is accounted. The behaviour of different heating sources and CHP systems is dealt with, as well as proper heat exchangers and thermal energy storage device with internal temperature variation. These devices are connected to a comprehensive water-based heating circuit where they mutually interact. The sources include fuel-based CHP systems, boilers and solar thermal collectors. External thermal sources as heat pumps are modeled as well, representing at the same time a controllable electric load. Thermal comfort in the building is ensured in terms of room air temperature, accounting for heat exchange with the external environment. The proposed model is therefore embedded in an energy management procedure for multi-energy microgrid operation. The optimal day-ahead plan of the microgrid is evaluated by minimizing operation and emission costs, satisfying electric demand and thermal comfort requirements. Tests are carried out on a model of the experimental microgrid system built at the premises of Electric Power System laboratory of Politecnico di Bari, considering an interval of 15 days in winter season with varying building occupancy and external weather conditions.

2.2.1 Literature review

The concept of Microgrid (MG) is based on two typical aspects: it is designed to supply electrical and thermal loads for a small community, operating as a controlled entity connected to the distribution grid by the Point of Common Coupling, and can operate either in grid-connected or islanded mode [70][98]. The use of combined heat and power (CHP) facilities enforces the interaction between the electric side and the heating, ventilation and air-conditioning (HVAC) system [1][99], along with technologies for heating/cooling demand coverage such as heat pumps [27][95]. Moreover, the presence of feasibility in energy demand, represented by controllable loads and energy storage devices, can improve the integration of MGs as entities for regulation services in the energy distribution systems [100][101].

Control and supervision of a MG is carried out by SCADA system that, through proper Energy Management System (EMS), can optimize operation and reliability [70]. EMS outputs are

reference values of the control system for each dispatchable power production device and energy storage system (ESS), on suitable time intervals, according to inputs related to renewable source availability, energy prices and loads [102].

Therefore, in order to carry out suitable MG operation programs, a focus is devoted to methods to model energy demand of users. In this process, a distinction among heating, cooling and electricity demands is required, along with an estimate of yearly, daily and instantaneous peak values for each type of energy [1]. In particular, the forecast of electric load demand for microgrids, exploiting historical data and the influence of ambient conditions, is carried out by means of statistical regression models as in [103] or artificial intelligence techniques as proposed by [104][105], considering cycling behavior over typical days.

As regards thermal energy demand, different taxonomies are introduced in previous works concerning estimate methodologies, with particular focus on building energy needs. A first distinction is proposed by [106] between steady-state and dynamic models, according to the minimum allowable time step of the analysis, namely higher/lower than one day, respectively. In [107] residential energy prediction procedures are divided into top-down and bottom-up approaches, according to policy and physical visions of the problem, respectively. Whereas, [108] proposed a classification involving engineering models, based on thermodynamic properties, statistical models, based on historical data process and a detail on artificial intelligence methods. A further review is proposed by [109], distinguishing physical models, statistical models, and hybrid models as the coupling of the previous ones. In [110], a synthetic classification of statistical models (including regression and intelligent models) and engineering models is illustrated. In particular, for engineering models, a further subdivision is proposed between forward models, exploiting a defined mathematical model accounting for the phenomena affecting system behavior, and calibrated models, including fitting/validation process based on collected data and empirical estimation according to regression analysis of measurements. Finally, [111] introduced the importance of geographical information system for the energy consumption estimate of buildings at district/urban scale.

In the reviews analyzed in the above, statistical models include the exploitation of data regression techniques, such as ARIMA models as proposed by [112] but mainly rely on concepts of artificial intelligence applied to measured data analysis. The most common approaches are represented by artificial neural networks, exploited by [113]-[115] and by support vector machines, as reported in [116].

As regards engineering-based energy estimation models, it can be argued that four main elements affect the process: (i) building features as dimensions and construction materials; (ii)

energy production device features, as fuels, efficiencies, control schemes; (iii) weather conditions, involving temperature, wind speed, humidity; (iv) occupancy pattern, including number of occupants, time frames, specific habits and needs. Engineering models can exploit commercial/open software tools, that can integrate the four elements reported in the above, aiming at optimizing the operation and control of building energy system. In particular, [117] proposed a thorough and recent review of major programs exploited in this field, and discussed their interaction with control systems. An exploitation of TRNSYS is described in [118].

Among engineering approaches for dynamic energy need estimate, a threefold distinction can be made according to the specific focus of the physical model. In particular, an approach based on energy flows represent the most direct choice for energy models, since it individuates the contributions entering/leaving the ambient to cover a defined energy demand, estimated by means of other techniques such as statistic ones, as can be found in [93][119]-[123]. A more detailed class of models is comfort temperature-based, where the interest is on the thermal behavior of the building, according to specific thermal comfort levels, while keeping energy flow representation of energy exchange [124]-[128]. Moreover, some other models include a temperature-based model for all aspects of the energy system, from building envelope behavior to all the devices taking part to the energy supply/storage infrastructure [129][130]. These approaches show an increasing degree of detail in the modelization of the phenomena determining the level of thermal demand and of the processes involved in heat production and carrying. Some other models are developed by means of an electric equivalence, representing thermal resistance and capacitance of building elements in order to enhance the dynamic description of the heat transfer and consequently of thermal demand, as illustrated in [99], [131]-[133].

The proposed approach embeds thermal energy demand variation according to ambient conditions and thermal comfort in microgrid framework, differently from [134]-[136], where thermal energy demand is an estimated known value. In particular, thermal comfort is included as a procedure constraint, therefore its satisfaction is of primary importance for microgrid operation, whereas in [84][137] it is one of the objectives and therefore could not be ensured. The determination of room temperature is based on building energy flows as in [124]-[125], [138]-[140], although in the proposed model those flows are function of decision variables. Analogously to [129][141], where a detailed model of a single-source thermal system based on CHP is integrated in microgrid analysis, the adopted model includes different thermal energy sources within a water-based thermal production facility. This implies an interaction among thermal sources at production level, involving thermal storage, and a further energy balance to

account for thermal comfort needs. As compared to other models of multi-source CHP-based microgrid, a deep detail of temperatures and mass flow rates interesting thermal storage is adopted, instead of energy-based representation exploited in [136][142] or temperature-based model driven by energy flows as in [143][144]. Furthermore, flexible ratio of electricity and thermal yields of CHP is not accounted in [122] or considered as excess heat and electricity [145][146], whereas the proposed model involves a description of exhaust production, partial release to the atmosphere and heat exchange with water-based system.

2.2.2 Building thermal model

The proposed building thermal model is driven by the satisfaction of a comfort level associated to keeping room temperature within a specified range. In order to determine the needed thermal demand and consequent temperature variations, the various contributions to building thermal balance are accounted, as sketched in Figure 2.7.

In the adopted framework, taking the cue from [99], energy flows include intentional thermal production, represented by water-based heating system supply $\dot{Q}_Y$ and heat pumps production $\dot{Q}_H$. Whereas, thermal energy exchanges of the building with the external environment are represented by heating effect of solar irradiance $\dot{Q}_S$ and heat exchange through room ventilation $\dot{Q}_V$ and walls $\dot{Q}_W$. Furthermore, internal heat gains coming from occupants and appliances $\dot{Q}_{ihg}(t)$ are considered as well. It is assumed that thermal losses of heating system $\dot{Q}_L$ do not usefully contribute to the balance, where possible temperature variations are accounted through the residual demand $\dot{Q}_D$.

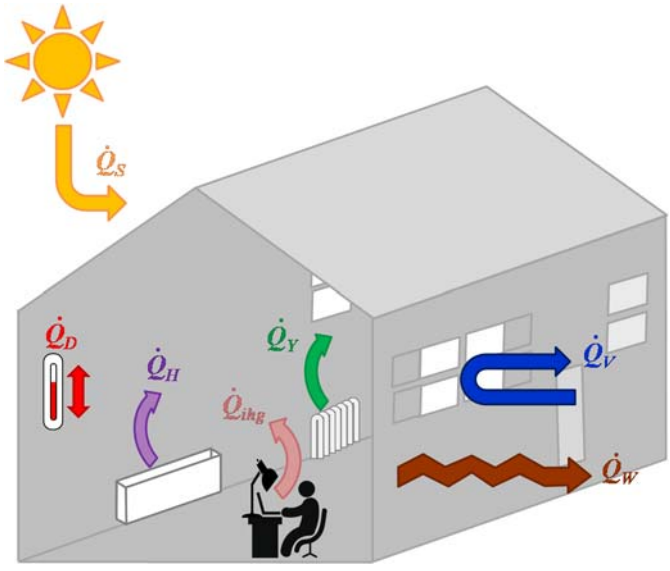

Figure 2.7. Building heat energy flows scheme

Therefore, the heat balance of the building is determined for each time interval *t* through the following relation:

$$\dot{Q}_Y(t)+\dot{Q}_H(t)+\dot{Q}_D(t)=\dot{Q}_V(t)+\dot{Q}_W(t)-\dot{Q}_S(t)-\dot{Q}_{ihg}(t) \tag{2.18}$$

The next subsections include a description of the contributions to building thermal balance, with a particular focus on water-based heat production system.

Energy exchange through walls between the building and the external environment $\dot{Q}_W(t)$, in a specific time step *t* is obtained through the following expression:

$$\dot{Q}_W(t)=U_W\cdot A_W\cdot\left(\vartheta_i(t)-\vartheta_e(t)\right) \tag{2.19}$$

where U_W and A_W represent, the average thermal transmittance [W/(m^2·K)] and the total area [m^2] of peripheral walls, respectively. These latter divide the internal ambient of the building, at temperature $\vartheta_i(t)$, from the external environment, at temperature $\vartheta_e(t)$.

The contribution of room ventilation $\dot{Q}_V(t)$ is determined by means of the following relation, in each time step *t*:

$$\dot{Q}_V(t)=\frac{1}{3600}\cdot n_V(t)\cdot\rho_a\cdot V_i\cdot c_a\cdot\left(\vartheta_i(t)-\vartheta_e(t)\right) \tag{2.20}$$

where the term $n_V(t)$ [1/h] stands for the ventilation rate, depending on building end use (e.g. residential, office, school etc…), on room occupancy, and on specific time step, expressed in times of room volume V_i [m^3] [147], whereas ρ_a and c_a represent air density [kg/m^3] and specific heat [J/(kg·K)], respectively.

Heating effect of solar irradiance is evaluated through the following expression [148][149]:

$$\dot{Q}_S(t)=\sum_j\alpha_{S,j}\cdot A_{S,j}\cdot I_{S,j}(t) \tag{2.21}$$

where $I_{S,j}(t)$ [W/m^2] is the direct solar radiation on the equivalent plane of the *j*-th wall, characterized by slope and azimuth orientation and depending on location and day [45], in the time step *t*, $A_{S,j}$ [m^2] is the window surface interested by direct solar radiation, and $\alpha_{S,j}$ represents a reduction coefficient due to shadowing, glass absorption, etc. In this model, the radiating effect on wall temperature is neglected.

The model of internal heat gains includes the influence of person occupancy, along with heat contribution from lighting system and thermal losses of other equipment (e.g. computers, household appliances, …). In general, these contributions are expressed per unit of area, and depend on the destination of the building (residential, office, …) and on the specific activities

(e.g. common rooms, open space offices, canteens, …) [150][151]. Therefore, they are evaluated for the whole building through the sum over the rooms r as per the following expression:

$$\dot{Q}_{ihg}(t) = \sum_{r} \left[A_r \cdot \left(\dot{q}_{occ,r}(t) + \dot{q}_{lit,r}(t) + \dot{q}_{apl,r}(t) \right) \right] \tag{2.22}$$

where A_r [m^2] is the area of the r-th room of the building, and $\dot{q}_{occ,r}(t)$, $\dot{q}_{lit,r}(t)$, $\dot{q}_{apl,r}(t)$ [W/m^2] represent heat contribution per unit of surface from occupants, from lighting equipment and from other appliances, respectively, in the r-th room at t-th time step.

Whether the heat sources, the heat demand is determined by imposing that the internal temperature of the room $\vartheta_i(t)$ has to comply with comfort requirements of building occupants. However, some deviations are admitted, and residual internal heat demand $\dot{Q}_D$ may occur, being represented by the energy required to cover temperature deviation over time:

$$\dot{Q}_D(t) = \frac{1}{3600} \cdot \rho_a \cdot V_i \cdot c_a \cdot \left(\vartheta_i(t) - \vartheta_i(t-1) \right) \tag{2.23}$$

A sketch of water-based heat production model is reported in Fig. 2.8. The possibility of integrating several thermal production technologies is provided, considering CHPs, boilers, solar thermal devices, connected to a proper thermal storage.

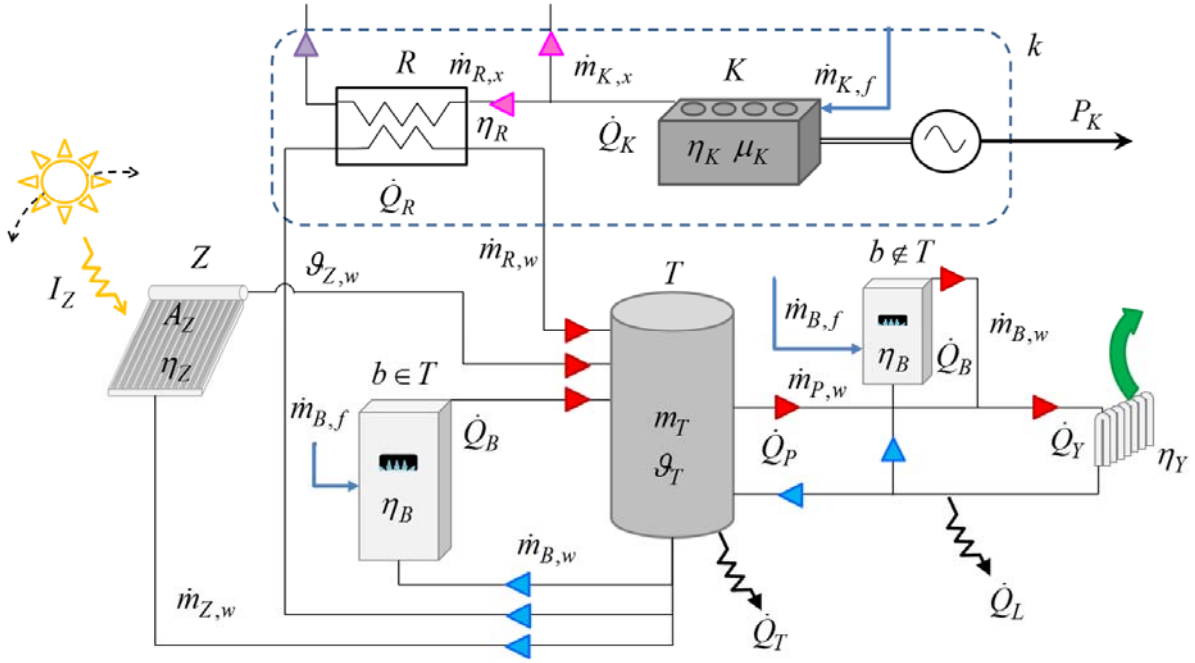

Figure 2.8. Water-based room heat production outline

The supply of energy to the building comes from the storage and can be integrated by downstream boilers. Moreover, each component of this system is appropriately modeled, involving either the regulation of mass flow rate of working fluid (for CHPs, boilers and heat exchangers), or temperature-based control when thermal production cannot be directly handled (thermal storage, solar thermal collectors). In the following, details on models of devices and their integration are provided.

Heat recovery $\dot{Q}_R(k,t)$ from the *k*-th CHP system at time interval *t*, is considered as follows:

$$\dot{Q}_R(k,t) = \eta_R(k) \cdot \dot{m}_{R,x}(k,t) \cdot c_x(k) \cdot \Delta\vartheta_{R,x}(k) \tag{2.24.a}$$

where $\dot{m}_{R,x}(k,t)$ [kg/s] is the mass flow rate of exhaust gases, characterized by specific heat $c_x(k)$ [J/(kg·K)], flowing through the heat recovery exchanger, moreover $\Delta\vartheta_{R,x}(k)$ is the set point temperature variation of combustion exhaust in the exchanger and $\eta_R(k)$ is exchanger efficiency. The recovered heat is transferred to water flowing in the other section of the heat exchanger, therefore it can also be expressed as follows:

$$\dot{Q}_R(k,t) = \dot{m}_{R,w}(k,t) \cdot c_w \cdot \Delta\vartheta_{R,w}(k) \tag{2.24.b}$$

where $\dot{m}_{R,w}(t)$ [kg/s] is water mass flow rate in the heat exchanger, c_w is specific heat of water [J/(kg·K)] and $\Delta\vartheta_{R,w}(k)$ is the design temperature gain of the water flow in the exchanger. Maching the right sides of eq. (2.24.a) and (2.24.b), the following relation holds:

$$\dot{m}_{R,w}(k,t) \cdot c_w \cdot \Delta\vartheta_{R,w}(k) = \eta_R(k) \cdot \dot{m}_{R,x}(k,t) \cdot c_x(k) \cdot \Delta\vartheta_{R,x}(k) \tag{2.24.c}$$

In each CHP system, electric power output $P_K(k,t)$ and thermal power recovery are linked through available heat $\dot{Q}_K(k,t)$, since it can be stated that:

$$P_K(k,t) = \frac{\eta_K(k)}{\mu_K(k)} \dot{Q}_K(k,t) \tag{2.24.d}$$

$$\dot{Q}_K(k,t) \geq \frac{\dot{Q}_R(k,t)}{\eta_R(k)} \tag{2.24.e}$$

where $\eta_K(k)$ and $\mu_K(k)$ represent electric and thermal efficiency of the *k*-th CHP system, respectively. The inequality (2.24.e) can be expressed in terms of mass flow rates and temperatures as follows:

$$\dot{m}_{K,x}(k,t)\cdot\Delta\vartheta_{K,e}(k)\geq\dot{m}_{R,x}(k,t)\cdot\Delta\vartheta_{R,x}(k) \tag{2.24.f}$$

$$\dot{m}_{K,x}(k,t)\geq\dot{m}_{R,x}(k,t) \tag{2.24.g}$$

where $\dot{m}_{K,x}(k,t)$ is the total mass flow rate of exhausts leaving the *k*-th CHP and $\Delta\vartheta_{K,e}(k)$ is the difference between exhausts temperature at CHP exit and external air temperature. In relation (2.24.f), exhausts specific heat $c_x(k)$ is the same at both sides and is therefore simplified. Whereas, relation (2.24.g) ensures exhausts mass flow rate conservation between CHP outlet and heat exchanger inlet. In addition, fuel consumption in the *k*-th CHP systems can be linked directly to electric power production, as follows:

$$\dot{m}_{K,f}(k,t)=\frac{P_K(k,t)}{\eta_K(k)\cdot h_{K,f}(k)} \tag{2.24.h}$$

where $h_{K,f}(k)$ [J/kg] is the heating value of the fuel exploited in the *k*-th CHP system.

Moreover, suitable upward and down way ramp rate limits are included in the model between two consecutive time intervals:

$$-RD_K(k)\cdot\Delta t\leq P_K(k,t)-P_K(k,t-1)\leq RU_K(k)\cdot\Delta t \tag{2.24.i}$$

where $RD_K(k)$ and $RU_K(k)$ [kW/h] represent the maximum ramp-down rate and ramp-up rate, respectively, for the *k*-th CHP system in each time interval Δt [h] between two consecutive steps.

Heat production of the *b*-th boiler at *t*-th time interval, $\dot{Q}_B(b,t)$ is determined as follows:

$$\dot{Q}_B(b,t)=\eta_B(b)\cdot\dot{m}_{B,f}(b,t)\cdot h_{B,f}(b) \tag{2.25.a}$$

where $\dot{m}_{B,f}(b,t)$ [kg/s] is the mass flow rate of fuel exploited in the *b*-th boiler, characterized by heating value $h_{B,f}(b)$ [J/kg], and $\eta_B(b)$ is boiler efficiency. The produced heat is therefore transferred to water flowing in the boiler by means of the following expression:

$$\dot{Q}_B(b,t)=\dot{m}_{B,w}(b,t)\cdot c_w\cdot\Delta\vartheta_{B,w}(b) \tag{2.25.b}$$

where $\dot{m}_{B,w}(b,t)$ [kg/s] is water mass flow rate in the boiler and $\Delta\vartheta_{B,w}(b)$ is relevant water temperature gain. By equating the right sides of eq. (2.25.a) and (2.25.b), the following relation holds:

$$\eta_B(b)\cdot\dot{m}_{B,f}(b,t)\cdot h_{B,f}(b)=\dot{m}_{B,w}(b,t)\cdot c_w\cdot\Delta\vartheta_{B,w}(b) \tag{2.25.c}$$

Heat production level of the *z*-th solar thermal system $\dot{Q}_Z(z,t)$ is evaluated by means of the following expression:

$$\dot{Q}_Z(z,t) = \eta_Z(z,t) \cdot A_Z(z) \cdot I_Z(z,t) \tag{2.26.a}$$

where $I_Z(z,t)$ [W/m^2] is the total solar radiation absorbed by the *z*-th solar thermal collector system, characterized by slope and azimuth orientation, $A_Z(z)$ [m^2] is the equivalent solar absorption area of the adopted collector technology, and $\eta_Z(z,t)$ represents efficiency of the *z*-th solar thermal system [129], determined as follows:

$$\eta_Z(z,t) = \eta_Z^{nom}(z) - \frac{\alpha_1(z)}{I_Z(z,t)} \cdot \left(\vartheta_{Z,w}^m(z) - \vartheta_e(t)\right) \tag{2.26.b}$$

where $\eta_Z^{nom}(z)$ is the nominal efficiency value, and $\alpha_1(z)$ [W/(m^2·K)] is the coefficient of efficiency reduction term, depending on solar radiation and on the difference between average fluid temperature in the collectors $\vartheta_{Z,w}^m(z)$ and external air temperature.

It is worth to remark that, if the incident solar radiation falls below a critical radiation value $I_Z^{crit}(z,t)$, determined as follows, the efficiency is negative:

$$I_Z^{crit}(z,t) = \frac{\alpha_1(z)}{\eta_Z^{nom}(z)} \cdot \left(\vartheta_{Z,w}^m(z) - \vartheta_e(t)\right) \tag{2.26.c}$$

where a specific value of $\vartheta_{Z,w}^m(z)$ is exploited and the critical radiation level varies over time according to external temperature. In order to avoid undesired heat exchange from the solar collectors to the environment due to negative value of efficiency, water flow is stopped, therefore water mass flow rate in the solar thermal system $\dot{m}_{Z,w}(z,t)$ considering the nominal value $\dot{m}_{Z,w}^{nom}(z,t)$, is determined as follows:

$$\dot{m}_{Z,w}(z,t) = \begin{cases} 0 & I_Z(z,t) < I_Z^{crit}(z,t) \\ \dot{m}_{Z,w}^{nom}(z,t) & I_Z(z,t) \geq I_Z^{crit}(z,t) \end{cases} \tag{2.26.d}$$

Once $\dot{m}_{Z,w}(z,t)$ is determined, recovered heat from solar thermal collectors can be evaluated according to the following relation:

$$\dot{Q}_Z(z,t) = \dot{m}_{Z,w}(z,t) \cdot c_w \cdot \Delta\vartheta_{Z,w}(z,t) \tag{2.26.e}$$

where $\Delta\vartheta_{Z,w}(z,t)$ is water temperature increase in the collectors.

By accounting that the *z*-th solar thermal system warms the water from a starting temperature $\vartheta_{Z,c}(z,t)$ to a final value $\vartheta_{Z,w}(z,t)$, eq. (2.26.e) can be expressed as follows:

$$\dot{Q}_Z(z,t) = \dot{m}_{Z,w}(z,t) \cdot c_w \cdot \left[\vartheta_{Z,w}(z,t) - \vartheta_{Z,c}(z,t)\right] \tag{2.26.f}$$

whereas solar thermal panel efficiency can be drawn from (2.26.b) by considering $\vartheta^m_{Z,w}(z,t) = \left[\vartheta_{Z,w}(z,t) + \vartheta_{Z,c}(z,t)\right]/2$:

$$\eta_Z(z,t) = \eta_Z^{nom}(z) - \frac{\alpha_1(z)}{I_Z(z,t)} \cdot \left(\frac{\vartheta_{Z,w}(z,t) + \vartheta_{Z,c}(z,t)}{2} - \vartheta_e(t) \right) \tag{2.26.g}$$

Therefore substituting (2.26.g) in (2.26.a) provides :

$$\begin{aligned} &\dot{Q}_Z(z,t) = \eta_Z^{nom}(z) \cdot A_Z(z) \cdot I_Z(z,t) \\ &-\alpha_1(z) \cdot A_Z(z) \cdot \left[0.5 \cdot \left(\vartheta_{Z,w}(z,t) + \vartheta_{Z,c}(z,t)\right) - \vartheta_e(t)\right] \end{aligned} \tag{2.26.h}$$

By equating (2.26.h) with (2.26.f) the following linear relation between $\vartheta_{Z,w}(z,t)$ and $\vartheta_{Z,c}(z,t)$ can be drawn

$$\vartheta_{Z,w}(z,t) = \Gamma(z,t) \cdot \vartheta_{Z,c}(t) + \Phi(z,t) \tag{2.26.i}$$

where coefficients $\Gamma(z,t)$ and $\Phi(z,t)$ are defined as follows:

$$\Gamma(z,t) = \frac{\dot{m}_{Z,w}(z,t) \cdot c_w - 0.5 \cdot \alpha_1(z) \cdot A_Z(z)}{\dot{m}_{Z,w}(z,t) \cdot c_w + 0.5 \cdot \alpha_1(z) \cdot A_Z(z)} \tag{2.26.l}$$

$$\Phi(z,t) = \frac{A_Z(z) \cdot \left[\eta_Z^{nom}(z) \cdot I_Z(z,t) + \alpha_1(z) \cdot \vartheta_e(t)\right]}{\dot{m}_{Z,w}(z,t) \cdot c_w + 0.5 \cdot \alpha_1(z) \cdot A_Z(z)} \tag{2.26.m}$$

Hot water amounts coming from different production devices are conveyed to a centralized thermal energy storage equipment, basically constituted by a hot water tank.

For the description of thermal storage behaviour, the following equilibrium relations on energy and mass are accounted:

$$\begin{aligned} &H_T(t) = H_T(t-1) - H_{TL}(t) + \sum_{b \in T} H_B(b,t) + \sum_{k=1}^{N_k} H_R(k,t) \\ &+ \sum_{z=1}^{N_z} H_Z(z,t) - H_{EX}(t) - H_P^i(t) + H_P^o(t) + H_{IN}(t) \end{aligned} \tag{2.27.a}$$

$$m_T(t) = m_T(t-1) + \Delta t \cdot \left[\sum_{b \in T} \dot{m}_{B,w}(b,t) + \sum_{k=1}^{N_k} \dot{m}_{R,w}(k,t) + \right.$$
$$\left. + \sum_{z=1}^{N_z} \dot{m}_{Z,w}(z,t) - \dot{m}_{EX}(t) - \dot{m}_P^i(t) + \dot{m}_P^o(t) + \dot{m}_{IN}(t) \right] \quad (2.27.b)$$

In (2.27.a), the terms H represent the fluid enthalpy of each of the contributions, determined as the product of mass flow rate, water specific heat, fluid temperature and time interval duration. Whereas, in (2.27.b) the term *m* is the mass. In both equations, subscript *T* refers to the quantities of the thermal storage, whereas the subscript *EX* represents water extraction from the tank to feed heat generation sources, subscript *IN* stands for water integration and subscript *TL* refers to thermal storage heating losses. Moreover, it can be noted that all CHP systems and solar thermal collectors are supposed to contribute to thermal storage balance, whereas only a subset of boilers, indicated as $b \in T$, takes part to this relation. Finally, building heating system is represented by subscript *P*, where superscript *i* and *o* represent water inlet and outlet in the building heating system, respectively.

In the following, the need of water integration is considered negligible, and fluid withdrawal and injection in each water circuit of the system are supposed to happen with the same amount at the same time, neglecting delays due to circulation, which is suitable in a day-ahead analysis with time steps of 15-30 minutes.

Under these assumptions, $\dot{m}_{IN}(t) = 0$, $\dot{m}_{EX}(t) = \sum_{b \in T} \dot{m}_{B,w}(b,t) + \sum_{k=1}^{N_k} \dot{m}_{R,w}(k,t) + \sum_{z=1}^{N_z} \dot{m}_{Z,w}(z,t)$ and $\dot{m}_P^i(t) = \dot{m}_P^o(t)$, therefore the mass balance in (2.27.b) turns out to reduce to a straightforward mass conservation relation in the tank over time, i.e. $m_T(t) = m_T(t-1)$. As a consequence, energy balance (2.27.a) can be written as follows:

$$m_T \cdot c_w \cdot \left(\vartheta_T(t) - \vartheta_T(t-1)\right) = \Delta t \cdot \left[\sum_{b \in T} \dot{m}_{B,w}(b,t) \cdot c_w \cdot \left(\vartheta_{B,w}(b,t) - \vartheta_T(t)\right) \right.$$
$$+ \sum_{k=1}^{N_k} \dot{m}_{R,w}(k,t) \cdot c_w \cdot \left(\vartheta_{R,w}(k,t) - \vartheta_T(t)\right) + \sum_{z=1}^{N_z} \dot{m}_{Z,w}(z,t) \cdot c_w \cdot \left(\vartheta_{Z,w}(z,t) - \vartheta_T(t)\right) \quad (2.27.c)$$
$$\left. - \dot{m}_{P,w}(t) \cdot c_w \cdot \left(\vartheta_T(t) - \vartheta_L(t)\right) - U_T \cdot A_T \cdot \left(\vartheta_T(t) - \vartheta_e(t)\right) \right]$$

where U_T and A_T represent heat transmittance [W/m^{2}K] and external surface [m^2] of water storage system, respectively.

By considering that solar thermal collectors are all connected to the thermal storage, in relation (2.26.i) $\vartheta_{Z,c}(z,t)=\vartheta_T(t)$. By substituting it in energy balance of storage (2.27.c), and properly grouping terms, the temporal evolution of water temperature in the thermal storage tank is determined through the following equation:

$$\begin{aligned}&\left\{m_T c_w+\Delta t\left[U_T A_T+\sum_{z=1}^{N_z}\dot{m}_{Z,w}(z,t)\cdot c_w\cdot\left(1-\Gamma(z,t)\right)\right]\right\}\cdot\vartheta_T(t)=m_T\cdot c_w\cdot\vartheta_T(t-1)\\&+\Delta t\cdot\left[\sum_{b\in T}\dot{m}_{B,w}(b,t)\cdot c_w\cdot\Delta\vartheta_{B,w}(b)+\sum_{k=1}^{N_k}\dot{m}_{R,w}(k,t)\cdot c_w\cdot\Delta\vartheta_{R,w}(k)\right.\\&\left.+\sum_{z=1}^{N_z}\dot{m}_{Z,w}(z,t)\cdot c_w\cdot\Phi(z,t)-\dot{m}_{P,w}(t)\cdot c_w\cdot\left(\Delta\vartheta_{P,w}+\Delta\vartheta_{L,w}\right)\right]+U_T\cdot A_T\cdot\vartheta_e(t)\end{aligned}\qquad(2.27.d)$$

In the proposed formulation, temperature variations for boilers, $\vartheta_{B,w}(b,t)-\vartheta_T(t)=\Delta\vartheta_{B,w}(b)$, for CHP systems $\vartheta_{R,w}(k,t)-\vartheta_T(t)=\Delta\vartheta_{R,w}(k)$ and for thermal storage output, $\vartheta_T(t)-\vartheta_L(t)=\Delta\vartheta_{P,w}+\Delta\vartheta_{L,w}$ are defined as set-point constant values, as reported in (2.24.b), (2.25.b), and in the following (2.28.a)-(2.28.b).

Total heat supply from the storage system to hot water circuit of the building heating facility $\dot{Q}_P(t)$ is related to water mass flow rate in the heating system $\dot{m}_{P,w}(t)$ through the following expression:

$$\dot{Q}_P(t)=\dot{m}_{P,w}(t)\cdot c_w\cdot\Delta\vartheta_{P,w}\qquad(2.28.a)$$

where $\Delta\vartheta_{P,w}$ is the set-point of water temperature reduction in the radiators of heating system. The contribution of pipe losses in the water-based heating system is:

$$\dot{Q}_L(t)=\dot{m}_w(t)\cdot c_w\cdot\Delta\vartheta_{L,w}\qquad(2.28.b)$$

where $\Delta\vartheta_{L,w}$ is a goal temperature deviation from the output of room heating system to the cold water inlet in thermal storage.

Some boilers, indicated as $b\notin T$, are supposed to be installed after the thermal storage, adding another freedom degree to the system. By neglecting fluid circulation delays and temperature deviation with respect to water heating system downstream to thermal storage, i.e. $\Delta\vartheta_{B,w}(b)\approx\Delta\vartheta_{P,w}+\Delta\vartheta_{L,w}$, these boilers further contribute to thermal power supply of the building when required.

Therefore, the total yield of water-based heating system is determined as follows:

$$\dot{Q}_Y(t) = \eta_Y \cdot \left(\dot{Q}_P(t) + \sum_{b \notin T} \dot{Q}_B(b,t) \right) \tag{2.28.c}$$

where η_Y represents the efficiency of room heating system.

In order to ensure further flexibility to the system, another different source of heating energy is represented by air-based heat pumps. Their energy output $\dot{Q}_H(t)$ is related to electric power consumption $P_H(t)$ by means of proper Coefficient of Performance COP_H, as follows:

$$\dot{Q}_H(t) = COP_H(t) \cdot P_H(t) \tag{2.29.a}$$

The COP_H depends on the temperature of HP outlet $\vartheta_{out,H}$ and of thermal sink $\vartheta_{ts,H}$ through the following expression:

$$COP_H(t) = \psi_H \cdot \frac{\vartheta_{out,H}}{\vartheta_{out,H} - \vartheta_{ts,H}(t)} \tag{2.29.b}$$

where ψ_H represent the deviation from ideal efficiency, and can range between 10% and 70% [152]. Assuming the external air as thermal sink, $\vartheta_{ts,H}(t) = \vartheta_e(t)$, whereas $\vartheta_{out,H}$ is considered as a set-point value. Moreover, electric power consumption $P_H(t)$ makes electric power demand increase, and electric demand response can be realized to a certain extent.

2.2.3 Microgrid Daily Operation Programming

The engineering model for thermal energy production and demand aforementioned is integrated in a methodology to determine day-ahead operation programme of a Microgrid. This methodology is focused at solving an optimization problem, aiming at minimizing an objective function subject to equality and inequality constraints and limits on state variables, as follows:

$$\begin{aligned} &\min f(\mathbf{x}) \\ &s.t. \begin{cases} g(\mathbf{x}) = 0 \\ h(\mathbf{x}) \geq 0 \\ \underline{\mathbf{x}} \leq \mathbf{x} \leq \overline{\mathbf{x}} \end{cases} \end{aligned} \tag{2.30}$$

The state variable vector **x** of the methodology includes:

- electric power generation from each CHP unit $P_K(k,t)$;
- mass flow rates of exhaust gases and water in the heat exchanger of each CHP unit, $\dot{m}_{R,x}(k,t)$ and $\dot{m}_{R,w}(k,t)$;

- mass flow rates of fuel and water in each boiler, $\dot{m}_{B,f}(t)$ and $\dot{m}_{B,w}(t)$;
- water mass flow rate in the building heat supply system $\dot{m}_{P,w}(t)$;
- internal room temperature of the building $\vartheta_i(t)$;
- temperature of hot water in the storage device $\vartheta_T(t)$;
- power withdrawn and injected at grid connection point $P_G^p(t)$ and $P_G^j(t)$;
- electric power consumption of heat pump $P_H(t)$.

In particular, the objective function $f(\mathbf{x})$ represents the operation cost in the considered time horizon, divided into N_t time steps with Δt duration, determined as follows:

$$f(\mathbf{x}) = \sum_{t=1}^{N_t} \left[C_O(t) + C_E(t) + C_G(t) \right] \tag{2.31}$$

where $C_O(t)$ and $C_E(t)$ represent the operation cost and the emission cost, respectively, related to microgrid energy production and storage devices, and $C_G(t)$ is the net cost for energy withdrawal from the grid connection point, all evaluated at t-th time interval. In particular, it can be stated that operation and emission costs are linked to CHPs and boilers, as follows:

$$C_O(t) = \sum_{k=1}^{N_k} C_O(k,t) + \sum_{b=1}^{N_b} C_O(b,t) \tag{2.32.a}$$

$$C_E(t) = \sum_{k=1}^{N_k} C_E(k,t) + \sum_{b=1}^{N_b} C_E(b,t) \tag{2.32.b}$$

In these expressions, operation and emission costs for the k-th CHP unit, $C_O(k,t)$ and $C_E(k,t)$ respectively, depend on power production level $P_K(k,t)$ as follows:

$$C_O(k,t) = \frac{fc(k) \cdot \Delta t \cdot P_K(k,t)}{h_{K,f}(k) \cdot \eta_K(k)} \tag{2.33.a}$$

$$C_E(k,t) = \chi_E \cdot \varepsilon(k) \cdot \Delta t \cdot P_K(k,t) \tag{2.33.b}$$

where $fc(k)$ stands for unitary fuel cost in the k-th CHP system; moreover χ_E and $\varepsilon(k)$ represent unitary emission cost and electric emission factor.

Moreover, operation and emission costs for the b-th boiler, $C_O(b,t)$ and $C_E(b,t)$ respectively, are related to fuel consumption level $\dot{m}_{B,f}(b,t)$ as follows:

$$C_O(b,t) = fc(b) \cdot \Delta t \cdot \dot{m}_{B,f}(b,t) \tag{2.34.a}$$

$$C_E(b,t) = \chi_E \cdot \varepsilon(b) \cdot \Delta t \cdot \eta_B(b) \cdot \dot{m}_{B,f}(b,t) \cdot h_{B,f}(b) \tag{2.34.b}$$

where $fc(b)$ and $\varepsilon(b)$ represent unitary fuel cost and thermal emission factor for the *b*-th boiler, respectively.

Net cost of grid connection is related to grid power exchange levels:

$$C_G(t) = gc(t) \cdot P_G^p(t) \cdot \Delta t - gr(t) \cdot P_G^j(t) \cdot \Delta t \tag{2.35}$$

where $P_G^p(t)$ and $P_G^j(t)$ represent drained power from the grid and injected power to the grid, respectively, whereas $gc(t)$ and $gr(t)$ stand for unitary cost of grid energy withdrawal and unitary revenue for sold energy, respectively.

Equality constraints $g(\mathbf{x}) = 0$ involve CHP exchanger balance (2.24.c), boiler energy balance (2.25.c), thermal storage balance (2.27.d). Moreover, the electric power balance of the MG is considered at each time interval *t* is expressed as follows:

$$\sum_{k=1}^{N_k} P_K(k,t) + \tilde{P}_F(t) + \left[P_G^w(t) - P_G^j(t) \right] + P_A^d(t) = \tilde{P}_D(t) + P_H(t) + P_A^c(t) \tag{2.36}$$

where $\tilde{P}_F(t)$ and $\tilde{P}_D(t)$ correspond to forecast values of power generation from non-programmable renewable sources and electric power demand, respectively. Moreover, $P_A^c(t)$ and $P_A^d(t)$ represent charge and discharge electric power of the electric energy storage device, respectively.

A further equality constraint deals with the variation over time of the state of charge (SOC) of the electric energy storage $E_A(t)$, expressed as follows, where η_A^c and η_A^d represent charge and discharge efficiency, respectively:

$$E_A(t) = E_A(t-1) + \Delta t \cdot \left(\eta_A^c \cdot P_A^c(t) - P_A^d(t) / \eta_A^d \right) \tag{2.37}$$

Finally, building thermal energy balance is considered. It is taken from (2.18), and the influence of all terms is explicated by means of the engineering model, obtaining the following relation:

$$
\begin{aligned}
&\left[\frac{\rho_a V_i c_a}{3600}\cdot\left(1-n_V(t)\right)-U_W\cdot A_W\right]\cdot\vartheta_i(t)-\frac{\rho_a V_i c_a}{3600}\cdot\vartheta_i(t-1)\\
&+\eta_Y\cdot\sum_{b\notin T}\left[\eta_B(b)\cdot h_{B,f}(b)\cdot\dot{m}_{B,f}(b,t)\right]\\
&+\eta_Y\cdot c_w\cdot\Delta\vartheta_{P,w}\cdot\dot{m}_{P,w}(t)+COP_H(t)\cdot P_H(t)=\\
&-\left(\frac{n_V(t)\cdot\rho_a V_i c_a}{3600}+U_W\cdot A_W\right)\cdot\vartheta_e(t)-\sum_j\alpha_{S,j}\cdot A_{S,j}\cdot I_{S,j}(t)\\
&-\sum_r\left[A_r\cdot\left(\dot{q}_{occ,r}(t)+\dot{q}_{lit,r}(t)+\dot{q}_{apl,r}(t)\right)\right]
\end{aligned}
\tag{2.38}
$$

Inequality constraints $h(\mathbf{x})\geq 0$ include CHP exhaust heat recovery relations (2.24.e)-(2.24.g) and CHP ramp rate limits (2.24.i).

Upper and lower limits on state variables $\underline{\mathbf{x}}\leq\mathbf{x}\leq\overline{\mathbf{x}}$ are placed according to installed size limits and characteristics of devices and system. All state variables are non-negative as well. A significant limit represents thermal comfort conditions in the building, bounding the internal temperature between appropriate minimum and maximum values, that can in general depend on the specific time interval:

$$
\vartheta_i^{\min}(t)\leq\vartheta_i(t)\leq\vartheta_i^{\max}(t) \tag{2.39}
$$

2.2.4 Test system

The procedure for determining day-ahead operation program of a MG is carried out to a daily time frame with 96 time steps of 15 minutes each. The proposed approach is applied to the test microgrid shown in Fig. 2.7, representing a configuration of the low-voltage three-phase testbed network realized in Electric Power System Laboratory of Politecnico di Bari where thermal section is added. The microgrid includes:

- a photovoltaic field (PV) with a total power of 45 kW, composed of five independent sections equipped with different panel technologies;
- a wind system (WT) including one 20-kW horizontal axis mini wind turbine and two 6-kW vertical axis wind turbines;
- an electric energy storage system (ESS) based on sodium-nickel batteries, with 141 kWh capacity and 48 kW maximum charge/discharge power at 0.85 charge/discharge efficiency;
- grid connection with 200 kW maximum exchange in both directions;
- a gas-fueled internal combustion engine in cogeneration layout (CHP1), with installed electric power of 105 kW and nominal thermal power of 180 kW, capped at half values (52

kW / 90 kW) for operation matters, rated electric efficiency of 31.5%, thermal efficiency of 56%, ramp-up and ramp-down rates at 1/3 of installed power per 15-min time step;

- a gas microturbine in cogeneration layout (CHP2), with installed electric power of 28 kW, nominal thermal power equal to 57 kW; rated electric efficiency of 24.8%, thermal efficiency equal to 50%, no ramp rate limits (the maximum variation corresponds to the installed power);
- a 10-kW air-to-water heat pump (HP), with outlet temperature 55°C;
- a 75-kW wood-fueled boiler (Boiler1) with 82.5% rated efficiency, not connected to thermal storage, and a 20-kW pellet-fueled boiler (Boiler2) with 88% rated efficiency feeding the thermal storage;
- a hot-water thermal storage system (TSTO) made up by three isolated tanks with total capacity of 17 m^3 with a temperature range between 55°C and 70°C;
- a solar thermal collector system composed by two types of collectors (STH1 and STH2) covering a total area of 70 m^2, with 25 kW nominal power, with nominal efficiency of 0.68 and equivalent solar absorption area of 35 m^2.

The final user is represented by a former industrial warehouse, currently hosting a part of offices and laboratories of Politecnico di Bari, (latitude 41.11°). It is characterized by the following features:

- building volume V_i = 46,200 m^3 (70 x 66 x 10 m) and A_W = 2,720 m^2 is the total area of peripheral walls;
- average thermal transmittance of peripheral walls U_W = 0.6 W/m^2K;
- percentage of window surface 15% and reduction coefficient $\alpha_{S,j}$ = 0.6 for all walls, no shadow is provided;
- amount of air ventilations $n_V(t)$ = 1 volume per hour, in the working time period (from 7:00 to 20:00),
- minimum internal temperature of 20°C in working hours, 15°C in the evening and 12°C in the morning;
- maximum internal temperature of 24°C in working hours, 21°C in other intervals;
- electric load with nominal power of 180 kW;
- internal heat gains amount to at most 30 kW.

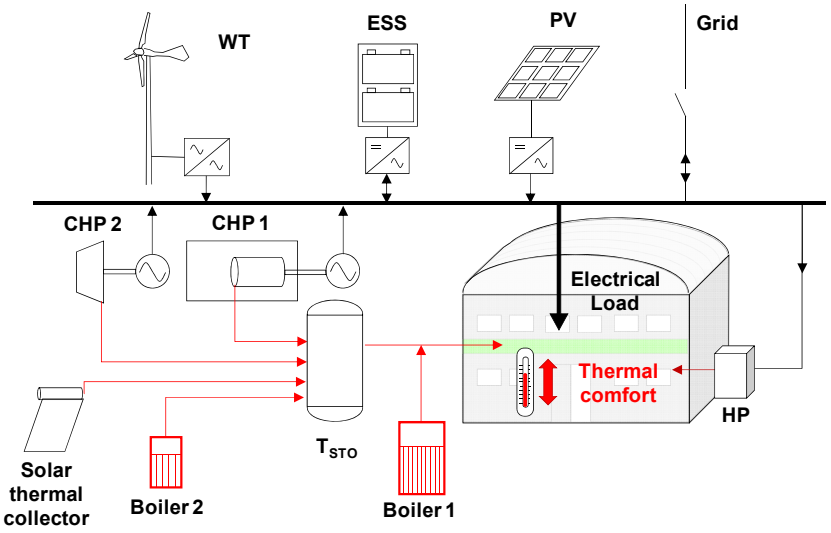

Figure 2.9. Test microgrid layout

2.2.5 Test cases

The test is carried out over a period of 15 consecutive winter days, thus encompassing working days and holydays under different weather and renewable source availability conditions. A synthesis of input conditions for the considered days is reported in Table 2.5. In particular, temperature values are derived from a meteorological station placed in the nearby of the microgrid site [59], where solar radiation and wind speed are collected as well. These two last quantities are reported to the conditions of the microgrid devices, by accounting for orientation and slope of PV as well as for hub height of WT [45][153]. Electric load is derived from measured data in the university settlement hosting the microgrid, where a term related to electric storage consumption in idle state, roughly 2.3 kW, is added in order to balance ESS self-discharge losses. It can be seen that the electric load assumes lower values in the weekends. The procedure is therefore carried out for all the 15 days, with equal starting conditions for energy storage devices, at the beginning and at end of each day the battery SOC is fixed at 65% of maximum capacity (i.e. 91.65 kWh) and water temperature in the thermal storage has to reach 60°C. Moreover, the continuity of building internal temperature is ensured in (2.38), by assuming the starting temperature of the first day $\vartheta_i(0) =$ 15°C, and for the next days $\vartheta_i(0)\Big|_{day} = \vartheta_i(N_t)\Big|_{day-1}$.

Simulations are performed in MATLAB® optimization tools. The procedure is run on an Intel ® Xeon ® E5-1620 3.50 GHz with 16 GB RAM, operating system Windows 7 (64 bit).

Table 2.5. Features of the days of simulation horizon

Day	Week day	Temperature			Renewable production		Electric load [kWh]
		Avg	Max	Min	PV [kWh]	WT [kWh]	
1	Sat	7.7	8.4	6.9	83.90	555.52	1723.83
2	Sun	7.4	8.1	6.7	66.48	114.36	1290.24
3	Mon	7.6	11.0	3.7	107.48	23.84	2023.53
4	Tue	7.6	12.2	4.9	116.64	0.00	2013.80
5	Wed	7.5	12.2	3.9	118.03	0.00	1978.80
6	Thu	9.8	13.8	5.3	39.45	9.47	1970.11
7	Fri	8.2	11.2	5.6	121.75	5.88	1932.08
8	Sat	7.0	8.5	5.8	10.21	252.07	1699.01
9	Sun	3.1	6.4	1.7	29.52	382.56	1289.30
10	Mon	0.3	1.9	-2.0	36.19	390.05	2213.09
11	Tue	2.8	4.5	0.7	61.90	276.83	2223.93
12	Wed	4.1	5.4	2.4	69.07	161.47	2233.41
13	Thu	1.1	2.6	-0.5	23.69	48.33	2191.77
14	Fri	1.3	5.0	-0.7	129.14	8.76	1975.95
15	Sat	4.8	9.3	-0.7	138.17	14.78	1662.71

The behaviour of internal temperature, in comparison with comfort limits and external conditions, is reported for the considered simulation horizon in Fig. 2.10. It can be seen that, according to the specific days of the week, different comfort performances are required and suitably reached by the overall system, both in the case of warm periods (days 3-7) and cold ones (days 9-14). Mid-day temperature spikes are seldom observed, due to remarkable solar absorption contribution.

The behavior of electric and thermal storage systems over the 15-day horizon is illustrated in Fig. 2.11 and Fig. 2.12, respectively. It is worth to remark that ESS is charged in the presence of an electricity production excess, preferably coming from renewable sources. The SOC attains maximum level in Day1, when an extra production of WT is observed with limited load, and in Day13, when CHPs are heavily exploited.

Thermal storage shows a deep exploitation in all days. Water in the storage is usually warmed during the night and in early morning, when the thermal comfort level is lower, whereas it decreases down to minimum value in central hours of the day, when the minimum level of internal building temperature is increased. Maximum temperature level is reached in Day10 due to high thermal needs and electric demand, and in Day4 as well, due to high contributions of CHP, STH and low thermal demand.

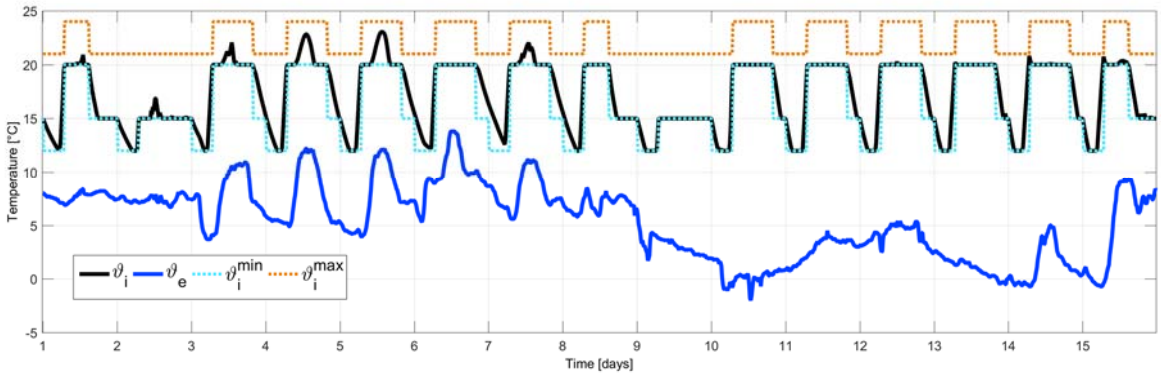

Figure 2.10. Internal and external temperature trends.

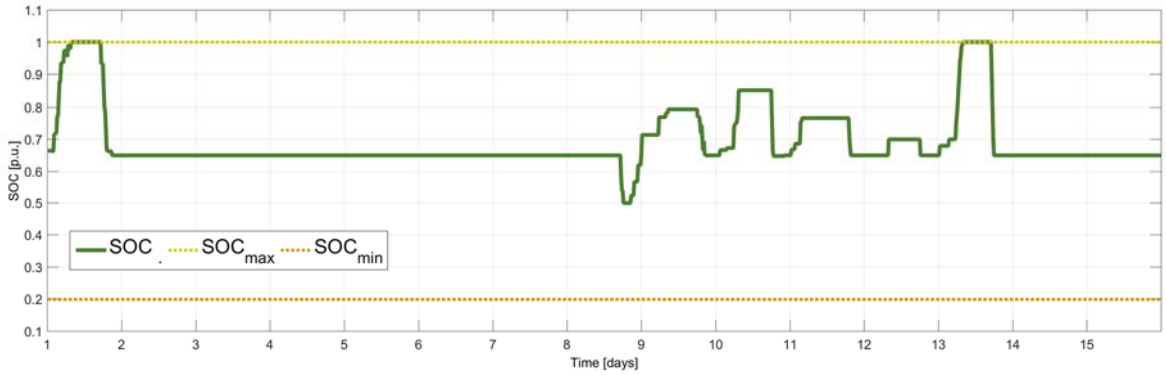

Figure 2.11. SOC of electric storage and limits.

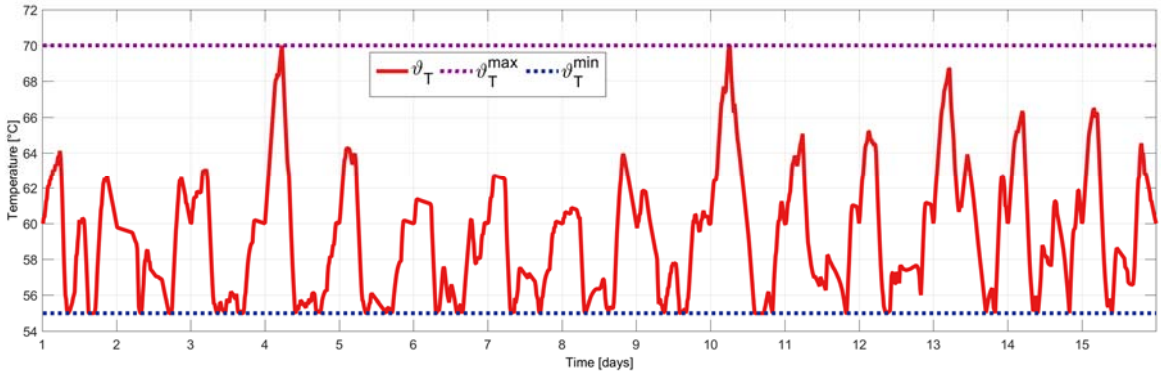

Figure 2.12. Water temperature of thermal storage and limits.

The synthesis of electric balance for each day is reported in Table 2.6. It can be seen that grid contribution is higher in warmer days, where renewable production is usually lower (PV contribution is limited, even in sunny days). In colder days, the use of CHP1 is more intense, and even CHP2 is called to produce in days 10-14, in order to cover higher thermal needs. Being HP operation expensive, it turns out to be convenient only when no-cost electric energy is available (i.e. renewable or CHP excess). For the conditions described in the above, the ESS is operated, whereas in more than half of the days it is in idle state.

Table 2.6. Daily Electric energy balance [kWh]

	Production						Consumption		
Day	PV	WT	CHP1	CHP2	Grid	ESS_d	ESS_c	HP	Load
1	83.90	555.52	444.94	0.00	669.01	45.55	63.04	12.04	1723.83
2	66.48	114.36	216.84	0.00	892.57	0.00	0.00	0.00	1290.24
3	107.48	23.84	468.02	0.00	1424.19	0.00	0.00	0.00	2023.53
4	116.64	0.00	438.59	0.00	1458.57	0.00	0.00	0.00	2013.80
5	118.03	0.00	469.13	0.00	1391.64	0.00	0.00	0.00	1978.80
6	39.45	9.47	418.18	0.00	1503.01	0.00	0.00	0.00	1970.11
7	121.75	5.88	425.01	0.00	1379.43	0.00	0.00	0.00	1932.08
8	10.21	252.07	592.75	0.00	854.79	18.15	25.12	3.83	1699.01
9	29.52	382.56	474.89	0.00	411.63	24.20	33.50	0.00	1289.30
10	36.19	390.05	943.73	52.34	846.13	24.42	33.80	45.97	2213.09
11	61.90	276.83	912.42	3.03	982.60	13.94	19.30	7.50	2223.93
12	69.07	161.47	825.77	0.00	1179.39	5.98	8.27	0.00	2233.41
13	23.69	48.33	1000.37	136.16	999.33	41.95	58.06	0.00	2191.77
14	129.14	8.76	873.13	21.00	943.91	0.00	0.00	0.00	1975.95
15	138.17	14.78	536.78	0.00	972.99	0.00	0.00	0.00	1662.71

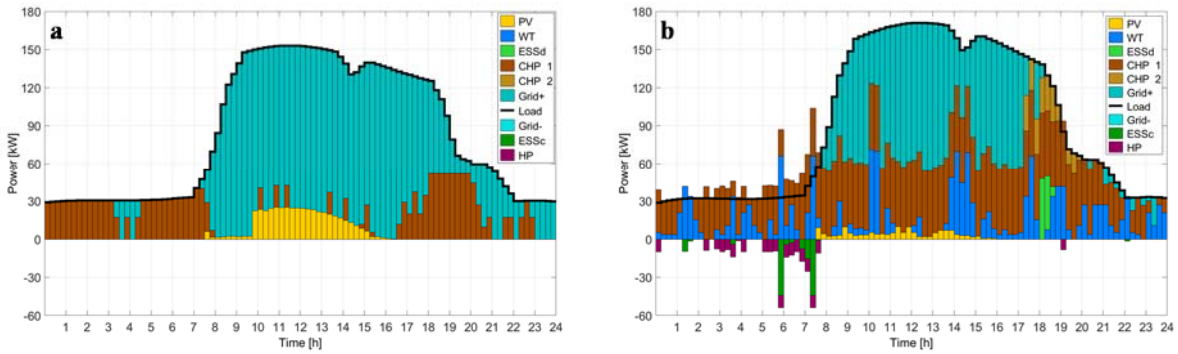

Figure 2.13. Electric power production/consumption shares in Day4 (a) and Day10 (b).

An example of trends of electric power production and consumption in Day4 and Day10, is reported in Fig. 2.13.a and 2.13.b respectively, where negative values represent further consumption terms. The considered days are both working ones, but with different ambient conditions (high temperature – high solar in Day4 and low temperature – low solar in Day10). It can be seen that, in Day4 only three sources contribute to electric load coverage, i.e. solar PV, CHP1 and power from the grid connection. This is due to the lack of wind production and to warm temperature conditions, limiting the exploitation of CHPs. Moreover, in central hours of the day, the microgrid electric balance only relies on PV and grid. HP and ESS do not give contribution at all. Whereas, in Day10, PV production is limited and remarkable generation by WT is present though varying during the day. Moreover, CHP1 is almost always on and is run for several intervals at nominal power, and CHP2 is exploited in late afternoon. In some periods,

the sum of internal production exceeds load, due to remarkable free contribution from WT, and this excess is exploited to feed HP and to charge the ESS. The ESS is discharged in peak price hour of late afternoon, and no power is delivered to the grid.

Analogously to electric contributions, daily thermal production and daily building thermal balance are illustrated in Table 2.7 and Table 2.8, respectively.

In particular, in Table 2.8 each column represents $Q = \sum_{t=1}^{N_t} \dot{Q}(t)$. It can be argued that solar thermal panels give a limited contribution, but it is never negative, even in low-radiation days (e.g. Day8 and Day13) thanks to the mass flow rate management strategy reported in (2.26.d). Moreover, CHP1 contribution is the most remarkable one, and CHP2 is exploited only in the cold period, as well as Boiler1 that helps the demand coverage independently of thermal storage, whereas Boiler 2 is unexploited. The building thermal balance puts in evidence the limited contribution of HP with respect to water-based heating system. The presence of non-negligible solar absorption and internal heat gains is pointed out, and their combined effect can reduce the daily thermal energy needs up to 40% in clear sky conditions. The term Q_D is null when the internal temperature at the end of the day returns to the initial value, whereas it is negative when the final temperature is higher than the initial one (Days 3, 5, 6) and positive in the opposite case (Days 4, 7, 8) However, the difference between initial and final internal temperature in each day does not exceed ±1°C.

Table 2.7. Daily Thermal Production [kWh]

Day	STH1	STH2	CHP1	CHP2	Boiler1	Boiler2
1	8.31	30.19	711.91	0.00	0.00	0.00
2	5.84	21.91	346.94	0.00	0.00	0.00
3	12.11	44.58	748.83	0.00	0.00	0.00
4	13.96	50.95	701.75	0.00	0.00	0.00
5	14.00	51.03	750.61	0.00	0.00	0.00
6	0.81	5.22	669.09	0.00	0.00	0.00
7	14.05	52.12	680.01	0.00	0.00	0.00
8	0.00	0.00	948.39	0.00	0.00	0.00
9	0.18	1.69	759.83	0.00	0.00	0.00
10	0.51	3.04	1509.96	94.21	171.46	0.00
11	2.99	12.96	1459.87	5.46	16.54	0.00
12	5.34	20.10	1321.24	0.00	0.00	0.00
13	0.00	0.20	1600.59	245.09	2.59	0.00
14	14.14	51.93	1397.01	37.80	4.11	0.00
15	16.18	59.72	858.84	0.00	0.00	0.00

Table 2.8. Daily Building Thermal Balance [kWh]

Day	QY	QH	QS	QW	QV	QD	Qihg
1	532.91	33.01	143.12	449.35	473.41	0.00	213.71
2	245.97	0.00	98.26	361.63	79.87	0.00	97.27
3	557.19	0.00	198.63	526.51	583.39	-8.50	362.58
4	518.18	0.00	231.18	534.06	581.79	7.82	358.67
5	556.92	0.00	243.12	545.68	601.80	-11.22	358.67
6	500.23	0.00	9.02	411.09	455.22	-13.35	370.41
7	499.23	0.00	237.23	514.18	593.20	12.26	358.67
8	729.28	10.59	0.90	483.94	489.56	12.99	219.74
9	577.31	0.00	7.03	567.26	115.24	0.00	98.16
10	1384.69	109.76	23.97	863.94	1024.89	0.00	370.41
11	1142.83	18.57	65.02	743.87	852.97	0.00	370.41
12	1016.32	0.00	88.17	684.09	786.90	0.00	366.50
13	1440.30	0.00	1.43	835.22	976.92	0.00	370.41
14	1102.65	0.00	269.05	826.43	903.93	0.00	358.67
15	639.24	0.00	288.26	600.04	534.65	0.00	207.19

An example of trends of fuel consumption levels, water/exhaust flows, water temperatures, thermal storage balance and building thermal balance are reported in Figg. 2.14÷2.18, respectively, for Day4 (sub-figure a) and Day10 (sub-figure b).

It can be seen that in Day4 fuel is burnt only by CHP1, and maximum level of 0.48 m^3/h is experienced in the evening, corresponding to maximum exhaust and water flows in CHP1 exchanger. Moreover, no water is flowing in other fuel-based sources, and solar thermal plants are exploited in sunny hours according to (2.26.d). Whereas, thermal storage outlet towards the building heating system reaches the maximum in early morning, to comply with comfort level requirements in successive time intervals, and is null in central hours of the day. Temperature variations of thermal storage are within the imposed range, moreover source temperature depend on solar radiation in STH1 and STH2 and on CHP1 exploitation, however it does not exceed 100°C in any device for any condition. Thermal storage, therefore, is charged (temperature rises) in early morning, and is discharged in late morning and afternoon. At noon, solar thermal plants contribute only to cover storage losses, since the temperature does not show remarkable variations. At the end of the day, the exploitation of CHP1 causes the return of storage temperature to initial values. As regards building thermal balance, it can be seen that wall and ventilation losses depend on temperature difference, that is low in the central hours of the day, when solar absorption and internal heat gains exceed losses. Thus the water-based heating system is unexploited and residual demand is positive, corresponding to internal temperature increase. No contribution from HP and auxiliary boiler is observed over the whole day.

In Day10, fuel consumption occurs in CHP1, CHP2 and Boiler1, reaching maximum levels in different time intervals. Water flows show remarkable levels, except for solar thermal plants and Boiler2, and thermal storage output is close to maximum for long periods. In central hours of the day it minimum temperature of thermal storage is attained, therefore the exploitation of Boiler1 as auxiliary reaches again the maximum. CHP2 contributes to keep thermal storage in the defined range in late afternoon, in the presence of peak thermal demand, maximum CHP1 production and low storage temperatures. Building thermal losses reach remarkable values, almost constant during occupancy period, and solar absorption gives low contribution, therefore auxiliary boiler and HP in early hours help the system to respect the thermal comfort limits. . It is observed that COP_H assumes values in the range 3.5-4.5.

In both days, as in all the 15 analyzed days, CHP heat production is not wasted, i.e. exhaust flow rate in the heat exchanger corresponds to the level related to power production amount, and constraint (2.24.g) reduces to an equality. Therefore CHPs are always planned to be operated, though implicitly, in thermal-leading (or electric-following) mode.

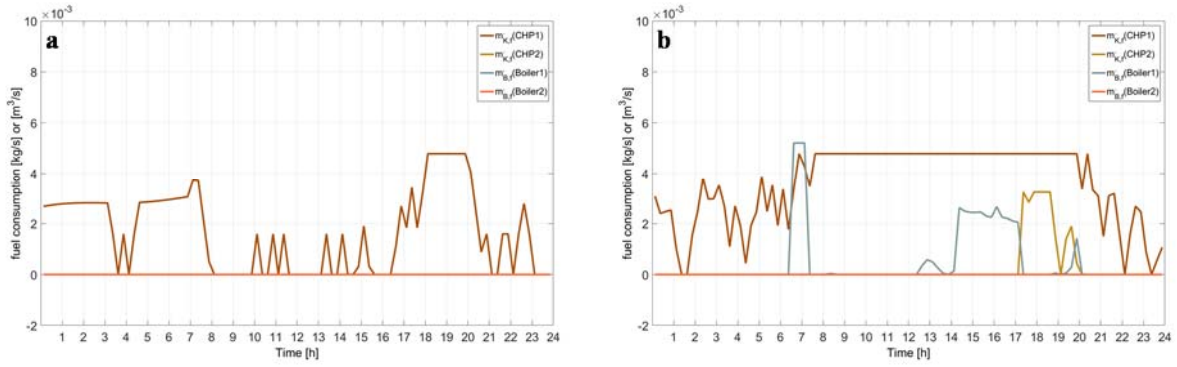

Figure 2.14. Fuel consumption levels in Day4 (a) and Day10 (b).

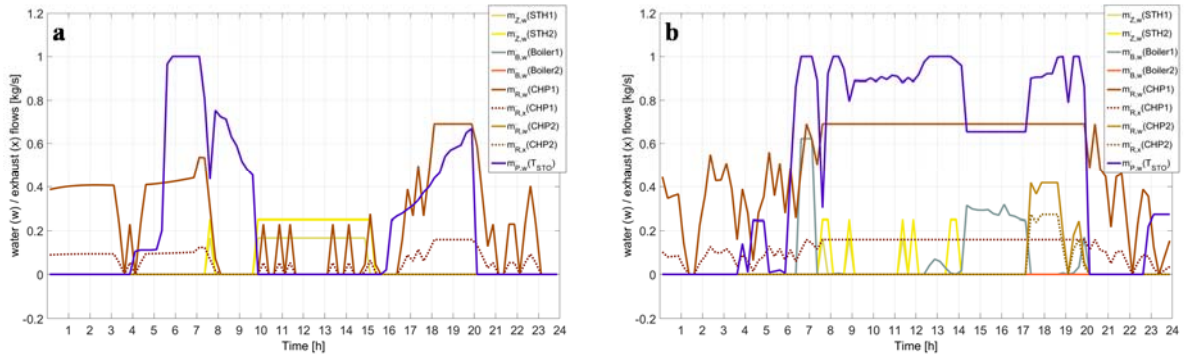

Figure 2.15. Water/exhaust flow rates in Day4 (a) and Day10 (b).

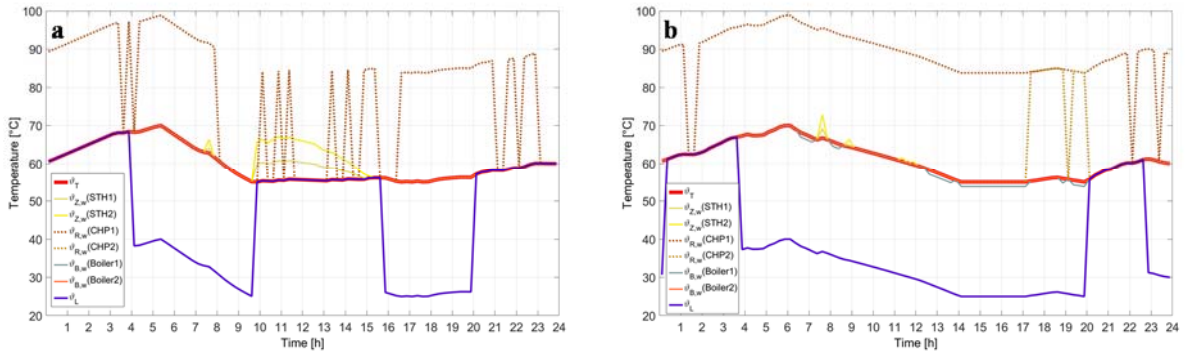

Figure 2.16. Water temperature in each circuit in Day4 (a) and Day10 (b).

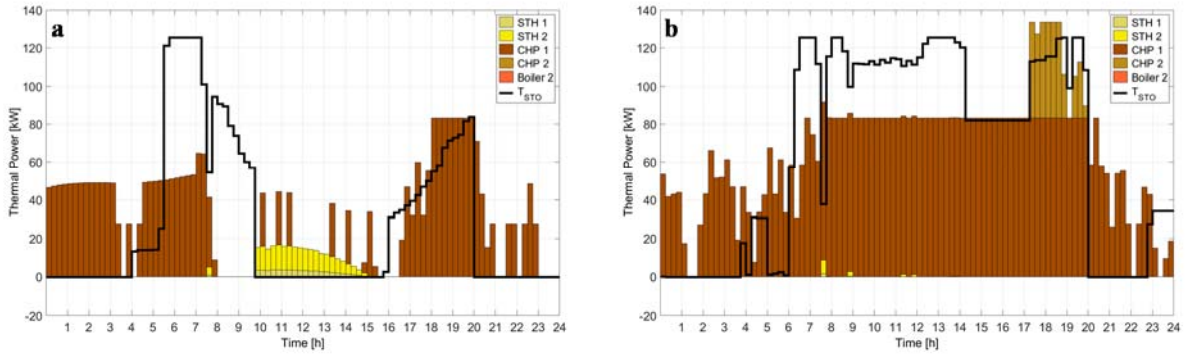

Figure 2.17. Thermal storage balance in Day4 (a) and Day10 (b).

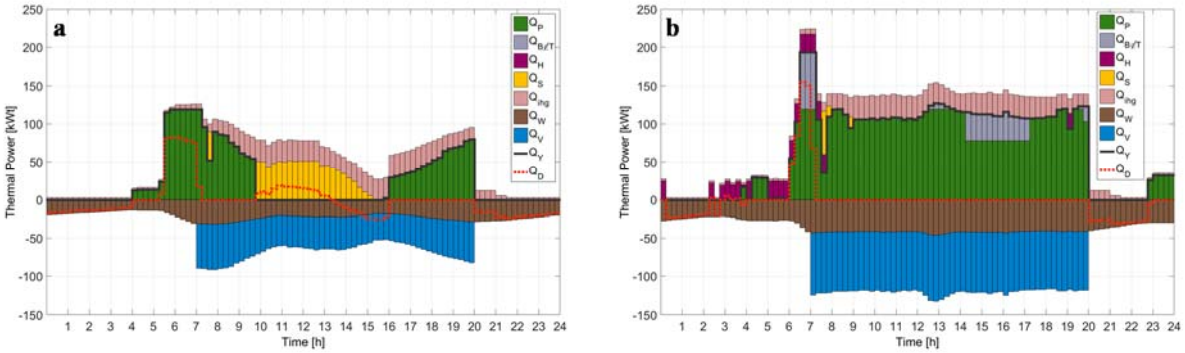

Figure 2.18. Building thermal energy balance in Day4 (a) and Day10 (b).

A synthesis of economic performance of the system under study over the considered period is reported in Table 2.9. It can be seen that the main cost contribution is given by grid power withdrawal in warmer period, whereas the influence of CHPs is prevailing in colder days. Moreover, since no power injection to the grid is provided, relevant revenues do not occur. The influence of emission costs is well below 1% of total economic effort, and boilers yield limited costs.

Table 2.9. Daily Cost Contributions [€]

		CHPs		Boilers		
Day	C_g	C_O	C_E	C_O	C_E	Total
1	92.19	75.27	1.09	0.00	0.00	168.55
2	129.50	36.68	0.52	0.00	0.00	166.70
3	202.61	79.17	1.13	0.00	0.00	282.91
4	196.94	79.32	1.21	0.00	0.00	277.47
5	203.21	84.84	1.30	0.00	0.00	289.35
6	215.29	75.63	1.03	0.00	0.00	291.94
7	204.04	76.86	1.08	0.00	0.00	281.98
8	120.03	107.20	1.42	0.00	0.00	228.65
9	56.19	85.88	1.08	0.00	0.00	143.16
10	120.62	182.59	2.37	7.37	0.34	313.30
11	139.76	165.70	2.18	0.71	0.03	308.38
12	183.50	149.34	1.96	0.00	0.00	334.80
13	176.79	211.94	2.83	0.11	0.01	391.68
14	157.82	162.69	2.23	0.18	0.01	322.91
15	166.47	97.07	1.22	0.00	0.00	264.77

Moreover, a comparison of the results of microgrid operation is carried out with respect to conventional energy supply technologies in Italy, i.e. by withdrawing electric energy from the grid, and covering thermal demand by means of gas-fuelled high efficiency boilers, in the absence of any other generation or storage device. In order to reproduce the same energy needs and thermal comfort levels achieved in test results, electric demand corresponds to forecasted electric load $\tilde{P}_L(t)$, whereas thermal demand is determined as the right side of eq. (2.18), i.e. $\dot{Q}_V(t)+\dot{Q}_W(t)-\dot{Q}_S(t)-\dot{Q}_{ihg}(t)$, as obtained by simulations. A comparison of average daily unit costs for electric energy (EL) and thermal energy (TH) in the conventional case and in simulation results is carried out. While in the conventional case these daily values are straightforwardly obtained, their evaluation from simulation results is given by splitting cost items of CHPs among electric and thermal part according to the ratio of useful electric and thermal effects $P_K(k,t)$ and $\dot{Q}_R(k,t)$ i.e, by simplifying Δt:

$$C_{EL}(k)=\sum_{t=1}^{N_t}\left[C_O(k,t)+C_E(k,t)\right]\cdot\frac{\sum_{t=1}^{N_t}P_K(k,t)}{\sum_{t=1}^{N_t}\dot{Q}_R(k,t)+\sum_{t=1}^{N_t}P_K(k,t)} \tag{2.40.a}$$

$$C_{TH}(k)=\sum_{t=1}^{N_t}\left[C_O(k,t)+C_E(k,t)\right]\cdot\frac{\sum_{t=1}^{N_t}\dot{Q}_R(k,t)}{\sum_{t=1}^{N_t}\dot{Q}_R(k,t)+\sum_{t=1}^{N_t}P_K(k,t)} \tag{2.40.b}$$

Therefore, the average daily unit cost for electricity production is determined as the ratio of the cost of energy exchange with the network and electricity cost of CHPs on total electricity consumption:

$$uc_{EL}=\frac{\sum_{t=1}^{N_t}C_G(t)+\sum_{k=1}^{N_k}C_{EL}(k)}{\sum_{t=1}^{N_t}\left[\tilde{P}_L(t)+\sum_{h=1}^{N_h}P_H(t)+P_A^c(t)\right]} \tag{2.41.a}$$

Furthermore, the average daily unit cost for thermal energy production is evaluated as the ratio of the sum of thermal cost of CHPs, total cost of boilers and the total cost related to the operation of HPs (defined as C_{HP}) on total thermal energy demand of the building:

$$uc_{TH}=\frac{\sum_{k=1}^{N_k}C_{TH}(k)+\sum_{b=1}^{N_b}\sum_{t=1}^{N_t}\left[C_O(b,t)+C_E(b,t)\right]+C_{HP}}{\sum_{t=1}^{N_t}\left[\dot{Q}_V(t)+\dot{Q}_W(t)-\dot{Q}_S(t)-\dot{Q}_{ihg}(t)\right]} \tag{2.41.b}$$

The evaluation of C_{HP} is not direct, since HPs exploit electricity within the microgrid for producing heat. To this purpose, average electricity production cost per time step is first determined, by determining the component of CHP cost related to electric energy:

$$C_{EL}(k,t)=\left[C_O(k,t)+C_E(k,t)\right]\cdot\frac{P_K(k,t)}{\dot{Q}_R(k,t)+P_K(k,t)} \tag{2.42.a}$$

$$uc_{EL}(t)=\frac{C_G(t)+\sum_{k=1}^{N_k}C_{EL}(k,t)}{\tilde{P}_L(t)+\sum_{h=1}^{N_h}P_H(t)+P_A^c(t)} \tag{2.42.b}$$

Therefore, the daily cost for HP operation is determined as follows:

$$C_{HP}=\sum_{t=1}^{N_t}\left(uc_{EL}(t)\cdot\sum_{h=1}^{N_h}P_H(h,t)\right) \tag{2.42.c}$$

The outcomes of the analysis are reported in Fig. 2.19, and it can be seen that unit cost of electricity is lower in the proposed approach than in the conventional case, whereas thermal unit cost is slightly higher, due to the lower thermal efficiency related to CHPs with respect to boilers. The whole MG management results less expensive than the conventional energy supply, as reported in Fig. 2.20, where total daily costs are compared. It can be seen that minimum variations are observed in Day13, where the advantage of the proposed approach is only 0.55 €, whereas in other days the saving can be higher than 100 €. The relative saving reaches maximum values of 38% in holydays, whereas the average value over the 15 Days is 17.9%. In all cases, since HP is operated only in the presence of excess internal electricity production, C_{HP} gives limited contribution.

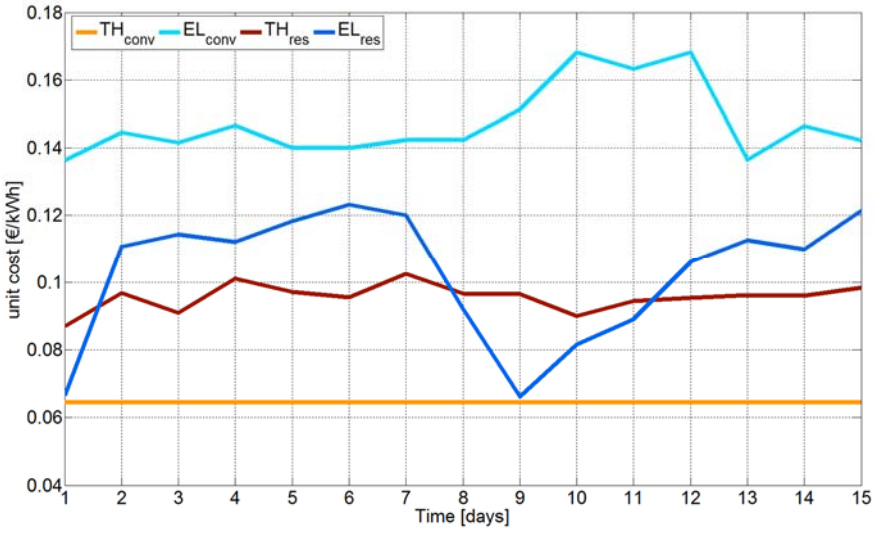

Figure 2.19. Comparison of unit cost for electric and thermal energy.

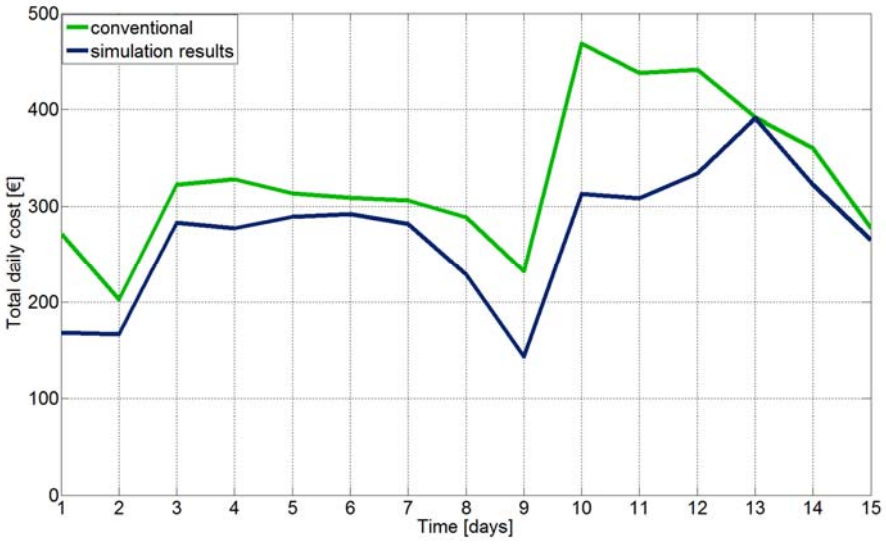

Figure 2.20. Comparison of total daily cost.

The application to a realistic system under different conditions proved the validity of the proposed methodology to represent the behavior of multi-source microgrid and interaction between thermal and electric demand supply. The detailed representation of integrated water-based heating system allows to catch specific mass flows and temperature variations for each device, in order to comply with thermal comfort needs while minimizing operating costs of the whole microgrid.

2.2.6 Conclusions

In order to address the increasing interest in developing integrated multi-energy system at local level, a methodology for assessing microgrid operation plan in the presence of a detailed thermal energy model has been proposed. The formulation of this model allows to monitor room temperature according to specific comfort levels, along with water mass flows and temperature in a multi-source thermal production system. The employment of different energy production technologies, renewable and conventional, as well as thermal or electric or combined, along with thermal and electric storage, provides flexibility to the procedure for individuating the most suitable combination to achieve the required thermal comfort and to cover electricity needs. This objective has been pursued by an optimization procedure able to define the optimal daily plan at minimum operation and emission costs,. Investigation results allow to define the day-ahead operation plan with 15-min time step for each device, compatible with technical constraints, driven by external conditions on weather and electric demand. The application of the proposed approach to a multi-energy experimental microgrid, exploiting real data from weather observations, ensures the trustworthiness of the obtained results and the economic convenience of a multi-source microgrid with respect to distinct conventional supply technologies. Moreover, the modularity of the formulation allows to tailor the procedure to the features of specific application.

3. The integration of Electric Vehicles in Distribution network

3.1 Optimal operation planning of V2G-equipped Microgrid in the presence of EV aggregator

An optimal day-ahead operation planning procedure for Microgrids (MGs) integrating Electric Vehicles (EVs) in vehicle-to-grid (V2G) configuration is described in this sub-section. It aims to determine the day-ahead operation plan by solving a non-linear optimization procedure involving daily cost and subject to dynamic operating constraints. The main goal is to minimize MG operation daily costs, according to suitable load demand and source availability forecast, taking into account an EV aggregator. In order to evaluate possible economic relationships between the EV aggregator and the MG operator, two different objective functions are considered. Taking in the cue from multiobjective approaches, based on forecasted generation of renewable-based sources and load demand [2]-[20], the proposed optimization procedure further allows to assess benefits from EV fleet in V2G configuration, by accounting the EV aggregator role. In particular, it is envisaged the case that MG operator and EV aggregator could be represent separate entities or single entity, with different objectives for MG operator in the elaboration of the optimal plan. The methodology is applied to a test MG including several devices for electric and thermal power production and storage, along with V2G systems, in charge to satisfy energy needs at premises of residential or commercial users. Indeed, the EVs can lead to new opportunities for the implementation of MG [155][156] and the constitution of EV aggregator can be introduced.

The proposed procedure aims to get the following novelty:

- The influence of EV fleet seen as mobile storage in the frame of MG;
- The adoption of actually models for thermal and electrical sources;
- The techno-economic analysis of interactions between EV aggregator and MG operator;
- Different EV use patterns are proposed according to specific users.

3.1.1 Literature review

The integration of large amount of distributed energy resources and of Electric Vehicles (EVs) has introduced several challenges to the planning and operation of modern electric power system [157]. The lack of coordination of Distributed Generation (DG) sources and Vehicle-to-Grid (V2G) charging point can give rise to issues such as reverse flows, unintentional islanding, overloads. To deal with these concerns MGs more and more employed [158][159]. In fact, they are able to integrate DG technologies, Energy Storage Systems (ESSs) and

charging station, as well as electric and thermal loads. The recent diffusion of EVs in V2G configuration, along with station technological improvement, has also shifted EV role from dispersed loads to small-sized distributed virtual generator. Moreover, V2G scheme can support to the distribution grid in regulation services, as illustrated in [160]-[165], whereas the influence of V2G system on MG operation is evaluated in [166]-[169].

The EV charging process (or energy exchange in V2G configuration) can be optimally managed in order to provide economic benefit to EV owners and to support MG operation, particularly when a small number of EVs are organized in fleet. Indeed, it can be connected into the grid simultaneously at the same connection point [170]. In this case, the MG operator interacts with vehicle fleets through EV aggregators, which provide proper control of the parked vehicles and their interaction with the grid [171]. The EV aggregator is in charge of performing the "smart charging" service, by exploiting time flexibility given by the difference between needed charging time and parking time to provide grid services and meet the needs of the driver [172]. The EV aggregator performs the smart charging service by determining how and when each vehicle is to be charged, thereby providing a demand-dispatch service to a utility or grid operator [173].

In the other hand, the MG operator is in charge to elaborate a suitable operation scheduling in the day-ahead horizon, in order to plan its units accounting for economic burdens, environmental impact and reliability issues [102][174][175]. For the development of procedures for MG day-ahead operation planning, different approaches are present in literature to take into account the variability of PV and wind production, load demand, energy prices, EV parking intervals and energy requirements. A distinction can be made among stochastic methods accounting for possible deviations of forecasts with proper probability distribution functions (pdfs) [176][178], procedures based on the generation of different scenarios with relevant probability [179]-[183], and methodologies based on deterministic data [4][186]-[193]. The proposed approach falls in this last field, i.e. considering as inputs the most probable value of the forecasts of different quantities subject to prediction instead of decision, since it represents the most realistic form to determine plans to be implemented by actual SCADA in MGs. For this reason, advanced prediction methods should be accounted [194]-[196], that are beyond the scope of this procedure. Moreover, even exploiting stochastic methods (e.g. chance constrained, robust optimization, …), the presence of variation during operation outside the pdfs or not considered in scenarios will cause a different behaviour with respect to the plan. It should be remarked that the risk reduction due to stochastic optimization is negligible in this case with respect to a deterministic procedure with suitable operation margins of the devices

[190]. Therefore a second-stage procedure, closer to real time operation and entrusted to cope with those variations, operating over shorter time intervals (e.g. an hour or a group of hours) and accounting for even faster variations (down to minutes or some seconds), should be carried out as indicated also in [4], [167], [184]-[187], [189], [192], [197].

3.1.2 Microgrid Operation Planning

The formulation of the problem starts from modelling of the involved energy equipment. Different kinds of devices can be individuated: fuel-based energy production systems (caring for electricity or thermal energy, or even both in cogeneration layout), renewable-based generation devices, energy storage systems, grid connection, EVs, energy consumption. In order to represent the time variation of energy flows, the daily horizon is divided in N_t time steps with a time width of Δt each, typically ranging between 5 minutes to 1 hour [198] compatibly with granularity of day-ahead forecast methods ensuring acceptable uncertainty levels [194]-[196]. Since MG-sized devices reaching the required power reference planned condition in some seconds [199][200], the adoption of static models allows a powerful representation of the devices in the described time steps without losing accuracy.

In particular, the *i*-th fuel-based production device can operate in different electric production level $P(i,t)$, within its technical features, although fuel procurement is incurred and local emissions are produced. Therefore, its operation can be characterized by determining fuel consumption $F(i,t)$ and emission amount $E(i,t)$ and bounding production level through the following relations:

$$F(i,t) = \frac{\Delta t \cdot P(i,t)}{fv(i) \cdot \eta_E\left(P(i,t)\right)} \tag{3.1.a}$$

$$E(i,t) = \varepsilon\left(P(i,t)\right) \cdot \Delta t \cdot P(i,t) \tag{3.1.b}$$

$$P^m(i) \le P(i,t) \le P^M(i) \tag{3.1.c}$$

where $fv(i)$ represents fuel heating value, and electric efficiency $\eta_E\left(P(i,t)\right)$ depends on power production level through a polynomial function. Since emissions are related to fuel energy consumption, emission factor $\varepsilon\left(P(i,t)\right)$ is inversely proportional to electric efficiency, i.e. $\varepsilon\left(P(i,t)\right) = k\varepsilon(i) / \eta_E\left(P(i,t)\right)$, where $k\varepsilon(i)$ is a constant factor depending of the technology of the *i*-th fuel-based production device. Moreover, $P^m(i)$ and $P^M(i)$ stand for lower and upper limits of power output, respectively. The use of discrete variables for on-off status of generators

accounting for experimental nonlinear efficiency functions would involve MINLP formulation, although it could not lead to feasible results [201] and does not involve remarkable advantage with respect to NLP. Therefore, the proposed NLP formulation allows to ensure convergence and to lose as low information as possible.

As regards the thermal energy production, the previous formulations keep valid by expressing the quantities in terms of heat production level $Q(i,t)$:

$$F(i,t) = \frac{\Delta t \cdot Q(i,t)}{fv(i) \cdot \eta_T\left(Q(i,t)\right)} \tag{3.2.a}$$

$$E(i,t) = \varepsilon_T\left(Q(i,t)\right) \cdot \Delta t \cdot Q(i,t) \tag{3.2.b}$$

$$Q^m(i) \le Q(i,t) \le Q^M(i) \tag{3.2.c}$$

where thermal efficiency is represented by $\eta_T\left(Q(i,t)\right)$, and unitary emission factor per thermal energy $\varepsilon_T\left(Q(i,t)\right)$ (inversely proportional to thermal efficiency). Lower and upper limits related to thermal power production, $Q^m(i)$ and $Q^M(i)$ are considered.

The electric power production $P(i,t)$ and heat production $Q(i,t)$ are directly linked in MG-sized cogeneration systems, as suggested in, [11][33][197] that proves more appropriate than other possible representations, such as feasible electricity-heat operating region reported in [202]. Therefore, either electric or thermal power represent the decision variable, since the following relation holds:

$$Q(i,t) = \frac{\eta_T\left(Q(i,t)\right)}{\eta_E\left(P(i,t)\right)} \cdot P(i,t) \tag{3.3}$$

As regards the *r*-th technology based on a non-programmable renewable energy source (RES), e.g. wind, solar radiation, water flow, relevant power production level $P(r,t)$ or thermal production level $Q(r,t)$ can be obtained by forecasting source availability, and accounting for the specific function of energy conversion, e.g. wind turbine power related to speed and PV panel conversion according to solar radiation and temperature effects [203].

Energy storage devices are characterized by internal state of charge $S(s,t)$. For the *s*-th storage system, this value is linked to electric power charge/discharge of the device ($P_c(s,t)$ and $P_d(s,t)$, respectively) and to technical features of the system through the following expressions:

$$S(s,t) = S(s,t-1) + \psi_c(s) \cdot \Delta t \cdot P_c(s,t) - \frac{P_d(s,t)}{\psi_d(s)} \cdot \Delta t - \rho(s) \cdot S^M(s) \tag{3.4.a}$$

$$S^m(s) \le S(s,t) \le S^M(s) \tag{3.4.b}$$

$$0 \le P_c(s,t) \le P_c^M(s) \tag{3.4.c}$$

$$0 \le P_d(s,t) \le P_d^M(s) \tag{3.4.d}$$

$$P_c(s,t) \cdot P_d(s,t) = 0 \tag{3.4.e}$$

$$S(s,0) - \psi_c(s) \cdot \Delta t \cdot P_c^M(s) \le S(s,N_t) \le S(s,0) + \frac{P_d^M(s)}{\psi_d(s)} \cdot \Delta t \tag{3.4.f}$$

where, $S(s,t-1)$ is the state of charge at previous time step, $S(s,0)$ is the initial state of charge of the considered day connected to the final state of charge at the end of the day before, that is a known value for the operation planning of the considered day. Moreover, $\psi_c(s)$ and $\psi_d(s)$ are charge and discharge efficiency, respectively, $S^M(s)$ and $S^m(s)$ are the maximum and minimum charge capacity, respectively, $P_c^M(s)$ and $P_d^M(s)$ are the maximum charge and discharge rates, respectively, and $\rho(s)$ is the self-discharge rate. Equation (3.4.e) does not allows bidirectional excange of the device in the same period. Constraint (3.4.f) bounds the final state of charge of the considered day in an feasible range around the initial state of charge. This assumptions ensures more flexibility to the optimal management of MG and allows to account for self-discharge of ESS. In other works as [175][193][204] initial and final values in the considered day are equal, whereas in [205][206] this range is considered as a defined percentage of maximum charge capacity. In the proposed constraint (3.4.f), the limits correspond to maximum variation of the state of charge that the ESS can perform in a single time step based on ramp up and ramp down characteristics. ESS parameters depend on the history of the device due to degradation phenomena, however, for the investigation of a single day, they are univocally determined referring to the specific ESS lifetime condition and level of use. The MG is typically connected to the distribution grid through a single point, and the level of power purchase $P_{Pur}(t)$ and power injection $P_{Inj}(t)$ is considered, taking into account the unidirectional flow per each time step and appropriate limits, the following relations hold:

$$0 \le P_{Pur}(t) \le P_{Pur}^M(t) \tag{3.5.a}$$

$$0 \le P_{Inj}(t) \le P_{Inj}^{M}(t) \tag{3.5.b}$$

$$P_{Pur}(t) \cdot P_{Inj}(t) = 0 \tag{3.5.c}$$

where $P_{Pur}^{M}(t)$ and $P_{Inj}^{M}(t)$ are the maximum electric power purchasable and deliverable at grid connection, respectively.

As regards the EV fleet in V2G configuration, managed by an aggregator, can be modelled as an mobile ESS, connected to the grid only in same periods. Let *j* be the interval (set of time steps) for which the *v*-th EV fleet is plugged, and therefore for that *j*-th interval, define $t_A(v,j)$ as the forecasted time step when the *v*-th EV fleet arrives to the station with energy content $S(v,t_A(v,j))$, and $t_L(v,j)$ as the predicted time step according the owner habits, when the *v*-th EV fleet leaves the station with energy content $S(v,t_L(v,j))$. Hence, the following relations are valid for each time step of the *j*-th stationing interval, considering that the energy exchange process can start a time step after the arrival [179], i.e. $t_A(v,j)+1 \le t \le t_L(v,j)$.

$$S(v,t) = S(v,t-1) + \psi_c(v) \cdot \Delta t \cdot P_c(v,t) - \Delta t \cdot \frac{P_d(v,t)}{\psi_d(v)} \tag{3.6.a}$$

$$S^{m}(v) \le S(v,t) \le S^{M}(v) \tag{3.6.b}$$

$$0 \le P_c(v,t) \le P_c^{M}(v) \tag{3.6.c}$$

$$0 \le P_d(v,t) \le P_d^{M}(v) \tag{3.6.d}$$

$$P_c(v,t) \cdot P_d(v,t) = 0 \tag{3.6.e}$$

The terms assume the same meaning with respect to (3.4.a)-(3.4.e), but referred to the *v*-th EV fleet. Self-discharging effect can be neglected for the EVs [207]. The presence of several parking intervals of the same EV fleet during the day can be considered. In particular, the case of a night parking of the EV fleet is dealt with by assuming at least two intervals, one starting at the first time step of the day and one ending at the last time step of the day. To account for a continuity of EV charging, it is assumed that the energy state of EV fleet at the extreme time steps in the day, pertaining to different parking intervals, is the same, i.e. $S(v,1) = S(v,N_t)$. Moreover, the maximum power amount in charge and discharge phase ($P_c^{M}(v)$ and $P_d^{M}(v)$, respectively) are affected by technical features of the EVs, of the charging/V2G stations and of the connection network.

The energy consumption of final users in the MG can be subdivided in electricity loads $P_L(k,t)$ and thermal loads $Q_L(h,t)$. It is assumed that in MG framework, the users are connected to the same electric distribution system, that is mainly realized by means of radial schemes covering distances of few hundred meters. As discussed in the chapter 1, this configuration yields voltage magnitudes at each node close to nominal value and small angle displacements, therefore no power flow violations are expectable and power losses can be negligible [175][176][180]. Analogously, all thermal loads are considered to refer to a well-designed heat distribution system with negligible losses. Therefore, the satisfaction of the internal demand can be represented by means of following balance relations:

$$\begin{aligned}&\sum_{k=1}^{N_L} P_L(k,t) + \sum_{s=1}^{N_S} P_c(s,t) + \sum_{v=1}^{N_V} P_c(v,t) + P_{Inj}(t) = \\ &= \sum_{i=1}^{N_G} P(i,t) + \sum_{r=1}^{N_R} P(r,t) + \sum_{s=1}^{N_S} P_d(s,t) + \sum_{v=1}^{N_V} P_d(v,t) + P_{Pur}(t)\end{aligned} \tag{3.7}$$

$$\sum_{j=1}^{N_H} Q_L(h,t) \le \sum_{i=1}^{N_G} Q(i,t) + \sum_{r=1}^{N_R} Q(r,t) \tag{3.8}$$

In (3.7), N_L represents the total number of electric loads, N_S is the number of energy storage systems, N_V represents the number of EV fleets, whereas in (3.8) N_H is the number of thermal loads. In both equations, N_G stands for the number of fuel-based generation facilities, and N_R represents the number of RES-based energy production devices.

It should be remarked that the electric power balance is adopted as equality constraint, in order to avoid electricity wasted, whereas thermal balance is expressed by an inequality, allowing the flexibility to release excess heat in the atmosphere, with a view to give up on economic performance of the procedure.

The operation planning aims to minimize an objective function according to appropriate constraints, as per the following expression:

$$\begin{aligned}&\min f(\mathbf{x}) \\ &\text{s.t.} \begin{cases} g(\mathbf{x}) = 0 \\ h(\mathbf{x}) \le 0 \end{cases}\end{aligned} \tag{3.9}$$

The state variable vector **x** includes power production/exchange trends for the controllable sources (fuel-based generators, energy storage, EV fleets, grid connection) over the daily horizon, along with the state of charge of energy storage devices and EVs. The set of equality constraints $g(\mathbf{x}) = 0$ is built by (3.3), (3.4.a), (3.4.e), (3.5.c), (3.6.a), (3.6.e) and (3.7), whereas

inequality constraints $h(\mathbf{x}) \leq 0$ are characterized by (3.1.c), (3.2.c), (3.4.b)-(3.4.d), (3.4.f), (3.5.a)-(3.5.b), (3.6.b)-(3.6.d) and (3.8).

The MG operation planning can include several goals as economic, environmental and technical optimization [207]. In the proposed methodology, a hybrid objective function is adopted, minimizing the total variable costs for MG operation and properly weighed equivalent CO_2 emission cost, in order to achieve feasible planning with limited environmental impact.

The objective function can be expressed as the sum of different terms related to the devices described in the previous section. In particular, actualized investment cost is neglected, along with variable costs for RES-based technologies, since maintenance is quite inexpensive [208], and for ESSs, as the effort for keeping the system in correct operation is already taken into account by the self-discharge amount.

The EV aggregator is in charge to manage the energy exchange of EVs plugged to MG. It is assumed that the EV stations are physically connected to the MG and not directly linked to the distribution network. Moreover, the relationship between EV aggregator and MG operator determines the share of the cost related to EV management, as described in Fig. 3.1.

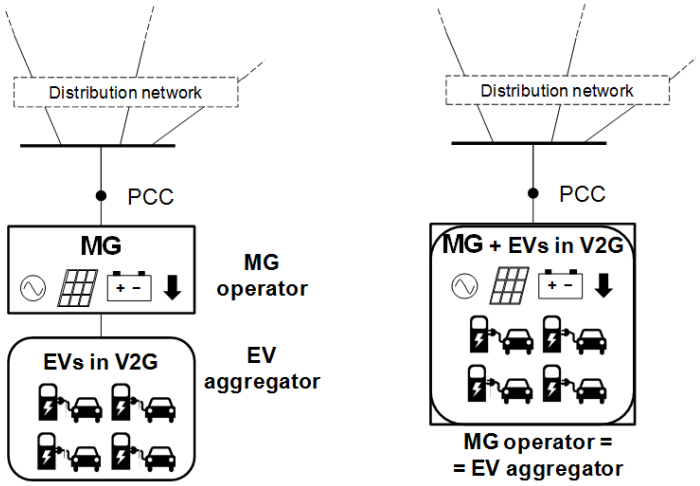

Figure 3.1. Different relations between MG operator and EV aggregator

In particular, two situations are presented and analyzed. In the first case, the EV aggregator is an entity with a specific tariff for the electricity exchange independent respect to MG operator. The MG operator is in charge of exchanging power with the distributor (see left side of Fig. 3.1). This condition can reproduce the presence of an EV management entity at residential premises or for EV parking lot adjacent to a commercial or tertiary activity. Under these

assumptions, the objective function of MG operator in the first case $f_1(\mathbf{x})$ can be defined as follows:

$$f_1(\mathbf{x}) = \sum_{t=1}^{N_t} \Delta t \cdot \left\{ \left[\pi(t) P_{Pur}(t) + \sum_{i=1}^{N_G} \varphi(i) F(i,t) \right] + \sigma \left[\varepsilon_P P_{Pur}(t) + \sum_{i=1}^{N_G} E(i,t) \right] - \beta(t) P_{Inj}(t) + \sum_{v=1}^{N_V} \left[\xi(t) P_c(v,t) - \chi(t) P_d(v,t) \right] \right\} \tag{3.10}$$

where $\pi(t)$ and $\beta(t)$ represent electricity purchase cost and electricity delivery price, respectively, in the *t*-th time step. Moreover, $\xi(t)$ and $\chi(t)$ are the unitary cost for EV charging and the unitary revenue for V2G discharging, respectively. Finally, $\varphi(i)$ is the fuel price for the *i*-th fuel-based generator, σ is the penalty cost applied to the CO_2 emissions and ε_P is the average emission factor related to electricity coming from the distribution network.

In the second case, the role of EV aggregator has become a task of MG operator. Therefore, the EV fleet plugged to V2G technology is considered and managed as a storage. However, the unique managing subject would preserve lifetime of EVs avoiding deep cycling operation, along with supplying energy to the MG and to EVs for covering travel needs, at reasonable cost (see right side of Fig. 3.1). This scheme can be realized by the energy management system of a residential building with EV parking, or in the presence of service vehicles owned by a factory or a public body.

The objective function of MG operator in this second case $f_2(\mathbf{x})$ can be written as:

$$f_2(\mathbf{x}) = \sum_{t=1}^{N_t} \Delta t \cdot \left\{ \left[\pi(t) P_{Pur}(t) + \sum_{i=1}^{N_G} \varphi(i) F(i,t) \right] + \sigma \left[\varepsilon_P P_{Pur}(t) + \sum_{i=1}^{N_G} E(i,t) \right] - \beta(t) P_{Inj}(t) + \sum_{v=1}^{N_V} \omega(v) P_c(v,t) \right\} \tag{3.11}$$

where $\omega(v)$ is the wearing cost of the *v*-th EV fleet, taking into account the actualization of EV battery cost over the forecasted throughput during the provided battery lifetime [154][190][298], obtained as the product of nominal capacity by the provided number of cycles at the target depth of discharge $S^M(v) - S^m(v)$ [210]. Therefore, the wearing cost is determined *a priori*, as an input of the problem, once the technology of EV battery and the desired depth of discharge are defined, and it is applied to the equivalent cycle given by charge power $P_c(v,t)$.

Since both $f_1(\mathbf{x})$ and $f_2(\mathbf{x})$ represent the total daily cost of MG operator with different tariff associated to EV exchange. In $f_1(\mathbf{x})$, the energy flows between MG operator and EV aggregator is ruled by a contract with different rates for EV charge and discharge. In $f_2(\mathbf{x})$, EVs are dealt with just as other internal MG sources, and MG operator aims to minimize the production costs, that for EVs are represented by wearing costs. Each function is therefore minimized in the presence of the same inputs, and relevant results are compared in order to investigate the effectiveness of different relations between MG operator and EV aggregator. Having MG a size of some hundreds of kW, MG operator is not called to actively participate in market sessions and to deal with relevant risk, but it acts as a price taker, in accordance with various analogous approaches [177][204][211]. According to this assumption, $\pi(t)$ and $\beta(t)$ account for a proper forecast of market prices and for additional burdens according to specified tariff schemes.

3.1.3 Test cases and Results

In order to investigate the performance of the proposed procedure along with its possible application, a case study is carried out, based on a test MG reproducing the features of an experimental facility realized at the Power and Energy System Laboratory of Politecnico di Bari (see Chapter 1) with provisional enhancements. Inputs depending on site condition as weather and habits, are referred to forecasts derived from historical data at laboratory location. The test MG includes as generation sources a gas-based Internal Combustion Engine (ICE) in cogeneration mode, a Microturbine (MT) in cogeneration mode, a PV plant, a wind emulator to replicate various wind turbine (WT) response to wind speed. Moreover, an energy storage system and a fast-charging V2G station are provided, and programmable loads can simulate the presence of different consumers as well. A boiler section is envisaged to auxiliary source for thermal demand coverage. The features of the components are reported in the following Tables 3.1, 3.2 and 3.3 for RES devices, energy production and energy storage, respectively, along with the relevant name exploited in the test. The parameters are derived from nameplate data of the devices included in the experimental facility, or obtained by relevant characterization tests, or taken from literature references where indicated. The case study, as the optimal planning procedures reported in previous chapters, includes a daily horizon subdivided in 96 time steps with a duration of 15 minutes. For CHP1 and CHP2, trends of electric efficiency are reported in Fig. 3.2. Thermal efficiencies for CHPs and Boilers are considered constant, since no remarkable variation is observed. Therefore, emission factor is inversely proportional to electric efficiency for CHPs, whereas for boilers it is constant at rated value.

Table 3.1. Test MG – Renewable Based Generator Features

Device name	Device type	Rated electric power [kW]
PV 1	Mono-crystalline silicon	20
PV 2	Poly-crystalline silicon	20
PV 3	Amorphous thin film PV	20
WT 1	Horizontal axis WT	40
WT 2	Vertical axis WT	20

Table 3.2. Test MG – Energy Production Devices Features

Device name	Device type	Rated electric/ thermal power [kW]	Rated electric/ thermal efficiency [%]	Rated emission factor [kg/kWh]
CHP 1	ICE	105 / 185	31.5 / 56	0.594
CHP 2	MT	28 / 57	25 / 50	0.725
HB 1	Wood boiler	--- / 75	--- / 82.5	0.02
HB 2	Pellet boiler	--- / 20	--- / 88.2	0.00
Grid	Power exchange	80 / ---	---	0.309 [212]

Table 3.3. Test MG – Energy Storage device features

Device name	Device type	Rated capacity [kWh]	Rated electric power [kW]	Charge/ discharge efficiency [%]	Self-discharge rate [%/h]
ESS	Na-Ni battery	180	48	85	1.36
EVs	10-EV fleet with 10 V2G stations	240	100	90.9 [213]	---

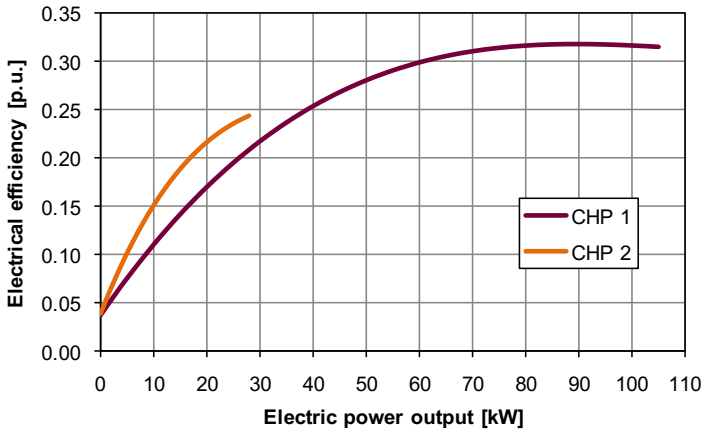

Figure 3.2. Electrical efficiency curve of the CHPs.

The case study is applied to a typical winter day with residential and commercial load supplied by the MG. Power and heat demand curves for users are taken from U.S. data in [214] and accounting for similar climate conditions with respect to the location of the experimental facility. User features are reported in Table 3.4.

The total predicted RES production amounts to 334.4 kWh with a wind contribution higher than PV yield. This quantity covers 14.7% of the residential load and 19.3% of the commercial one, of the set day.

Table 3.4. Test MG – User features

User Description	Electric / thermal peak power [kW]	Electric / thermal daily demand [kWh]
Residential 50 twin apartments	160 / 250	2,278.5 / 3,911.5
Commercial Medium-size office	140 / 250	1,731.5 / 2,167.3

In order to best exploit the potential of MG components and not to jeopardize the security of system in emergency cases, as involuntary islanding, the maximum flow of electric power with the distribution network is limited at 80 kW.

In Figure 3.3 the EV fleet connection to the V2G charging station is characterized by time intervals depending on dwellers and employees behaviour for residential and commercial building, respectively, with a number of V2G charging stations equals to 10. In particular, in the residential case (upper part of Fig. 3.3), parking interval starts at 6:45 p.m. at 60% charge (red) and ends at 8 a.m. at 80% (green), therefore two intervals are included in simulation, as described in previous paragraph, involving the continuity of energy content variation at extremes of the day (blue). Whereas, for the office building (lower part of Fig. 3.3), clerks arrive

at workplace at 8 a.m. with 40% charge (red) and leave at 6:30 p.m. at 80% (green), with a single parking interval.

The energy content of the EVs departing is supposed at 80% of rated capacity, to decrease the effects of range anxiety [215]. The state of charge at fleet arrival is provided according to average routes of the EV drivers. The choice of the variation range of state of charge between 20% and 90% helps extending EVs lifetime preventing full charge and deep discharge [188][216][217].

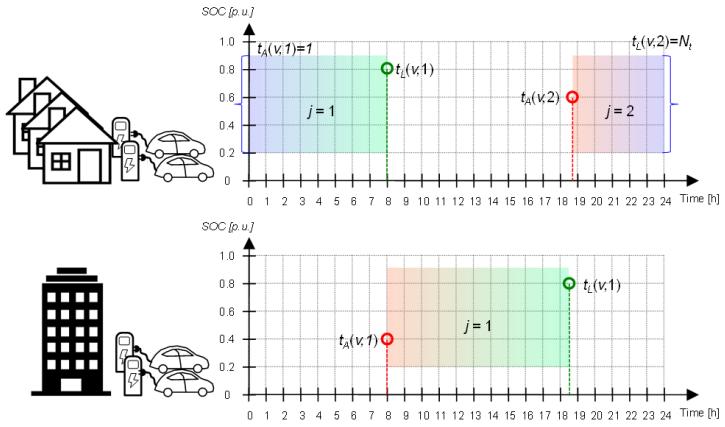

Figure 3.3. EV fleet characterization for the considered users.

The electricity purchase price $\pi(t)$ is determined as sum of hourly spot market prices and additional burdens to cover transport and distribution service included in tariffs for domestic and non-domestic users, whereas electricity delivery cost $\beta(t)$ is characterized by three levels for peak, average and off-peak hours respectively, according to Italian energy service operator [57]. Fuel cost $\varphi(i)$ derives from tariffs of an Italian fuel distribution company [60] and are equal to 0.51 €/Sm^3 for gas, 0.172 €/kg for wood, 0.32 €/kg for pellet, supposed constant over the whole day. Moreover, emission cost σ is equal to 0.57 c€/kg [61].

The two formulations of the objective function of the day-ahead scheduling problem, as defined in the previous sub-section, are both applied to the two user profiles. In particular, while considering $f_1(\mathbf{x})$, different tariff schemes are analysed, and the best solution is obtained with a flat EV discharge cost $\chi(t)$ equal to 18 c€/kW and with an EV charge price $\xi(t)$ having two levels for residential user and a constant value for the commercial one. Cost trends are reported in Fig. 3.4, indicating with subscribed *res* and *com* the costs for residential commercial users, respectively. When $f_2(\mathbf{x})$ is minimized, EV wearing cost $\omega(v)$ is equal to 5 c€/kWh.

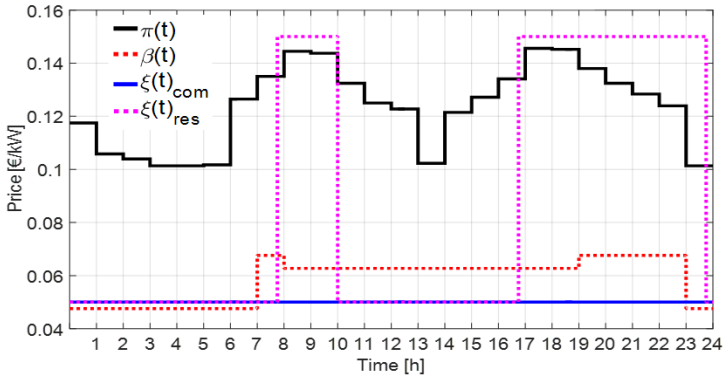

Figure 3.4. Cost diagram for each time step.

The optimization is performed in MatLAB® environment, exploiting *fmincon* function by means of the SQP algorithm [65]. It is a Newton-type method, characterized by super-linear convergence, and proved robust for the solution of nonlinear optimization problems, even in non-convex formulations [219][220].

SQP algorithm solves a sequence of optimization sub-problems, characterized by a quadratic model of the main problem. The basis of the algorithm consists of the calculation of Lagrangian function $L(\mathbf{x})$ related to problem (9), defined as follows:

$$L(\mathbf{x}) = f(\mathbf{x}) + \sum_{w} \lambda_w \cdot g_w(\mathbf{x}) + \sum_{b} \mu_b \cdot h_b(\mathbf{x}) \tag{3.12}$$

where w is the generic equality constraint and λ_w is the correspondent Lagrangian multiplier, whereas b is the generic inequality constraint and μ_b is the correspondent Lagrangian multiplier. It is assumed that bound constraints are expressed as inequality constraints. Therefore, Karush-Kuhn-Tucker (KKT) conditions are posed and approximated by means of second-term truncated Taylor series, thus obtaining, for the κ-th iteration, the following quadratic subproblem:

$$\min_{\mathbf{d}} \nabla f\left(\mathbf{x}^{\kappa}\right)^{T} \cdot \mathbf{d}^{\kappa} + \frac{1}{2}\mathbf{d}^{\kappa} \cdot \mathbf{H}^{\kappa} \cdot \mathbf{d}^{\kappa}$$
$$\text{s.t.} \begin{cases} \nabla g_w\left(\mathbf{x}^{\kappa}\right)^{T} \cdot \mathbf{d}^{\kappa} + g_w\left(\mathbf{x}^{\kappa}\right) = 0 \\ \nabla h_b\left(\mathbf{x}^{\kappa}\right)^{T} \cdot \mathbf{d}^{\kappa} + h_b\left(\mathbf{x}^{\kappa}\right) \le 0 \end{cases} \tag{3.13}$$

where $\mathbf{H}^{\kappa} = \nabla^2_{\mathbf{x}} L\left(\mathbf{x}^{\kappa}, \boldsymbol{\lambda}^{\kappa}, \boldsymbol{\mu}^{\kappa}\right)$ is the Hessian matrix of KKT conditions at the κ-th iteration and $\mathbf{d}^{\kappa}$ is the solution search direction. For each iteration, the algorithm updates the Hessian matrix through an approximate gradient evaluation method, therefore solves the quadratic subproblem

(3.14), that can be modified in order to account for feasibility limits (for instance by means of a quadratic approximation of constraints instead of linear) and updates the solution as follows:

$$\mathbf{x}^{\kappa+1} = \mathbf{x}^{\kappa} + \alpha^{\kappa} \cdot \mathbf{d}^{\kappa} \tag{3.14}$$

where α^{κ} is the step-length parameter, determined in order to decrease a merit function, with larger penalty contribution of active constraints.

The relative tolerance levels on decision variables, constraints and objective function are all set to $1 \cdot 10^{-4}$.

As most of the methods for nonlinear problem solution, the algorithm efficiently searches for a local minimum, therefore a proper initial condition is provided [221].This is done through the solution of the linearized formulation of problem (3.9), by accounting for rated efficiencies of fuel-based devices (see Table 3.2) in (3.1.a), (3.1.b), (3.2.a), (3.2.b) and (3.3), and discarding non-contemporaneity constraints for bidirectional power exchanges (3.4.e), (3.5.c), (3.6.e). These constraints are verified *a posteriori*, and where they are not satisfied, the solution is corrected by subtracting to both values the minimum one. The proposed procedure to solve the non-linear problem (3.9) is managed automatically in all its parts, as explicated in the flowchart reported in Fig. 3.5, where the stages of initial solution determination (through the linearized problem) and of solution of complete NLP problem (3.9) are illustrated.

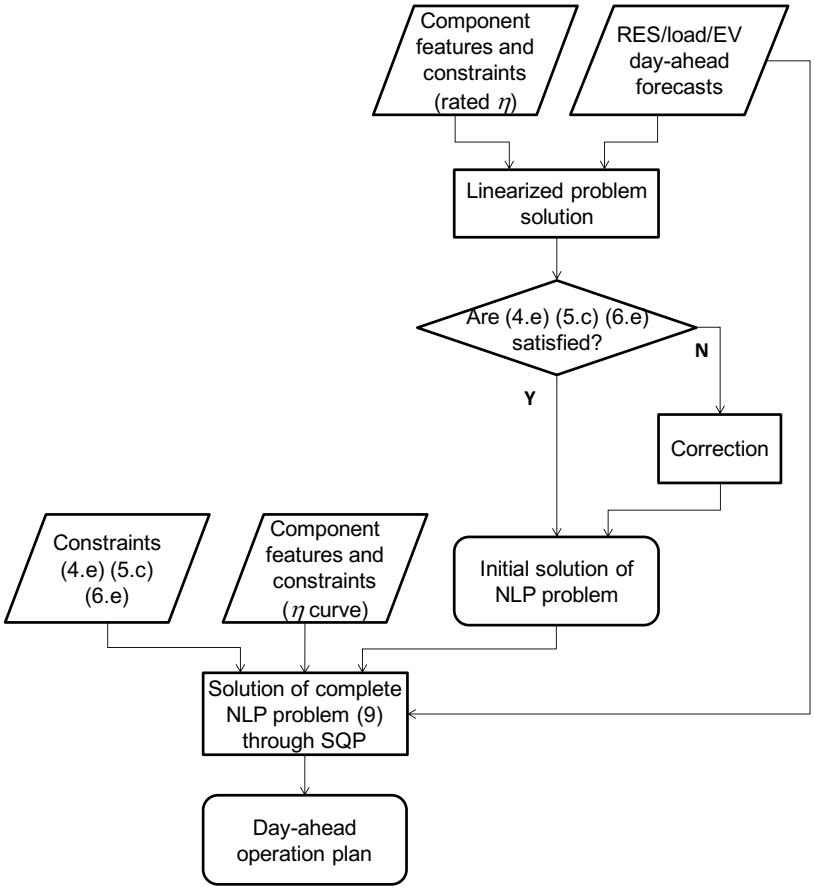

Figure 3.5. Solution flowchart of the proposed day-ahead procedure.

The results of optimal operation planning of the test MG in the presence of the described residential load are presented.

As the results of $f_1(\mathbf{x})$, in Figs 3.6.a, 3.7.a and 3.8.a, where electric balance, thermal balance and SOC of storage devices are shown, respectively. In Fig. 3.8.a, positive values of power by ESS and EVs correspond to discharge power, whereas negative values stand for charge power. As regards grid power, positive values represent power purchase and negative ones correspond to delivery. It can be seen that the EV discharge guarantees the coverage of the electric load in periods when production by RES is low, for instance between hours 3.19 and 3.22, as remarked by the SOC trend of EVs in Fig. 3.8.a. Moreover, the excess power production by CHPs with respect to the original load trend, along with grid withdrawal, is addressed at charging ESS and EVs. In particular, ESS is charged in central hours of the day, in the presence of remarkable RES production. EVs are charged in late evening and early morning, when electricity purchase price is lower and thermal demand drives CHP extra production. Due to low delivery price, no power injection to the main network is observed.

Whereas, the application to residential user of $f_2(\mathbf{x})$ objective leads to results depicted in Figs 3.6.b, 3.7.b and 3.8.b. In this case, the EV SOC experiences less fluctuations, keeping constant for most of the parking interval. This is ascribable to the presence of the wearing cost, that prevents V2G to occur. EV charge is observed only in early morning, when thermal load trend involves an excess of electricity production by CHP1 with respect to the demand. The ESS is more deeply employed in the presence of EV wearing cost due to lack of EV discharge.

As regards thermal energy, the demand is covered mostly by CHP1 in both cases (see Fig. 3.7.a and 3.7.b), respecting the technical limits, whereas the CHP2 and HBs are exploited during peak demand periods.

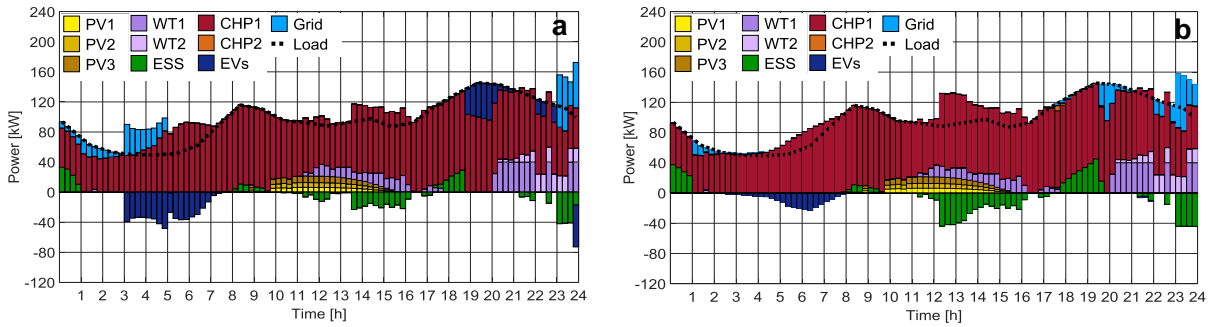

Figure 3.6. Electric power balance of Residential user with $f_1(\mathbf{x})$ objective (a) and $f_2(\mathbf{x})$ objective (b).

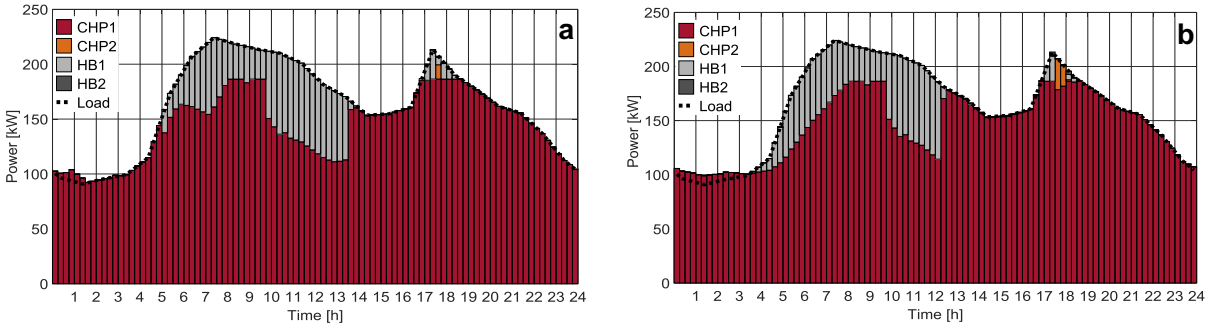

Figure 3.7. Thermal power balance of Residential user with $f_1(\mathbf{x})$ objective (a) and $f_2(\mathbf{x})$ objective (b).

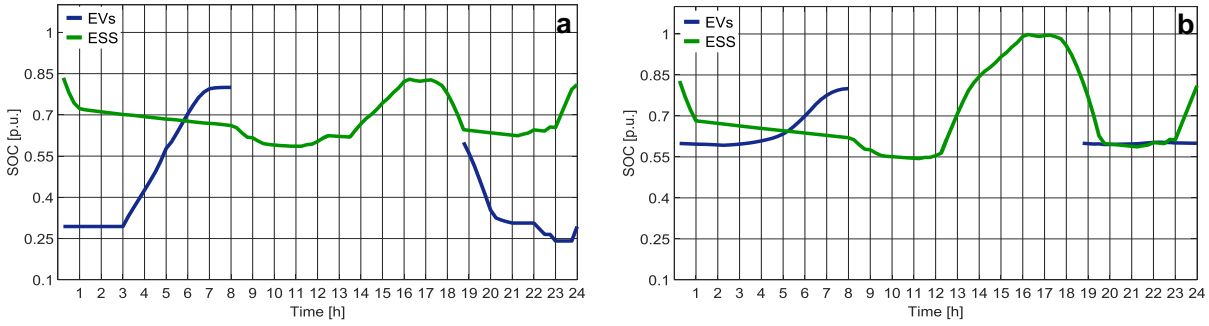

Figure 3.8. Storage state-of-charge of Residential user with $f_1(\mathbf{x})$ objective (a) and $f_2(\mathbf{x})$ objective (b).

The optimal MG operation plan in the presence of commercial load is illustrated in Figs. 3.9.a, 3.10.a and 3.11.a in the case of $f_1(\mathbf{x})$ objective, and in Figs. 3.9.b, 3.10.b and 3.11.b in the case

of $f_2(\mathbf{x})$ minimization. It can be noted that the different load profiles of this user involve a different exploitation of internal sources. In particular, in the first and last hours of the day, when heat is not needed, the CHPs are not fired on, since it reveals more convenient to purchase energy from the grid at low price levels rather than exploiting CHP at partial load, with low efficiency. The pursuit of $f_1(\mathbf{x})$ objective implies a deeper EV employment due to the difference of price levels. In particular, EVs are intensively charged at arrival, in central hours of the day and at the end of parking time, even withdrawing additional electricity from the grid. This trend is supported by the ESS as well, in fact ESS discharges in periods when EVs require to charge and vice versa, as shown in Fig. 3.11.a. However, the described curves entail a peak of total demand up to 210 kW, almost doubling the predicted load. As regards thermal load (Fig. 10.a), according to economic and environmental merit order, the baseload is covered by the CHP1, and HBs and CHP2 are called to produce in peak periods. When the demand is low, CHP1 is less convenient than HB1.

When $f_2(\mathbf{x})$ is minimized, EVs charge only in central hours of the day, as reported in Fig. 3.9.b. Indeed, the saddle in thermal demand (Fig. 3.10.b) does not allow for intense CHP exploitation, therefore further grid withdrawal is necessary for EV charging in low-price periods. This involves a deeper discharge of ESS during hours 8-11 to cover the demand in peak price period. In all cases, self-discharge effect of ESS in idle state is observed.

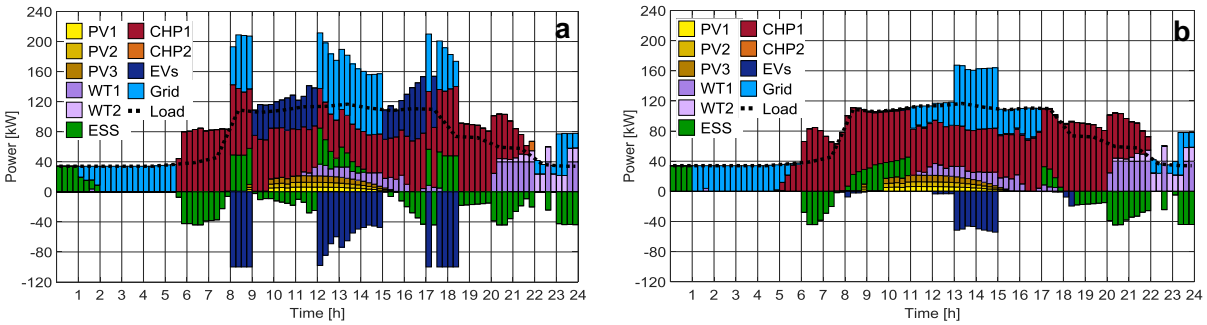

Figure 3.9. Electric power balance of Commercial user with $f_1(\mathbf{x})$ objective (a) and $f_2(\mathbf{x})$ objective (b).

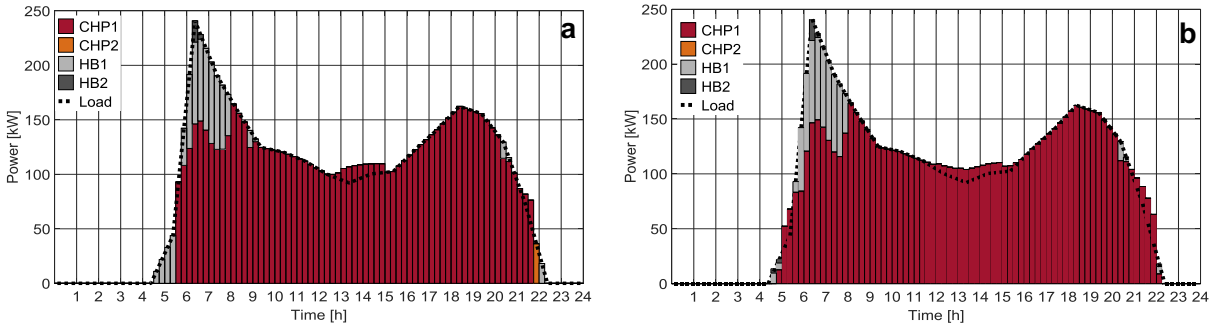

Figure 3.10. Thermal power balance of Commercial user with $f_1(\mathbf{x})$ objective (a) and $f_2(\mathbf{x})$ objective (b).

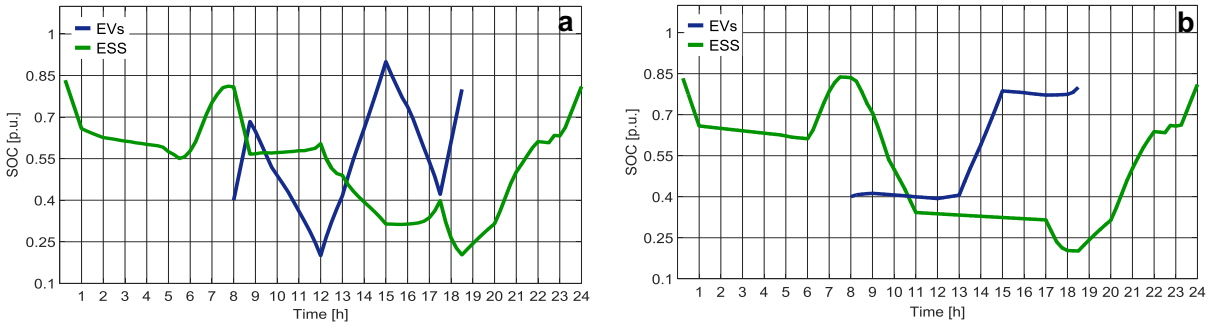

Figure 3.11. Storage state-of-charge of Commercial user with $f_1(\mathbf{x})$ objective (a) and $f_2(\mathbf{x})$ objective (b).

It can be seen that the adoption of realistic electric efficiency curve, that has remarkably low values at low production levels, avoids operation of CHPs below the minimum stable generation level in all cases. In this way, analogous results are obtained with respect to other approaches introducing integer on/off variables.

The comparison of total daily costs and relevant main contributions is reported in Table 3.5. It allows to state that the $f_1(\mathbf{x})$ objective reveals cheaper than the $f_2(\mathbf{x})$ for both users (3% in residential case and 7% in commercial case), revealing that an *ad hoc* tariff scheme applied by the aggregator for EV charge and discharge can encourage their use for MG optimal operation purposes. Grid purchase has a higher impact for the commercial user (18-24% with respect to 3-4% for the residential one), due to the different demand trend, whereas emission costs do not affect significantly the total expenses, contributing in each case to less than 2%.

Table 3.5. Test MG – Daily Cost contributions [€]

	Residential		**Commercial**	
	$f_1(\mathbf{x})$	$f_2(\mathbf{x})$	$f_1(\mathbf{x})$	$f_2(\mathbf{x})$
Grid purchase cost	15.0	13.6	63.1	52.5
Grid delivery revenue	0.0	0.0	0.1	0.0
Fuels cost	376.4	379.6	214.6	218.6
EV charging cost	7.4	2.8	18.0	5.7
EV discharging revenue	14.1	0.0	37.8	0.0
Grid emission cost	0.3	0.2	0.9	0.8
Generators emission cost	6.6	6.7	3.7	3.7
Total cost	**391.6**	**402.9**	**262.5**	**281.3**

Computational efforts obtained by running the procedure on a 64-bit workstation equipped with 3.50 GHz processor and 16 MB RAM and exploiting virtual parallel calculus on 4 processors are synthetically compared in Table 3.6. It can be seen that the problem solution takes from 3 min to 22 min to reach an optimal solution where error levels are below selected thresholds, and this time is well compatible with day-ahead programming horizon. The solution involves

heavier computations (either number of iterations or computation time) in the presence of $f_1(\mathbf{x})$ objective, due to the involvement of conflicting terms in the objective function, see positive and negative cost contribution due to EV charge and discharge, respectively, in (3.10). The determination of initial solution is quite fast and does not affect remarkably the total solution time.

3.1.4 Conclusions

In this sub-section, strategies for optimal day-ahead operation planning of MG integrating V2G-based EV fleets have been proposed. The procedure, involving electric and thermal load coverage, has been tested on a selected MG configuration, where typical load profiles of residential and commercial users have been considered. The presence of different goals, according to various interaction frameworks between EV aggregator and MG operator, have yielded different operation plans, with particular regard to EV exploitation. Indeed, the presence of suitable cost schemes for EV charge and discharge, in the presence of EV aggregator relating with MG operator, have led to a deeper EV exploitation and a more efficient operation of MG resources, achieving lower total MG cost. Whereas, wearing cost drives the preservation of EVs lifetime, preventing their depletion and providing a service only by defining optimal charging intervals. V2G behaviour has allowed the coverage of demand peaks, and can be efficiently utilized when high electricity price occurs. Moreover, the presence of CHPs and ESS has brought to reduce the need of electricity purchase from the external grid to charge EVs. The proposed methodology has proved powerful to deal with the operation planning problem in a suitable time for day-ahead horizon.

3.2 Energy Efficiency Improvements in Port Areas: towards an Integrated Energy Management

In this sub-section, different measures for the improvement of energy performance of port areas are illustrated, and a set of suitable initiatives is considered for the port area of Bari, evaluating their impact on energy, environmental and economic point of view. These measures are aimed to be integrated into the energy and environment plan of the port, as required by recent enhancement of Italian legislation, and eventually supervised and controlled by a future port energy management system. The presence of intense human activities in port areas raise the necessity to frame the management of energy in port in an integrated outline. In view of the realization of the energy development plan for the port area of Bari, the aim of this paper is to provide an overview of the candidate proposals to improve the energy and environmental performance of the port. Results of studies and analysis carried out for the evaluation of initiatives are presented.

3.2.1 Introduction

The structure of ports usually includes several activities of different nature, and, depending on the specific situation, a prevalence of industrial settlements (e.g. shipyards) or commercial services (e.g. passenger management and port employees) or logistics (e.g. cargo handling) can be present [222]. In any case, high energy demand can be observed in port areas, under the responsibility of different entities [223]. Moreover, the usual proximity of ports to city context involves several issues, such as the interaction of urban traffic with movement of passengers and goods, the presence of concentrated emission and noise sources. Therefore, the need of monitoring environmental issues of ports has gained significant importance. In particular, European Sea Ports Organisation has carried out periodical surveys on port environmental concerns, and results show the main attention to air quality and the rapidly increasing growth of the importance of energy efficiency [224][225]. In this sense, the Port Authorities are called to adopt proper actions to reduce environmental impact, such as exemplifying through good practices, enabling infrastructural conditions, engaging the different subject present in port areas, placing incentives for a correct energy behaviour [226]. These actions should therefore be integrated in an environment-energy development plan, carried out by port authorities by means of suitable methodologies in order to address the pillars of resilience, availability, reliability, efficiency and sustainability [223][226]. Suitable technical measures depend on port specific features, involving onshore power supply to ships at berth [227][228], integration of renewable energy production [229] and of LNG onshore generation [230], and the use of

alternative means of transports [231][232]. Moreover, an environment-energy management framework should be envisaged, where the initiatives can be harmonized in order to increase their potential benefits [231].

The port of Bari is of remarkable importance in trans-european transport network, as it represents the western terminal of European Corridor 8 for the connection between Southern Europe and Balkan zone. The port area, as depicted in Fig. 3.12, is placed in the north-western part of the seashore of the city of Bari, almost in continuity with the historical center.

Figure 3.12. Depiction of Bari port area

The port includes five main basins, and is equipped with 27 mooring places, for a total of 5750 m of docks and quays, with sea depths up to 13 m, as well as 740000 m^2 of service areas and warehouses. It has two main entrances, well connected to the city center for customers and passengers mobility and to urban motorways.

The port of Bari has a multi-purpose organization, involving several activities in the field of ro-ro connections, of cargo shipping and agricultural goods management, of cruising for routes throughout the Mediterranean sea, of little shipyards and of private yachting. The Bari Port Authority, a public entity, operates all port infrastructures and one of its goals is the setup of an energy-environmental plan.

3.2.2 Proposals and early results

The feasibility analysis of the proposed interventions is carried out by considering the assumptions reported in Table 3.6.

Table 3.6. Project feasibility common assumptions

Lifetime duration	20 years
Discount rate	5%
Investment mortgage period	10 years
Taxation of net revenues	31.4%

Moreover, Net Present Value (NPV) of initiatives developing over N_y years with discount rate α is determined through the following relation:

$$NPV = -I_0 + \sum_{y=1}^{N_y} \frac{R_V(y) - C_V(y)}{(1+\alpha)^y} \tag{3.15}$$

where I_0 represents the initial investment, whereas $R_V(y)$ and $C_V(y)$ are the revenues and costs obtained during operation at year *y*, and their difference represents the yearly cash flow. Moreover, the levelized cost of energy production is determined as follows:

$$LCOE = \frac{I_0 + A_f \cdot C_V^m}{N_y \cdot E^m} \tag{3.16}$$

where C_V^m represent the yearly average variable cost, E^m is the yearly average energy yield of the initiative, and A_f is the annuity factor, determined as follows:

$$A_f = \frac{1}{\alpha} \cdot \left[1 - (1+\alpha)^{-N_y}\right] \tag{3.17}$$

Moreover, Internal Rate of Return (IRR) is determined as the discount rate able to make NPV zero at the end of time horizon, and Pay-Back Period (PBP) is the number of years at which the actual NPV is null.

In some cases, the profitability of the investment is not determined by a positive NPV, but considering a positive difference between NPV in the considered scenario with the NPV in the reference case.

3.2.2.1 Renewable energy production

A first intervention is devoted to the installation of photovoltaic (PV) systems on suitable oriented and low-shadowed roofs of buildings pertaining to port authority. In particular, three main locations, dedicated to ro-ro passengers and ticketing, cruise terminal and auxiliary activities, are taken into account for possible installation. From preliminary analysis, for a total available roof surface of 3000 m^2 is individuated, as depicted in Fig. 3.13.

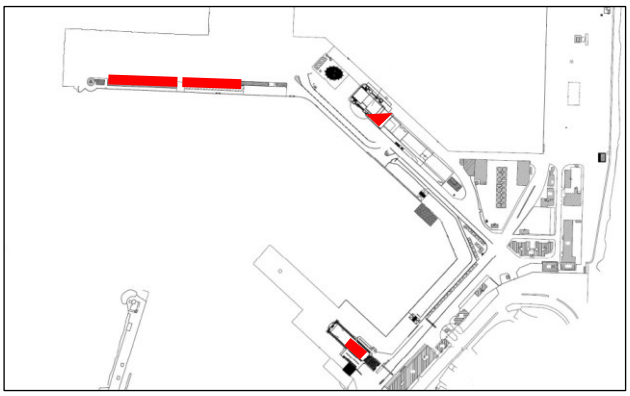

Figure 3.13. Position of available surfaces for PV installations

Due to different orientation of buildings, a total PV surface of 1834 m^2 is exploited by installing 318 kW of monocrystalline PV panels, properly organized in sub-fields with separate inverters. The total estimated power production amounts to 560.5 MWh/year by means of normalized data [233]. The total investment of the PV system amounts to 640 k€. It should be remarked that power and energy yield of each PV section is not exceeding building power demand, therefore not affecting the capability of the current internal electric network. The techno-economic feasibility analysis, developed according to current grid parity condition of PV systems in Italy, is synthesized in Table 3.7, considering that half of energy production is exploited for self-consumption. It can be seen that the intervention results profitable over lifetime horizon.

Table 3.7. PV System Investment Analysis

Investment Cost	640.0 k€
Yearly Fixed O&M	4.6 k€
Yearly revenues energy sold	10.9 k€
Yearly revenues self-consumption	47.9 k€
NPV	36.4 k€
IRR	5.66%
PBP	18.3 years
LCOE	62.20 €/MWh

Moreover, the exploitation of perimeter piers for the installation of mini-wind turbines is investigated. In particular, 20-kW vertical axis turbines are considered, in order to determine turbine placement on piers aiming not to hamper the activities of ships. The wind distribution of coastal area of Bari, including port, is analyzed over 1 year of observations, resulting in the average power distribution reported in Fig.3.14. The relevant Weibull distribution is derived, with shape and scale coefficients equal to 5.642 and 2.0, respectively, as shown in Fig. 3.15 along with wind turbine power curve. It can be seen that the main wind directions are included

between N and W and do not coincide with pier orientation, therefore turbine alignment on piers is viable with limited wake losses.

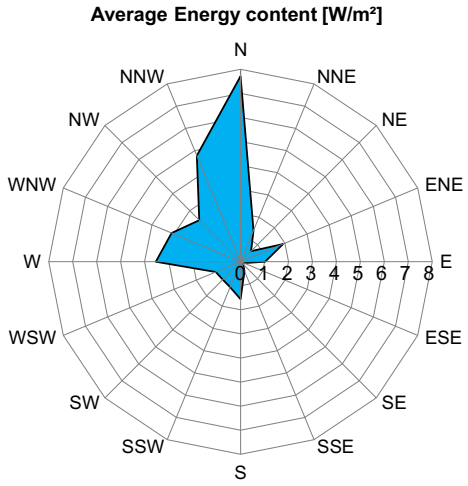

Figure 3.14. Energy content analysis of wind data according to direction.

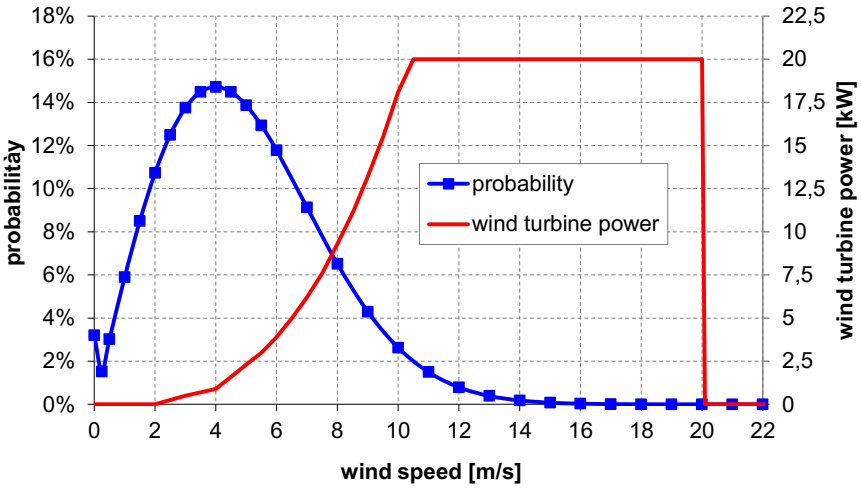

Figure 3.15. Wind Weibull distribution and wind turbine power.

In the total port area, 43 wind turbines are envisaged, with a total installed power of 860 kW. The internal network is planned with LV subfields and MV collection points, sketched in Fig. 3.16, covering a total distance of 5.2 km with LV cables and 2.2 km with MV cables. Network analysis are carried out, highlighting 1.2÷1.3% of active power losses during operation, therefore provisional energy yield of 1380.7 MWh/year is estimated. Preliminary investigations reveal that the current electric network of port area is able to host the connection of the mini-wind system without considerable empowering. The total investment cost amounts to 2026.9 k€. The feasibility analysis according to current feed-in tariff for mini wind systems in Italy

[234] is synthesized in Table III, considering 10% of self-consumption. Since the economic indicators are positive, the investment turns out to be feasible.

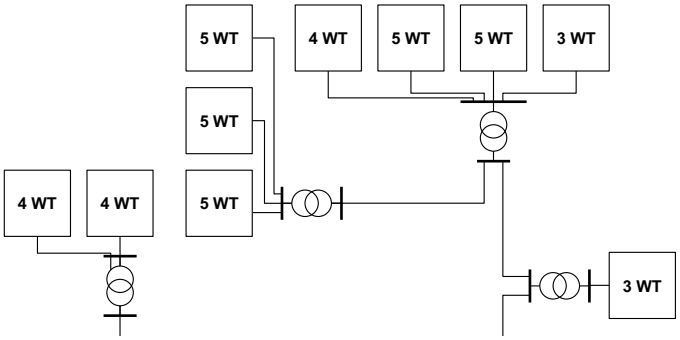

Figure 3.16. Wind turbine system: internal network

Table 3.8. Wind Turbine System Investment Analysis

Investment Cost	2026.9 k€
Yearly Fixed O&M	13.8 k€
Yearly revenues feed-in tariff	158.3 k€
Yearly revenues self-consumption	42.8 k€
NPV	307.0 k€
IRR	6.73%
PBP	16.2 years
Production cost	79.64 €/MWh

3.2.2.2 Electric mobility

As a first solution, the opportunity to implement a charging infrastructure for a small fleet of electric buses for transport of customers and operators to/from the port area is investigated. In particular, buses are meant to travel on three routes: port/railway station, port/airport and a connection of different activities inside port area. The main features of the routes are reported in Table 3.9. The price of ticket for each trip is analogous to similar public transport services within the city and for direct connection with the airport.

Table 3.10. Features of port bus routes

Route	Round-trip Length [km]	Daily trips	Price per trip [€]
Railway station	8	25	1.60
Airport	25	12	5.00
Internal	6	30	1.20

For covering the provided trips, a fleet of 7 electric buses is envisaged (6 buses will be en route per day), whose main features are reported in Table 3.10 and compared with conventional fuel-based analogous model. Suitable parking area of buses is individuated in the western part of the port, where a large parking area for trucks and ticket offices is situated. In this zone, the installation 6 of public pole charging points is provided, with a maximum power of 22 kW and Type 2 sockets, allowing for full recharge in roughly 6 hours. A cost of 10 k€ per charging point, including electric connections with existing network, is considered. Different number of passengers per route is envisaged, as reported in Table 3.11. according to the fact that electric mobility could be fostered through proper promotional campaign.

Table 3.10. Features of bus model

		Electric	Traditional
Max passengers		35	35
Price [k€]		400	90
Battery capacity		180 Ah	---
Max route		125 km	250 km
Consumption		1.18 km/kWh	3 km/lit
Cost of energy		0.4 €/kWh 0.16-0.19 €/kWh	1.65 €/lit
Maintenance cost [€/y]	Base	1000	600
	Increase	1300	800

Table 3.11. Number of passengers per route

Route	Electric			Traditional		
	min	base	max	min	base	max
Railway station (one-way)	8	12	20	7	10	18
Airport (one-way)	6	10	18	5	8	15
Internal (round-trip)	12	20	30	10	15	25

Investment evaluation over period of 10 years is reported in Fig. 3.17 where NPV trends are shown for conventional and electric solutions, according to different number of passengers reported in Table 3.11, and considering driver salaries as costs. It can be seen that the initiative could not be feasible in the case of minimum number of passengers, whereas it is profitable with base and maximum exploitation, notwithstanding higher investment.

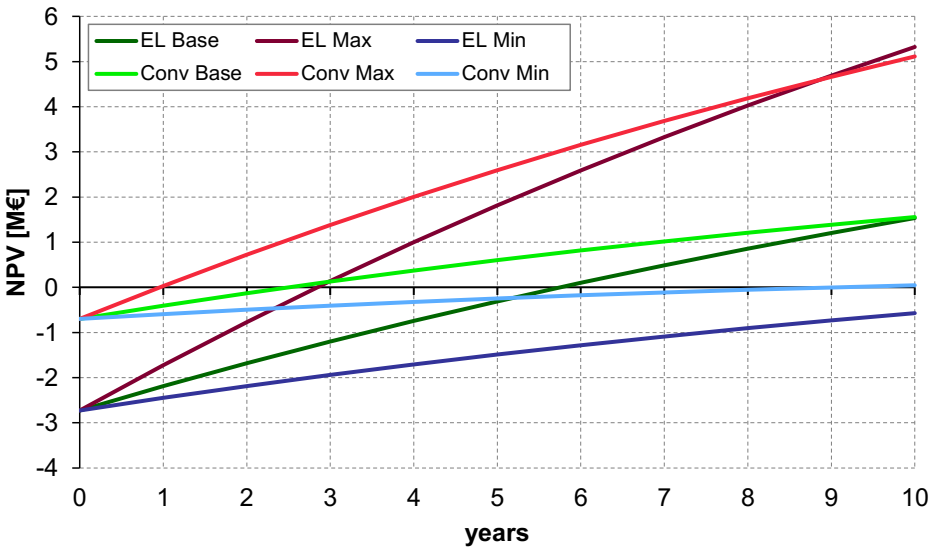

Figure 3.17. Investment analysis of electric buses.

3.2.2.3 Cleaner energy supply to ships

Further studies are carried out in the field of onshore power supply (OPS), encouraged by the presence of a new HV/MV substation at the boundary of port area. The structure of system is reported in Fig. 3.18 . It includes the equipment of two docks for OPS, that can supply indifferently and independently ships with 50 Hz or 60 Hz onboard system thanks to the interlocks of the conversion switchboard.

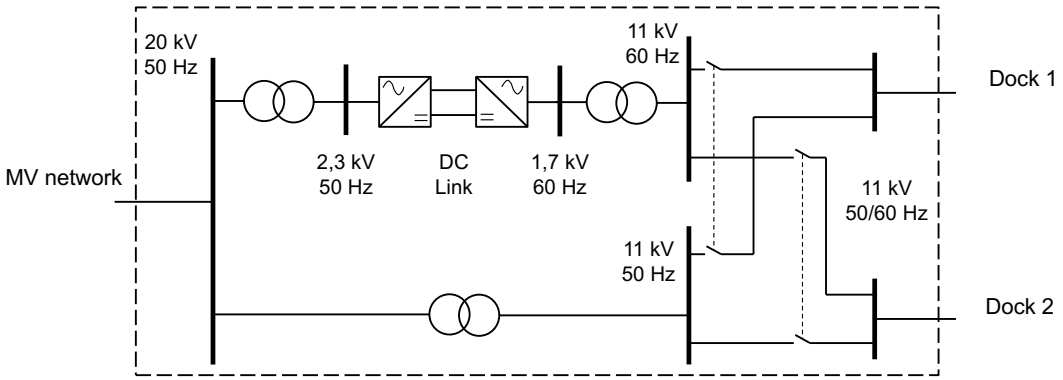

Figure 3.18. Scheme of the conceived onshore power supply system.

The system has been designed for ships with power demand up to 1.7 MW when stationing at berth, that has been derived from studies on ro-ro vessels interesting Bari port. The total investment, including the MV network connection, cable handling solutions and upgrade of shipboard power system for two vessels according to proper safety issues, amounts to roughly 4.2 M€, i.e. 1.2 M€/MW. Moreover, power flow analysis and short circuit studies are carried

out by means of PSAT® [237] on different configurations, reported in Fig. 3.19. In particular, the case of two 50-Hz ships, (1), of two 60-Hz ships (2) and of two ship at different frequency (3) are analyzed. Results of this preliminary analysis, reported in Table 3.12, allow to compare the performance of the supply system in the various conditions and to individuate proper control actions to be implemented by the supervisory and control apparatus of the OPS system. For instance, reactive power losses should be controlled and compensated in order to reduce possible penalties, particularly in Case 3. Moreover due to the operation of MV network with isolated or compensated neutral, minimum short-circuit current is remarkably low, and proper ground protection relays should be adopted.

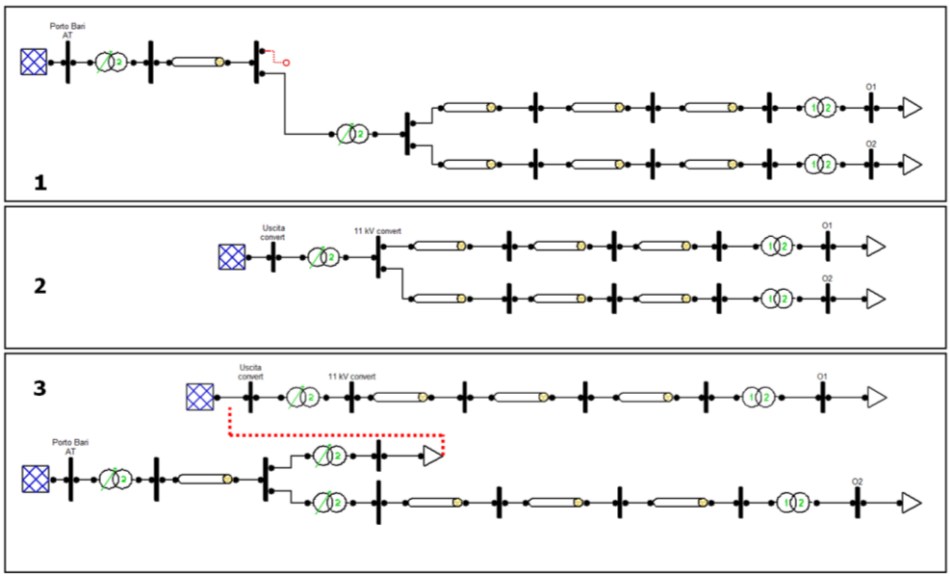

Figure 3.19. Power flow and short circuit cases in PSAT®.

Table 3.12. Power Flow and Short Circuit analysis of OPS

	Minimum voltage at ship [p.u.]	Active Losses [MW]	Reactive losses [MVAr]	Max Short-circuit Current [kA]	Min Short-circuit Current [A]
Case 1	0.925	0.5	21.5	3.42	0.16
Case 2	0.947	0.5	24.3	1.16	0.19
Case 3	0.939	0.5	30.0	3.42	0.16

As regards electric tariffs, under the current conditions of Italian regulating authority, OPS supply would be paid at 0.176 €/kWh. Whereas, by considering the efficiency of onboard auxiliary diesel engines exploited in port and relevant fuel cost, the current energy production of ships at berth costs roughly 0.162 €/kWh. Therefore, in order to encourage OPS solution, and to leave the margin for revenues to intermediate power supply societies, the need to define

special tariff conditions or emission penalty tax arises. Indeed, an evaluation of environmental performances is carried out, by comparing ship engine emissions with average emissions of electric power production in Italy [238]. Results are reported in Table 3.13, where the advantage of OPS clearly spouts, with a unitary reduction of 7.0% for CO2 and ranging from 74% to 98% for other pollutants.

Table 3.13. Emission comparison of OPS

	Ship engine		OPS		
Pollutant agent	Unitary emission rate [g/kWh]	Yearly emissions [t]	Unitary emission rate [g/kWh]	Yearly emissions [t]	Yearly emission savings [t]
CO2	422.8	2778.0	393.10	2582.7	195.3
SOx	0.259	1.7	0.066	0.43	1.27
NOx	9.741	64.0	0.112	0.83	63.27
PM	0.143	0.94	0.003	0.02	0.92

Currently, further studies are being carried out in order to evaluate the economic and environmental performances of LNG utilization of moored ships

3.2.3 Vision for port energy development

The described projects are part of a broader strategy aimed at defining the energy system of the port area. The final goal is to operate the whole port as an intelligent microgrid, with a proper control system, able to allocate resources for covering energy needs of different subjects acting in the port area and to interact efficiently with distribution networks of electric energy and other services (gas, water, …). To this purpose, the rearrangement of the internal MV electric network [231] will be investigated, in order to interconnect the electrical power system of the port area to the external distributor through a single connection point, preferably by exploiting the new HV/MV substation. Moreover, a deeper analysis on electric and thermal load demand will be carried out, in order to obtain load profiles useful for the adoption and the evaluation of net metering with the integration of local renewable energy sources. Further investigation on energy efficiency improvement of final users, with particular care on lighting systems and thermal performances of buildings will be provided. The possibility of equipping the port area with combined heat and power production system or even with tri-generation devices will be carefully analyzed. All these studies will therefore be compared on technical and economic viewpoints, and the most feasible, suitable or profitable interventions will be eventually considered in the operation planning and management procedures of the integrated energy system.

3.3 Electric Vehicle Supply Infrastructure in Port Areas

In this sub-section, the concept of Electric Vehicle Supply Infrastructure (EVSI) is introduced, as an integrated microgrid including photovoltaic, energy storage and charging stations, to feed a fleet of plugin electric vehicles (PEVs). The connection points for PEVs can be envisaged with charging sockets or V2G-based technologies. Furthermore, suitable grid connection capacity at PCC is provided. An exemplifying outline of the EVSI is reported in Fig. 3.20. The EVSI can be realized with different design structures, e.g. by adopting internal AC or DC distribution, or by accounting for the integration of several technologies of the three basic components. Moreover, the modularity of EVSI can encourage their diffusion in public and private domains.

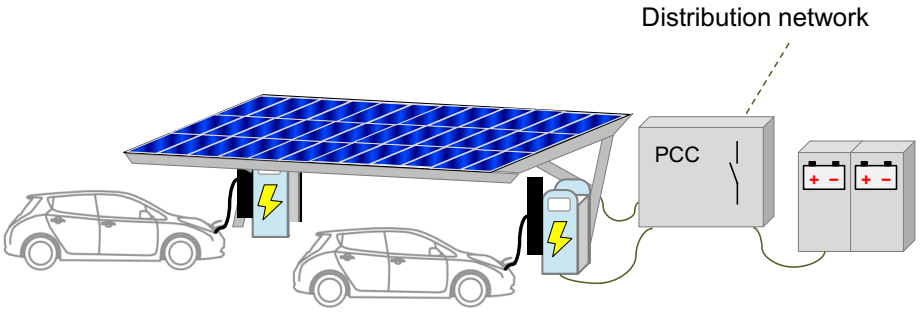

Figure 3.20. Outline of the EVSI.

A procedure for optimal design of an EVSI is proposed, aiming at defining the size and technology of devices, by accounting for suitable operating conditions and specific mobility needs of PEV fleet. The procedure is applied to the test benchmark represented by Bari Port authority, according to stochastic variations of current routes covered by service vehicles, carrying out a Monte Carlo analysis of optimal investment and operation of different runs. Moreover, the evaluation of investment feasibility is dealt with by comparison with conventional fuel-based vehicles and a set of PEV charging stations.

3.3.1 Nomenclature

Indices

t Time step

s Scenario

p Photovoltaic system (PV)

i Energy storage system (ESS)

j Electric vehicle (PEVs)

k Vehicle station

r Charging/V2G standards

Parameters

N_t Total number of time steps

N_s Total number of scenarios

N_p Total number of PV technologies

N_i Total number of ESS technologies

N_j Total number of PEVs

N_k Total number of stations

N_r Total number of PEV charging/V2G standards

α Discount rate

N_y Total number of years of the analysis

Δt Duration of each time step [h]

D_s Total number of occurrences of the s-th scenario in a year

c_p Unitary investment cost of the p-th PV technology [€/kW]

c_i Unitary investment cost of the i-th ESS technology [€/kWh]

c_r Unitary investment cost of the r-th technology for vehicle charging/V2G station [€/kW]

c^g Unitary investment cost of grid connection capacity of the EVSI [€/kW]

$q_{w,s,t}$ Cost for electric energy purchase from the grid at PCC at the t-th time step in the s-th scenario [€/kWh]

$\gamma_{g,s,t}$ Revenue for electric energy delivery to the grid at PCC at the t-th time step in the s-th scenario [€/kWh]

q_j Wearing cost for PEV [€/kWh]

$\overline{P}^g$ Maximum level of power exchange with the grid [kW]

η_i^c, η_i^d charge and discharge efficiency of the i-th ESS

$\overline{e}_i, \underline{e}_i$ maximum and minimum SOC for the i-th ESS [p.u.]

$E_{i,s,0}$ initial SOC of the i-th ESS in the s-th scenario [kWh]

V_T available volume for placing ESS [m^3]

σ_i specific energy for the i-th ESS [kWh/m^3]

ω_i^c, ω_i^d nominal duration of the i-th ESS in charge and discharge [kWh/kW]

ρ_j^c, ρ_j^d charge and discharge efficiency of the j-th PEV

$\bar{v}_j$, $\underline{v}_j$ maximum and minimum SOC for the *j*-th PEV

E_{j,s,τ_A} , E_{j,s,τ_L} SOC at arrival and leaving for the *j*-th PEV in the *s*-th scenario [kWh]

$\bar{P}_j^c$, $\bar{P}_j^d$ maximum charge and discharge power of the *j*-th PEV [kW]

Ψ_r^c , Ψ_r^d maximum power levels deliverable/withdrawable by means of the *r*-th standard of PEV station [kW]

A_T total available area for parking shelters [m^2]

A_j standard parking surface for the *j*-th PEV [m^2]

η_p^{BOS} system efficiency of the *p*-th PV technology

η_p^{std} efficiency of the *p*-th PV technology in standard conditions

μ_p standard operating temperature of the *p*-th PV

λ_p efficiency temperature derating coefficient of the *p*-th PV

$G_{p,s,t}$ solar radiation on the *p*-th PV at the t-th time step in the *s*-th scenario [kW/m^2]

$\theta_{s,t}$ external temperature at the t-th time step in the *s*-th scenario

$\tau_{j,s}^A$, $\tau_{j,s}^L$ arrival and leaving time step of the *j*-th PEV at the EVSI in the *s*-th scenario

$\beta_{j,k,s}$ Binary value assigning the connection of the *j*-th PEV at the *k*-th station in the *s*-th scenario

Real State Variables:

$P_{s,t}^w$ Power taken from the grid at the *t*-th time step in the *s*-th scenario [kW]

$P_{s,t}^g$ Power injected into the grid at the *t*-th time step in the *s*-th scenario [kW]

$P_{i,s,t}^c$ Charge power of the *i*-th ESS at the *t*-th time step in the *s*-th scenario [kW]

$P_{i,s,t}^d$ Discharge power of the *i*-th ESS at the *t*-th time step in the *s*-th scenario [kW]

$E_{i,s,t}$ State of charge (SOC) of the *i*-th ESS at the *t*-th time step in the *s*-th scenario [kWh]

$P_{j,s,t}^c$ Charge power of the *j*-th PEV at the *t*-th time step in the *s*-th scenario [kW]

$P_{j,s,t}^d$ Discharge power of the *j*-th PEV at the *t*-th time step in the *s*-th scenario [kW]

$E_{j,s,t}$ State of charge (SOC) of the *j*-th EV at the *t*-th time step in the *s*-th scenario [kWh]

R_p Installed power for the *p*-th PV plant [kW]

R_i Installed energy level for the *i*-th ESS [kWh]

R^g Contractual power exchange level with the grid at PCC [kW]

Binary State Variables:

$b^g_{s,t}$ Selection of either power withdrawal or injection from the grid at the *t*-th time step in the *s*-th scenario

$b_{i,s,t}$ Selection of either charge or discharge for the *i*-th ESS at the *t*-th time step in the *s*-th scenario

$b_{j,s,t}$ Selection of either charge or discharge for the *j*-th EV at the *t*-th time step in the *s*-th scenario

$b_{r,k}$ Selection of the *r*-th standard for the equipment of the *k*-th station.

3.3.2 EVSI Sizing Methodology

In order to determine the most suitable design of the EVSI for a selected user, an optimization procedure is proposed in this section. The procedure is based on the hypothesis that the operation of the system can be led to the occurrence of a defined set of scenario representing typical days of operation, according to user habits and/or external conditions.

The power output of the *p*-th PV system for each *t*-th time step in the *s*-th scenario, depends on the available solar radiation and technological features, by means of the following expression:

$$P_{p,s,t} = R_p \cdot \frac{\eta_{p,s,t} \cdot G_{p,s,t}}{\eta_p^{std} \cdot 1000} \tag{3.18}$$

where the factor 1000 represents the relevant solar radiation [kW/m^2]. The amount of PV power is related to the installed power R_p, that is a decision variable, by means of a linear relation, therefore it does not represent a further state variable.

In (3.18), the conversion efficiency of the *p*-th PV system $\eta_{p,s,t}$ depends on the forecasted weather conditions of the specific time step by coefficients μ_p and λ_p, relating to reference solar radiation 800 kW/m^2, reference temperature of 20°C for performance derating, and standard external temperature of 25 °C, as follows:

$$\eta_{p,s,t} = \eta_p^{std} \cdot \left[1 - \lambda_p \cdot \left(\vartheta_{s,t} + G_{p,s,t} \cdot \frac{\mu_p - 20}{800} - 25\right)\right] \tag{3.19}$$

Moreover, the incident solar radiation $G_{p,s,t}$ is affected by forecasted solar radiation, incidence angle between PV panel orientation (due to parking roof structure) and variable beam radiation direction, as well as on diffusion of the atmosphere and reflection from the surroundings [45]. The total installation of PV system, even with different technologies, is limited by available surface of parking roofs and minimum parking surface for the vehicles, accounting for shelters providing vehicle shadowing for all parking places:

$$A_j \cdot N_k \leq \sum_{p=1}^{N_p} \frac{R_p}{\eta_p^{std} \cdot 1000} \leq A_T \tag{3.20}$$

The behaviour of ESSs is characterized by SOC variation due to the actions of charging or discharging the device. The following relation holds for the *t*-th time step:

$$E_{i,s,t} = E_{i,s,t-1} + \Delta t \cdot \left(\eta_i^c \cdot P_{i,s,t}^c - \frac{P_{i,s,t}^d}{\eta_i^d} \right) \tag{3.21.a}$$

where $E_{i,s,t-1}$ represents the SOC of the *i*-th ESS in the previous time step preceding the *t*-th ore in the *s*-th scenario; this term is replaced by the imposed initial condition $E_{i,s,0}$ at the beginning of each scenario. Moreover, the SOC at the end of the scenario is imposed equal to the initial value, allowing to replicate the behaviour for consecutive days even pertaining to different scenarios, i.e.:

$$E_{i,s,N_t} = E_{i,s,0} \tag{3.21.b}$$

Operational features of the *i*-th ESS are accounted by means of constraints on charge, discharge and SOC, depending on installed amount R_i:

$$0 \leq P_{i,s,t}^c \leq \frac{R_i}{\omega_i^c} \cdot b_{i,s,t} \tag{3.22.a}$$

$$0 \leq P_{i,s,t}^d \leq \frac{R_i}{\omega_i^d} \cdot \left(1 - b_{i,s,t}\right) \tag{3.22.b}$$

$$\underline{e}_i \cdot R_i \leq E_{i,s,t} \leq \overline{e}_i \cdot R_i \tag{3.22.c}$$

The total installation of ESSs is limited by the available volume:

$$\sum_{i=1}^{N_i} \sigma_i \cdot R_i \leq V_T \tag{3.23}$$

Analogously to ESSs, PEVs are dealt with as storage devices, as long as they are connected to a station. However, if the station is equipped with a charging technology, the charge process can be controlled without allowing discharge, whereas in the presence of a V2G-based station, the PEV can effectively provide energy to the EVSI by discharging its batteries.

The relation for SOC update of PEV is valid for the *t*-th time step between $\tau_{j,s}^{A}+1$ and $\tau_{j,s}^{L}$:

$$E_{j,s,t} = E_{j,s,t-1} + \Delta t \cdot \left(\rho_j^c \cdot P_{j,s,t}^c - \frac{P_{j,s,t}^d}{\rho_j^d} \right) \tag{3.24}$$

where $E_{j,s,t-1}$ represents the SOC of the *j*-th PEV in the previous time step of the *s*-th scenario; this term is replaced by the imposed initial condition E_{j,s,τ_A} at the time step $\tau_{j,s}^{A}$, beginning of parking time interval.

At specified leaving time $\tau_{j,s}^{L}$ the PEV should leave the parking place with a SOC level E_{j,s,τ_L} ensuring the coverage of route by drivers. This final value is related to initial one accounting for cycling operation.

Technical limits of the *j*-th PEV, during parking interval, are accounted by means of constraints on SOC and exchange power levels defined by PEV features:

$$0 \le P_{j,s,t}^c \le \bar{P}_j^c \cdot b_{j,s,t} \tag{3.25.a}$$

$$0 \le P_{j,s,t}^d \le \bar{P}_j^d \cdot \left(1 - b_{j,s,t}\right) \tag{3.25.b}$$

$$\underline{v}_j \le E_{j,s,t} \le \bar{v}_j \tag{3.25.c}$$

However, the consideration of station characteristics to connect the *j*-th PEV to the EVSI are accounted. The number of stations to be included in the EVSI, N_k, is set to the minimum necessary, i.e. the maximum amount of PEVs parked at the same time in any scenario.

Once N_k is determined, the stations are exploited according to a specific priority order. The priority is based on the evaluation for the *j*-th PEV in *s*-th scenario, of the following power index $\pi_{j,s}$, representing the average power to be fed into the PEV over the defined parking interval to fulfil the defined charging (or discharging) needs:

$$\pi_{j,s} = \frac{\left| E_{j,s,\tau_L} - E_{j,s,\tau_A} \right|}{\tau_{j,s}^{L} - \tau_{j,s}^{A}} \tag{3.26}$$

Therefore, for each scenario, the maximum number of PEVs contemporaneously parked in any time step is evaluated, and these PEVs are associated to the charging station according to the

power index $\pi_{j,s}$: the PEV with the highest index is connected to the first station, $k = 1$, and so on. For the remaining PEVs, again ordered according to the power index, the procedure connects the PEV with highest power index and to the station with lower index k, allowing to avoid superposition of parking/connection time with the PEVs previously linked. This procedure can leave in idle state the last stations (with higher index k). In this way, the binary parameter $\beta_{j,k,s}$ is determined a priori for all EVs, stations and scenarios.

In order to select the most appropriate technology for a station, according to the PEV connection pattern defined by $\beta_{j,k,s}$, the following relation between stations and technologies hold:

$$\bar{P}_k^c = \sum_{r=1}^{N_r} b_{r,k} \cdot \Psi_r^c \tag{3.27.a}$$

$$\bar{P}_k^d = \sum_{r=1}^{N_r} b_{r,k} \cdot \Psi_r^d \tag{3.27.b}$$

$$\sum_{r=1}^{N_r} b_{r,k} = 1 \quad \forall k \tag{3.27.c}$$

In particular, (3.27.a) and (3.27.b) allow to determine the maximum charge/discharge power at the k-th station, $\bar{P}_k^c$ and $\bar{P}_k^d$ respectively, on the basis of the maximum levels admitted by the r-th technology, whereas the univocal association of the r-th standard, to the k-th station at design stage is ensured by (3.27.c). If the r-th technology is aimed to provide only PEV charge, it is assumed that $\Psi_r^d = 0$.

As a consequence, the charge and discharge power of the j-th PEV depends on the features of the k-th station where the PEV is connected in the s-th scenario, as follows:

$$0 \le P_{j,s,t}^c \le \bar{P}_k^c \cdot \beta_{j,k,s} \tag{3.8.a}$$

$$0 \le P_{j,s,t}^d \le \bar{P}_k^d \cdot \beta_{j,k,s} \tag{3.28.b}$$

A power balance relation is imposed for the EVSI, where the generation is represented by net PV production, ESS discharge, possible PEV discharge and grid withdrawal, and the load includes ESS and EV charge and grid power delivery:

$$\begin{aligned} &\sum_{p=1}^{N_p} \eta_p^{BOS} \cdot P_{p,s,t} + \sum_{i=1}^{N_i} P_{i,s,t}^d + \sum_{j=1}^{N_j} P_{j,s,t}^d + P_{s,t}^w = \\ &\sum_{i=1}^{N_i} P_{i,s,t}^c + \sum_{j=1}^{N_j} P_{j,s,t}^c + P_{s,t}^g \end{aligned} \tag{3.29}$$

The grid power exchange of the EVSI is limited in each direction through the following relations, avoiding contemporaneous withdrawal and injection, in the same time step, according to technical features of the connection:

$$0 \le P_{s,t}^{g} \le \bar{P}^{g} \cdot b_{s,t}^{g} \tag{3.30.a}$$

$$0 \le P_{s,t}^{w} \le \bar{P}^{g} \cdot \left(1 - b_{s,t}^{g}\right) \tag{3.30.b}$$

Moreover, the contractual power level imposes a further limits on the power exchange, as follows:

$$0 \le P_{s,t}^{g} \le R^{g} \tag{3.30.c}$$

$$0 \le P_{s,t}^{w} \le R^{g} \tag{3.30.d}$$

and it is limited by the maximum exchange, due to technical features:

$$0 \le R^{g} \le \bar{P}^{g} \tag{3.30.e}$$

The objective of optimal design of the EVSI under the provided PEV operation (parking time, route lengths, SOC levels) and in the presence of space limitations is aimed to be reached through the minimization of EVSI total lifetime cost C_T, determined as follows:

$$C_T(\mathbf{x}) = C_B + C_O \tag{3.31.a}$$

where C_B represents the total investment cost in EVSI components, and C_O is the total operation cost of the EVSI over the whole useful lifetime.

In this case, the EVSI realization is fulfilled in one year prior to the operation lifetime, the building cost C_B is determined as the sum of device purchasing and installation costs, as follows:

$$C_B = \sum_{p=1}^{N_p} c_p \cdot R_p + \sum_{i=1}^{N_i} c_i \cdot R_i + \sum_{r=1}^{N_r} c_r \cdot \Psi_{c,r} \cdot \sum_{k=1}^{N_k} b_{r,k} + c^{g} \cdot R^{g} \tag{3.31.b}$$

Indeed, the *p*-th PV technology is installed when $R_p > 0$, and the *i*-th ESS technology is included in the EVSI if $R_i > 0$. Whereas, the installation of vehicle charging/V2G stations is a discrete quantity, and the amount of installed stations equipped with the *r*-th technology is given by summing the values of binary variable $b_{r,k}$ for all the N_k stations.

The yearly operation cost of the EVSI C^{y}, determined by considering the occurrence of the *s*-th scenario or typical day, for D_s times over one year, as follows:

$$C^y = \sum_{s=1}^{N_s} D_s \cdot \sum_{t=1}^{N_t} \left[q_{s,t}^w \cdot P_{s,t}^w - \gamma_{s,t}^g \cdot P_{s,t}^g + \sum_{j=1}^{N_j} \left(q_{j,s,t} \cdot P_{j,s,t}^c \right) \right] \tag{3.31.c}$$

By assuming that the behaviour of the system during the analysed year occurs in the same way along the considered lifetime, the overall operation cost C_O is determined multiplying C^y by the annuity factor:

$$C_O = \frac{1-(1+\alpha)^{-N_t}}{\alpha} \cdot C^y \tag{3.31.d}$$

The methodology of EVSI optimal design can be synthesized in a Mixed Integer Linear Programming formulation, as in the following expression:

$$\begin{aligned} &\min C_T(\mathbf{x}) \\ &\text{s.t.} \begin{cases} g(\mathbf{x}) = 0 \\ h(\mathbf{x}) \le 0 \end{cases} \end{aligned} \tag{3.32}$$

The state variable vector $\mathbf{x}$ includes only non-negative values for $N_s \cdot N_t \cdot (2 + 3 \cdot N_i + 3 \cdot N_j) + N_p + N_i + 1$ real variables, involving installed PV and ESS size ($N_j + 1$ variables), power exchanged at connection point with the distribution grid at each time step t the s-th scenario of day n ($2 \cdot N_s \cdot N_t$ variables), charge/discharge power and energy content of each ESS ($3 \cdot N_s \cdot N_t \cdot N_i$ variables), charge/discharge power and energy content of PEVs ($3 \cdot N_s \cdot N_t \cdot N_j$ variables). Moreover, $N_s \cdot N_t \cdot (1 + N_i + N_j) + N_k \cdot N_r$ binary variables, including the selection of V2G station technology for each vehicle ($N_i \cdot N_k$ variables), the selection of power withdrawal or injection at grid connection point ($N_s \cdot N_t$ variables), the selection of charge/discharge process of each ESS and of each PEV ($(N_i + N_j) \cdot N_s \cdot N_t$ variables. The set of equality constraints $g(\mathbf{x}) = 0$ includes (3.21.a), (3.21.b), (3.23), (3.27.c), and (3.28), whereas inequality constraints $h(\mathbf{x}) \le 0$ include (3.19), (3.21.a)-(3.21.c), (3.22), (3.24.a)-(3.24.c), (3.28.a)-(3.28.b) and (3.30.a)-(3.30.e).

In the proposed approach PEV exploitation parameters are supposed known prior to the solution procedure. However, PEV parking intervals and energy use are intrinsically uncertain, due to the possibility of different actual vehicle exploitation. For this reason, a stochastic procedure is carried out in order to investigate the influence of those parameters on EVSI sizing and operation based on the Monte-Carlo method. This allows to determine average results and

extreme conditions according to suitable stochastic distributions of PEV exploitation parameters.

Moreover, in order to evaluate the economic outcome of the investment in this kind of initiative, the evolution of the net present value over the investment horizon obtained by means of the described procedure is compared to reference cases. A first reference is the conventional mobility case, where the considered routes are covered by new fuel-based vehicles and relevant consumption and expenses are accounted. A further comparison is carried out with respect to a case, where there is the substitution of fuel-based vehicle fleet with PEV fleet, but no microgrid installation is provided, therefore installation of conventional charging station, where electricity consumption is tariffed at specific price for PEV charge.

3.3.3 Test user: port authority

The procedure is applied to the evaluation of feasibility of service PEV fleet equipping and EVSI installation in the context of the Bari Port Authority. In particular, the considered authority currently detains 5 diesel-fueled service cars identified by V1-V5, and their current yearly exploitation data for service matters by Port employees (route lengths, travel times) have been collected. The results of this preliminary investigation are described in Table 3.14, for average route length distinguishing for seasons and working/vacation days, and in Fig. 3.21 for average parking intervals. It can be seen that V1, V2 and V3 are mainly used for internal services, even on holidays, with different time intervals, whereas V4 covers larger distances and is less used on holidays, and V5 is used for two distinct periods, with a little parking interval at lunch time.

Table 3.14. Current Vehicle Uses

	Average daily path length (km)				
	V1	V2	V3	V4	V5
Winter Working	26.3	78.9	29.6	109.6	48.1
Winter Holiday	8.2	1.3	4.8	6.4	---
Mid-season Working	19.5	35.4	23.5	76.0	61.7
Mid-season Holiday	2.9	6.5	3.2	10.6	2.3
Summer Working	27.7	28.1	27.4	40.4	30.8
Summer Holiday	10.6	10.8	10.6	---	3.3

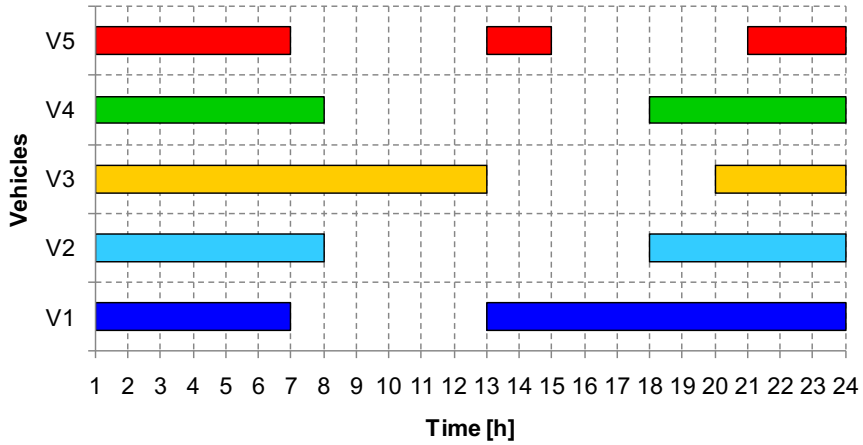

Figure 3.21. Test case: Average vehicle parking time

For the replacement of this service vehicle fleet, the exploitation of Nissan Leaf 24 kWh as available PEV is considered, since it is able to cover the average uses, having a NEDC range of 200 km with 80% energy range [235][239]. Furthermore, the charge/discharge efficiency of PEVs is estimated at 0.909 [240] and vehicle wearing cost is equal to 0.05 €/kWh [218]. In order to properly exploit the PEVs without affecting battery lifetime, an operating range of SOC between 0.2 p.u. and 0.9 p.u. is considered.

In order to develop the EVSI, a parking place has been individuated in the neighboring of authority headquarters, with maximum available surface of 120 m^2, whereas the minimum shadowing surface in (3.20) is estimated in 15 m^2 per vehicle according to the dimensions of the selected PEV. Since all vehicles are averagely parked over the night, five charging stations will be provided, although each PEV could be connected indifferently to any of them. Moreover, when no routes are required to vehicles (i.e. Winter Holidays for V5 and Summer Holidays for V4), they are supposed to be parked all day long.

Features of the selected canopy include orientation due south and a 10° slope. As regards PV technology, the market analysis has lead to the choice of polycrystalline modules, with standard efficiency of 15.3%, power/temperature coefficient of -0.407 %/K [241] and installation cost of 981 €/kW [242], whereas ESS is based on lithium-polymer (LiPo) technology with a nominal duration of 30 min in charge and discharge at 0.9 efficiency [243] and installation cost of 375 €/kWh [244].

Table 3.15. Available Vehicle Station technologies

Technology	$\bar{P}_r^c$	$\bar{P}_r^d$	Installation cost [€/kW]
Type 2 16 A	3.7	3.7	1388
Type 2 32 A	7.4	7.4	1370
CHAdeMO	50	50	1520

As regards PEV station technologies, the procedure inputs are limited to the compatible standards with the chosen PEV [245], and the main features are reported in Table 3.15. The maximum power flow at the connection to the distribution grid is fixed at 6.6 kW, according to standard Italian contractual values for low-voltage single-phase users. Moreover, energy purchase is priced in a range between 0.2 and 0.3 €/kWh, with hourly variations, whereas energy sold is remunerated with a time-of-use tariffs included in the range 0.03-0.07 €/kWh [246][247]. The analysis is carried out over a time horizon of 20 years with 5% discount rate.

In order to analyse the operation of the EVSI in the presence of different frameworks for vehicle use and generation availability that can occur over its operational lifetime, a scenario-based analysis is proposed.

Usually, the analysis of solar power production in the design stage is carried out by means of average condition on typical days of each month . However, the exploitation of storage devices is most affected by extreme conditions rather than average. This implies that more conditions should be analyzed, including full sun days as well as cloudy ones, in order to examine storage exploitation. Moreover, the results of investigation on the use of vehicles has highlighted different use in working days and holidays and in seasons of the year (Winter, from December to March, Summer, from June to September, and Mid-Season for the months left). In each season, three kind of days are individuated, named Sunny, Cloudy and Rainy, according to daily serenity index. Furthermore, in order to account for different exploitation of the PEVs, during weekdays, Working-days and Holidays are distinguished. Therefore, a total of $N_s = 18$ scenarios are individuated by the combination of seasonality, weather and weekdays, as detailed in Table 3.16, where the Scenario numeration and occurrence times D_s are reported.

Table 3.16. Scenario numeration and occurrence times

		Weather					
Season	Weekday	Sunny		Cloudy		Rainy	
		s	D_s	s	D_s	s	D_s
Winter	Working day	1	9	2	33	3	22
	Holiday	4	4	5	13	6	9
Mid-season	Working day	7	56	8	49	9	25
	Holiday	10	22	11	20	12	10
Summer	Working day	13	46	14	18	15	3
	Holiday	16	18	17	7	18	1

3.3.4 Results and discussion

The procedure is implemented in MatLAB2015b® framework, and it is solved by means of *intlinprog* function, through the exploitation of branch and bound technique. Simulations are carried out on a workstation HP Z440 equipped with Intel Xeon 3.50 GHz processor and a RAM capacity of 16 GB.

The proposed approach is first applied to the test user by accounting for the deterministic average data, considering that each PEV leaves the parking lot with 80% of energy content. This value is set in order to ensure path length coverage with suitable margin, allowing for V2G operation as well. According to this assumption, to required route lenghts and to PEV consumption per km, initial values of PEV SOC are determined.

In order to test different mileage for the considered PEVs, 100 stochastic cases are generated (named EC1÷EC100), where a Gaussian distribution with zero mean and a standard deviation of 0.8 kWh is summed to the deterministic values of initial and final SOC levels of each PEV in each scenario. This corresponds to a variation of route length up to 30 km per each trip, and initial/final PEV energy content values can vary by ±10% with respect to the average deterministic value, thus remaning in PEV allowed range. Moreover, stochastic variability of parking time is considered through 10 stochastic cases (named TC1÷TC10), where parking and leaving time of each PEV are varied from average by means of a normal-distributed value with a maximum variation of 2 h from average values, approximated to integer of hours. Therefore, considering the application of stochastic variations to the base case represented by average values (EC0-TC0), a total number of 1111 stochastic cases is investigated.

Results of the analysis are described in Table 3.17, where deterministic results in the Base Case are presented along with cases with extreme values of objective function terms and grid exchange levels. Note that, in all cases, yearly operating costs C_{Opr} are negative, meaning that revenues from energy sold exceed energy purchasing costs and PEV wearing costs. Moreover, PV installation is equal to the minimum amount, whereas the ESS size is not constant. As regards PEV stations, a remarkable presence of 3.7-kW solutions is observed, whereas in the 13% of cases a 7.4-kW station is installed along with four 3.7-kW ones. This causes higher investment, roughly by 5 k€, but other performances aere not remarkably affected, since the installation of a more powerful station is related to higher values of power index $\pi_{j,s}$, mainly due to reduced parking time, with minimum of 1 h. PV production is sold to the grid by 68.5% average, whereas only 3.7% of PEV energy demand is covered by grid withdrawals.

Table 3.17. Statistic analysis of case studies

		Base Case	Average			C_{Inv}		C_{Opr}		$f(\mathbf{x})$		Grid withdrawal		Grid Injection	
			global	1 7.4	no 7.4	min	max	min	max	min	max	min	max	min	max
PEV time case		0	---	144 cases	967 cases	4	6	5	4	9	6	2	4	3	5
PEV Energy case		0	---			55	87	19	10	18	87	1	13	6	97
Installation	PV [kW]	11.925	11.925	11.925	11.925	11.925	11.925	11.925	11.925	11.925	11.925	11.925	11.925	11.925	11.925
	ESS [kWh]	3.901	3.472	3.70	3.43	1.059	7.364	5.678	2.09	1.374	7.364	5.757	1.899	3.477	3.88
	Stations [n. @ kW]	5@3.7	---	1@7.4 4@3.7	5@3.7	5@3.7	1@7.4 4@3.7	5@3.7	5@3.7	5@3.7	1@7.4 4@3.7	5@3.7	5@3.7	5@3.7	5@3.7
Energy production [MWh/y]	PV	17.53	17.53	17.53	17.53	17.53	17.53	17.53	17.53	17.53	17.53	17.53	17.53	17.53	17.53
	grid withdrawal	0.26	0.31	0.31	0.31	0.27	0.14	0.12	0.59	0.29	0.14	0.10	0.67	0.27	0.23
	ESS discharge	1.59	1.44	1.56	1.42	0.48	2.99	2.29	0.94	0.59	2.99	2.24	0.83	1.44	1.65
	PEV discharge	2.4	2.26	2.09	2.28	3.00	2.07	1.18	2.44	2.56	2.07	1.86	2.36	2.24	1.71
Energy consumption [MWh/y]	Grid injection	11.93	12.02	12.05	12.01	11.88	11.87	12.53	11.72	12.13	11.87	12.25	12.27	11.41	12.65
	ESS charge	1.35	1.22	1.33	1.20	0.43	2.53	1.93	0.82	0.51	2.53	1.95	0.71	1.22	1.40
	PEV charge	8.51	8.31	8.11	8.33	8.97	8.34	6.66	8.97	8.34	8.34	7.53	8.41	8.86	7.08
Economic efforts [k€]	$f(\mathbf{x})$	34.236	34.840	39.229	34.187	33.436	40.216	33.927	34.767	33.363	40.216	34.188	34.529	34.531	33.562
	C_{Inv}	38.839	39.327	43.765	38.666	37.774	45.140	39.506	38.160	37.891	45.140	39.535	38.088	38.680	38.831
	C_{Opr}	-0.369	-0.360	-0.364	-0.359	-0.348	-0.395	-0.448	-0.272	-0.363	-0.395	-0.429	-0.286	-0.333	-0.423
total yearly distance [km]		58868	59861	59997	59841	57958	63515	56150	64105	56699	63515	57087	59502	65969	54972
PEV energy need [MWh/y]		5.09	5.18	5.19	5.18	5.01	5.49	4.86	5.55	4.90	5.49	4.94	5.15	5.71	4.76
simulation time [s]		120.0	322.7	199.5	341.1	137.6	41.3	356.2	61.0	61.5	41.3	67.1	1122.7	143.8	615.1

The exploitation of V2G technology involves an increase of PEV charge energy, related to higher wearing cost that could prevent further PEV discharge. However, the presence of low revenues for energy injection to the grid and high ESS installation cost implies an effective exploitation of V2G operation. In particular, an average increase of 60% of PEV charge with respect to the energy amount required to cover the mobility routes at nominal consumption rate is observed. The 1111 simulations are run in roughly 4 days and 4 hours.

An example of daily trends SOC and power amounts of each PEV and electric power balance is reported, for a summer working day with sunny conditions, in Fig. 3.22 for the Base Case and in Fig. 3.23 for the case with maximum value of objective function (TC 6 – EC 87). PEV power and electricity balance contributions are represented with the convention adopted in (3.29), i.e. positive values represent generation and negative are loads.

It can be seen that PEVs can exchange energy among each other, especially in the morning, when a limited power withdrawal is observed. In daylight period, PV production is primarily exploited to charge PEVs and ESS, and the excess power is injected in the grid. ESS is discharged in the evening to supply parked PEVs. Energy content of each PEV does not exceed specified limits (0.2÷0.9 p.u), even in stochastic cases with different starting and final points. In the Base Case, PEV power does not exceed 3.7 kW due to the installed station size, whereas PEV4 is connected to the 7.4-kW station in the maximum $f(\mathbf{x})$ case in the shown day.

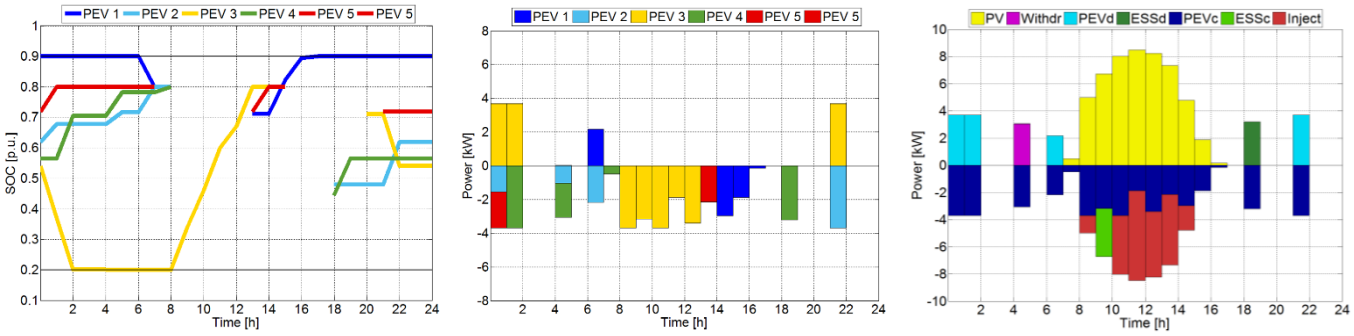

Figure 3.22. Trends of PEV energy content (left), PEV power (middle) and EVSI electric balance (right) in the Base Case in a summer working day.

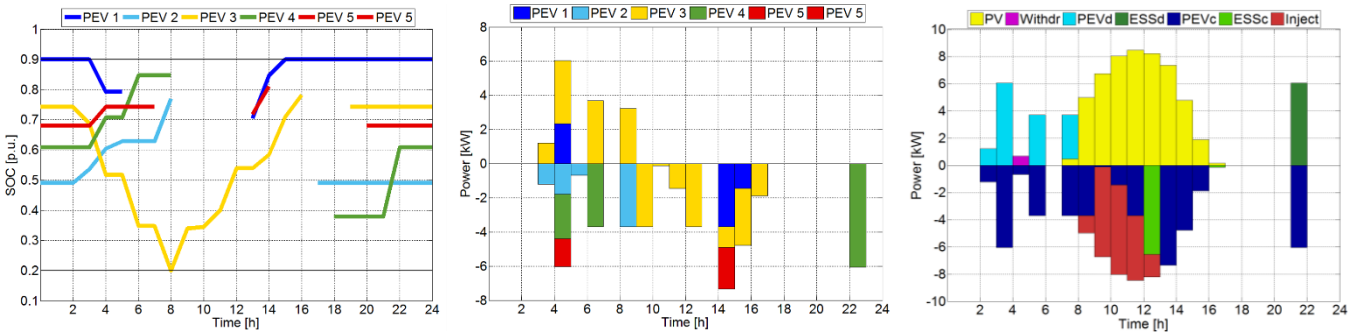

Figure 3.23. Trends of PEV energy content (left), PEV power (middle) and EVSI electric balance (right) in the maximum f(x) case in a summer working day.

The objective function value is detailed for all the stochastic cases in Fig. 3.24, where the different symbols represent PEV time cases (TC). In particular, the cases are plotted according to yearly parking time, depending on TC, and to PEV yearly route length, depending on EC. It can be highlighted that $f(\mathbf{x})$ shows an increase as the route length increases, whereas a slightly decreasing trend can be observed with respect to parking time. Moreover, 144 cases with the installation of more powerful V2G station, characterized by higher values of objective function, are clearly placed in the upper part of the figure. These cases are more frequently obtained in cases with lower parking time, with a majority in TC1. The distribution of these values can be described with an approximation to a normal distribution with 39.229 k€ mean and 0.378 k€ standard deviation. For the other 967 cases, the approximation is to a normal distribution with 34.187 k€ mean and 0.355 k€ standard deviation.

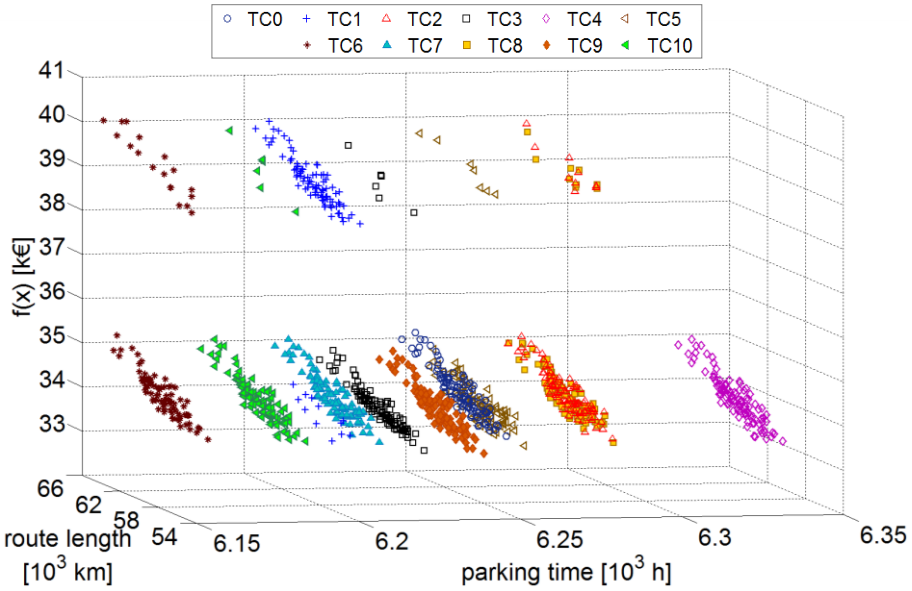

Figure 3.24. Objective function value in stochastic cases.

ESS installation in the stochastic cases is illustrated in Fig. 3.25 with the same representation of Fig. 3.24. Values range between 1.06 and 7.36 kWh, and their distribution can approximate a normal one with 3.472 kWh mean and 1.048 kWh standard deviation. These values are weakly dependent on parking time, whereas a slight increase along with total route length can be pointed out, as shown in Fig. 3.26 where average values are reported. Although, maximum and minimum ESS installation levels are observed in cases with intermediate route lengths.

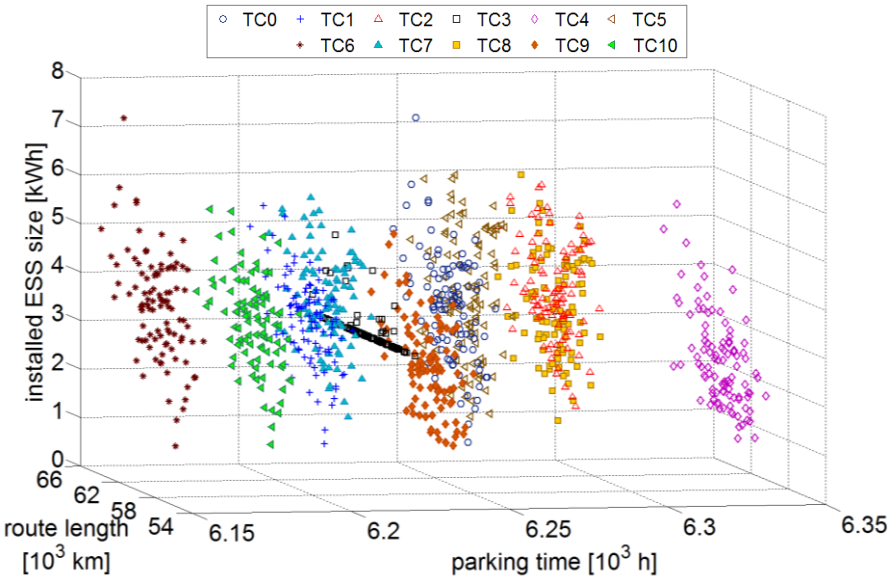

Figure 3.25. ESS installation in stochastic cases.

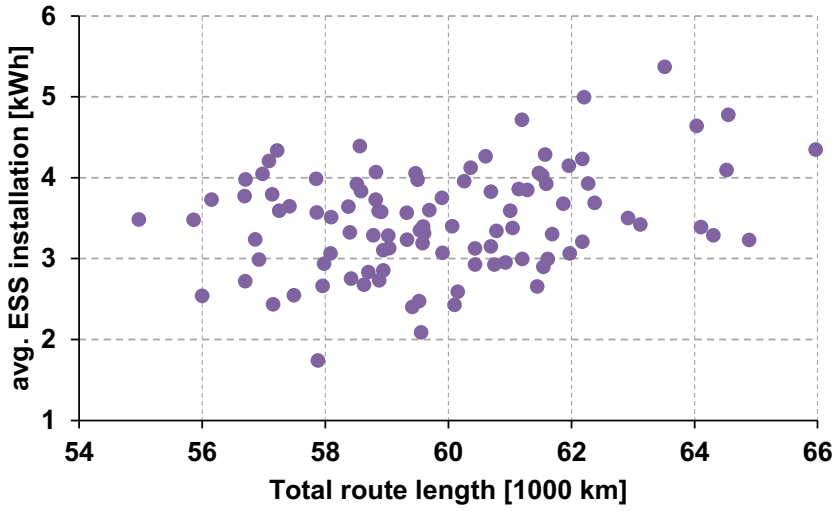

Figure 3.26. Average ESS installation with respect to route length in EC

The profitability of the initiative, including the integrated infrastructure and PEVs, is assessed with respect to conventional fuel-based mobility. To this purpose, the PEV cost is assumed equal to 27 k€, whereas the cost of a new diesel-based vehicle is considered 20 k€. The conventional vehicle operation cost is determined by assuming a performance index of 18 km/l and average fuel price of 1.35 €/l. Moreover, in the presence of PEVs fed by simple charging points, a tariff of 0.40 €/kWh is applied to energy supply for PEV charging [236].

With these assumptions, for deterministic case (EC0-TC0), the Net Present Value (NPV) and the Pay Back Period (PBP) are determined by accounting for the difference in investment and

yearly operation costs, named ΔC_I and ΔC_O respectively, with respect to the selected reference case, according to the following relations:

$$NPV = -\Delta C_I - a_f \cdot \Delta C_O \tag{3.33}$$

$$PBP = \log_{\frac{1}{1+\alpha}} \left(1 + \frac{\alpha \cdot \Delta C_I}{\Delta C_O} \right) \tag{3.34}$$

In Fig. 3.27, the trends of NPV are reported for the aforementioned cases. A proper saving for yearly vehicle maintenance in the presence of PEVs is considered, along with circulation tax exemption, in accordance with current regulatory framework in Apulia region [248]. By considering the conventional fuel-based mobility as the reference case, the NPV variation of the integrated infrastructure case is slightly positive (3.3 k€) and PBP is 18.6 years, within the time horizon of the analysis. As an alternative to tax exemption, an incentive on PEV purchasing cost equal to 15% of PEV cost is considered, in order to achieve higher profitability of the initiative. This value is comparable with the current incentive plans for PEVs provided by some countries [249]. This yields to NPV difference of 14.2 k€ NPV and PBP of 14.0 years. Whereas the intermediate case, in the absence of integrated infrastructure, does not experience profitability, although investment is limited.

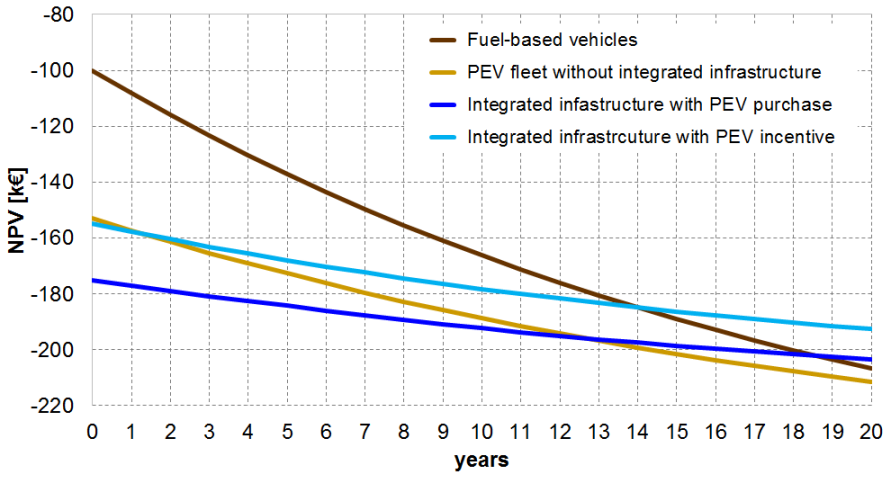

Figure 3.27. Economic performance of integrated infrastructure for PEV fleet

3.4 A demonstrator for integration of electric vehicles: DC EVSI

In the previous sub-section, the EVSI characterized by single AC bus, where different AC components are connected by AC/DC converter is proposed. However several problems are associated with the AC MGs, such as the need for synchronization of the distributed generations, the inrush currents due to transformers, reactive power flow, harmonic currents and three-phase unbalances [250]-[252]. Moreover, the integration of the DC based sources, as PV plants, fuel cells and energy storage systems can pave the way towards the DC microgrids [253][254]. Indeed, in the EVSI, the DC-based DG units and energy storage devices can produce the DC power with an easy connection to the DC bus line or to a low-voltage DC (LVDC) network. An ESS can also exchange energy with the LVDC network and cover loads [255][256]. In this case, the AC power sources need an AC/DC power converter for their connection to the LVDC network [257]-[259]. In Fig. 3.28, the LVDC network with DG units connected to it via the common bus bar at PCC is depicted. To this end, the AC-based DG units (wind turbines) and distribution network connection to the LVDC network require inverters while the DC based DG units are connected through DC/DC converters as indicated in the figure.

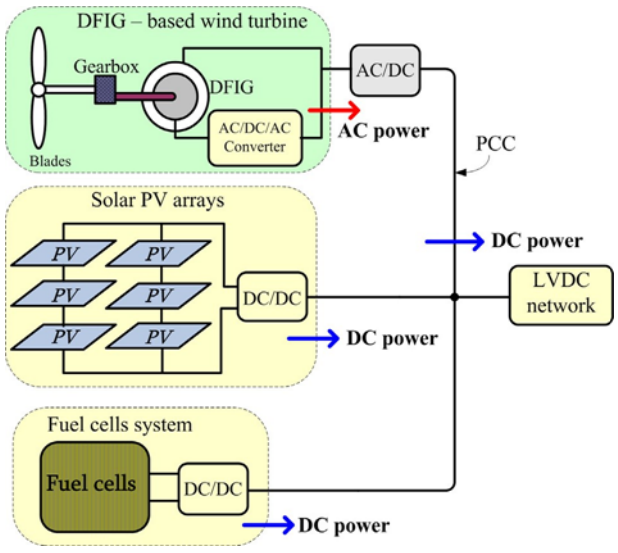

Figure 3.28. Typical configuration of the DG units in DC network.

The DC power systems have been used hitherto in industrial power distribution systems, telecommunication infrastructures and high voltage transmission over long distances or via sea cables and for interconnecting AC grids with different frequencies. An increasing amount of devices for everyday electric energy users (computers, fluorescent lights, variable speed drives)

bases its operation on DC. However, the DC devices require conversion of the available AC power into DC, typically using inefficient rectifiers at the moment. Moreover, the power from DC based DG units must be converted into AC to tie with the existing AC electric network, to be converted later to DC required by end-users. These DC–AC–DC power conversion stages result in substantial energy losses. Using the positive experiences in the HVDC operation and the advance in power electronics technology, interests in pursuit for effective solutions has increased. The LVDC distribution network is a new concept which is one possibility to tackle the current power distribution problems and realize the future power system [260]. In particular, DC MG systems are used as testing prototypes or typically installed for most of the data centre or critical load applications. In the case of DC MG configurations, the low voltage DC links are based on bipolar configurations where the loads can be connected across the positive polarity and the ground or between the two polarities, to enhance flexibility.

The LVDC distribution network can improve the efficiency of power exchange with the AC distribution network, ensuring a higher power quality to the customers and facilitating DG connection [261]. Results of DC MG application show a significant reduction in power quality problems, losses and downtime and protection malfunctions [250][251][262].

The opportunities and challenges associated with a DC distribution system for industrial power system are dealt with in [263]. In particular, the focus is directed on the interaction between the power converters and the challenging issues of the system grounding. The DC MG for small-scale residential houses is investigated to find out the influence of current balancing, system losses and stability [255][256], illustrating the attractive features of DC MG in terms of simple structure, low system cost and the overall improved efficiency since few power converters are needed compared to the AC MGs [259][261]. The DC MGs control strategies in grid-connected and islanding mode are reported in [264][266][267]. For instance, a control strategy for the grid-connected DC MG with renewable based DG units and ESSs is adopted in [268]. Nevertheless, a detailed discussion on control strategies for the battery energy storage system during islanded and grid-connected operation to adjust the DC bus voltage is studied and presented in [266]. More details about the control strategies for grid connected and islanded DC MGs operation are available in [269].

Protection issues in the LVDC distribution system are a challenging problem addressed by few studies in literature. In [270], the philosophy of protecting the DC MG systems with the DG units, sensitive loads and power converters is presented. The grounding system, protection devices, power converters, battery protection methods, and DC feeder protection approach together with their coordination are stated as the potential areas in designing any effective

protection scheme in the LVDC distribution systems [271][272]. The DC MG protection mechanisms are investigated in [273]-[275]. Moreover, the dynamic behavior and stabilization of DC MG with constant power loads are also given in detail by [266]. The electric vehicles (i.e. PHEV and EV) charging stations represent an attractive area for the DC MG implementation and diffusion [265][268][276]. In this perspective the vehicle-to-grid (V2G) concept could widely become a reality.

Moreover, optimal planning and operation of the smart grids with the EV interconnection has shown that the EV-ESSs can be used to offer different kinds of ancillary services, for instance controlling and managing part of the smart grid or commercial buildings following the arbitrage of energy between buildings with different tariffs [277]. Meanwhile, in [278] the influence of the EVs charging stations to the Polish power network is proposed. Therefore, the literature analysis shows the feasibility of DC microgrids and the possibility to integrate in a common DC bus with different EV batteries and power sources [279]-[282].

In this outline, the proposition of a DC-based architecture for the EVSI can be charming, in order to take advantage from DC-based sources, storage and users. This vision has given rise to the activities of Italian Cluster within CONNECT project, in which the Electric Energy System research group of Politecnico di Bari is involved, as described in detail in the following paragraph.

3.4.1 The CONNECT project: general frame and DC EVSI

The Project named CONNECT, “Innovative smart components, modules and appliances for a truly connected, efficient and secure smart grid”, has been submitted in response to the call of European Commission H2020-ECSEL-2016-1-RIA-two-stage, in the framework of Horizon 2020 program. The call is issued by the Electronic Components & Systems for European Leadership (ECSEL) Joint Undertaking, under the Research and Innovation Action. The project partnership is composed by 19 participants coming from 5 nations and involves university, research center and big, medium and small enterprises. The coordinator partner is Infineon Technologies AG.

The key objective of the CONNECT project is the reduction of the peak power demand by at least 50%. This objective includes techniques for the reduction of power fluctuations of the grid over time and for reduction of power consumption and losses. In order to achieve this ambitious objective, solutions are provided for three research challenges at the technical level for the smart grid architecture, which will define and motivate the research conducted by the CONNECT participants:

- Power Conversion, referring to radical changes in the power conversion technologies.
- Smart energy management, referring to pervasive changes in the energy management procedures and infrastructures.
- Communication infrastructure, referring to far-reaching changes in the smart-grid communication infrastructure.

To deal with these challenges, the partners are involved in the research of innovative solutions, among them: i) higher conversion efficiency with reduction of power losses; ii) a smart energy management able to reduce the power demand, especially in peak demand periods, through effective load scheduling, smart use of energy storage, and efficient utilization of renewable energy sources; iii) the development of innovative solutions for the communication infrastructure for both the optimal utilization of converters and the execution of energy management procedures.

Moreover, these solutions are integrated in use cases, in order to demonstrate the peak demand reduction compared to the state of the art.

In particular, the Italian cluster is in charge of the Use Case 3, aiming at designing, realizing and testing a DC micro-grid. This demonstrator will incorporate technologies such as power converters, sensors, as well as control algorithms, in order to demonstrate an overall examination of the performance of DC micro-grids, mainly in fields of the reduction of the energy demand from the external grid, of the minimization of DC distribution losses, of more efficient integration of DC sources (e.g. photovoltaic, batteries) and of the benefits of controlling V2G parking lots. Indeed, the EVSI system is intended to be a modular infrastructure consisting of four main components appropriately designed: a storage appliance, a PV system, a DC busbar connected to external AC network and a set of EV charging stations, as depicted in Fig. 3.29.

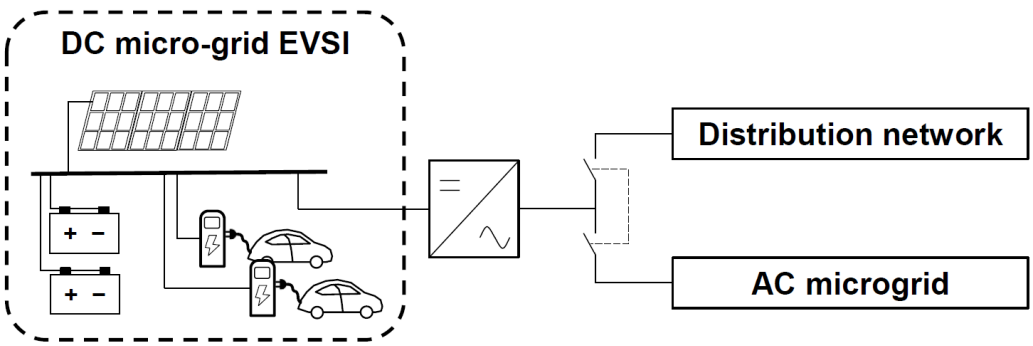

Figure 3.29. DC micro-grid EVSI structure in CONNECT Project.

This type of configuration can contribute to facilitate the penetration of EVs, and its optimal management can reduce the costs for electric energy supply.

An embryo realization of the EVSI will be set up by properly assembling various components of the existing experimental micro-grid at POLIBA premises and by testing new components and algorithms (DC-DC converters, sensors, communication devices, energy management methodologies). The final demonstrator will be installed in the Bari port area, thanks to the availability of the local Port Authority. To this purpose, the definitive project is aimed to determine the most suitable placement of the EVSI in the selected area, accounting for mobility needs of employees of the Authority.

Moreover, the Italian partners, with the focus of energy management have the goal to conceive network architectures and algorithms for the optimal utilization of the energy generated by renewable energy sources and available in local storage devices, as well as for the increase of the reliability of the MG infrastructure and the development and optimization of communication network. The main tasks for achieving these goals include: i) efficient smart metering solutions that improve the state-of-the-art bidirectional solutions with higher efficiency, lifetime and recording capabilities of both energy consumption and generation; ii) development of pervasive energy consumption monitoring sensor networks and infrastructures by exploiting dedicated custom integrated circuits;, iii) innovative energy management algorithms that will be developed for the cooperation of AC grid, in order to achieve optimal utilization of the generated energy; iv) development of power flow control methodology and of a stochastic optimization model for DC micro-grids that takes into account the uncertainties of load consumption, power production from renewables and departing and arriving of EVs, that could be also exploited as energy sources based on their schedule of usage; v) design of a distributed management approach that represents the top level of the hierarchical control structure adopted for the automatic operation of the DC micro-grid. The performances that will be obtained by using the distributed approach will be tested in a simulation platform of the DC micro-grid and will be compared with the results of the stochastic optimization model. Then, the developed algorithms, sensors and circuits will be tested on-field and validated in experimental facilities.

3.4.2 Optimal configuration of DC EVSI

In the first stage of the aforementioned project, the Electric Energy System research group of Politecnico di Bari is involved to the definition of the optimal configuration of the EVSI test-bed based on the DC micro-grid framework. To this purpose, in this paragraph an investment

analysis based on optimal sizing and planning of DC EVSI is proposed. The procedure is applied to four configurations of the DC Microgrid that includes PV system, energy storage systems (ESSs), a DC bus, a PCC with the AC distribution network, and charging point for EV in V2G configuration. These technical solutions (T.S.) are characterized by several interface systems that connect the different components, the AC system and the DC bus.

In particular, the T.S.A is based on single stage converter for each device of the Microgrid, in order to control bidirectional flux of EV charging point and ESS, and to ensure MPPT operation of PV. The PV system is connected to DC bus by unidirectional DC-DC converter. In these applications the multilevel boost converter is proposed in [283], presenting the advantages of a continuous input current, a large conversion ratio in the lack of transformer, along with a modular realization, where more levels can be added without modifying the main circuit. The adoption of bi-directional DC-DC converters with low cost, high efficiency and high reliability is crucial for the charging stations and ESS. The non-isolated bi-directional DC-DC converters can be considered for this application. In this field, in [284] the Half bridge and three-level converter have been compared, showing that the latter presents a higher efficiency. Moreover, the DC EVSI is connected to distribution grid through a bidirectional AC/DC converter that permits the delivery of excess energy and the electricity purchase in case of need. The grid-related power converter aims to optimally control and coordinate the reactive power output of inverter-interfaced DG and storage units in the distribution network, while also achieving overvoltage correction, predictive maintenance and significant loss reduction in LV and MV lines. A three-phase four-leg voltage source converter is considered, in order to demonstrate the possibilities of flexible grid-interfacing of residential or commercial buildings with local storage batteries. A fourth switching leg not only brings one more control degree-of-freedom than three-leg converters, but also prevents neutral currents causing voltage ripple on DC capacitors (in other words, reduced number of DC capacitors is needed). Moreover, the control of bidirectional power flow in AC/DC converter is applied for the enhancement of the quality of the grid voltage at the point of connection. The layout of T.S.A is reported in Figure 3.30, with four EV charging points, one ESSs and a PV plant.

The T.S.B, as sketched in Fig. 3.31, differs from the previous, due to a different connection of ESS, that is directly linked to DC bus. In this way, the charge and discharge of storage occurs thanks to the control of the amount of voltage difference between the DC Bus and ESS. This solution is proposed in [285], with the integration of static var compensator (SVC) in the AC/DC converter interface, in order to provide stable AC bus voltage at the AC side of DC/AC converter, to compensate reactive power and to exchange power between the DC sub-grid,

utility and AC sub-grid. When the output power of the DC sources is greater than the DC loads, the inverter injects power from DC to AC sub-grid and utility grid. When the total power generation is less than the total load demand at the DC side, the inverter acts as a converter and injects power from the AC sub-grid and utility grid to DC side. In both cases, the DC bus voltage is controlled by AC/DC converter, in a way that, if it is higher than ESS voltage (depending on temperature and SOC), ESS is charged, or otherwise ESS is discharged. Therefore, in this configuration the control system increases its complexity and cost with respect to the T.S.A.

The T.S.C is characterized by the presence of three-ports AC-DC-DC converter for interfacing DC bus and AC distribution network, as shown in Fig. 3.32. The three-ports converter is used to integrate the renewable energy and energy storage converters into one converter with two inputs, specifically. The three-port converter can accept two DC inputs, one for the DC output of the PV, and the second DC input, characterized by the connection of energy system in bidirectional configuration, to perform charging and discharging. The output of the three-port DC−DC converter can be connected to the DC load directly or to the grid or AC load by an inverter through a DC link capacitor, as discussed in [286]. In T.S.C, the three-ports converter presents a unidirectional power flow path with MPPT operating mode and two bidirectional power flow paths.

Finally, the T.S.D provides an AC/DC converter connected to the DC bus that includes only EV parking lots, and a three-ports converter to interface ESS and PV to the AC distribution network and DC bus, as illustrated in Figure 3.33. This solution permits to enhance the reliability of the system with a higher economic impact, due to the presence of two interface converters. The three-port converter can achieve maximum power harvesting for the solar port, battery charge control for the battery port, while keeping a regulated rectified AC output, as illustrated in [287]. However, the increase in the number of branches reduces the possible power flow paths in AC side. Indeed, this system can be considered as a multi-microgrid, integrated by an AC bus.

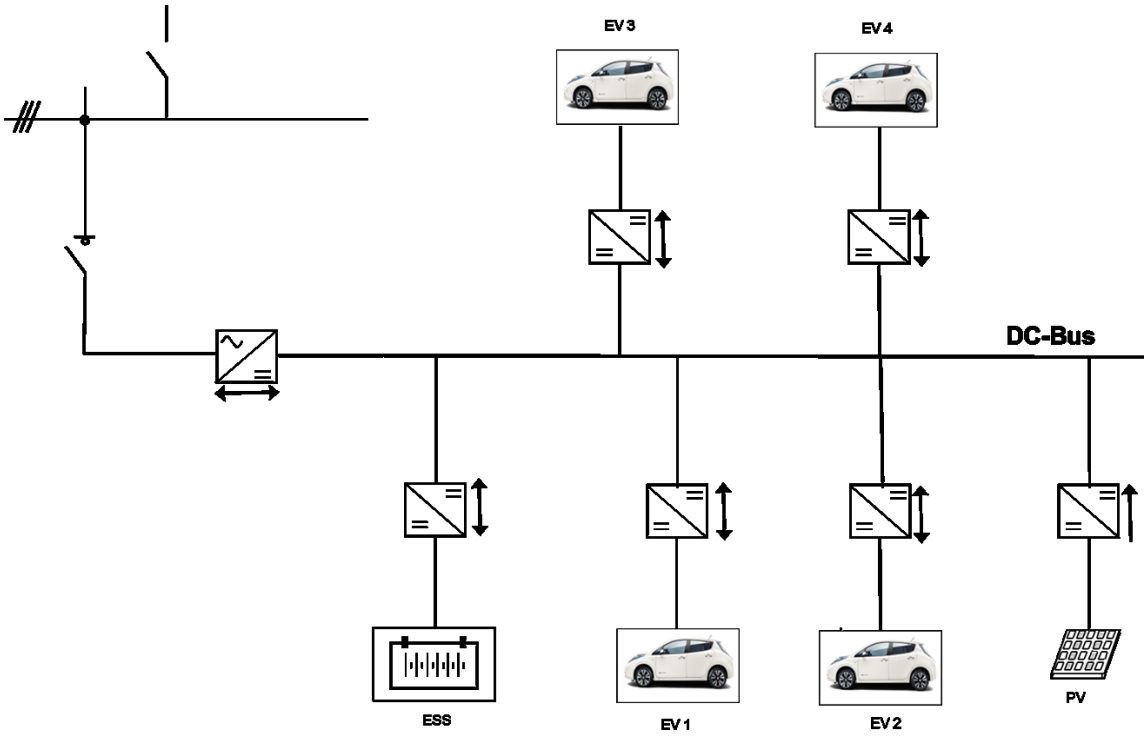

Figure 3.30. DC EVSI, Technical solution A (T.S.A).

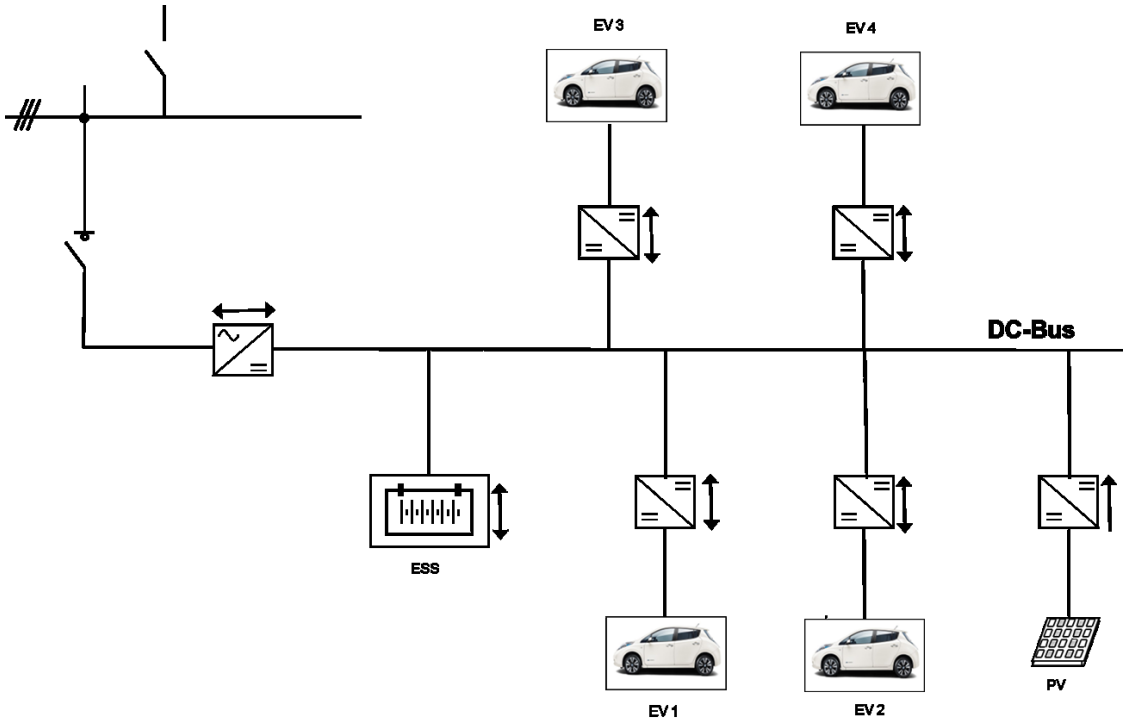

Figure 3.31. DC EVSI, Technical solution B (T.S.B).

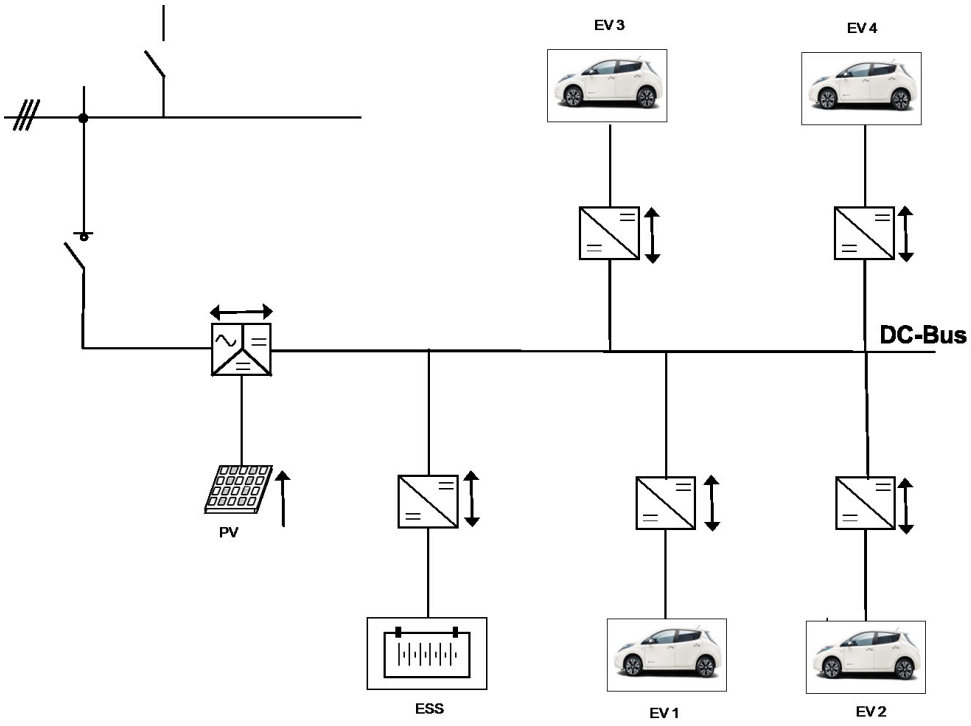

Figure 3.32. DC EVSI, Technical solution C (T.S.C).

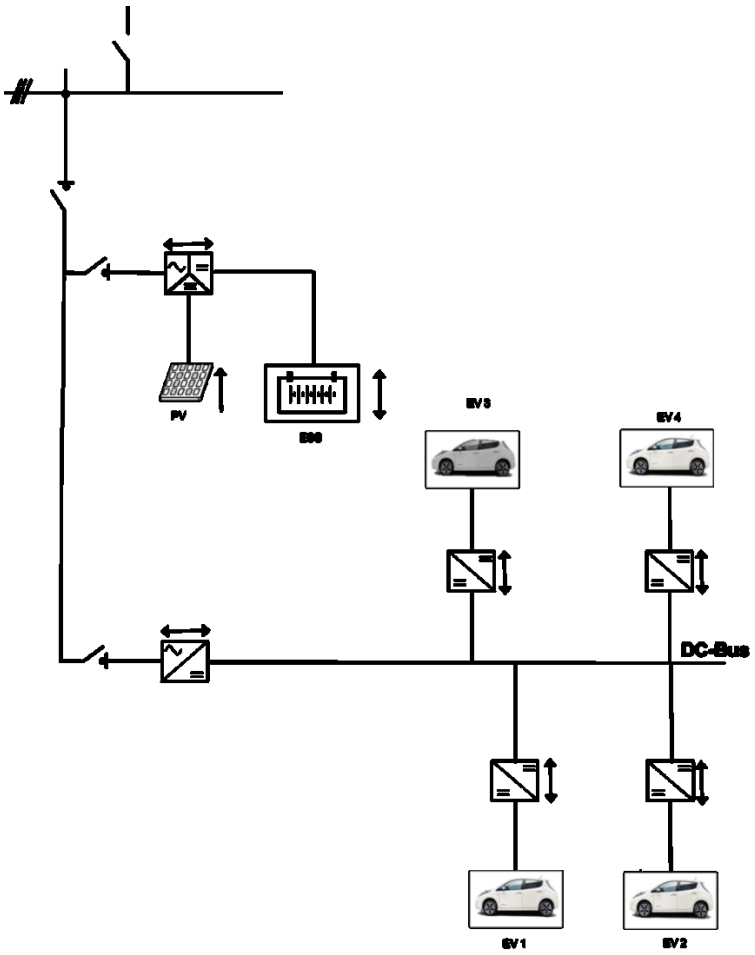

Figure 3.33. DC EVSI, Technical solution D (T.S.D).

The investment analysis, based on optimal sizing and planning of the different T.S. of DC EVSI, is carried out exploiting the methodology described in the section 3.3.2. Moreover, the considered test user is the port authority, with the same assumption described in the previous sub-section. As regards the cost of PV, ESS and charging stations, the values reported in sub-section 3.3 are considered as the base for the determination of new cost coefficients, in the presence of peculiar DC circuit components (e.g. converters, fuses, circuit breaker, buses, cables), according to a thorough market analysis. This analysis has pointed out the limited diffusion of commercial devices of the considered size (some tens of kW) and voltage levels (in the range 400÷800 V DC), and suitable sizes for each device are derived. For instance, bidirectional DC/DC converters for V2G stations are considered in the set of 5, 10, 20 or 30 kW.

The simulation results are reported in the Tables 3.18-3.20, where the sizing of components, the average yearly energy exchanges within the EVSI and the economic performances are reported, respectively. As regards installations, it can be seen that in each T.S. the procedure selects the maximum PV size, according to the available surface in order to cover all the considered electric vehicle parking places. Moreover, the forecasted utilization of EVs does not imply the need of high-speed charging stations, therefore their size is defined at the lowest available power level accordingly to cost reduction goal. The installation of battery storage is highly variable, with maximum in T.S.B due to reduced unit cost in the absence of relevant converter. Whereas in T.S.D no storage is provided, due to the higher cost of three-port converter. This reflects also in the size of the interface with AC network, that is slightly reduced in T.S.C. in the presence of three-ports converter. In T.S.D., three interfaces are reported, i.e. the AC connection to the network (i), the AC-DC converter of the EV connectors (ii) and the three-port converter (iii).

In the planning framework, the procedure considers the sale of excess energy more profitable even in the case of greater installation of ESS. However, in the T.S.B, the deep utilization of ESS reduces the V2G exchange power of EV batteries. In the T.S.D, in order to cover the lack of ESS, the DC EVSI imports the higher amount of power by the distribution grid, leading to a minimum export value with respect the other solutions. These remarks are highlighted in the economic results shown in Table 3.20, where the T.S.B is cheaper due to a greater value of purchase power, to the detriment of a slightly higher investment cost, on the contrary, the T.S.D is the solution with a minimum investment cost but with a maximum value of the objective function, due to higher dependence on grid connection.

Table 3.18. Optimal sizing/operation results. Installed size of DC EVSI components.

	Storage [kWh]	PV [kW]	CS (x5) [kW]	Interface [kW]		
T.S.A.	3.92	11.10	5.00	4.76		
T.S.B.	17.82	11.10	5.00	4.62		
T.S.C.	10.00	11.10	5.00	4.19		
T.S.D.	0	11.10	5.00	4.82 (i)	5.26 (ii)	9.59 (iii)

Table 3.19. Optimal sizing/operation results. Yearly energy flow in the DC EVSI [MWh]

T.S.	Withdrawal	Injection	Charge ESS	Discharge ESS	Charge EV	Discharge EV	PV
A	0.308	9.935	1.205	1.443	11.365	4.762	15.992
B	0.002	10.961	4.487	5.596	8.712	2.570	15.992
C	0.132	10.305	3.046	3.608	10.093	3.711	15.992
D	0.911	9.171	0	0	11.078	4.525	15.992

Table 3.20. Optimal sizing/operation results. Economic yields [€]

T.S.	Objective Function	Investment Cost	Operative Cost
A	63474.59	67273.04	-3798.45
B	62764.29	68061.99	-5297.70
C	65131.05	67375.12	-2244.08
D	71161.48	65724.28	5437.20

In order to compare the different T.S. and to facilitate the interpretation of results, performance indices are introduced. In particular, the energy index represents the impact of each component on the T.S. energy balance of the DC EVSI. The exchanged energy in the system by each component is subdivided between energy generation E_g and energy load E_l, and the energy indices $E_{g\%}$ and $E_{l\%}$ are calculated as the percentage of generation energy and load energy given by each component on the total production/consumption in the EVSI, as reported in (3.35)(3.36).

$$E_{g\%} = \frac{E_g}{\sum_{g=1}^{N_g} E_g} \cdot 100 \quad g = 1,...,N_g \tag{3.35}$$

$$E_{l\%} = \frac{E_l}{\sum_{l=1}^{N_l} E_l} \cdot 100 \quad l = 1,...,N_l \tag{3.36}$$

where N_g and N_l indicate the number of generators and loads, respectively.

In Figg. 3.34-3.35 the energy indices for generation and load are reported for the four T.S. It can be noted that the PV reaches the 70% of total generation in any case, the ESS discharge is in the range 5 – 20 %, the EV is discharged between 10-20% and the withdrawn energy by the grid is at maximum 4% in T.S.B. As regards the energy index of load, the maximum contribution is related to EV charge with 56% in T.S.D and 36% in T.S.B, whereas the injected energy in the distribution grid is approximately 40% in each case.

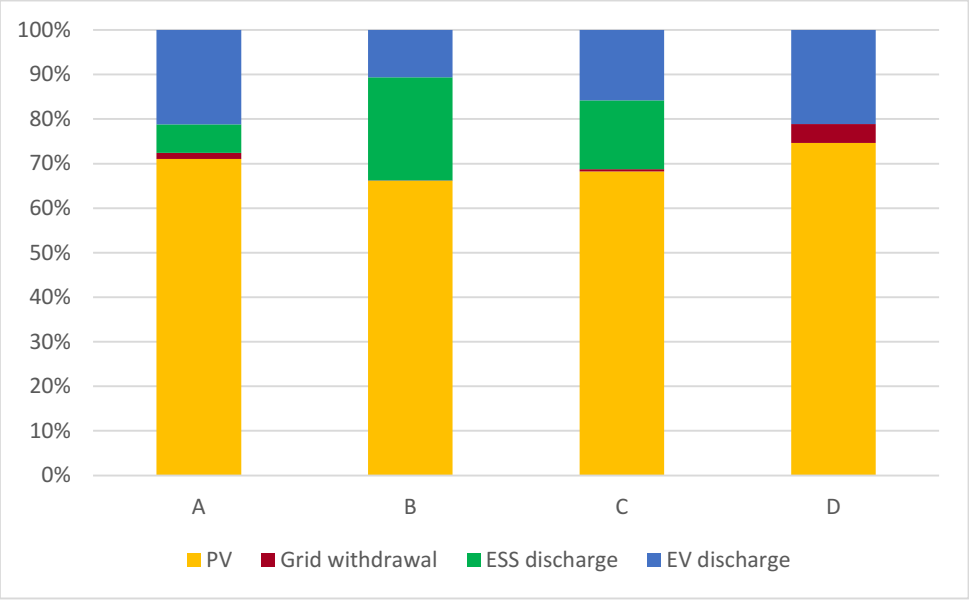

Figure 3.34. Energy index of generation in the T.S.s.

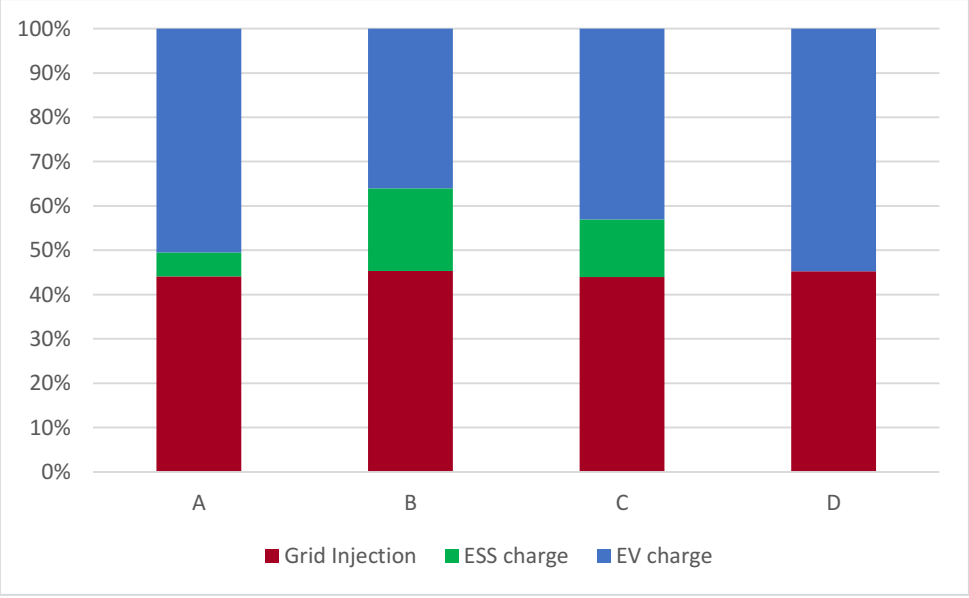

Figure 3.35. Energy index of load in the T.S.s.

The contribution of each component to total investment cost of DC EVSI, in the T.S. frame, is reported in Fig. 3.35. It can be noted that the higher investment is related to charging point with a cost of approximately 50 k€, whereas the PV system reaches the investment cost of 16.5 k€. The cost of AC grid connection is highly variable, with maximum in T.S.D due to interface converter. Finally, the investment cost of ESS is equal to 0.650 k€ in T.S.A and 1.423 k€ in T.S.B, representing the maximum value, according to increased size.

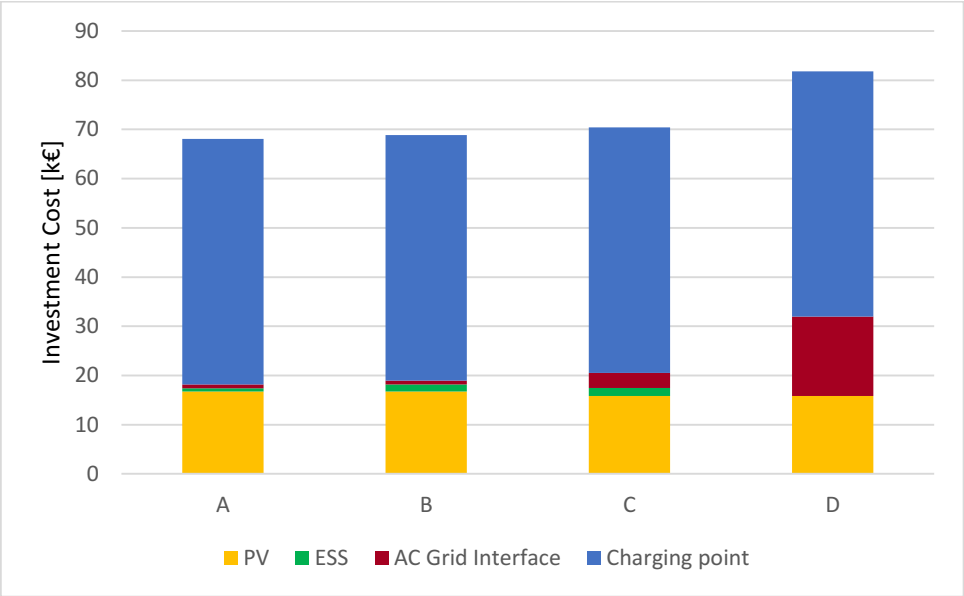

Figure 3.36. Investment cost in the T.S.s.

As regards the unitary cost of energy for each component, it is determined as the ratio between investment cost of the component and the total amount of planned energy flow in the lifetime horizon, as reported in (3.37).

$$C_{en,c} = \frac{C_{inv,c}}{N_t \cdot E_g} \quad c = 1,\ldots,N_c \tag{3.37}$$

where $C_{inv,c}$ is the investment cost for each component c, N_c and is a total number of components, and N_t is the number of years of EVSI lifetime horizon, supposed at 20 years. In Fig. 3.36, the unitary costs of each component in the four T.S.s are reported. It can be noted that the higher cost is associated to charge and discharge of EV, whereas the ESS is cheaper. In particular, the cost of EV discharge is higher with respect to charge, on the contrary the ESS charge is more expensive.

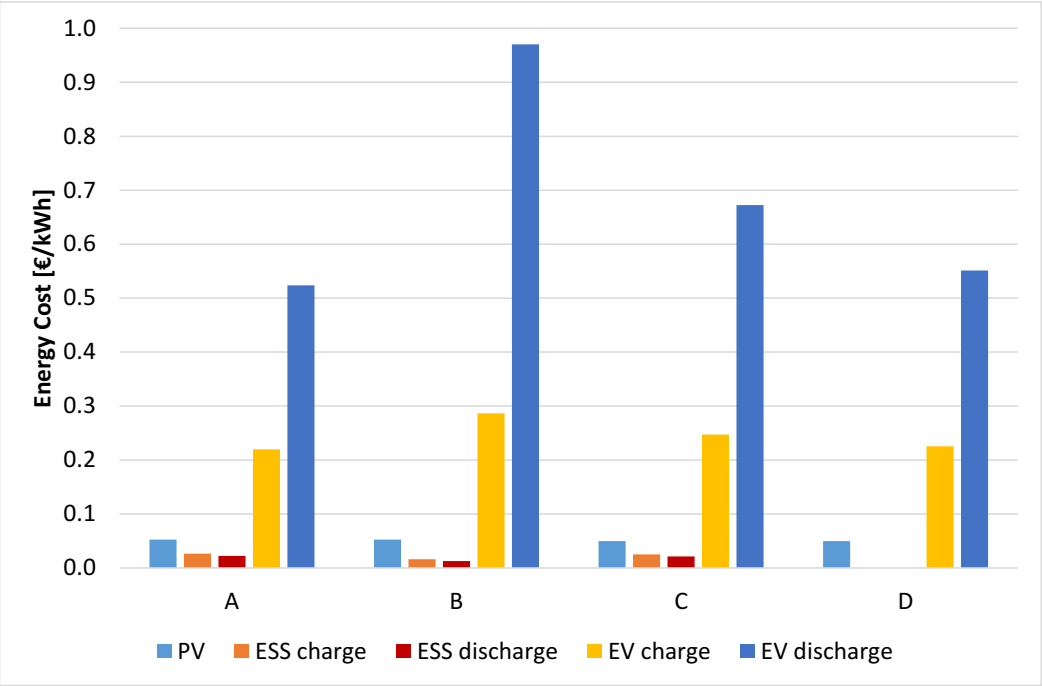

Figure 3.37. Energy cost of components in the T.S.

One of the main goals of the optimal operation planning of DC EVSI is the exchange power with the V2G system. To this purpose, the energy coverage index I_{cov}, V2G coverage index I_{V2G} and EV charge coverage index I_{ch} are evaluated. These indices are referred to an energy theoretical value V_t, defined in (3.38).

$$Vt = \sum_{b=1}^{N_{EV}} \sum_{s=1}^{N_s} \frac{(E_{a,s} - E_{d,s}) \cdot E_{\max,EV}}{100} \cdot D_s \tag{3.38}$$

where $E_{a,s}$ and $E_{d,s}$ indicate the initial and final p.u. level of SOC for the EV in the parking interval in each scenario, $E_{\max,EV}$ is the maximum level of energy in the EV battery, and D_s is the number of occurrences of each scenario in the analyzed year. The coverage indices are evaluated according to (3.39) – (3.41), where E_{ch} and E_{dis} indicate the EV charge and discharge energy, respectively, on the basis on 20 years planning horizon.

$$I_{\text{cov}} = \frac{E_{ch} - E_{dis}}{Vt} \tag{3.39}$$

$$I_{V2G} = \frac{E_{dis}}{Vt} \tag{3.40}$$

$$I_{ch} = \frac{E_{ch}}{Vt} \tag{3.41}$$

The evaluation of these indices for each T.S. is illustrated in the Table 3.31. In particular, a value of I_{cov} greater than 1 indicates that, in any case, a complete coverage of EV mobility

needs is achieved. The second index is characterized by high variability, and the maximum is reported in T.S.A where it can be argued that V2G mechanism is exploited at levels close to the energy needs for EVs. The last index indicates the excess of total charge energy with respect the charge energy request to reach the desired SOC at EV departure. It assumes a minimum value in T.S.B of 71% and the maximum in T.S.A equal to 123%.

Finally, it can be concluded that the T.S.A permits the greater coverage of energy in total exchange energy with EV, both separating charge and V2G processes. Whereas the T.S.B provides a lower value of objective function but less intense exploitation of EVs.

Table 3.31. Coverage Index of EVs in the T.S.s.

T. S.	I_{cov}	I_{V2G}	I_{charge}
A	1.297	0.935	2.232
B	1.206	0.505	1.711
C	1.253	0.729	1.982
D	1.287	0.889	2.175

The study is intended to proceed with the reliability analysis of the different T.S. will be performed. These analyses will permit to evaluate the robustness of the system in the normal and emergency condition. In this way, the balance between economic effort and reliable operation will ensure the choice of the best configuration of T.S. to serve as embryo.

Moreover, the attainment of the objectives of the CONNECT project requires that the algorithms for the operation management of microgrid in grid connected and islanded mode will be tested. In particular, on the basis on the previously described algorithms, optimum schedules will be identified based on customer consumption profiles, renewable forecasts (in order to estimate energy production), distribution system constraints and storage SOC including EV usage. In addition, a distributed control strategy will be developed, which will achieve operational conditions similar to those obtained by the optimization model.

For the control of the DC micro-grid, modulation strategies for each single interface converter will be developed for: i) ensuring minimum conversion and distribution losses in steady state conditions, ii) connecting and disconnecting seamlessly from the distribution grid, and, iii) operating in islanded condition for a predefined time interval. Several advanced control techniques both at the converter and at the DC micro-grid level will be investigated, aimed to a holistic efficiency optimization of the micro-grid and subcomponents. The model will take into account optimal DC voltage values, minimization of capacitive elements in the DC-bus by

means of control and tuning functions. It is expected that the solutions of CONNECT will contribute significantly to the reduction of losses. Reduction of peak power demand to the grid and increased efficiency at the device and component level would boost the system level efficiency. Furthermore, it can be expected that the EVSI with V2G energy transfers for DC microgrids will be characterized, after CONNECT, by a Technology Readiness Level 5-6 starting from Level 3.

Conclusions and future work

The research activity, developed in the field of microgrid (MG), has included several aspects, analyzed from different points of view.

Starting from the energy management perspective in the MG framework, several methodologies have been proposed for the day-ahead planning, and applied to the experimental MG facility realized at Politecnico di Bari. These procedures are validated by means of static and dynamic assessment on a detailed model of the system in software environment and through real test. Moreover, a particular focus has been devoted to the presence of different energy vectors in MG such as electric and thermal demand, as well as the integration in these systems of electric vehicles.

As regard the multi-energy MG, the operation plan in the presence of a detailed thermal energy model has revealed the economic convenience of a multi-source microgrid with respect to distinct conventional supply technologies. Moreover, electric and thermal storage options have been evaluated, implying flexibility improvement of energy management, economic efforts minimization and global microgrid performance enhancement.

The integration of Electric vehicles in the distribution network has been initially proposed by the economic interaction of MG operator and EV aggregator leading to a deeper EV exploitation and a more efficient operation of MG resources, achieving lower total MG cost.

Subsequently, the electric vehicle supply infrastructure has been introduced, and optimal sizing and planning procedure has been proposed, proving the feasibility of the initiative, including the integrated infrastructure and PEVs, with respect to conventional fuel-based mobility.

Future work will deal with the application in actual SCADA/EMS of the experimental MG, through Open Platform Communications systems, of the day-ahead and real time MG management based on proposed procedures. However, this task requires a refined model of MG components, even coming from field experience, to account for several aspects of device behavior that could be shadowed by simple models in day-ahead programming stage, and the implementation in the simulation tool of the transition of the MG between islanded and grid-connected operation mode.

Finally, in order to accomplish the goals of CONNECT project, the energy management of electric vehicle supply infrastructure will be evaluated, in day-ahead and real-time frameworks, as well as the control and communication system will be investigated, in order to carry out the demonstration tasks.

References

[1] W. Gu, Z. Wu, R. Bo, W. Liu, G. Zhou, W. Chen, Z. Wu, “Modeling, planning and optimal energy management of combined cooling, heating and power microgrid: A review”, International Journal of Electrical Power & Energy Systems, vol. 54, Jan. 2014, pp. 26-37.

[2] A. Chaouachi, R.M. Kamel, R. Andoulsi, K. Nagasaka, “Multiobjective intelligent energy management for a Microgrid”, IEEE Trans. Ind. Electronics, Vol. 60, no. 4, Apr. 2013, pp. 1688-1699.

[3] J.A. Peças Lopes, C.L. Moreira, A.G. Madureira, “Defining control strategies for microgrids islanded operation” IEEE Trans. Pow. Syst., vol. 21, no. 2, 2006, pp. 916-924.

[4] Q. Jiang, M. Xue, G. Geng, “Energy Management of Microgrid in Grid-Connected and Stand-Alone Modes”, IEEE Transactions on Power Systems, vol. 28, no. 3, Aug. 2013, pp. 3380-3389.

[5] C.S. Wang, X.L. Li, L. Guo, Y.W. Li, “A seamless operation mode transition control strategy for a microgrid based on master-slave control”, Science China Technological Science, Vol. 5, no. 6, June 2012, pp. 1644-1654

[6] P. Tenti, T. Caldognetto, A. Costabeber, P. Mattavelli, “Microgrids operation based on master-slave cooperative control”, Proc. of 2013 IECON, Vienna (Austria), 10-13 Nov. 2013, pp. 7623-7628.

[7] T.L. Vandoorn, J.D.M. De Kooning, B. Meersman, L. Vandevelde, "Review of primary control strategies for islanded microgrids with power-electronic interfaces", Renewable and Sustainable Energy Reviews, vol. 19, March 2013, pp. 613-628.

[8] D. Ramasubramanian, V. Vittal, J. Undrill, “Transient Stability Analysis of an all Converter Interfaced Generation WECC System”, Proc. of 2016 PSCC Conference, pp. 1-7.

[9] S. T. Cody, C. N. Hadjicostis, A.D. Dominguez-Garcia, “Distributed frequency control of inertia-less AC microgrids, Proc. of 2015 IEEE CDC Conf. 15-18 Dec. 2015, Osaka (Japan), pp. 2018-2013

[10] C. Natesan, S.K. Ajithan, S. Chozhavendhan, A. Devendhiran, “Power Management Strategies in Microgrid: A Survey”, International Journal of Renewable Energy Research, Vol. 5 No. 2, pp. 1-7, 2015.

[11] Z. Bao, Q. Zhou, Z. Yang, Q. Yang, L. Xu, T. Wu, “A Multi Time-Scale and Multi Energy-Type Coordinated Microgrid Scheduling Solution-Part I: Model and Methodology”, IEEE Transactions on Power Systems, vol. 30, No. 5, pp. 2257-2266, Sept. 2015, http://dx.doi.org/10.1109/TPWRS.2014.2367127 .

[12] A. A. Khan, M. Naeem, M. Iqbal, S. Qaisar, A. Anpalagan, “A compendium of optimization objectives, constraints, tools and algorithms for energy management in microgrids”, Renewable and Sustainable Energy Reviews vol. 58, pp. 1164-1683, 2016, http://dx.doi.org/10.1016/j.rser.2015.12.259 .

[13] H. Daneshi, H. Khorashadi-Zadeh, “Microgrid Energy Management System: A Study of Reliability and Economic Issues”, ” in Proc. IEEE Power Energy Soc. Gen. Meeting, San Diego, CA, 2012, pp. 1-5. http://dx.doi.org/10.1109/PESGM.2012.6344957 .

[14] J. Chen, X. Yang, L. Zhu, M. Zhang, “Microgrid Economic Operation and Research on Dispatch Strategy”, In Proc. Power Engineering and Automation Conference (PEAM), Wuhan, 2012 pp. 1-6. http://dx.doi.org/10.1109/PEAM.2012.6612416 .

[15] G.-C. Liao, “The Optimal Economic Dispatch of Smart Microgrid Including Distributed Generation”, In Proc. IEEE 2nd Int. Symp. on Next-Generation Electronics (ISNE), Kaohsiung, 2013, pp. 473-477. http://dx.doi.org/10.1109/ISNE.2013.6512401 .

[16] R. Palma-Behnke, C. Benavides, F. Lanas, B. Severino, L. Reyes, J. Llanos, D. Saez, "A Microgrid Energy Management System Based on the Rolling Horizon Strategy", IEEE Trans. Smart Grid, vol. 4, no. 2, pp. 996-1006, Jun. 2013. http://dx.doi.org/10.1109/TSG.2012.2231440

[17] M. Strrelec, J. Berka, "Microgrid Energy Management based on Approximate Dynamic Programming", in Proc. 4th IEEE/PES ISGT Europe, Copenhagen, Denmark, 2013, pp. 1-5. http://dx.doi.org/10.1109/ISGTEurope.2013.6695439 .

[18] M. Mahmoodi, P. Shamsi, B. Fahimi, "Optimal Scheduling of Microgrid Operation Considering the Time-of-Use Price of Electricity", Industrial Electronics Society, IECON 2013, Vienna, 2013, Pages 2127-2132. http://dx.doi.org/10.1109/IECON.2013.6699460 .

[19] D. Zhang, S. Li, P. Zeng, C. Zang, "Optimal Microgrid Control and Power Flow Study With Different Bidding Policies by Using PowerWorld Simulator", IEEE Trans. Sustain. Energy, vol. 5, no. 1, pp. 282-292, Oct. 2014. http://dx.doi.org/10.1109/TSTE.2013.2281811

[20] M. Ross, C. Abbey, F. Bouffard, G. Joos, "Multiobjective Optimization Dispatch for Microgrids With a High Penetration of Renewable Generation", IEEE Trans. Sustain. Energy, vol. 6, no. 4, pp. 1306-1314, Oct. 2015. http://dx.doi.org/10.1109/TSTE.2015.2428676 .

[21] V. Prema, K. Uma Rao, "Predictive Models For a Power Management Of a Hybrid Microgrid- A Review", in Proc. Int. Conf. Advances in Energy Conversion Technologies (ICAECT), Manipal, 2014, pp. 7-12. http://dx.doi.org/10.1109/ICAECT.2014.6757053 .

[22] I. Prodan, E. Zio, "An optimization-based control approach for reliable microgrid energy management under uncertainties", in Proc. IEEE ISEPS Workshop, Bucharest, 2013, pp. 4-7. http://dx.doi.org/10.1109/ISEPS.2013.6707950 .

[23] R. A. Gupta, N. K. Gupta, "A robust optimization based approach for microgrid operation in deregulated environment", Energy Conversion and Management, vol. 93, pp. 131-131, 2015, http://dx.doi.org/10.1016/j.enconman.2015.01.008 .

[24] S. A. Alavi, A. Ahmadian, M. Aliakbar-Golkar, "Optimal probabilistic energy management in a typical micro-grid based-on robust optimization and point estimate method", Energy Conversion and Management, vol. 95, pp. 314-325, 2015, http://dx.doi.org/10.1016/j.enconman.2015.02.042

[25] C. Marnay, G. Venkataramanan, G. Stadler, A. Siddiqui, R. Firestone, R. Chandran "Optimal technology selection and operation of microgrids in commercial buildings", IEEE Trans Power Syst. Vol. 23, no. 3, pp. 975-982, 2008, http://dx.doi.org/10.1109/TPWRS.2008.922654 .

[26] M. Motevasel, A. R. Seifi, T. Nikham, "Multi-objective Energy management of CHP (combined heat and power)-based micro-grid", Energy, vol. 51, pp. 123-136, 2013, http://dx.doi.org/10.1016/j.energy.2012.11.035 .

[27] G. Bruni, S. Cordiner, V. Mulone, V. Rocco, F. Spagnolo, "A study on the Energy management in domestic micro-grids based on Model Predictive Control Strategies", Energy Conversion and Management, vol. 102, pp. 50-58, 2015, http://dx.doi.org/10.1016/j.enconman.2015.01.067 .

[28] X. Lin, P. Li, J. Ma, Y. Tian, D. Su, "Dynamic Optimal Dispatch of Combined Heating and Power Microgrid Based on Leapfrog Firefly Algorithm", Proc. of 2015 IEEE 12th Int. Conf. on Networking, Sensing and Control, Taipei, Taiwan April 9-11, 2015, pp. 416-420.

[29] M. Alipour, B. Mohammadi-Ivatloo, "Stochastic Scheduling of Renewable and CHP-Based Microgrids", IEEE Trans. Industrial Informatics, vol. 11, no. 5, pp. 1049-1058, October 2015, http://dx.doi.org/10.1109/TII.2015.2462296 .

[30] K. Basu, A. Bhattacharya, S. Chowdhury, S.P. Chowdhury, "Planned Scheduling for Economic Power Sharing in a CHP-Based Micro-Grid", IEEE Trans. Power Systems, vol. 27, no. 1, pp. 30-38, February 2012, http://dx.doi.org/10.1109/TPWRS.2011.2162754 .

[31] X. Jin, H. Li, T. Jin, X. Xu, M. Wang, J., Meng, "Economical and Coordinated Dispatch of CHP Based Microgrid with Renewable Energy Resources", Advanced Materials Research Vols. 960-961, pp. 1022-1028, 2014 http://dx.doi.org/10.4028/www.scientific.net/AMR.960-961.1022

[32] L. Majic, I. Krzelj, M. Delimar, "Optimal scheduling of a CHP system with energy storage", Proc. of MIPRO 2013, May 20-24, 2013, Opatija, Croatia, pp. 1253-1257.

[33] D. Zhang, S. Evangelisti, P. Lettieri, L.G. Papageorgiou, "Economic and environmental scheduling of smart homes with microgrid: DER operation and electrical tasks", Energy Conversion and Management, vol. 110, pp. 113-124, 2016, http://dx.doi.org/10.1016/j.enconman.2015.11.056

[34] K.C. Kavvadias, A.P. Tosios, Z.B. Maroulis, "Design of a combined heating, cooling and power system: Sizing, operation strategy selection and parametric analysis", Energy Convers. and Managem., vol. 51, pp. 833-845, 2010, http://dx.doi.org/10.1016/j.enconman.2009.11.019

[35] E. Carpaneto, G. Chicco, P. Mancarella, A. Russo, "Cogeneration planning under uncertainty-Part I: Multiple time frame approach", Appl. Energy, vol. 88, no. 4, pp. 1075-1083, 2011. http://dx.doi.org/10.1016/j.apenergy.2010.10.014 .

[36] E. Perea, N. Ruiz, I. Cobelo, Z. Lizuain, A. Carrascal, "A novel optimization algorithm for efficient economic dispatch of Combined Heat and Power devices", Energy and Buildings, vol. 111, pp. 207-514, January 2016. http://dx.doi.org/10.1016/j.enbuild.2015.11.025

[37] H. Bowen. Z. Zhanghua, "Stochastic Multi-objective Dynamic Optimal Dispatch for Combined Heat and Power Microgrid", Proc. of 2016 IEEE PES Asia-Pacific Power and Energy Conference (APPEEC) - Xi'an, China, 25-28 October 2016, pp. 2369-2373, http://dx.doi.org/10.1109/APPEEC.2016.7779908

[38] M. Barbarić, D. Lončar, "Energy management strategies for combined heat and electric power micro-grid", Thermal Science, vol. 20, no. 4, pp. 1091-1103, 2016. http://dx.doi.org/10.2298/TSCI151215081B .

[39] L. Ma, N. Liu, J. Zhang, W. Tushar, C. Yuen, "Energy Management for Joint Operation of CHP and PV Prosumers Inside a Grid-Connected Microgrid: A Game Theoretic Approach", IEEE Trans. Industrial Informatics, vol. 12, no. 5, pp. 1930-1942, October 2016. http://dx.doi.org/10.1109/TII.2016.2578184 .

[40] T. Schittekatte, M. Stadler, G. Cardoso, S. Mashayekh, N. Sankar, "The impact of short-term stochastic variability in solar irradiance on optimal microgrid design", IEEE Transactions on Smart Grid, accepted 2016 http://dx.doi.org/10.1109/TSG.2016.2596709 .

[41] M.J. Sanjari, H. Karami, H.B. Gooi, "Micro-generation dispatch in a smart residential multi-carrier energy system considering demand forecast error", Energy Conv. and Manag. vol. 120, pp. 90-99, July 2016. http://dx.doi.org/10.1016/j.enconman.2016.04.092 .

[42] J. Aghaei, M.-I. Alizadeh, "Multi-objective self-scheduling of CHP (Combined heat and power)-based microgrids considering demand response programs and ESSs (energy storage systems)", Energy, vol. 55, pp. 1044-1054, June 2013. http://dx.doi.org/10.1016/j.energy.2013.04.048 .

[43] M. Restepo, C. A. Canizares, M. Kazerani, "Three-Stage Distribution Feeder Control Considering Four-Quadrant EV Chargers", IEEE Transactions on Smart Grid, Accepted December 2016, http://dx.doi.org/10.1109/TSG.2016.2640202 .

[44] S. S. Soman, H. Zareipour, O. Malik, P. Mandal, "A review of wind power and speed forecasting methods with different time horizons", in Proc. North Amer. Power Symp. (NAPS), Arlington, 2010, pp.1-8. http://dx.doi.org/10.1109/NAPS.2010.5619586 .

[45] J. A. Duffie, W. A. Beckman, Solar Engineering of Thermal Processes. Fourth Edition , John Wiley & Sons, Inc., Hoboken, NJ, USA.2013.. http://dx.doi.org/10.1002/9781118671603

[46] E. Skoplaki, A.G. Boudouvis, J.A. Palyvos, “A simple correlation for the operating temperature of photovoltaic modules of arbitrary mounting”, Solar Energy Mater. Solar Cells, vol. 92, no. 11, pp.1393-1402, 2008. http://dx.doi.org/10.1016/j.solmat.2008.05.016 .

[47] J. Shi, W.-J. Lee, Y. Liu, Y. Yang, P. Wang, “Forecasting Power Output of Photovoltaic Systems Based on Weather Classification and Support Vector Machines”, IEEE Trans. Ind. Appl., vol. 48, no. 3, pp. 1064-1069, May/June 2012: http://dx.doi.org/10.1109/TIA.2012.2190816 .

[48] O. H. Mohammed, Y. Amirat, M. Benbouzid, T. Tang, “Hybrid Generation Systems Planning Expansion Forecast: A critical State of the art review”, Proc. of 39th IECON IEEE IES Annual Conference, Vienna, 2013, pp. 1668-1673: http://dx.doi.org/10.1109/IECON.2013.6699383 .

[49] L. H. Macedo, J. F. Franco, M. J. Rider, R. Romero, “Optimal Operation of Distribution Networks Considering Energy Storage Devices”, IEEE Trans. Smart Grid, vol. 6 no. 6, Nov. 2015, pp. 2825-2836: http://dx.doi.org/10.1109/TSG.2015.2419134 .

[50] B. Zhao, X. Zhang, J. Chan, C. Wang, L. Guo, “Operation Optimization of Standalone Microgrids Considering Lifetime Characteristics of Battery Energy Storage System”, IEEE Trans. Sust. Energy, vol. 4, no., 4, pp. 934-943, October 2013. http://dx.doi.org/10.1109/TSTE.2013.2248400

[51] M. Gitizadeh, H. Fakharzadegan, “Battery capacity determination with respect to optimized energy dispatch schedule in grid-connected photocvoltaic (PV) systems”, Energy, vol. 65, pp. 665-674, February 2014. http://dx.doi.org/10.106/j.energy.2013.12.018

[52] E. Hittinger, T. Wiley, J. Kluza, J. Whitacre, “Evaluating the value of batteries in microgrid electricity systems using an improved Energy Systems Model”, Energy Conv. and Manag., vol. 89, pp. 458-472, January 2015. http://dx.doi.org/10.1016/j.enconman.2014.10.011

[53] A.F. Orlando, M.M. Huamaní, L. DoVala, J.V. Araujo, “A methodology for evaluating field performance and emissions of a gas microturbine based cogeneration system”, Engenharia Térmica, vol. 7, n. 1, pp.21-30, 2008.

[54] H. Kanchev, F. Colas, V. Lazarov, B. Francois, “Emission reduction and economical optimization of an urban microgrid operation including dispatched PV-based active generators”, IEEE Transactions On Sustainable Energy, vol. 5, no. 4, pp. 1397-1405, Oct. 2014. http://dx.doi.org/10.1109/TSTE.2014.2331712 .

[55] A. Rosato, S. Sibilio, “Calibration and validation of a model for simulating thermal and electric performance of an internal combustion engine-based micro-cogeneration device”, Applied Thermal Engineering, vol. 45-46, pp. 79-98, Dec. 2012. http://dx.doi.org/10.1016/j.applthermaleng.2012.04.020

[56] N. Badea, Design for Micro-Combined Cooling, Heating and Power Systems. London: Springer, 2015. http://dx.doi.org/10.1007/978-1-4471-6254-4

[57] Deliberazione AEEG 493/2012/R/efr “Approvazione delle modalità per l’attribuzione dei corrispettivi di sbilanciamento e dei corrispettivi a copertura dei costi amministrativi da attribuire ai produttori in regime di ritiro dedicato e di tariffa fissa onnicomprensiva”, 22 November 2012 (in Italian).

[58] A. Cagnano, E. De Tuglie, M. Dicorato, G. Forte, M. Trovato, “PrInCE Lab experimental microgrid - Planning and operation issues”, Proc. of 2015 IEEE 15th EEEIC Int. Conf., Rome, Italy, pp. 1671-1676, http://dx.doi.org/10.1109/EEEIC.2015.7165423 .

[59] http://www.wunderground.com/

[60] http://www.amgasbarisrl.it/ (in Italian)

[61] http://www.sendeco2.com .

[62] A. Bhatt, A. Shrivastava, M. Pandit, H. M. Dubey, “Dynamic Scheduling of Operating Energy and Reserve in Electricity Market with Ramp Rate Constraints”, in Proc. IEEE IET CRAIE-2014 Conf., Jaipur, India, May 2014, pp. 1-6. http://dx.doi.org/10.1109/ICRAIE.2014.6909313

[63] F. A. Bayer, G. Notarstefano, F. Allgower, “A Projected SQP method for Nonlinear Optimal Control with Quadratic Convergence”, Proc. of 52nd IEEE Conference on Decision and Control, December 10-13, 2013, Florence, Italy, pp. 6463-6468, http://dx.doi.org/10.1109/CDC.2013.6760912

[64] P. E. Gill., E. Wong, “Sequential quadratic programming methods”, in: J. Lee, S. Leyffer, “Mixed Integer Nonlinear Programming”, Vol. 147 of The IMA Volumes in Mathematics its Applications, Springer Science, 2012, pp. 147-224, http://dx.doi.org/10.1007/978-1-4614-1927-3_6

[65] J. Nocedal, S. J. Wright, “Numerical Optimization - Second Edition”. Springer Series in Operations Research, Springer Verlag, 2006.

[66] A. D. Belegundu, T. R. Chandrupatla, “Optimization Concepts and Applications in Engineering - Second Edition”, Cambridge University Press, 2011.

[67] D. P. Bertsekas, “Nonlinear Programming: 3rd Edition”, Athena Scientific, 2016.

[68] I. G. Moghaddam, M. Saniei, E. Mashhour, “A comprehensive model for self-scheduling an energy hub to supply cooling, heating and electrical demands of a building”, Energy, vol. 94, pp. 157-170, January 2016. http://dx.doi.org/10.1016/j.energy.2015.10.137

[69] R. Fourer, D. M. Gay, B. W. Kernighan, “AMPL: A Modeling Language for Mathematical Programming - Second Edition”, Duxbury Press / Brooks / Cole Publishing Company, 2003.

[70] D. E. Olivares et al., “Trends in microgrid control”, IEEE Trans. Smart Grid, vol. 5, no. 4, pp. 1905-1919, Jul. 2014.

[71] M. Almassalkhi et al., “Incorporating Storage as a Flexible Tranmission Asset in Power System Operation Procedure”, Proc. of 2016 PSCC Power Systems Computation Conference, 20-24 June 2016, pp. 1-7.

[72] L. Wang, P. Pourbeik, “Assessment of Power System Stability and Dynamic Security Performance”, in L. Grisby, “Power System Stability and Control - Third Edition”, CRC Press, 2012.

[73] W. Shi, X. Xie, C.-C. Chu, R. Gadh, “Distributed Optimal Energy Management in Microgrids”, IEEE Transactions on Smart Grid, vol. 3, no. 6, pp. 1137-1146, May 2015.

[74] C. Deckmyn, T. L. Vandoorn, M. Moradzadeh, L. Vandevelde,“Multi-objective optimization of environomic scheduling in microgrids”, Porc. of IEEE PES General Meeting 2014, 27-31 July 2014, pp. 1-5.

[75] B. Dag, A. R. Boynuegri, Y. Ates, A. Karakas, A. Nadar, M. Uzunoglu, “Static Modeling of Microgrid for Load Flow and Fault Analysis”, IEEE Trans. on Power Systems, Vol. 32, no. 3, pp. 1990-2000, May 2017.

[76] A. Elrayyah, Y. Sozer, M. E. Elbuluk, “A Novel Load-Flow Analysis for Stable and Optimized Microgrid Operation”, IEEE Transactions on Power Delivery, vol. 29, no. 4, pp. 1709-1717, Aug. 2014.

[77] W. Chen, A. M. Bazzi, J. Hare, S. Gupta, “Real-time integrated model of a micro-grid with distributed clean energy generators and their power electronics”, Proc. of 2016 IEEE APEC Conference, 20-24 March 2016, pp. 2666-2672.

[78] M. J. Hossain, H. R. Pota, M. A. Mahmud, M. Aldeen, “Robust Control for Power Sharing in Microgrids With Low-Inertia Wind and PV Generators”, IEEE Trans. on Sustainable Energy, Vol. 6, no. 3, pp. 1067-1077, July 2015.

[79] M. M. Mahfouz, A. A. El-Deib, M. El-Marsafawy, "Modeling and Stability Assessment of AC Microgrids Using Time-Domain Simulations", Proc. of 2016 IEEE POWERCON, pp. 1-6.

[80] H. Reza Baghaee, M. Mirsalim, G. B. Ghaerhpetian, H. A. Talebi, "Three-phase AC/DC power-flow for balanced/unbalanced microgrids including wind/solar, droop-controlled and electronically-coupled distributed energy resources using radial basis function neural networks", IET Power Electrocnics, Vol. 10, no. 3, 2017, pp. 313-328.

[81] T. Xia, L. He, N. An, M. Li, X. Li, "Electromechanical transient modeling research of energy storage system based on power system security and stability analysis ", Proc. of Powercon 2014 International Conference on Power System Technology, 20-22 Oct. 2014, Paper No CP1343, pp. 1-6.

[82] A. Ulbig, T. S. Borsche, G. Andersson, "Impact of Low Rotational Inetria on Power System Stability and Operation", IFAC Proceedings Volumes, Vol. 47, Issue 3, 2014, pp. 7290-7297.

[83] S. Dhopie, "Control of low-inertia AC microgrids", Proc. of 2017 CISS, 51st Annual Conference on Information Sciences and Systems, 22-24 March 2017, pp. 1-2.

[84] A. A. Moghaddam, H. Monsef, A. R. Kian, "Optimal smart home energy management considering energy saving and a comfortable lifestyle," IEEE Trans. Smart Grid vol. 6, no. 1, pp. 324-332, Jan. 2015.

[85] P. Mancarella, "MES (multi-energy systems): An overview of concepts and evaluation models," Energy , vol. 65, pp. 1-17, Feb. 2014.

[86] M. C. Bozchalui, S. A. Hashmi, H. Hassen, C. A. Canizares, K. Bhattacharya, "Optimal operation of residential energy hubs in smart grids," IEEE Trans. Smart Grid , vol. 3, no. 4, pp. 1755-1766, Dec. 2012.

[87] P. Asmus, "Microgrids, virtual power plants and our distributed energy future," Electricity J. vol. 23, pp. 72-82, 2010

[88] S. Chowdhury, S. P. Chowdhury, and P. Crossley, Microgrids and Active Distribution Networks. London, U.K.: The Institution of Engineering and Technology (IET), 2009.

[89] S. Cao, A. Mohamed, A. Hasan, K. Sirén, "Energy matching analysis of on-site micro-cogeneration for a single-family house with thermal and electrical tracking strategies," Energy and Buildings vol.68, part A, pp. 351-363, Jan. 2014.

[90] G. Comodi, A. Giantomassi, M. Severini, S. Squartini, F. Ferracuti, A. Fonti, D. N. Cesarini, M. Morodo, F. Polonara, "Multi- apartment residential microgrid with electrical and thermal storage devices: Experimental analysis and simulation of energy management strategies," Applied Energy, vol. 137, pp. 854-866, 2015.

[91] M. Bianchi, A. De Pascale, F. Melino, "Performance analysis of an integrated CHP system with thermal and Electric Energy Storage for residential application," Applied Energy, vol. 112, pp. 928-938, Dec. 2013

[92] Y Lu, S. Wang, Y. Sun C. Yan, "Optimal scheduling of buildings with energy generation and thermal energy storage under dynamic electricity pricing using mixed-integer nonlinear programming," Applied Energy, vol. 147, pp. 49-58, June 2015.

[93] C. Wouters, E. S. Fraga, A. M. James, "An energy integrated, multi-microgrid, MILP (mixed-integer linear programming) approach for residential distributed energy system planning-A South Australian case- study," Energy, vol. 85, pp. 30-44, Apr. 2015.

[94] C. Korkas, S. Baldi, I. Michailidis, E. B. Kosmatopoulos, "Intelligent energy and thermal comfort management in grid-connected microgrids with heterogeneous occupancy schedule," Applied Energy, vol. 149, p.p. 194-203, July 2015.

[95] L. Yang, N. Tai, C. Fan, Y. Meng, "Energy regulating and fluctuation stabilizing by air source heat pump and battery energy storage system in microgrid," Renewable Energy, vol. 95, pp. 202-212, Sept. 2016.

[96] S. Kawachi, J. Baba, H. Hagiwara, E. Shimoda, S. Numata, E. Masada, T. Nitta, "Energy capacity reduction of energy storage system in microgrid by use of heat pump: characteristic study by use of actual machine," in Proc. 2010 IEEE Int. Pow. Electron. and Motion Control Conf., pp.T11-52-T11-58.

[97] A. Jambagi, M. Kramer, V. Cheng, "Energy Storage within a Multi-Energy Carrier Optimisation Framework" in Proc. 2016 ENERGYCON Conf., 4-8 April 2016, pp. 1-6.

[98] C. Chowdhury, S.P. Chowdhury, P. Crossley, Microgrids and Active Distribution Networks. London, UK: IET, 2009.

[99] X. Jin, X. Wang, Y. Mu, H. Jia, X. Xu, Y. Qi, X. Yu, F. Qi, "Optimal scheduling approach for a combined cooling, heating and power building microgrid considering virtual storage system", in Proc. of 2016 PES GM Conf., 17-21 July 2016, pp. 1-5.

[100] Y. Li, J. Zuo, W. Mao, X. Guo, "The flexibility of Thermostatically Controlled Loads for Regulation", in Proc. of 2016 IEEE APPEEC Conf., Xi'an, China, 25-28 Oct. 2016,pp. 305-309.

[101] O. Ma, N. Alkadi, P. Cappers, P. Denholm, J. Dudley, S. Goli, M.Hummon, S. Kiliccote, J. MacDonald, N. Matson, D. Olsen, C. Rose, M. D. Sohn, M. Starke, B. Kirby, M. O'Malley, "Demand Response for Ancillary Services", IEEE Trans. Smart Grid, Vol. 4, Issue: 4, Dec. 2013, pp. 1988 - 1995.

[102] M. Mao, P. Jin, N. D. Hatziargyriou, L. Chang, "Multiagent-Based Hybrid Energy management System for MIcrogrids", IEEE Trans. Sust. Energy, Vol. 5, no. 3, pp. 938-946, July 2014.

[103] G. Dudek, "Pattern-based local linear regression models for short-term load forecasting", Electric Power Systems Research, Vol. 130, pp. 139-147, January 2016.

[104] A.S. Ahmad, M.Y Hassan, M.P. Abdullah, H.A. Rahman, F. Hussin, H. Abdullah, R. Saidur, "A review on applications of ANN and SVM for building electrical energy consumption forecasting", Renewable and Sustainable Energy Reviews, Vol. 33, May 2014, pp. 102-109.

[105] H. Chitsaz, H. Shaker, H. Zairepour, D. Wood, N. Amjady, "Short-term electricity load forecasting of buildings in microgrids", Energy and Buildings, Vol. 99, July 2015, pp. 50-60.

[106] ASHRAE Handbook - fundamentals. "Energy Estimation and modeling methods", 2009.

[107] L. G. Swan, V. I. Ugursal, "Modeling of end-use energy consumption in the residential sector: A review of modeling techniques", Renewable and Sustainable Energy Reviews, Vol. 13, n. 8, October 2009, pp. 1819-1835.

[108] H.X. Zhao, F. Magoulès, "A review on the prediction of building energy consumption", Renewable and Sustainable Energy Reviews, Vol. 16, no. 6, August 2012, pp. 3586-3592.

[109] A. Foucquier, S. Robert, F. Suard, L. Stéphan, A. Jay, "State of the art in building modelling and energy performances prediction: A review", Renewable and Sustainable Energy Reviews, Vol. 23, July 2013, pp. 272-288.

[110] N. Fumo, "A review on the basics of building energy estimation", Renewable and Sustainable Energy Reviews, Vol. 31, March 2014, pp. 53-60.

[111] M. L. Chalal, M. Benachir, M. White, R. Shrahily, "Energy planning and forecast approaches for supporting physical improvement strategies in the building sector: A review", Renewable and Sustainable Energy Reviews, Vol. 64, October 2016, pp. 761-776

[112] T. Fang, R. Lahdelma, "Evaluation of a multiple linear regression model and SARIMA model in forecasting heat demand for district heating system", Applied Energy, Vol. 179, October 2016, pp. 544-552.

[113] E. Shimoda, S. Numata, J. Baba, T. Nitta, E. Masada, "Operation planning and load prediction for microgrid using thermal demand estimation", in Proc. of 2012 IEEE PES GM Conf., pp. 1-7.

[114] K. M. Powell, A. Sriprasad, W. J. Cole., T. F. Edgar, "Heating, cooling, and electrical load forecasting for a large-scale district energy system", Energy, Vol. 74, Sept. 2014, pp. 887-885.

[115] R. Ž. Jovanović, A A. Sretenović, B. D. Živković, "Ensemble of various neural networks for prediction of heating energy consumption", Energy and Buildings, Vol. 94, May 2015, pp. 189-199.

[116] R. K. Jain, K. M. Smith, P. J. Culligan, J. E. Taylor, "Forecasting energy consumption of multi-family residential buildings using support vector regression: Investigating the impact of temporal and spatial monitoring granularity on performance accuracy", Applied Energy, Vol. 123, June 2014, pp. 168-178.

[117] E. Atam, "Current software barriers to advanced model-based control design for energy-efficient buildings", Renewable and Sustainable Energy Reviews, Vol. 73, June 2017, pp. 1031-1040.

[118] R.P. van Leeuwen, J. B. de Wit, J. Fink, G.J.M. Smit, "House thermal model parameter estimation method for Model Predictive Control applications", in Proc. of 2015 IEEE Eindhoven PowerTech Conf., pp. 1-6.

[119] H. Harb, J.-N. Paprott, P. Matthes, T. Schütz, R. Streblow, D. Müller, "Decentralized scheduling strategy of heating systems for balancing the residual load", Building and Environment, Vol. 86, April 2015, pp. 132-140.

[120] P. O. Kriett, M. Salani, "Optimal control of a residential microgrid", Energy, Vol. 42, no. 1, June 2012, pp. 321-330.

[121] R. Halvgaard, N. K. Poulsen, H. Madsen, J. B. Jørgensen, "Economic Model Predictive Control for building climate control in a Smart Grid", in Proc. of 2012 IEEE PES ISGT Conf., pp. 1-6.

[122] X. Ou, Y. Shen, Z. Zeng, G. Zhang, L. Wang, "Cost Minimization Online Energy management for Microgrids with Power and Thermal Storages", in Proc. of 2015 24th International Conference on Computer Communication and Networks (ICCCN), pp. 1-6.

[123] M. Kia, M. S. Nazar, M. S. Sepasian, A. Hediari, P. Siano, "Optimal day ahead scheduling of combined heat and power units with electrical and thermal storage considering security of power system", Energy, Vol. 120, February 2017, pp. 241-252.

[124] M. Tasdighi, H. Ghasemi, A. Rahimi-Kian, "Residential Microgrid Scheduling Based on Smart Meters Data and Temperature Dependent Thermal Load Modeling", IEEE Trans. Smart Grid, Vol. 5, no. 1, January 2014, pp. 349-357.

[125] F. Brahman, M. Honarmand, S. Jadid, "Optimal electrical and thermal energy management of a residential energy hub, integrating demand response and energy storage system", Energy and Buildings, vol. 90, March 2015, pp. 65-75.

[126] D. T. Nguyen, L. B. Le, "Optimal Bidding Strategy for Microgrids Considering Renewable Energy and Building Thermal Dynamics", IEEE Trans. Smart Grid, Vol. 5, no. 4, July 2014, pp. 1068-1620.

[127] D. Arcos-Aviles, J. Pasucal, L. Marroyo, P. Sanchis, F. Guinjoan, M.P. Marietta, "Optimal Fuzzy Logic EMS design for residential grid-connected microgrid with hybrid renewable generation and storage", in Proc. of 2015 IEEE 24th International Symposium on Industrial Electronics (ISIE), pp. 742-747.

[128] J. Yao, G. T. Costanzo, G. Zhu, B. Wen, "Power Admission Control With Predictive Thermal Management in Smart Buildings", IEEE Trans. Ind. Electronics, vol. 62, no. 4, 2015, pp. 2642 - 2650.

[129] H. T. Nguyen, D. T. Nguyen, L. B. Le, “Energy management for Households With Solar Assisted Thermal Load Considering Renewable Energy and Price Uncertainty”, IEEE Trans. Smart Grid, Vol. 6, no. 1, January 2015, pp. 301-314.

[130] G. Mantovani, L. Ferrarini, “Temperature Control of a Commercial Building With Model Predictive Control Techniques”, IEEE Trans. Ind. Electronics, vol. 62, no. 4, 2015, pp. 2651-2660.

[131] Q. Chen, R.-H. Fu, Y.-C. Xu, “Electrical circuit analogy for heat transfer analysis and optimization in heat exchanger networks”, Applied Energy, Vol. 139, February 2015, pp. 81-92.

[132] I. Hazyuk, C. Ghiaus, D. Penhouet, “Optimal temperature control of intermittently heated buildings using Model Predictive Control: Part I - Building modeling”, Building and Environment, vol. 51, May 2012, pp. 379-387.

[133] S. F. Fux, A. Ashouri, M. J. Benz, L. Guzzella, “EKF based self-adaptive thermal model for a passive house”, Energy and Buildings, vol. 68, part C, January 2014, pp. 811-817.

[134] M. Badami, G. Chicco, A. Dacio, A. Portoraro, F. Spertino, “Micro-Multigeneration Modelling and Operational Assessment for Residential Applications”, in Proc. of UPEC 2015 Conf., pp. 1-5.

[135] X. Xu, H. Jia, D. Wang, D. C. Yu, H.-D. Chiang, “Hierarchical energy management system for multi-source multi-product microgrids” Renewable Energy, vol. 78, June 2015, pp. 621-630.

[136] A. Zidan, H. A. Gabbar, A. Eldessouky, “Optimal planning of combined heat and power systems within microgrids”, Energy, vol. 93 Part 1, Dec. 2015, pp. 235-244.

[137] V. Lešić, A. Martinčević, M. Vašak, “Modular energy cost optimization for buildings with integrated microgrid”, Applied Energy, Vol. 197, July 2017, pp. 14-28.

[138] S. M. Hakimi, S. M. Moghaddas-Tafreshi, “Optimal Planning of a Smart Microgrid Including Demand Response and Intermittent Renewable Energy Sources”, IEEE Trans. Smart Grid, vol. 5, no. 6, Nov. 2014, pp. 2889-2900.

[139] J. Wang, H. Zhong, Q. Xia, C. Kang, E. Du, “Optimal joint-dispatch of energy and reserve for CCHP-based microgrids”, IET Generation, Transmission & Distribution, vol. 11, no. 3, 2017, pp. 785-794.

[140] J. Deboever, S. Grijalva, “Modeling and Optimal Scheduling of Integrated Thermal and Electric Energy Microgrid”, in Proc. of NAPS 2016 - North American Power Symposium, 18-20 Sept. 2016, Denver, CO, U.S.A., pp. 1-6.

[141] X. Jin, Y. Mu, H. Jia, J. Wu, T. Jiang, X. Yu, “Dynamic economic dispatch of a hybrid energy microgrid considering building based virtual energy storage system”, Applied Energy, Vol. 194, May 2017, pp. 386-398

[142] S. Ikeda, R. Ooka, “Metaheuristic optimization methods for a comprehensive operating schedule of battery, thermal energy storage and heat source in a building energy system”, Applied Energy, Vol. 151, Aug. 2015, pp. 192-205.

[143] W. Gu, Z. Wang, Z. Wu, Z. Luo, Y. Tang, J. Wang, “An Online Optimal Dispatch Schedule for CCHP Microgrids Based on Model Predictive Control”, IEEE Trans. On Smart Grids, DOI:10.1109/TSG.2016.2523504

[144] D. Arcos-Aviles, C. Vega, F. Guinjoan, L. Marroyo, P. Sanchis, “Fuzzy Logic Controller Design for Battery Energy Management in a Grid Controlled Electro-Thermal Microgrid”, Proc. of ISIE 2014 -IEEE 23rd International Symposium on Industrial Electronics, 1-4 June 2014, Istanbul (Turkey), pp. 2014-2019.

[145] L. Wang, Q. Li, R. Ding, M. Sung, G. Wang, "Integrated scheduling of energy supply and demand in microgrids under uncertainty: A robust multi-objective optimization approach", Energy, Vol. 130, July 2017, pp. 1-14.

[146] N.-O. Song, J.-H. Lee, H.-M. Kim, "Optimal Electric and Heat Energy Management of Multi-Microgrids with Sequentially-Coordinated Operations", Energies, vol. 9,(6), 2016, 473.

[147] EN 15251 "Indoor environmental parameters for assessment of energy performance of buildings, addressing indoor air quality, thermal environment, lighting and acoustics", 2006.

[148] M. De Rosa, V. Bianco, F. Scarpa, L. A. Tagliafico "Heating and cooling building energy demand evaluation; a simplified model and a modified degree days approach", Applied Energy, Vol. 128, Spet. 2014, pp. 217-229.

[149] P. Bacher, H. Madsen, "Identifying suitable models for the heat dynamics of buildings", Energy and Buildings, Vol. 43, no. 7, July 2011, pp. 1511-1522.

[150] G. Y. Yun, J. Choi, J. T. Kim, "Energy performance of direct expansion air handling unit in office buildings", Energy and Buildings, Vol. 77, July 2014, pp. 425-431.

[151] I. Korolja, L. Marjanovic-Halburd, Y. Zhang, V. I. Hanby, "UK office buildings archetypal model as methodological approach in development of regression models for predicting building energy consumption from heating and cooling demands", Energy and Buildings, Vol. 60, May 2013, pp. 152-162.

[152] R. Yumrutas, M. Unsal, "Energy analysis and modeling of a solar assisted house heating system with a heat pump and an underground energy storage tank", Solar Energy, Vol. 86, no. 3, March 2012, pp. 983-993.

[153] G. M. Masters, Renewable and Efficient Electric Power Systems, 2nd Edition, Wiley-IEEE Press, August 2013

[154] B. Zhao, X. Zhang, J. Chen, C. Wang, L. Guo, "Operation optimization of standalone Microgrids considering lifetime characteristics of battery energy storage system," IEEE Trans. Sust. Energy, vol. 4, no. 4, pp. 934-943, Oct. 2013.

[155] Z. Wang, L. Wang, A. I. Dounis, R. Yang, "Integration of plug-in hybrid electric vehicles into energy and comfort management for smart building", Energy Build. 47 (April) (2012) 260-266.

[156] S. Beer, T. Gomez, D. Dallinger, I. Momber, C. Marnay, M. Stadler, and J. Lai, "An economic analysis of used electric vehicle batteries integrated into commercial building microgrids," IEEE Trans. Smart Grid, vol. 3, no. 1, pp. 517-525, 2012.

[157] A. Gaviano, K. Weber, C. Dirmeier, "Challenges and integration of PV and wind energy facilities from a smart grid point of view," Energy Procedia, vol. 25, pp. 118-125, 2012.

[158] J. M. Guerrero, M. Chandokar, T. Lee, P. C. Loh, "Advanced control architectures for intelligent microgrids-Part I: Decentralized and hierarchical control," IEEE Trans. Ind. Electron., vol. 60, no. 4, pp. 1254-1262, Apr. 2013.

[159] Y. Wang, O. Sheikh, B. Hu, C.-C. Chu, R. Gadh, "Integration of V2H/V2G hybrid system for demand response in distribution network", in:2014 IEEE Int. Conf. on Smart Grid Communications, Nov. 2014, pp. 812-817.

[160] Y. Ota, H. Taniguchi, T. Nakajima, K.M. Liyanage, J. Baba, A. Yokoyama, "Autonomous distributed V2G (Vehicle-to-Grid) satisfying scheduled charging", IEEE Trans. Smart Grid 3 (March (1)) (2012) 559-564.

[161] E. Sortomme and M. A. El-Sharkawi, "Optimal charging strategies for unidirectional vehicle-to-grid," IEEE Trans. Smart Grid, vol. 2, no. 1, pp. 131-138, Mar. 2011.

[162] C. Sabillon Antunez, J.F. Franco, M.J. Rider, R. Romero "A New Methodology for the Optimal Charging Coordination of Electric Vehicles Considering Vehicle-to-Grid Technology." IEEE Trans. Sust. Energy, vol. 7, no. 2, pp. 596-607, Apr. 2016.

[163] A. Kavousi-Fard, T. Niknam, M. Fotuhi-Firuzabad, "Stochastic reconfiguration and optimal coordination of V2G plug-in electric vehicles considering correlated wind power generation", IEEE Trans. Sust. Energy, vol. 6, no. 3, pp. 822-830, Jul. 2015.

[164] M. González Vayá, G. Andersson, "Self Scheduling of Plug-In Electric Vehicle Aggregator to Provide Balancing Services for Wind Power," IEEE Trans. Sust. Energy, vol. 7, no. 2, pp. 886-899, Apr. 2016.

[165] Y. Wang, H. Nazaripouya, C.-C. Chu, R. Gadh, H.R. Pota, "Vehicle-to-grid automatic load sharing with driver preference in micro-grids", Proc. of 2014 IEEE PES ISGT Conf. Europe, Oct, 2014, pp. 1-6.

[166] L. Igualada, C. Corchero, M. Cruz-Zambrano, F.-J. Heredia, "Optimal Energy Management for a Residential Microgrid Including a Vehicle-to-Grid System," IEEE Trans. on Smart Grid, vol. 5, no. 4, pp. 2163-2172, Jul. 2014.

[167] V.N. Coelho, I. M. Coelho, B.N. Coelho, M. Weiss Cohen, A.J.R. Reis, S.M. Silva, M.J.F. Souza, P.J. Fleming, F.G. Guimarães, "Multi-objective energy storage power dispatching using plug-in vehicles in a smart-microgrid", Renewable Energy, vol. 89, April 2016, pp. 730-742.

[168] K. M. Tan, V. K. Ramachandaramurthy, J. Y. Yong, "Integration of electric vehicles in smart grid: a review on vehicle to grid technologies and optimization techniques" Renew. Sustain. Energy Rev. 2016, 53, pp. 720-732.

[169] W. Kempton, J. Tomic, "Using fleets of electric-vehicle for grid support". J Power Sources 2007; 168: pp. 459-468.

[170] A. Bracale, G. Carpinelli, F. Mottola, D. Proto, "Single-objective optimal scheduling of a low voltage microgrid: a minimum-cost strategy with peak shaving issues". In: 2012 11th Int. Conf. EEEIC, Venice; May 2012.

[171] A. Brooks, A. Lu, D. Reicher, J. Spirakis, B. Weihl, "Demand dispatch". IEEE Power Energy Mag 2010; vol. 8, pp. 20-29.

[172] Z. Liu, D. Wang, H. Jia, N. Djilali, W. Zhang, "Aggregation and Bidirectional Charging Power Control of Plug-in Hybrid Electric Vehicles: Generation System Adequacy Analysis", IEEE Trans. Sust. Energy, vol. 6 no. 4, pp. 325-335, 2015.

[173] T.N. Le, S. Al-Rubaye, Hao Liang, B.J. Choi, "Dynamic charging and discharging for electric vehicles in microgrids", in Proc. 2015 ICCW London; June 2015 p. 2018-2022.

[174] C. Deckmyn, J. Van de Vyver, T. L. Vandoorn, B. Meersman, J. Desmet, L. Vandevelde, "Day-ahead unit commitment model for microgrids", IET Generation, Transmission and Distribution, vol. 11, iss. 1, pp. 1-9, 2017.

[175] H. Kamankesh, V. G. Agelidis, A. Kavousi-Fard, "Optimal scheduling of renewable microgrid considering plug-in hybrid electric vehicle charging demand", Energy, vol. 100, pp. 285-297, 2016.

[176] H. Yang, H. Pan, F. Luo, J. Qiu, Y. Deng, M. Lai, Z. Y. Dong, "Operational Planning of Electric Vehicles for Balancing Wind Power and Load Fluctuations in a Microgrid", IEEE Transactions on Sustainable Energy, Vol. 8, no. 2, April 2017, pp. 592-604

[177] A. G. Anastasiadis, S. Kostantinopoulos, G. P. Kondylis, G. A. Vokas, "Electric vehicle charging in stochastic smart microgrid operation with fuel cell and RES units", International Journal of Hydrogen Energy (2017) http://dx.doi.org/j.ijhydene.2017.01.208

[178] P. Kou, D. Liang, L. Gao, F. Gao, “Stochastic Coordination of Plug-In Electric Vehicles and Wind Turbines in Microgrid: A Model Predictive Control Approach”, IEEE Transactions on Smart Grid, vol. 7, no. 3, May 2016, pp. 1537-1551.

[179] A. Ravichandran, S. Sirouspour, P. Malysz, A. Emadi, “A Chance-Constraints-Based Control Strategy for Microgrids with Energy Storage and Integrated Electric Vehicles”, IEEE Transactions on Smart Grid, DOI 10.1109/TSG.2016.2552173.

[180] S. M. Moghaddas Tafreshi, H. Ranjbarzadeh, M. Jafari, H. Khayyam, “A probabilistic unit commitment model for optimal operation of plug-in electric vehicles in microgrid”, Renewable and Sustainable Energy Reviews, vol. 66, pp. 934-947, 2016.

[181] E. Mortaz, J. Valenzuela, “Microgrid energy scheduling using storage from electric vehicles”, Electric Power Systems Research, vol. 143, pp. 554-562, 2017.

[182] S. Mohammadi, S., Soleymani, B. Mozafari, “Scenario-based stochastic operation management of MicroGrid including Wind, Photovoltaic, Micro-Turbine, Fuel Cell and Energy Storage Devices”, International Journal on Electric Power and Energy Systems, vol. 54, pp. 525-535, 2014.

[183] D. Wu, D.C. Alyprantis, L. Ying, “Load Scheduling and Dispatch for Aggregators of Plug-In Electric Vehicles”, IEEE Trans. Smart Grid, vol. 3, no. 1, March 2012, pp. 368-376.

[184] R.J. Bessa, M.A. Matos, “Forecasting issues for Managing a Portfolio of Electric Vehicles under a Smart Grid Paradigm, Proc. of 2012 IEEE ISGT Europe Conf., Berlin (Germany), pp. 1-8.

[185] M. He, M. Giesselmann, “Reliability-constrained Self-organization and Energy Management towards a Resilient Microgrid Cluster”, Proc. of IEEE PES ISGT 2015 Conf., 2015, pp. 1-5.

[186] C. Li, E. Schaltz, J. C. Vasquez, J. M. Guerrero, “Distributed Coordination of Electric Vehicle Charging in a Community Microgrid Considering Real-Time Price”, Proc. of IEEE EPE’16 ECCE Europe Conf., pp. 1-8.

[187] L. K. Panwar, S. R. Konda, A. Verma, B. K. Panigrahi, R. Kumar, “Operation window constrained strategic energy management of microgrid with electric vehicle and distributed resources”, IET Generation, Transmission and Distribution, vol. 11, iss. 3, pp. 615-626, 2017.

[188] S. Parhizi, A. Khodaei, M. Shahidehpour, “Market-based vs. Price-based Microgrid Optimal Scheduling”, IEEE Transactions on Smart Grid, DOI: 10.1109/TSG.2016.2558517

[189] J. E. Contreras-Ocaña, M. R. Sarker, M. A. Ortega-Vazquez, “Decentralized Coordination of a Building Manager and an Electric Vehicle Aggregator”, IEEE Transactions on Smart Grid, DOI: 10.1109/TSG.2016.2614768

[190] T. Sherkari, S. Golshannavaz, F. Aminifar, “Techno-Economic Collabroation of PEV Fleets in Energy Management of Microgrids”, IEEE Transactions on Power Systems, DOI: 10.1109/TPWRS.2016.2644201

[191] H.S.V.S. Kuman Nunna, S. Battula, S. Doolla, D. Srinivasan, “Energy Management in Smart Distribution Systems with Vehicle-to-Grid Integrated Microgrids”, IEEE Transactions on Smart Grid, DOI: 10.1109/TSG.2016.2646779

[192] V. Hosseinnezhad, M. Rafiee, M. Ahmadian, P. Siano, “Optimal day-ahead operational planning of microgrids”, Energy Conversion and Management, vol. 126, pp. 142-157, 2016

[193] J. Jung, R. P. Broadwater, “Current status and future advances for wind speed and power forecasting”, Renewable and Sustainable Energy Reviews, vol. 31, pp. 762-777, March 2014.

[194] W. Cabrera, D. Benhaddou, C. Ordonez, “Solar Power Preduition for Smart Community Microgrid”, Proc. of 2016 IEEE SMARTCOMP Conf., 18-20 May 2016, St. Louis, MO, U.S.A., pp. 1-6.

[195] A. Dolara, S. Leva, M. Mussetta, E. Ogliari, “PV hourly day-ahead power forecast in a micro grid context”, Proc. of 2016 IEEE EEEIC Conf., Florence, Italy, pp. 1-6

[196] M.J. Sanjari, H. Karami, H.B. Gooi, “Micro-generation dispatch in a smart residential multi-carrier energy system considering demand forecast error”, Energy Conversion and Management, vol. 120, pp. 90-99, 2016.

[197] A.A. Khan, M. Naeem, M. Iqbal, S. Qaisar, A. Anpalagan, “A compendium of optimization objectives, constraints, tools and algorithms for energy management in microgrids”, Renew. Sustain. Energy Rev. 2016, 58, pp. 1664-1683.

[198] C.L. Moreira, J.A. Peças Lopes, “MicroGrids Operation and Control under Emergency Conditions”, in: A. Keyhani, M. Marwali, “Smart Power Grids 2011”, Springer, 2012, pp. 351-399.

[199] M. Falahi, S. Lotfifard, M. Ehsani, K. Butler-Perry, “Dynamic Model Predictive-Based Energy Management of DG Integrated Distribution Systems”, IEEE Trans. Power Delivery, vol. 28, no. 4, October 2013, pp. 2217-2227.

[200] M. Restepo, C. A. Canizares, M. Kazerani, “Three-Stage Distribution Feeder Control Considering Four-Quadrant EV Chargers”, IEEE Transactions on Smart Grid, Accepted December 2016, http://dx.doi.org/10.1109/TSG.2016.2640202

[201] I. Gerami Moghaddam, M. Saniei, E. Mashhour, “A comprehensive model for self-scheduling an energy hub to supply cooling, heating and electrical demands of a building”, Energy, vol. 94, pp. 157-170, 2016.

[202] M. Reyasudin Basir Khan, R. Jidin, J. Pasupuleti, “Multi-agent based distributed control architecture for microgrid energy management and optimization”, Energy Conversion and Management, vol. 112, March 2016, pp. 288-307.

[203] J. Fedjaev, S. A. Amamra, B. Francois, “Linear Programming based optimization tool for day ahead energy management of a lithium-ion battery for an industrial microgrid”, Proc. of 2016 IEEE PEMC Conf. Varna, Bulgaria, 25-28 Sept. 2016, pp. 406-411.

[204] M. S. Mahmoud, F. M. Al-Sunni, “Control and Optimization of Distributed Generation Systems”, Springer, 2015.

[205] A. C. Luna, N. L. Diaz, L. Mengg. M. Graells, J. C. Vasquez, J. M. Guerrero, “Generation-Side Power Scheduling in a Grid-Connected DC Microgrid”, Proc. of IEEE IDCM’15 conf., pp. 1-6.

[206] A. Seaman, T.S. Dao, J. McPhee, “A survey of mathematics-based equivalent-circuit and electrochemical battery models for hybrid and electric vehicle simulation”, J. Power Sources, vol. 256, pp. 410-423, 2014

[207] NREL (2016), Energy Technology Cost and Performance Data of Distributed Generation: Distributed Generation Energy Technology Operations and Maintenance Costs. Available online: http://www.nrel.gov/analysis/tech_cost_om_dg.html

[208] W. Su, J. Wang, J. Roh, “Stochatic Energy Scheduling in Microgrids With Intermittent Renewable Energy Resources”, IEEE Transactions on Smart Grid, vol. 5, no, 4, pp. 1876-1883, July 2014

[209] C. Zhou , K. Qian , M. Allan, W. Zhou, “Modeling of the cost of EV battery wear due to V2G application in power systems”, IEEE Trans. Energy Conversion, vol. 26, no. 4, pp. 1041-1050, 2011.

[210] C. T. Nguyen, L. B. Le, “Optimal Bidding Strategy for Microgrids Considering Renewable Energy and Building Thermal Dynamics”, IEEE Transactions on Smart Grid, Vol. 4, no. 4, pp. 1608-1620, July 2014

[211] ISPRA, (2015), "Fattori di emissione per la produzione ed il consumo di energia elettrica in Italia", (in Italian). [Online]. Available: http://www.sinanet.isprambiente.it

[212] Idaho National Laboratory, "Nissan Leaf - VIN 0356, Advanced Vehicle Testing - Baseline Testing Results," Available online: http://avt.inel.gov/pdf/fsev/fact2011nissanleaf.pdf

[213] EERE, "Commercial and Residential Hourly Load Profiles for all TMY3 locations in the United States" [Online]. Available: http://en.openei.org/datasets/dataset

[214] J. Neubauer, E. Wood, "The impact of range anxiety and home, workplace, and public charging infrastructure on simulated battery electric vehicle lifetime utility", J. Pow. Sources, vol. 257, pp. 12-20, 2014.

[215] A. Hoke, A. Brissette, K. Smith, A. Pratt, D. Maksimovic, "Accounting for Lithium-Ion Battery Degradation in Electric Vehicle Charging Optimization", IEEE Journal of Emerging and Selectred Topris in Power Electronics", vol. 2, no. 3, pp. 691-700, September 2014.

[216] T. Gnann, P. Plötz, A. Kühn, M. Wietschel, "Modelling market diffusion of electric vehicles with real world driving data - German market and policy options", Transportation Research Part A, vol. 77, pp. 95-112, 2015.

[217] A. Schuller, B. Dietz, C. M. Flath, C. Weinhardt, "Charging strategies for battery electric vehicles: Economic benchmark and V2G potential", IEEE Trans. Power Syst., vol. 29, no. 5, pp. 2014-2022, 2014.

[218] F. A. Bayer, G. Notarstefano, F. Allgower, "A Projected SQP method for Nonlinear Optimal Control with Quadratic Convergence", Proc. of 25nd IEEE Conference on Decision and Control, December 10-13, 2013, Florence, Italy, pp.6463-6468,

[219] P. E. Gill., E. Wong, "Sequential quadratic programming methods", in: J: Lee, S. Leyffer, "Mixed Integer Nonlinear Programming", Vol. 147 of The IMA Volumes in Mathematics its Applications, Springer Science, pp. 147-224, 2012.

[220] M. A. Gonzalez Chapa, J. R. Vega Galaz, "An Economic Dispatch Algorithm For Cogeneration Systems", Proc. of 2004 IEEE PES General Meeting, 6-10 June 2004, pp. 1-5.

[221] R. M. A. Hollen, F. A. J. van den Bosch, H. V. Volberda, "Strategic levers of port autorities for industrial ecosystem development", Maritime Economic & logistics, vol. 17, no 1, pp. 79-96, 2015.

[222] M. Acciaro, H. Ghiara, M. I. Cusano, "Energy management in seaports: A new role for port authorities", Energy Policy, vol. 71, pp. 4-12, 2014.

[223] F. Ballini, "Port and Energy Management Challenges", World Maritime University, 2016.

[224] M. Puig, C. Woolridge, A. Michail, R. M. Darbra, "Current status and trends of environmental performance in European ports", Envirnomental Science & Policy, vol. 48, pp. 57-66, 2015.

[225] M. Boile, S. Theofanidis, E. Sdoukopoulos, N. Plytas, "Developing a port energy management plan: Issues, challenges and prospects", Transportation Research Record: Journal of Transportation Research Board, issue 2549, pp. 19-28, 2016.

[226] F. Ballini, R. Bozzo, "Air pollution from ships in ports: The socio-ecnomic benefit of cold-ironing technology", Research in Transportation Business & Management, vol. 17, pp. 92-98, 2015.

[227] T. Coppola, M. Fantauzzi, D. Lauria, C. Pisani, F. Quaranta, "A sustainable electrical interface to mitigate emissions due to power supply in ports", Renewable and Sustainalbe Energy Reviews, vol. 54, pp. 816-823, 2016.

[228] A. M. Kotrikla, T. Lilas, N. Nikitakos, "Abatement of air pollution at an aegean island port utilizing shore side electricity and renewable energy", Marine Policy, vol. 75, pp. 238-248, Jan. 2017.

[229] E. A. Sciberras, B. Zahawi, D. J. Atkinson, A. Juandò, A. Sarasquete, "Cold ironing and onshore generation for airborne emission reductions in ports", Porceedings of Institution of Mechanical Engineers Part M: Journal of Engineering for the Maritime Environment, pp. 1-16, 2014.

[230] G. Parise, L. Parise, L. Martirano, P. Ben Chavdarian, C.-L. Su, A. Ferrante, "Wise Port and Business Energy Management: Port Facilities, Electrical Power Distribution", IEEE Transactions on Industry Applications, vol. 52, no. 1, Jan./Feb. 2016, pp. 18-24

[231] J.S.L. Lam, T. Notteboom, "The greening of ports: a comparison of port management tools used by leading ports in Asia and Europe", Transport Reviews, Vol. 34(2), pp. 169-189, 2014.

[232] Italian Technical Rule UNI 10349 "Riscaldamento e raffrescamento degli edifici - Dati climatici - Parte 1" - 2016 (in Italian)

[233] Italian Ministerial Decree 23 June 2016, "Incentivazione dell'energia elettrica prodotta da fonti rinnovabili diverse dal fotovoltaico" (in Italian)

[234] energy.gov/sites/prod/files/2015/01/f19/fact2013nissanleaf.pdf

[235] Deliberation of Italian Authority of Electric Energy, Gas and Water System, n. 654/2015 "Regolazione tariffaria dei servizi di trasmissione, distribuzione e misura dell'energia elettrica, per il periodo di regolazione 2016-2023" (in Italian)

[236] F. Milano, "An open source Power System Analysis Toolbox", IEEE Transactions on Power Systems, vol. 20, no. 3, Aug. 2005, pp. 1199-1206.

[237] ISPRA - Italian Superior Institute on Envirnomental Protection, "National Inventory Report 2017 - Italian Greenhouse Gas Inventory 1990-2015"

[238] www.nissan.co.uk/vehicles/new-vehicles/leaf/charging-range.html

[239] avt.inl.gov/sites/default/files/pdf/fsev/SteadyStateLoadCharacterization2015Leaf.pdf

[240] www.astronergy.com/attch/product/VIOLIN_CHSM6610P+HV_40mm_frame_20160516.pdf

[241] www.wholesalesolar.com

[242] kokam.com/wp-content/uploads/2016/03/Kokam-Battery-Module-460-Series-Brochure.pdf

[243] J.M. Grothoff, "Battery Storage for Renewables: Market Status and Technology Outlook", International Renewable Energy Agency (IRENA), Technical Report (2015)

[244] A. Schroeder, T. Traber "The economics of fast charging infrastructure for electric vehicles", Energy Policy, vol. 43, pp. 136-144, Apr. 2012.

[245] www.autorita.energia.it/it/prezzi.htm

[246] www.mercatoelettrico.org

[247] Decree-Law of Puglia Region n. 45, 30 december 2013, "Disposizioni per la formazione del bilancio di previsione 2014 e bilancio pluriennale 2014-2016 della Regione Puglia" (in Italian)

[248] ACEA - European Automobile Manufacturing Organization, "Overview on tax incentives for electric vehicles in the EU", 2017.

[249] D. Salomonsson, A. Sannino, "Low-Voltage DC. Distribution system for commercial power system with sensitive electronics loads" IEEE Transactions on Power Delivery 2007;22 :1620-7.

[250] P. Loh , Li D, Chai YK, Blaabjerg F. Autonomous operation of hybrid microgrid with AC and DC sub-grids. In: IEEE transactions on power electronics, '99, Early access.

[251] T.L.Vandoon , Meersman B, Degroote L, Renders B, Vandevelde L. A control strategy for islanded microgrids with DC-link voltage control. IEEE Transac- tions on Power Delivery 2011;26(2):703-13.

[252] J.M. Guerrero, Vasquez JC, Matas J, Garcia de Vicuna L, Castilla M. Hierarchical control of droop-controlled AC and DC microgrids-a general approach toward standardization. IEEE Transactions on Industrial Electronics 2011;58(1): 158-172.

[253] O. Erdinc , Uzunoglu M. “Optimum design of hybrid renewable energy systems: overview of different approaches”. Renewable and Sustainable Energy Reviews 2012;16(3):1412-25.

[254] A. Chakraborty, Advancements in power electronics and drives in interface with growing renewable energy resources. Renewable and Sustainable Energy Reviews 2011;15(4):1816-27.

[255] J.A. Baroudi, V. Dinavahi, A. Knight, “A review of power converter topologies for wind generators”. Renewable Energy, 2007;32:2369-85.

[256] J. Arai et al, “Power electronics and its application to renewable energy in Japan”, IEEE Circuits and Systems Magazine 2008;8(3):52-66.

[257] K. Sun, Zhang L, Xing Y, Guarrero JMA, “Distributed control strategy based on DC bus signaling for modular photovoltaic generation system with battery energy storage”, IEEE Transactions on Power Electronics 2011;26(10): 3032-3045.

[258] P. Biczel, “Power electronic converters in a DC microgrid”. In: 5th International conference - workshop - CPE; 2007.

[259] L. Xu, D. Chen , “Control and operation of a DC microgrid with variable generation and energy storage”, IEEE Transactions on Power Delivery 2011;26(4):2513-22.

[260] J. Lago , ML Heldwein, “Operation and control-oriented modeling of a power converter for current balancing and stability improvement of DC active distribution networks”, IEEE Transactions on Power Electronics 2011;26(3): 877-885.

[261] F. Katiraei , MR Iravani, PW Lehn, “Micro-grid autonomous operation during and subsequent to islanding process”, IEEE Transactions on Power Delivery 2005;20(1):248-57.

[262] M.E. Baran , Mahajan NRDC, “Distribution for industrial system: opportunities and challenges”, IEEE Transactions on Industry Applications 2003;39(6) 1596-1601.

[263] R. Noroozian, M Abedi, GB Gharehpetian, SH Hosseini, “Combined operation of DC isolated distribution and PV system for supplying unbalanced AC loads”, Renewable Energy 2009;34:899-1008.

[264] R. Noroozianar et al., “Distribution resources and DC distribution system combination for high power quality”, Electrical Power and Energy System 2010, 32:769-81.

[265] A. Kwasinski, CN Onwuchekwa, “Dynamic behavior and stabilization of DC microgrids with instantaneous constant-power loads”, IEEE Transactions on Power Electronics 2011, 26(3):822-34.

[266] C. Cho, Jeon JH, Kim JY, Kwon S, Park K, Kim S. Active synchronizing control of a microgrid. IEEE Transactions on Power Electronics 2011, 26 (12):3707-19.

[267] L.Chunhua, et al. “A new DC micro-grid system using renewable energy and electric vehicles for smart energy delivery”, in proc. IEEE 2010 IEEE Vehicle Power and Propulsion Conference; 2010. p. 1-6.

[268] T.S. Ustun, C. Ozansoy, A. Zayegh, “Modeling of a centralized microgrid protection system and distributed energy resources according to IEC 61850-7-420”, IEEE Transactions on Power Systems 2012;27(3):1560-7.

[269] D. Salomonsson, L. Soder, A. Sannino, “Protection of low-voltage DC microgrids”, IEEE Transactions on Power Delivery 2009;24(3):1045-53.

[270] E. Sortomme, S. Venkata, J. Mitra, “Microgrid protection using communication- assisted digital relays”, IEEE Transactions on Power Delivery 2010;25(4): 2789-2796.

[271] V. Peesapati, I. Cotton, T. Sorensen, T. Krogh, N. Kokkinos, “Lightning protection of wind turbines - a comparison of measured data with required protection levels”, IET Renewable Power Generation 2011, 5(1):48-57.

[272] P. Basak, S. Chowdhury, Dey SH, S.P. Chowdhury, “A literature review on integration of distributed energy resources in the perspective of control, protection and stability of microgrid”, Renewable and Sustainable Energy reviews 2012;16:5545-56.

[273] S.P. Chowdhury, S Chowdhury, CF Ten, PA Crossley, “Islanding protection of distribution systems with distributed generators-a comprehensive survey report”, In: Power and Energy Society meeting, 2008. p. 1-8.

[274] H. J. Laaksonen, “Protection principles for future microgrids”, IEEE Transactions on Power Electronics 2010, 25(12):2910-8.

[275] R. Viral, D.K. Khatod, “Optimal planning of distributed generation systems in distribution system: a review”, Renewable and Sustainable Energy Reviews 2012, 16(7):5146-65.

[276] M. Stadler et al. “Optimal planning and operation of smart grids with electric vehicle interconnection”, Journal of Energy Engineering 2012, 138(2):1-16.

[277] G. Benysek, M. Jarnut, “Electric vehicle charging infrastructure in Poland”, Renewable and Sustainable Energy Reviews 2012;16(1):320-8.

[278] M. Tabari, A. Yazdani, “A DC distribution system for power system integration of plug-in hybrid electric vehicles”, in: IEEE Power and Energy Society General Meeting (PES), 2013, pp. 1-5.

[279] A. Mohamed, V. Salehi, T. Ma, O. Mohammed, “Real-time energy management algorithm for plug-in hybrid electric vehicle charging parks involving sustainable energy”, IEEE Trans. Sustain. Energy 5 (2014) 577-586.

[280] B.E. Noriega, R.T. Pinto, P. Bauer, “Sustainable DC-microgrid control system for electric-vehicle charging stations”, in: 15th European Conference on Power Electronics and Applications (EPE), 2013, pp. 1-10.

[281] L. Roggia, C. Rech, L. Schuch, J.E. Baggio, H.L. Hey, J.R. Pinheiro, “Design of a sustainable residential microgrid system including PHEV and energy storage device”, in: 14th European Conference on Power Electronics and Applications (EPE), 2011, pp. 1-9.

[282] J.C. Rosas-Caro J.M. Ramirez F.Z. Peng A. Valderrabano, “A DC-DC multilevel boost converter", IET Power Electronics, 3 (2010), pp. 129-137

[283] Y. Du, X. Zhou, S. Bai, S. Lukic, and A. Huang, “Review of nonisolated bi-directional DC-DC converters for plug-in hybrid electric vehicle charge station application at municipal parking decks,” in Proc. IEEE Appl. Power Electron. Conf., Feb. 2010, pp. 1145-1151.

[284] A. H. Gabbar, AA Abdelsalam, “Microgrid energy management in grid-connected and islanding modes based on SVC”, Energy Conversion and Management. 2014;86:964-972.

[285] N. Zhang et al. “A review of topologies of three-port DC-DC converters for the integration of renewable energy and energy storage system”, Renew. Sustain. Energy Rev. 2016, 56, 388-401.

[286] Z. Qian, O. Abdel-Rahman, H. Hu, and I. Batarseh, “An integrated threeport inverter for stand-alone PV applications,” in Proc. IEEE Energy Convers. Congr. Expo., Sep. 2010, pp. 1471-1478.